RRDOPHSING01 - Research Degree: Institute of Ophthalmology
UCL Faculty of Brain Sciences – Institute of Ophthalmology

Neurodegeneration and Adaptation in Late Onset Sight Loss

Insights from MRI into Leber Hereditary Optic Neuropathy (LHON)

Hugo Thomas Chow-Wing-Bom ([redacted])

Supervisors: Dr Tessa Dekker, Prof Frederic Dick, Prof Martina Callaghan, and Dr Patrick Yu-Wai-Man

31st May 2025

Thesis submitted for the degree of Doctor of Philosophy

Declaration

“I, Hugo Chow-Wing-Bom, confirm that the work presented in my thesis is my own. Where information has been derived from other sources, I confirm that this has been indicated in the thesis.”

Abstract

Leber Hereditary Optic Neuropathy (LHON) is a mitochondrial disorder that leads to rapid central vision loss through degeneration of retinal ganglion cells. While structural MRI studies have identified volumetric and white matter changes along the visual pathways, the underlying microstructural mechanisms – whether demyelination, axonal loss, or both – remain unclear. Additionally, large central scotomas and associated fixation difficulties complicate the measurement of visual function, resulting in limited functional measures and understanding of visual processing in LHON.

This thesis addresses these gaps using advanced structural and functional MRI approaches to characterise changes beyond the retina in LHON. First, diffusion MRI and multi-parametric mapping (MPM) were combined with biophysical modelling to disentangle axonal and myelin loss along the visual pathways. Results showed concurrent axonal degeneration and demyelination in the optic tracts, and widespread axonal disruption with localised demyelination near V1 in the optic radiations. These changes were accompanied by volume loss in the lateral geniculate nucleus and V1, particularly in regions representing central vision.

Second, I developed a large-field fMRI approach to map contrast sensitivity across the visual field at the cortical level. This method, combining a contrast sensitivity task with population receptive field (pRF) mapping, reliably captured known sensitivity gradients across the visual field (up to 20º eccentricity) in normal-sighted individuals. Crucially, these patterns were preserved when using a fixation-free retinotopic atlas, enabling application in patients with impaired fixation. This approach yielded repeatable, eye-specific cortical sensitivity maps and showed partial correspondence with behavioural and retinal measures.

Overall, this work provides new insights into the microstructural mechanisms underlying neural changes along the visual pathways and introduces a novel fixation-free, brain-based approach for mapping visual field defects in LHON. These tools offer potential sensitive outcome measures, crucial for tracking disease progression and evaluating therapeutic efficacy, especially given promising sight recovery from gene-therapy.

Impact Statement

This PhD work introduces new methods and insights to better understand how the brain is affected in Leber Hereditary Optic Neuropathy (LHON), a rare genetic condition that causes sudden and severe central vision loss. While LHON is known to damage the retina, this work shifts the focus to the brain, using advanced MRI techniques to study how the visual system changes after vision loss. The findings reported in this thesis could benefit both scientific research and clinical development, with broader implications for public health, medical innovation, and patient quality of life.

A key achievement of this PhD work is the development of a large-field visual stimulation set-up for functional MRI, without requiring expensive, external devices (e.g., MRI-compatible goggles) or steady fixation – making it suitable for individuals with drastic, central vision loss. Combined with an approach to measuring visual function in the brain, this method enables non-invasive mapping of visual field defects and could be used to track changes over time or in response to treatment. Another major contribution of this PhD work is the use of advanced structural MRI techniques to characterise the neural mechanisms underlying tissue damage along the visual pathways in LHON. By combining these scans with models of brain tissue, this research provides new evidence of both nerve fibre damage and loss of protective myelin in LHON. This offers a more detailed understanding of how the disease affects the brain beyond the eye.

Within academia, this research contributes to vision science, neuroimaging, and neurodegeneration, and introduces methods that can be adapted to other conditions involving central and peripheral vision loss, or grey and white matter damage. It also supports future research into brain plasticity, rehabilitation, and sensory processing. It offers a framework for investigating visual processes across a large expanse of the visual field in typical and atypical populations, as well as understanding how the brain adapts to sudden sensory loss.

The broader impact lies in improving how we evaluate new treatments and addresses a need for non-invasive biomarkers to monitor disease progression and treatment response in eye diseases. While the methods developed in this PhD are not intended for routine clinical use due to the cost and complexity of MRI, they are designed to support research and clinical trials, especially in rare diseases like LHON

where sensitive and objective outcome measures are essential. The outcome measures developed here could help assess the effectiveness of emerging treatment – such as gene or neuroprotective therapies – by providing objective, brain-based markers of change.

Dissemination of this research is ongoing through peer-reviewed publications, conference presentations, and open-access tools. Future impact will be driven by continued collaboration with clinicians, researchers, industry partners, and patient communities. This work lays the foundation for future translational research and interdisciplinary collaborations that bridge basic science and clinical application, deepen our understanding of disease, and ultimately could lead to meaningful improvements in patient care.

UCL Research Paper Declaration Form #1 referencing the doctoral candidate's own published work(s)

For more information: https://www.grad.ucl.ac.uk/essinfo/guidance-on-selfplagiarism/

1. **For a research manuscript that has already been published** (if not yet published, please skip to section 2)

   a) **What is the title of the manuscript?**

   Neuroimaging in LHON: State-of-the-art and Future Prospects

   b) **Please include a link to or doi for the work**

   https://doi.org/10.1016/j.nicl.2022.103240

   c) **Where was the work published?**

   NeuroImaging: Clinical

   d) **Who published the work?** (e.g. OUP)

   Elsevier Inc.

   e) **When was the work published?**

   2022

   f) **List the manuscript's authors in the order they appear on the publication**

   Hugo T. Chow-Wing-Bom, Martina F. Callaghan, Junqing Wang, Shihui Wei, Frederic Dick, Patrick Yu-Wai-Man, Tessa M. Dekker

   g) **Was the work peer reviewed?**

   Yes

   h) **Have you retained the copyright?**

   Creative Commons CC-BY license (CC BY 4.0)

   i) **Was an earlier form of the manuscript uploaded to a preprint server?** (e.g. medRxiv). If 'Yes', please give a link or doi)

   No

   If 'No', please seek permission from the relevant publisher and check the box next to the below statement:

   ☒

*I acknowledge permission of the publisher named under **1d** to include in this thesis portions of the publication named as included in **1c**.*

2. **In which chapter(s) of your thesis can this material be found?**

   Chapter 1: Introduction

3. **e-Signatures confirming that the information above is accurate** (this form should be co-signed by the supervisor/ senior author unless this is not appropriate, e.g. if the paper was a single-author work)

Candidate
Hugo Chow-Wing-Bom
Date: 30th May 2025

Supervisor/ Senior Author (where appropriate)
Tessa Dekker
Date: 30th May 2025

UCL Research Paper Declaration Form #2 referencing the doctoral candidate's own published work(s)

1. **For a research manuscript that has already been published** (if not yet published, please skip to section 2)

   j) **What is the title of the manuscript?**

   Mapping Visual Contrast Sensitivity and Vision Loss Across the Visual Field with Model-Based fMRI

   k) **Please include a link to or doi for the work**

   https://doi.org/10.7554/eLife.105930.1

   l) **Where was the work published?**

   eLife

   m) **Who published the work?** (e.g. OUP)

   eLife Sciences Publications Ltd.

   n) **When was the work published?**

   2025

   o) **List the manuscript's authors in the order they appear on the publication**

   Hugo T. Chow-Wing-Bom, Matteo Lisi, Noah C. Benson, Freya Lygo-Frett, Patrick Yu-Wai-Man, Frederic Dick, Roni O. Maimon-Mor, Tessa M. Dekker

   p) **Was the work peer reviewed?**

   Y

   q) **Have you retained the copyright?**

   Creative Commons CC-BY license (CC BY 4.0)

   r) **Was an earlier form of the manuscript uploaded to a preprint server?** (e.g. medRxiv). If 'Yes', please give a link or doi)

   Yes, https://doi.org/10.1101/2024.10.29.619403 (BioRxiv)

   If 'No', please seek permission from the relevant publisher and check the box next to the below statement:

   ☐

*I acknowledge permission of the publisher named under **1d** to include in this thesis portions of the publication named as included in **1c**.*

2. **In which chapter(s) of your thesis can this material be found?**

   Chapter 3: Mapping cortical contrast sensitivity across the visual field: method implementation and validation in simulated and pathological vision loss

3. **e-Signatures confirming that the information above is accurate** (this form should be co-signed by the supervisor/ senior author unless this is not appropriate, e.g. if the paper was a single-author work)

Candidate

Hugo Chow-Wing-Bom

Date: 30th May 2025

[redacted]

Supervisor/ Senior Author (where appropriate)

Tessa Dekker

Date: 30th May 2025

[redacted]

Acknowledgment

This work was generously funded by Moorfields Eye Charity PhD Studentship (GR001315; London, UK) and the Birkbeck-UCL Centre for NeuroImaging (BUCNI; London, UK).

First and foremost, I am extremely thankful to my supervisors, Dr. Tessa Dekker, Prof. Frederic Dick, Prof. Martina Callaghan, and Dr. Patrick Yu-Wai-Man, for their invaluable guidance, support, and encouragement throughout this journey. I am especially grateful to Dr. Tessa Dekker for believing in me in 2017, when I started as a research assistant, and again a few years later when I began my PhD in her lab. Her tireless support, scientific insight, and dedication have been a constant source of inspiration: from her expertise in neuroscientific experimentation and MRI scanning to her dedication to research, which continually inspires me to grow into the scientist I aspire to become. I am also sincerely thankful to Prof. Frederic Dick and Prof. Martina Callaghan for sharing their deep knowledge of state-of-the-art MRI methodologies, and to Dr. Patrick Yu-Wai-Man for welcoming me into his clinical team and enriching my PhD experience with invaluable clinical knowledge and hands-on exposure.

I would like to acknowledge Prof. John Greenwood and Dr. Velia Cardin for their guidance as part of my thesis committee team, as well as Dr. Noah Benson, Dr. Freya Lygo-Frett, and Prof. Siawoosh Mohammadi and his team for their collaborative spirit and contributions throughout this project. I am also grateful to Prof Antony Morland and Dr Sara Ajina for agreeing to examine this thesis.

I extend my thanks to Dr Simon Richardson, Dr Oliver Josephs, and Dr Joerg Magerkurth at BUCNI for their technical expertise and support in developing the large-field fMRI setup, and to Dr Davide Bono for providing my MRI operator training. I also thank the Clinical Research Facility at the Moorfields Eye Hospital for granting access to their facilities and training me in the use the Compass perimetry device.

To my colleagues at the Child Vision Lab – thank you for your insightful contributions, consistent support, stimulating discussions, and for all the fun we had in the last few years. I am especially grateful to Letitia Schneider, Kim Staübli, and Oris Shenyan, for their daily encouragement and assistance with MRI data collection.

I am also deeply grateful to the patients and their families, who generously gave their time, energy, and effort to participate in this research. Their involvement and support have been essential to the success of this project.

Last but not least, I am profoundly thankful to my incredible parents, my brother, and my friends for their unconditional love, emotional support, and unwavering belief in me and my career aspirations. Despite the thousands of kilometres and oceans that separate us, their encouragement and infectious joie de vivre have been a guiding light, helping me navigate the long and challenging tunnel of my PhD journey, and ultimately leading me toward the light at the end.

Table of Contents

Table of Figures

Table of Tables

Table of Equations

Abbreviations

ACID: Artefact correction in diffusion MR
AD: Axial diffusivity
ATP: Adenosine triphosphate
BOLD: Blood-oxygenation level dependent
CSF: Cerebral spinal fluid/Contrast sensitivity function
Cpd: cycle per degree
(mt)DNA: (Mitochondrial) Deoxyribonucleic acid
DTI/DKI: Diffusion tensor/kurtosis imaging
EEG: Electroencephalography
FA: Fractional anisotropy
GM: Grey matter
LHON: Leber hereditary optic neuropathy
LGN: Lateral geniculate nucleus
LogMAR: Logarithm of the minimum angle of resolution
MD: Mean diffusivity
(d/f/q)MRI: (Diffusion/Functional/Quantitative) Magnetic resonance imaging
MS: Multiple sclerosis
MT(sat/R): Magnetisation transfer (saturation/ratio)
OCT: Optical coherence tomography
PD: Proton density
PET: Positron emission tomography
R1/T1: Longitudinal relaxation rate/time
R2*/T2*: Effective transverse relaxation rate/time
RD: Radial diffusivity
RGC: Retinal ganglion cell
RNFL: Retinal nerve fibre layer
(p)RF: Radio frequency/(Population) receptive field
SPM: Statistical parametric mapping
V1, V2, V3: Primary, secondary, tertiary visual cortices
VA: Visual acuity
WM: White matter

1. Introduction

The overall aim of this PhD thesis is (i) to better understand how Leber Hereditary Optic Neuropathy (LHON) impact the brain and (ii) to develop new end point to monitor changes in function and structure. Meeting these two objectives is particularly timely given the emergence of therapeutic options for LHON.

In this section, I am introducing LHON, providing an overview of its clinical features and the current treatment landscape. I then provide a review of MRI-based studies, which I published in *NeuroImage: Clinical* in 2022. This review explores the effects of LHON at the level of the brain, highlighting structural changes along the visual pathways and identifying gaps in our understanding of its mechanisms and treatment outcomes. Drawing on the conclusions of this review, I outline the specific objectives of this PhD, which aims to address these critical gaps and advance the field.

Leber Hereditary Optic Neuropathy (LHON) is a primary mitochondrial DNA (mtDNA) disorder characterised by bilateral subacute loss of central vision (Yu-Wai-Man & Chinnery, 2000; Carelli et al., 2019). The pathological hallmark is the preferential loss of retinal ganglion cells (RGCs) within the inner retina, causing optic nerve degeneration and loss of vision. The prevalence of this mitochondrial optic neuropathy is ~1 in 31,000 to 50,000 in the Northern European population (Yu-Wai-Man et al., 2003; Puomila et al., 2007). As the most common inherited optic neuropathy, LHON is an important cause of inherited blindness in young adults, with a higher prevalence in males, and a peak age of onset between the ages of 15-35 years (Yu-Wai-Man & Chinnery, 2000; Yu-Wai-Man et al., 2016; Carelli et al., 2019). Whilst promising regenerative therapies are currently being developed, idebenone is the only approved treatment to date for LHON. Idebenone stimulates ATP production by bypassing the complex I of the mitochondrial respiratory chain, which is impaired in LHON (Catarino & Klopstock, 2017), resulting in varying degrees of visual acuity improvements. Although most patients with LHON will develop isolated optic nerve involvement, a subgroup of patients manifest additional neurological features as part

of a syndromic “LHON plus” phenotype, or features associated with multiple sclerosis-like illness. Given the major role that the central visual pathways play in visual function, disease progression beyond the retina may contribute substantially to the prognosis of LHON.

Given its flexibility and high spatial resolution, Magnetic Resonance Imaging (MRI) is a particularly valuable imaging modality for uncovering the effects of LHON on central visual pathways. In particular, MRI makes it possible to localise brain regions, structures, and processes linked to specific types of visual field loss. Recent structural and functional MRI studies of LHON have identified widespread pathological changes in different stages of the disease process, and across the visual system, from the optic tracts to the cortex (Barcella et al., 2010; Manners et al., 2015; Takemura et al., 2019; Long et al., 2019; Jonak, Krukow, Symms, et al., 2020). These studies employ various informative MRI methodologies, which can answer important open questions about LHON. However, only a few of these methodologies are routinely used in clinics. As a result, techniques and approaches that could contribute to treatment and rehabilitation design may be overlooked. In this review, we discuss the new insights into the underlying pathophysiology that these studies provide, the important open questions that could be addressed using new MRI methods, and the challenges that need to be overcome to do so.

Specifically, we evaluate what is currently known from MRI research about the following questions about the neural mechanisms of LHON:

- Which changes in neural function and structure occur beyond the retinal ganglion cell layer in LHON, and when do they occur in time, i.e., when in the disease do changes in post-retinal brain structures from optic nerve to visually driven cortex occur?
- What are the mechanistic causes of these neural changes in LHON, and which microstructural processes might they reflect, i.e., demyelination and axonal loss?
- How do changes in neural structure and function predict visual outcome?
- What are the key challenges and limitations for current MRI research on LHON?
- What are the most important open questions about LHON that MRI could help resolve in the future?

By addressing these questions, we aim to provide a more comprehensive picture of the neural mechanisms of LHON than can be offered by RGC pathology in the retina alone. Given the key role post-retinal pathways play in visual function, these insights and methods may help inform prognoses and increase understanding of how, when, and why treatments work best. This is particularly important and timely in the light of new regenerative therapies (i.e., gene therapies; see response to Q5 in section 4) currently being developed for LHON, which would benefit from this knowledge. Other neuroimaging modalities such as electroencephalography (EEG) or positron emission tomography (PET) have also been used to study LHON but go beyond the scope of this review.

1.1. Genetics & clinical features of LHON

Leber Hereditary Optic Neuropathy (LHON) is primarily due to one of three pathogenic mtDNA mutations: m.11778G>A (most common), m.14484T>C, and m.3460G>A. These mutations impair NADH dehydrogenase activity in complex I of the mitochondrial respiratory chain, leading to reduced energy production within mitochondria. The resulting disruption in oxidative phosphorylation particularly affects the mitochondria of retinal ganglion cells (RGCs), with a preference for those within the papillomacular bundle, ultimately causing degeneration of RGCs and optic nerve axons. In a smaller proportion of cases where patients test negative to all common mutations, whole mitochondrial genome sequencing can help with the diagnosis of the disease (Moore & Yu-Wai-Man, 2021). Although LHON is commonly caused by point mutations in the mitochondrial DNA, patients with LHON-like phenotypes sometimes carry recessive nuclear genes (Moore & Yu-Wai-Man, 2021; Stenton et al., 2021). These diverse genetic aetiologies paint a more complex picture of LHON than was previously portrayed and highlight the challenges for diagnosis in some cases.

All types of RGCs (i.e., parvocellular, magnocellular and koniocellular cells) are impacted in LHON; however, parvocellular (P) cells within the papillomacular bundle are usually the most affected at early stages of the disease (i.e., acute phase), likely due to fewer mitochondria and smaller axons (Sadun et al., 2000; Pan et al., 2012; Majander et al., 2017). As a result of this, central vision rapidly deteriorates bilaterally, and colour vision and contrast sensitivity to high spatial frequencies are greatly diminished (Carelli et al., 2019). Optical Coherence Tomography has also revealed

dynamic LHON-related changes of the retinal fibre nerve layer (RNFL), with initial thickening during the asymptomatic and early acute phases (particularly in the temporal and inferior quadrants), followed by a thinning of the RNFL as the disease progresses to the chronic phase (Savini et al., 2005; Barboni et al., 2005; Zhang et al., 2014). Other clinical characteristics of LHON include pallor and increased blood flow (i.e., hyperaemia) in the optic disc, and tortuosity of the central retinal vessels (Yu-Wai-Man & Chinnery, 2000; Sadun et al., 2000; Savini et al., 2005; Barboni et al., 2005; Zhang et al., 2014; Majander et al., 2017; Carelli et al., 2019). There is also evidence for oedema of the optic nerve during the acute phase (Frisen, 2017; Blanc et al., 2018).

Clinical observations of LHON progression have led to the description of four different stages (Carelli et al., 2019): 1) asymptomatic (LHON carriers with no clinically significant symptoms); 2) subacute (<6 months after clinical onset); 3) dynamic (6-12 months after clinical onset); and 4) chronic (>12 months after clinical onset). From here on, we will use the term *acute* to describe the period within the first year after clinical onset of the disease (i.e., encapsulating both subacute and dynamic phases), which is mainly characterised by the loss of RGCs.

In some cases, however, loss of vision is not definitive. A proportion of LHON patients (less than 20%, all genotypes combined) experiences spontaneous visual recovery up to typical visual acuity levels a few years after disease onset (Carelli et al., 2019; Zuccarelli et al., 2020). A recent meta-analysis by Newman et al. (2020), which combined results from 12 prospective and 3 retrospective studies for a total of 695 LHON patients, all harbouring the m.G11778A variant, revealed that about 14% of these patients presented a history of visual recovery, although some may be due to idebenone use. Most frequent recovery has been observed in those carrying the relatively rare m.T14484C variant (~40-70% of recovery cases; Carelli et al., 2019; Zuccarelli et al., 2020), raising the question of why spontaneous recovery is less frequent in patients with the G11778A variant compared to those with rarer forms of LHON.

Visual recovery can also be achieved via the use of idebenone, which is the only approved treatment for LHON to date. This drug stimulates ATP production by bypassing the complex I of the mitochondrial respiratory chain which is impaired in LHON (Catarino & Klopstock, 2017), resulting in patients experiencing varying

degrees of visual acuity improvements. In the LEROS study, idebenone treatment led to clinically relevant visual improvements in a significantly higher proportion of patients compared to a matched natural history cohort, with up to 47.9% of subacute/dynamic eyes and 31.9% of chronic eyes showing clinically relevant recovery after 24 months of treatment. This was defined as either an improvement from off-chart visual acuity to reading at least 5 letters on-chart, or a gain of at least 10 letters (equivalent to 0.2 logMAR) for those already on-chart (Yu-Wai-Man et al., 2024). Although idebenone has been shown to improve vision in a subset of LHON patients, recently emerging gene therapies for LHON show promise for offering a 'one-shot' treatment that could either stop progression or even regenerate functions. This increases the urgency of understanding neural plasticity in different stages of this disease.

1.2. Gene therapy trials for LHON: progress and insights

There has been significant progress in gene therapy for Leber Hereditary Optic Neuropathy (LHON) over the last decade. Current strategies use adeno-associated viral (AAV) vectors, such as AAV2/2-ND4, to deliver a recoded version of the ND4 gene for patients carrying the m.11778G>A mutation – the most common genetic cause of LHON. This therapy replaces the defective gene in retinal ganglion cells (RGCs), aiming to preserve their function and prevent degeneration (Koilkonda et al., 2014; Wan et al., 2016; Newman et al., 2021).

Early trials, including RESCUE (Newman et al., 2021) and REVERSE (Yu-Wai-Man et al., 2020), tested lenadogene nolparvovec (Lumevoq), a therapy developed by GenSight Biologics using the AAV2/2-ND4 platform. These Phase III trials demonstrated visual acuity improvements in both eyes despite unilateral treatment, with over 70% of LHON patients achieving clinically significant gains (>0.3logMAR from the lowest recorded level or nadir) at 2 years post-injection in both eyes (Newman et al., 2021; Yu-Wai-Man et al., 2020; Wan et al., 2016; Moster et al., 2020). This unexpected bilateral improvement has raised questions about potential mechanisms, including the possibility of AAV vector transfer, mitochondrial migration, or neural plasticity (Yu-Wai-Man et al., 2020; Scholl & György, 2025). Still, this bilateral improvement is pertinent to treatment. Further analysis reported that treated patients experienced a progressive improvement in visual acuity from 12 to 52 months, becoming clinically significant after 48 months, compared to an independent,

untreated LHON control group (Newman et al., 2021; Yu-Wai-Man et al., 2025; Figure 1).

Recent studies have further expanded on these findings. A long-term follow-up of the RESCUE and REVERSE trials, known as the RESTORE trial, demonstrated the durability of these effects, confirming sustained visual improvements and better quality of life up to five years after unilateral treatment (Yu-Wai-Man et al., 2025). The REFLECT trial, which evaluated the effects of bilateral injections, showed enhanced visual acuity outcomes in the bilateral treatment group compared to the unilateral treatment group, in keeping with a biological dose effect (Newman et al., 2023).

These findings highlight the potential of AAV-based therapies as a transformative treatment for LHON, offering hope for restoring vision in affected individuals. The lasting effects of Lumevoq may not be surprising, as AAV vectors are specifically designed to support stable, long-term gene expression in RGCs and photoreceptors (Brommel et al., 2020; Leroy et al., 2023; Xia & Guo, 2023). Comparable outcomes have been documented in previously published 7-year follow-up data on AAV-ND4 injections in LHON patients (Yuan et al., 2020), as well as with another AAV-based therapy (voretigene neparvovec) used for RPE65-related inherited retinal dystrophy (Leroy et al., 2023). Both studies demonstrated long-term functional vision improvements, with sustained benefits lasting over 7-7.5 years. The observed bilateral visual improvement with unilateral treatment remains an open question and understanding the mechanisms driving this phenomenon – whether AAV vector transfer, mitochondrial migration, or neural plasticity – is crucial. Ongoing post-mortem analyses of ocular and brain tissues from patients treated with lenadogene nolparvovec could offer important insights at the molecular and cellular level (Carelli et al., 2024). In addition, functional MRI may play a key role in providing sensitive measures to study changes in cortical activity and visual function, as well as neural adaptations following gene therapy.

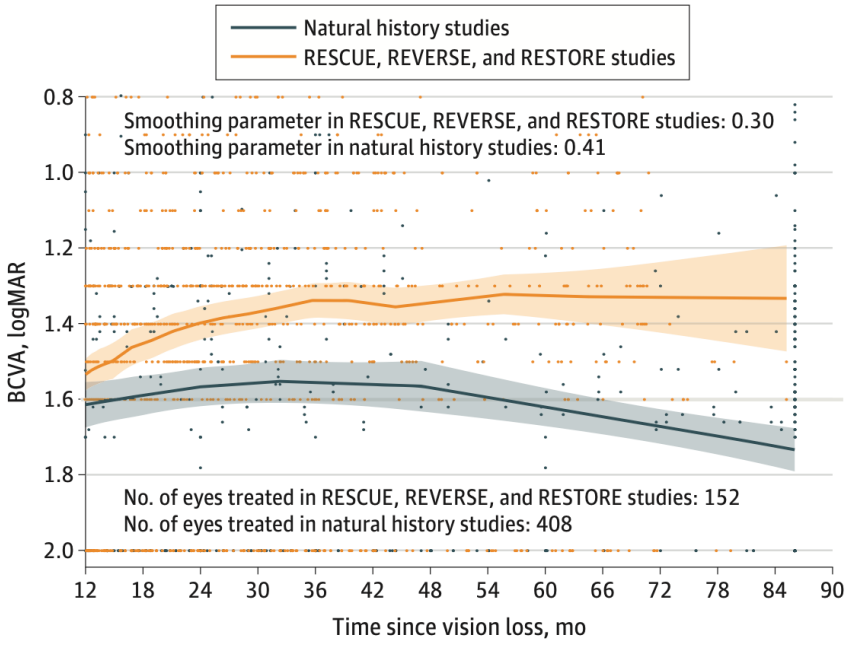

Figure 1. Evolution of Best-Corrected Visual Acuity (BCVA), over 5+ years post unilateral gene-therapy intervention.
Image from Yu-Wai-Man et al., 2025, JAMA Ophthalmology.

1.3. LHON-Plus phenotype and comorbidities with other diseases

The majority of LHON patients develop symptoms limited to loss of central vision, colour vision, and acuity, with diagnosed pathology limited to the optic nerve and structures along the visual pathways. In rare cases, patients develop additional neurological features, such as lack of muscular control, tremors, and cardiac arrhythmia. Patients with this variant of the disease, described as *LHON Plus*, also present with demyelinating lesions in their central nervous system, which has led to associations between LHON and multiple sclerosis (Matthews et al., 2015; Yu-Wai-Man et al., 2016; Carelli et al., 2019). For instance, similarities in clinical presentation and the appearance and location of brain lesions have been reported in LHON-MS and MS patients (Pfeffer et al., 2013; Inglese et al., 2001; Matthews et al., 2015). Moreover, despite no clear relationship between LHON mtDNA variants and MS risk, an association between mtDNA haplogroups J, T, and JT, and MS risk has been reported in MS patients (Andalib et al., 2013; Bargiela & Chinnery, 2019 for reviews). This association is of interest as a potential link between haplogroups and visual failure in LHON patients has been observed in the literature (Hudson et al., 2007). This leads to speculation regarding whether a relationship exists between haplogroups in LHON-

MS and MS patients, leading to similarities in clinical presentation and brain alterations.

The involvement of mitochondrial mutations in both MS and LHON raises questions on the impact of MS-related mitochondrial dysfunction on the pathology of LHON, and vice versa (Matthews et al., 2015; Bargiela & Chinnery, 2019; Rościszewska-Żukowska & Bartosik-Psujek, 2020). A fuller understanding of the relationship between LHON and demyelinating diseases could lead to potential insights into disease mechanisms, such as the role of mitochondrial dysfunction and demyelination. Finally, exploring the relationship between genotype and brain alterations might provide information for future prevention, monitoring, and treatment of these diseases.

1.4. Literature review on “Neuroimaging in LHON: State-of-the-Art and Future Prospects” (*NeuroImage: Clinical*, 36 (2022) 103240)

1.4.1. Criteria for study selection

Currently, there is no systematic review or meta-analysis summarising pre-treatment MRI changes in the LHON literature. We intend to address this gap by providing a review of the reported structural and functional changes in the brains of patients affected by “pure” LHON, without treatment or other known neurological diseases. Our approach was as follows:

Using PubMed with keywords: LHON and MRI, 113 results were found. References of identified papers were also evaluated, resulting in a total of 120 studies. Studies were excluded if they were animal studies, published in a language other than English, did not use neuroimaging (e.g., surveys or clinical examinations without MRI) or used MRI modalities that were not the focus of this review (e.g., Magnetic Resonance Spectroscopy, see section 2.2. for included MRI methods). Additional exclusion criteria included studies solely assessing the effectiveness of a drug or treatment, or looking at LHON that was comorbid with other diseases which did not separately report changes or differences in patients with “pure” LHON. We also excluded case studies that involved child-onset (<15 years) disease, as LHON most commonly occurs in late adolescence or early adulthood.

This resulted in a total of thirty studies being selected for this review. Eight of these reported qualitative changes in the brain. The remaining twenty-two studies

quantified neural differences between patients and healthy controls but covered a wide range of MRI modalities (e.g., structural MRI, DTI, qMRI). Within modality, the studies differed widely in terms of the regions of interest that were investigated (e.g., optic nerve, optic radiation, subcortical and cortical regions). This made it difficult to compare data from these studies quantitatively in any meaningful way, rendering a systematic review or meta-analysis unfeasible. Instead, we therefore systematically summarise and critically evaluate this literature. Table 1 lists the reviewed papers.

List of studies about MRI changes in the LHON brain, reviewed in section 3.

QUANTITATIVE STUDIES	QUALITATIVE STUDIES
Barcella et al., 2010, *Human Brain Mapping*	Batioğlu et al., 2003, *Journal of Neuro-Ophthalmology*
Blanc et al., 2018, *Journal of Neuro-Ophthalmology*	Honda et al., 2006, *Rinsho Shinkeigaku*
D'Almeida et al., 2013, *Neuroimage*	Lamirel et al., 2010, *Journal of Neurology, Neurosurgery, and Psychiatry*
Evangelisti et al., 2021, *Biochemical Pharmacology*	Mercuri et al., 2017, *Journal of Neuro-Ophthalmology*
Grochowski et al., 2020, *Journal of Clinical Medicine*	Ong et al., 2013, *Neurology*
Grochowski et al., 2021, *Journal of Clinical Medicine*	Phillips et al., 2003, *Archives of Ophthalmology*
Inglese et al., 2001, *Journal of Neurology, Neurosurgery, and Psychiatry*	Thouin et al., 2013, *PLoS ONE*
Jonak et al., 2020, *Brain Science*	Vaphiades et al., 2003, *Journal of Neuro-Ophthalmology*
Jonak et al., 2020, *Journal of Clinical Medicine*	
Jonak et al., 2021, *Neuroscience*	
Long et al., 2019, *Journal of Neurology*	
Manners et al., 2015, *American Journal of Neuroradiology*	
Mashima et al., 1998, *Journal of Neurology, Neurosurgery, and Psychiatry*	
Mateus et al., 2016, *Brain Structure and Function*	
Matthews et al., 2015, *Journal of Neurology, Neurosurgery, and Psychiatry*	
Milesi et al., 2012, *Journal of Neurology*	
Ogawa et al., 2014, *Investigative Ophthalmology and Visual Science*	
Rizzo et al., 2012, *PLoS ONE*	
Rocca et al., 2011, *PLoS ONE*	
Takemura et al., 2019, *Neuroimage Clinical*	
Wang et al., 2017, *European Journal of Radiology*	
Zhang et al., 2021, *Neuroimage Clinical*	

Table 1. List of studies about MRI changes in the LHON brain, reviewed in section 3. Table from Chow-Wing-Bom et al., 2022, NeuroImage: Clinical.

1.4.2. Neuroimaging methods used to study LHON

MRI is a non-invasive method that can be used to visualise the integrity of anatomical structures or evaluate dynamic metabolic function in the brain or other body areas (Symms et al., 2003). Some MRI applications, in particular those described under structural MRI, are widely used in clinics; for example, to visualise the shapes

and sizes of different brain structures to assess atrophy in these regions. *Structural MRI* methods exploit the sensitivity to brain tissue microstructure via MRI properties such as the longitudinal (T1) and transverse (T2) relaxation times, which govern the evolution of magnetisation over time. Lesions or potential inflammatory responses in the brains of LHON patients can alter these physical parameters and therefore the appearance of the different tissues in qualitative MRI images (e.g., brightness, size).

Quantitative MRI goes a step further by using (bio)physical signal models to quantify tissue properties, e.g., T1 and T2, directly in standardised units. This enhances the specificity of the measurement and therefore its capacity to characterise the microstructural integrity of the human brain *in vivo*. This approach is valuable in enabling the direct comparison of measures between sites and within individuals over time, thereby allowing disease progression or therapeutic intervention to be monitored more objectively across sites or timepoints. In addition, a rich range of metrics (e.g., relaxation times, proton density, macromolecular volume fraction, magnetic susceptibility) can be quantified, with greater sensitivity to specific biological quantities such as myelin, iron, or water (Weiskopf et al., 2015; Weiskopf et al., 2021). Some measures, however, are only semi-quantitative: for instance, the *magnetisation transfer ratio (MTR)* quantifies the degree of signal reduction that occurs following the application of an “off-resonance” pulse that selectively saturates signal originating in macromolecules, such as myelin (Grossman et al, 1994; Henkelman et al., 2001), rather than offering a direct measure of macromolecule concentrations. More robust measures have recently been developed that account for the influence of spatial variability in the generation of magnetisation and in T1 times (Helms et al., 2008) on quantitative MRI measures.

Diffusion imaging has also been used to investigate white matter integrity across the LHON brain. *Diffusion tensor imaging* provides outcome measures such as *Mean Diffusivity (MD) and Fractional Anisotropy (FA)*, which summarise the ease and directionality of diffusion (e.g., equal in all directions, or preferentially along one specific direction) within a voxel respectively. Additional measures can also be obtained, such as the diffusivity along the 'principal axis' of a fibre (*Axial Diffusivity – AD*), or the average diffusivity along the two minor axes (*Radial Diffusivity – RD*). Although the brain’s microstructural features are not obtained directly from diffusion signal models, the derived model parameters can be used to infer features such as

the long axes of larger neural white matter tracts. The consistency of changes or between-group differences in these parameters with processes like demyelination and axonal loss can also be assessed (Huisman, 2010; Wheeler-Kingshott & Cercignani, 2009; Winklewski et al., 2018). This is of particular interest for understanding LHON mechanisms since loss of both axons and myelin is thought to occur in this disease (Yu-Wai-Man et al., 2016).

Finally, *functional MRI (fMRI)* allows the study of dynamic functional changes in the brain, typically via the Blood-Oxygenation-Level-Dependent (BOLD) response (Buxton, 2013). This signal is sensitive to local changes in blood oxygenation over time following neural activity (Logothetis, 2002), and acts as a proxy for neural activation, either in response to specific stimuli (e.g., a visual stimulus), or functional connectivity as result of correlations between activity in remote brain regions under rest or other conditions. Using fMRI, it is possible to quantify loss or regain of sensitivity to retinal inputs in the brain, and assess how signals are transmitted across the hierarchy of visual cortex regions (Ritter et al., 2019; Halbertsma et al., 2021; Farahbakhsh et al., 2022).

1.4.3. Structural and functional changes in the LHON brain

As LHON is a fast-progressing disease, allowing only a short time window for the recruitment of patients in the acute phase, most studies to date have primarily recruited patients well after their disease onset. Here, we therefore first focus on post-retinal changes reported in the brains of people with *chronic* LHON. We then review the few MRI studies on potential neural changes during *acute* LHON, as well as those in the brains of *asymptomatic* carriers of genetic mutations that cause LHON. Tables summarising findings can be found throughout this section.

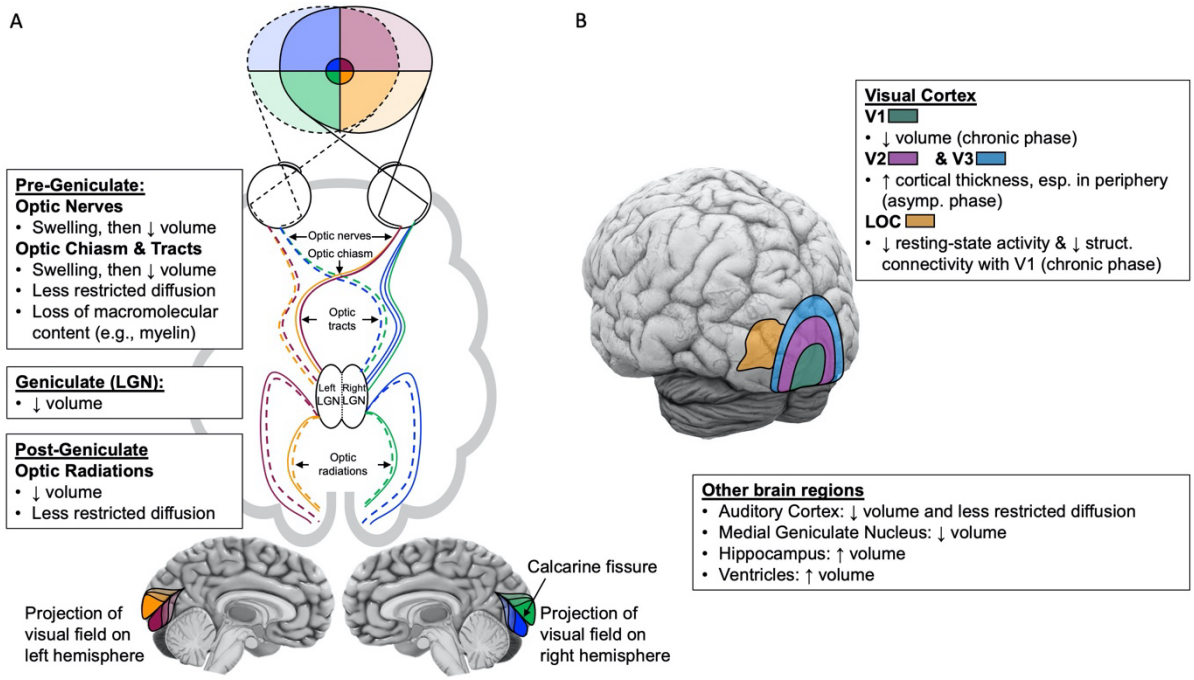

Figure 2. Summary of structural and functional changes (A) along the visual pathways, and (B) across the whole brain, in LHON.
Figure from Chow-Wing-Bom et al., 2022, NeuroImage: Clinical.

1.4.3.1. Chronic LHON

1.4.3.1.1. Pre-geniculate structural changes

Retinal ganglion cell axons project directly to the lateral geniculate nucleus (LGN; Figure 2A). Axons originating from the nasal side of the retina (receiving light from the ipsilateral visual field) decussate to the opposite hemisphere at the optic chiasm, while axons originating from the temporal side of the retina (receiving light from the contralateral visual field) do not. As a result, information from the right visual field is processed in the left hemisphere and information from the left visual field in the right hemisphere. Before the optic chiasm, axonal projections from the retinal ganglion cells are termed *optic nerves;* after the partial decussation in the chiasm, they are termed *optic tracts*.

In line with the characteristic loss of RGCs in LHON, Inglese et al. (2001) reported reductions of optic nerve volume in 10 adults with chronic LHON and 4 adults with chronic LHON-MS, compared to age- and sex-matched normal-sighted controls (Table 2). The authors also found reduced MTR in the optic nerve of both patient groups compared to controls, with lower values in LHON-MS patients compared to

those with chronic LHON. This suggests alterations in the white matter microstructure of the optic nerves in these patients. More recently, Wang et al. (2017) observed reduced fractional anisotropy, and increased mean, axial, and radial diffusivities in DTI measures from the optic nerves of 25 adults with chronic LHON compared to age-, and sex-matched, normal-sighted controls (Table 2). The authors also found that LHON patients with strong visual impairment (i.e., more than 3.0 logMAR) showed less well-constrained diffusion (i.e., fractional anisotropy values of less than 0.3) along the optic nerve, which in turn correlated with thinner peripapillary RNFL confirming that DTI measures of the optic nerve have functional relevance. These *in vivo* MRI results parallel those of a post-mortem investigation showing severe axonal loss (99%) in the optic nerve of a 75-year-old female LHON patient carrying the m.G3460C mutation who was first diagnosed with LHON at the age of 22 years (Rizzo et al., 2012).

Taken together, these studies suggest that changes in optic nerve properties in LHON may reflect myelin loss and axonal death. However, the time course of these changes, and which factors contribute to them, is less clear: while Inglese et al. (2001) found that overall loss of optic nerve volume in adults with chronic LHON correlated with disease duration ranging from 1-26 years, Wang et al. (2017) found that none of the DTI parameters correlated with age or disease duration in their cohort. Given these conflicting findings, it is therefore still unclear whether degeneration of optic nerve integrity principally occurs during the acute stage of LHON, or whether degeneration is more prolonged.

Beyond the optic nerves, reductions of volume have also been reported in the optic chiasm and tracts of adults with chronic LHON, compared to age-matched normal-sighted controls (Barcella et al., 2010; Jonak, Krukow, Symms, et al., 2020; Table 2). None of these studies found correlations of volume with disease duration, visual acuity, or visual field defects. When compared to age-match normal-sighted controls, reduced FA was also found in the optic tracts of adults with chronic LHON (Milesi et al., 2012; Ogawa et al., 2014; Takemura et al., 2019), which paired with a reduction in visual acuity (Milesi et al., 2012) supporting the functional relevance of DTI measures. Using quantitative MRI, Takemura et al. (2019) showed reduced FA and increased qT1 values in the optic tracts of 7 adults with chronic LHON, compared to 20 adult normal-sighted controls. This is further evidence that loss of

macromolecular content (i.e., from axonal or myelin loss) is pervasive across the retinogeniculate pathway.

In sum, while there is clear evidence for tissue loss with functional relevance across the pre-geniculate visual pathway in chronic LHON (Table 2; Figure 2A), it is still unclear which microcellular tissues are affected when, and whether most damage occurs early in the disease or whether gradual progression also plays an important role. Addressing these questions will be crucial for optimising timing of treatment regimes.

Structural changes observed in pre-geniculate visual regions of LHON individuals.

PRE-GENICULATE VISUAL REGIONS – STRUCTURAL CHANGES										
Reference	Normal-Sight. Controls (M ± SD age; [Range])	DISEASE STAGE			Mutation Type (N Individuals)	Notes	MRI Modalities	REGION OF INTEREST		Correlates
		Asymp. (M ± SD age; [Range])	Acute (M ± SD age; [Range])	Chronic (M ± SD age; [Range])				Optic Nerves	Optic Chiasm/ Tracts	
Inglese et al., 2001	N = 20 (37.3 ± 12.3yrs) Age- and sex-matched			10 LHON (32.3 ± 12.3yrs) 4 LHON-MS (44.5 ± 8.5yrs) Disease: 1-26yrs (LHON); 2-21yrs (LHON-MS)	G11778A (11) G3460A (2) T14484C (1)	Idebenone (2 LHON, 2 LHON-MS)	Struct. MRI MTI	↓ volume ↓ MTR		Optic nerve volume with disease duration (r = -0.7, p = 0.005)
Rizzo et al., 2012	N = 22 (37 ± 17yrs) Age- and sex-matched 1 post-mort. (♀75yrs)	N = 11 (45 ± 15yrs) Normal-sight.		22 LHON (33 ± 11yrs) Disease: 1–35yrs 1 post-mort. LHON (♀75yrs) Disease: 53yrs	G11778A (22: 8 asymp.) G3460A (10: 3 asymp.) T14484C (1 LHON) Post-mort.: G3460A	Idebenone (22 LHON) VA recovery (3 LHON)	Struct. MRI DWI Cell. Imag.	**Post-Mortem:** Severe axonal loss (↓99 %)		
Wang et al., 2017	N = 28 (27.8 ± 10.1yrs; [18-44yrs]) Age- and sex-matched			25 LHON (28.08 ± 10.66yrs; [18-50yrs]) Disease: 1.1–35.2yrs	G11778A (9) G3460A (2) T14484C (4)		Struct. MRI DTI	↓ FA ↑ MD, AD, and RD		FA in optic nerve with VA (r = -0.404, P = 0.003), mean defect of visual field (r = -0.445, P = 0.001) & average pRNFL thickness (r = 0.321, P = 0.023)
Barcella et al., 2010	N = 12 (M = 33.2yrs; [23-58yrs]) Age- and sex-matched			12 LHON (M = 33.6yrs; [20-60yrs]) Disease: 1-23yrs	G11778A (5) G3460A (4) T14484C (3)		Struct. MRI		↓ volume	
Jonak et al., 2020b	N = 15 (32.5 ± 7.4yrs) Age- and sex-matched			15 LHON (36.21 ± 14.41yrs) Disease: 1-40yrs	G11778A (15)		Struct. MRI		↓ volume	
Milesi et al., 2012	N = 25 (M = 35yrs; [25-57yrs]) Age-matched			13 LHON (M = 36.0yrs; [21-61yrs]) Disease: 2-34yrs	G11778A (8) G3460A (3) T14484C (2)		Struct. MRI DTI		↓ FA	FA in optic tracts with VA (r = 0.57, p = 0.04)
Ogawa et al., 2014	N = 14 (32.1 ± 5.4yrs; [24-40yrs])			6 LHON (37.5 ± 12.4yrs; [22-59yrs])	G11778A (6)		Struct. MRI DWI		↓ FA, esp. in portions close to LGN ↓ AD, slight ↑ RD	

(*continued on next page*)

PRE-GENICULATE VISUAL REGIONS – STRUCTURAL CHANGES

Reference	Normal-Sight. Controls (M ± SD age; [Range])	DISEASE STAGE			Mutation Type (N Individuals)	Notes	MRI Modalities	REGION OF INTEREST		Correlates
		Asymp. (M ± SD age; [Range])	Acute (M ± SD age; [Range])	Chronic (M ± SD age; [Range])				Optic Nerves	Optic Chiasm/ Tracts	
Takemura et al., 2019	Age-matched N = 20 (29.7 ± 9.7yrs; [19-44yrs]) Age-matched			Disease: 1-22yrs 7 LHON (28.6 ± 9.3yrs; [19-44yrs]) Disease: 1-22yrs	G11778A (5) T14484C (2)	Idebenone (3) VA recovery (1)	Struct. MRI DTI qMRI		↓ FA ↑ qT1	
Batioğlu et al., 2003			1 Case-study: ♂30yrs Disease < 1 yr		G11778A		Struct. MRI		T2 hyperintensity	
Honda et al., 2006			1 Case-study: ♂46yrs Disease < 1 yr		G11778A		Struct. MRI		T2 hyperintensity & no contrast enhancement	
Lamirel et al., 2012			1 Case-study: ♀19yrs 10 months post-onset		G11778A		Struct. MRI	Left T2 hyperintensity & pre-chiasmal contrast enhancement gone 1 month later	T2 hyperintensity & enlargement on the left side	
Blanc et al., 2018			N = 28 (M = 38.3yrs) Disease < 1 yr		G11778A (21) G3460A (4) T14484C (2) 14487 (1 – rare)		Struct. MRI	**3/28 patients (11 %):** T2 hyperintensity of the canalicular and intracranial segments & no contrast enhancement	**16/28 patients (57 %):** – Optic nerve T2 hyperintensity extend to the chiasm - Qualitative enlargement & no contrast enhancement	
Phillips et al., 2003			2 Case-studies: ♂7yrs & ♂19yrs Disease < 1 yr		G11778A (1) G3460A (1)		Struct. MRI	**♂7yrs:** Enlargement and intracranial optic nerve contrast enhancement, seen 2 months post-onset, reduced after 5 months and gone after 2yrs **♂19yrs:** No contrast enhancement from 1 to 4 months post-onset	**♂7yrs:** Enlargement & no contrast enhancement, seen ca. 2 months post-onset but not after 2yrs. **♂19yrs:** Enlargement & no contrast enhancement, seen ca. 1 month post-onset and still present after 4 months.	
Ong et al., 2013			1 Case-study: ♂19yrs Disease < 1 yr		G11778A		Struct. MRI		Asymmetrical T2 hyperintensity, enlargement & contrast enhancement	
Mercuri et al., 2017			1 Case-study: ♀30yrs 4 months post-onset		T14484C T3394C		Struct. MRI	Enlargement and contrast enhancement	Enlargement & contrast enhancement	
Vaphiades et al., 2003			3 Case-studies: ♂7yrs, ♂18yrs &		G11778A (2) G3460A (2)		Struct. MRI	Bilateral contrast enhancement in all patients	Enlargement, only in ♂7yrs	

(*continued on next page*)

PRE-GENICULATE VISUAL REGIONS – STRUCTURAL CHANGES										
Reference	Normal-Sight. Controls (M ± SD age; [Range])	DISEASE STAGE			Mutation Type (N Individuals)	Notes	MRI Modalities	REGION OF INTEREST		Correlates
		Asymp. (M ± SD age; [Range])	Acute (M ± SD age; [Range])	Chronic (M ± SD age; [Range])				Optic Nerves	Optic Chiasm/ Tracts	
			♂24yrs Disease < 1 yr							
Mashima et al., 1998			N = 5 (M = 25.8yrs; [21-38yrs])		G11778A (5)		Struct. MRI	Bilateral hyperintensity toward the orbital apex, ca. 6–12 months post-onset		
			Disease < 1 yr							
Thouin et al., 2013			3 Case-studies: ♂58yrs, ♂63yrs & ♂72yrs Disease < 1 yr		G11778A (3)		Struct. MRI	Normal & no contrast enhancement for all patients	Normal & no contrast enhancement for all patients	

MTI: magnetisation transfer imaging; MTR: magnetisation transfer ratio; DTI: Diffusion Tensor Imaging; DWI: Diffusion Weighted Imaging; qMRI: quantitative MRI; FA: fractional anisotropy; MD: mean diffusivity; AD: axial diffusivity; RD: radial diffusivity: RNFL: retinal nerve fibre layer; pRNFL: peripapillary RNFL; VA: visual acuity.

Table 2. Structural changes observed in pre-geniculate visual regions of LHON individuals. Tabel from Chow-Wing-Bom et al., 2022, NeuroImage: Clinical.

1.4.3.1.2. Geniculate and post-geniculate structural changes in optic radiation and primary visual cortex

Visual information is projected directly from the retina onto the parvo- and magnocellular layers of the LGN, the thalamic relay station of the visual system. It is subsequently conveyed to the primary visual cortex (V1) via single synapse projections termed the optic radiations (Figure 2A). Whereas alterations of pre-geniculate structures – such as loss of cells in the retinal nerve fibre layer (RNFL) and altered optic nerve integrity – are primary symptoms of LHON, several open questions can be raised regarding these 'downstream' structures, including (i) whether, how, and when LHON affects these regions, and (ii) whether such changes might be driven by visual deprivation due to retinal degeneration, or by primary disease processes in post-geniculate tracts. Answering these questions will be crucial for understanding the time course and mechanisms of potentially treatment-hindering central neural atrophy in LHON.

In the aforementioned post-mortem study on LHON (in a 75-year-old patient), Rizzo et al. (2012) found that the severe axonal loss described in the optic nerve (see above) was accompanied by atrophy of neuronal soma and loss of neuron density in both M- and P-cell layers of the LGN. In line with this, MRI studies have detected

reductions in volume in the LGN, optic radiations, and primary visual cortex (V1) of adults with chronic LHON, compared to normal-sighted adult controls (Barcella et al., 2010; Jonak, Krukow, Symms, et al., 2020; Jonak, Krukow, Jonak, et al., 2020; Table 3; Figure 2A). Barcella et al. (2010) found that loss of optic radiation and V1 volume correlated with decreased average and temporal peripapillary RNFL thickness in 12 adults with chronic LHON, but not with visual acuity or visual field sensitivity.

Diffusion tensor imaging (DTI) studies also reported altered diffusivity in post-geniculate tracts, with decreased fractional anisotropy (FA) and axial diffusivity (AD), and increased mean (MD) and radial diffusivities (RD) in the optic radiations of adults with chronic LHON (Rizzo et al., 2012; Ogawa et al., 2014; Manners et al., 2015; Takemura et al., 2019; Table 3; Figure 2A). These changes indicate less restricted diffusion along the principal direction of the diffusion tensor in the optic radiation white-matter tracts. Again, whether this is due to loss of axonal fibres, loss of myelinated membranes, and/or localised inflammation, cannot be distinguished based on these measures, but is important for understanding potential recovery mechanisms. Interestingly, when dividing optic radiations into subcomponents that convey visual inputs from different parts of the visual field, Ogawa et al. (2014) and Takemura et al. (2019) both found reduced FA in the subcomponents that carry inputs from the fovea and lower visual field. Although these results need to be reproduced in a larger sample of patients, the location of the FA reduction is in line with the pattern of RGC loss across the retinal sheet, and particularly the preferential loss of P-cells leading to impaired central vision characteristic of LHON (Sadun et al., 2000; Majander et al., 2017). This suggests that post-geniculate degeneration may primarily be a knock-on effect of neuronal loss in the retina, rather than a shared disease process simultaneously affecting all these brain regions.

It is important to note that although less restricted diffusion is observed in both optic tract and optic radiation in LHON, the biological reason for this may differ. Two studies from the same group reported reduced axial diffusion in optic tracts and increased radial diffusion in the optic radiations (Ogawa et al., 2014; Takemura et al., 2019). Whilst reductions in axial diffusivity have been linked to axonal loss, reduced radial diffusivity is thought to reflect myelin integrity (Wheeler-Kingshott & Cercignani, 2009; Winklewski et al., 2018). However, inflammation along the visual pathway can also affect diffusivity (Winklewski et al., 2018). It is therefore possible that less

restricted diffusion measured in chronic LHON involves loss of axons and inflammation in optic tracts, but loss of myelin in optic radiations.

Do changes in post-geniculate visual structures during the chronic phase occur suddenly or gradually? Whilst LGN and V1 volume correlated with RNFL thickness, these volume measures did not vary with disease duration (Barcella et al., 2010; Jonak, Krukow, Symms, et al., 2020; Jonak, Krukow, Jonak, et al., 2020; Table 3). Moreover, no correlation was found between DTI measures in the optic tracts and those in the optic radiations (Takemura et al., 2019). The absence of a clear link between disease duration and post-geniculate changes of neural integrity might suggest that these changes mainly occur during the acute phase in tandem with or very soon after RGC loss. However, as mentioned above, there have been conflicting reports about whether structural changes correlate with disease length in LHON (Rizzo, et al., 2012; Milesi et al., 2012; Manners et al., 2015). Interpreting these discrepancies is complicated by the typically small cohorts in studies on LHON, as well as whether patients received treatment with idebenone (Rizzo et al., 2012: N = 22/22 chronic patients; Manners et al., 2015: N = 11/17 chronic patients; Milesi et al., 2012: not reported). It is therefore still unclear when and why the posterior pre-cortical visual pathway is affected by LHON.

In sum, MRI studies have revealed structural differences, including reduced volume and impaired microstructural white-matter integrity, in the post-geniculate structures of adults with chronic LHON relative to controls (Table 3; Figure 2A). Correlations between decreased RNFL thickness, field loss, and reduced volume and diffusion along multi-synaptic projections of the pre-cortical visual pathway, suggest that atrophies in post-geniculate neuronal tracts are in part linked to the loss of specific RGCs. However, correlations between disease duration, visual function, and neural changes in post-geniculate structures are inconsistent across studies. Therefore, the degree to which these result from visual deprivation or other pathological processes, and how and when these changes emerge and contribute to function as the disease progresses, is still debated. Moreover, it is unclear whether these changes reflect myelin and/or axonal loss, as current measures can only index these processes indirectly.

GENICULATE AND POST-GENICULATE VISUAL REGIONS – STRUCTURAL CHANGES										
Reference	Normal-Sight. Controls (M ± SD age; [Range])	DISEASE STAGE			Mutation Type (N Individuals)	Notes	MRI Modalities	REGION OF INTEREST		Correlates
		Asymp. (M ± SD age; [Range])	Acute	Chronic LHON (M ± SD age; [Range])				LGN	Optic Radiations	
Rizzo et al., 2012	N = 22 (37 ± 17yrs) Age- and sex-matched 1 post-mort. (♀75yrs)	N = 11 (45 ± 15yrs) Normal-sight.		N = 22 (33 ± 11yrs) Disease: 1–35yrs 1 post-mort. (♀75yrs) Disease: 53yrs	G11778A (22: 8 asymp.) G3460A (10: 3 asymp.) T14484C (1 LHON) Post-mort.: G3460A	Idebenone (22 LHON) VA recovery (3 LHON)	Struct. MRI DWI Cell. Imag.	**Post-mortem:** – ↓ mean soma size in all 6 layers (layers 1–2: ↓ 41.6 %, layers 3–6: ↓ 44.7 %) – ↓ mean neuron density in all 6 layers (layers 1–2: ↓ 28.5 %, layers 3–6: ↓ 28.7 %)	↑ MD in LHON compared to asymp. & controls No change in MD between asymp. & controls	↑ MD in optic radiations of chronic LHON associated with lack of visual recovery (B = 0.060; P < 0.01) and disease duration (B = 0.002;P < 0.05)
Barcella et al., 2010	N = 12 (M = 33.2yrs; [23-58yrs]) Age- and sex-matched			N = 12 (M = 33.6yrs; [20-60yrs]) Disease: 1-23yrs	G11778A (5) G3460A (4) T14484C (3)		Struct. MRI		↓ volume	Right optic radiation volume with average pRNFL (r = 0.78, P_{uncorr} < 0.001) Left optic radiation volume with average pRNFL (r = 0.84, P_{uncorr} < 0.001) & temporal RNFL thickness (r = 0.79, P_{uncorr} < 0.001)
Jonak, Krukow, Jonak, et al., 2020	N = 15 (32.53 ± 7.42yrs) Age- and sex-matched			N = 15 (36.21 ± 14.41yrs) Disease: 1-40yrs	G11778A (15)		Struct. MRI	↓ volume of right LGN		Right LGN volume with right RNFL thickness (r = 0.891,p < 0.0001) & right optic nerve volume in its most proximal portion (r = 0.727,p = 0.001)
Ogawa et al., 2014	N = 14 (32.1 ± 5.4yrs; [24-40yrs]) Age-matched			N = 6 (37.5 ± 12.4yrs; [22-59yrs]) Disease: 1-22yrs	G11778A (6)		Struct. MRI DWI		↓ FA, esp. in subcomponents carrying lower and foveal inputs ↑ RD, slight ↓ AD	
Takemura et al., 2019	N = 20 (29.7 ± 9.7yrs; [19-44yrs]) Age-matched			N = 7 (28.6 ± 9.3yrs; [19-44yrs]) Disease: 1-22yrs	G11778A (5) T14484C (2)	Idebenone (3) VA recovery (1)	Struct. MRI DTI qMRI		↓ FA, esp. in subcomponents carrying foveal inputs No change in qT1 recovery	
Manners et al., 2015	N = 19 (37 ± 10yrs) Age- and sex-matched			N = 17 (37 ± 10yrs; [25-55yrs]) Disease: 1-43yrs	G11778A (13) G3460A (3) T14484C (1)	Idebenone (11) VA recovery (4)	Struct. MRI DTI		↓ FA and ↑ MD ↑ number of affected voxels if idebenone as a covariate (by 45 % for FA, 175 % for MD)	
Milesi et al., 2012	N = 25 (M = 35yrs; [25-57yrs]) Age-matched			N = 13 (M = 36.0yrs; [21-61yrs]) Disease: 2-34yrs	G11778A (8) G3460A (3) T14484C (2)		Struct. MRI DTI		↓ FA, ↑ MD and RD	

LGN: lateral geniculate nucleus; FA: fractional anisotropy; MD: mean diffusivity; RD: radial diffusivity; AD: axial diffusivity; RNFL: retinal nerve fibre layer; pRFNL: peripapillary RNFL; qT1: quantitative. T1.

Table 3. Structural changes observed in geniculate and post-geniculate visual regions of LHON individuals.

Table from Chow-Wing-Bom et al., 2022, NeuroImage: Clinical.

1.4.3.1.3. Structural changes beyond the primary visual cortex

While most white matter abnormalities have been reported along the visual pathways in LHON, more widespread white matter changes have also been found

(Table 4; Figure 2B). This raises the question of more general neural pathological mechanisms in LHON beyond the ophthalmic regions. Rocca et al. (2011) used a tractography seed-clustering analysis to assess structural connectivity between the primary visual and auditory cortices, and the rest of the brain, in 13 adults with chronic LHON compared to 13 age- and sex-matched controls. Similar seed clusters emerged from this analysis run separately in the two groups, although the authors noted some qualitative differences. These include altered clustering from visual cortex seeds (e.g., in lateral occipital cortex, fusiform gyrus, temporal pole, and frontal pole) as well as from auditory cortex seeds (in a range of visual-, motor-, multimodal-, and sub-cortical regions), in line with widespread effects of chronic LHON on brain structure beyond V1 (Table 4). Future studies should confirm if these reflect systematic differences between patients with LHON and controls or random variation in the measure. In a recent DTI study involving 19 acute and 34 chronic adults with LHON, Zhang et al. (2021) showed that although highly connected hub structures across the brain seemed to be preserved, impaired structural network connectivity (reduced FA, increased RD) and abnormal connections were found between regions involved in peripheral processing of visual/auditory sensation and motor control such as dorsal and ventral visual, auditory, and basal ganglia areas (Table 4). Jonak et al. (2021) also showed altered structural connectivity using DTI, with fewer connections between brain regions of chronic patients, including the optic chiasm (as expressed in decreased degree value and betweenness centrality). This resulted in a shift of large-scale network topology that correlated with disease duration and suggests less centralised organisation, and potentially, less efficient transfer of information between brain regions.

In line with these data suggesting that neural symptoms of LHON may be widespread and beyond brain structures involved in vision, Manners et al. (2015) found reduced FA and smaller acoustic radiations in 17 adults with chronic LHON compared to 19 controls. Jonak et al. also reported reduced volume in the medial geniculate nucleus of 15 patients with chronic LHON compared to age- and sex-matched controls (Jonak, Krukow, Jonak, et al., 2020; Table 4). This subcortical region is located between the inferior colliculus and the auditory cortex and acts as the auditory thalamic relay. These observations are in line with hearing abnormalities sometimes reported in LHON patients (Rance et al., 2012). Further changes in

subcortical structures have also been reported in chronic LHON, such as enlargement of the hippocampus (Grochowski et al., 2021) and ventricles (Jonak, Krukow, Symms, et al., 2020), which correlated with disease duration as well as age (Table 4). Ventricle enlargement and increased cerebrospinal fluid volume are reliable morphometric features of neural atrophy. Collectively, this work suggests that LHON may have a broadly neurodegenerative nature, involving brain regions beyond the visual system (Figure 2B).

V1 AND OTHER SUBCORTICAL AND CORTICAL REGIONS – STRUCTURAL CHANGES

Reference	Normal-Sight. Controls (M ± SD age; [Range])	DISEASE STAGE			Mutation Type (N Individuals)	Notes	MRI Modalities	REGION OF INTEREST			Correlates
		Asymp. (M ± SD age; [Range])	Acute	Chronic LHON (M ± SD age; [Range])				V1	Extrastriate Cortex	Other Cortical Or Subcortical Regions	
Barcella et al., 2010	N = 12 (M = 33.2yrs; [23-58yrs]) Age- and sex-matched			N = 12 (M = 33.6yrs; [20-60yrs]) Disease: 1-23yrs	G11778A (5) G3460A (4) T14484C (3)		Struct. MRI	↓ V1 volume			Right V1 volume with: - Average pRNFL (r = 0.89, P_{uncorr} < 0.001)- Temporal RNFL thickness (r = 0.76, P_{uncorr} < 0.001) Left V1 volume with:- Temporal RNFL thickness (r = 0.89, P_{uncorr} < 0.001)
Rocca et al., 2011	N = 13 (M = 35.2yrs; [19-59yrs]) Age- and sex-matched			N = 13 (M = 35.6yrs; [20-61yrs]) Disease: 2-34yrs	G11778A (8) G3460A (3) T14484C (2)		Struct. MRI RS-fMRI DTI	**Structural connectivity: Between right V1 &** - TFC (LHON only), OFC (↑ vs controls), LOC & OFG (↓ vs controls) **Between left V1 &** - MTG & IT (LHON only), Frontal pole & LOC (↑ vs controls), Temporal pole (↓ vs controls)		**Structural connectivity: Between right auditory cortex &** - Frontal pole, pallidum, and SMG (LHON only) **Between left auditory cortex &** - LOC (LHON only) - MTG and IT (Controls only)	
Manners et al., 2015	N = 19 (37 ± 10yrs) Age- and sex-matched			N = 17 (37 ± 10yrs; [25-55yrs]) Disease: 1-43yrs	G11778A (13) G3460A (3) T14484C (1)	Idebenone (11) VA recovery (4)	Struct. MRI DTI			↓ FA and ↑ MD: auditory radiations, right superior corona radiata, SLF, and medial corpus callosum If treated with idebenone: lower MD values within anterior cingulum, genu of corpus callosum, olfactory tracts, and left prefrontal white-matter	
Jonak et al., 2020b	N = 15 (32.5 ± 7.4yrs) Age- and			N = 15 (36.2 ± 14.4yrs) Disease: 1-40yrs	G11778A (15)		Struct. MRI			**↓ volume:** palladium and accumbens area	Volume of left and right lateral ventricles with disease

(*continued on next page*)

V1 AND OTHER SUBCORTICAL AND CORTICAL REGIONS – STRUCTURAL CHANGES

Reference	Normal-Sight. Controls (M ± SD age; [Range])	DISEASE STAGE			Mutation Type (N Individuals)	Notes	MRI Modalities	REGION OF INTEREST			Correlates
		Asymp. (M ± SD age; [Range])	Acute	Chronic LHON (M ± SD age; [Range])				V1	Extrastriate Cortex	Other Cortical Or Subcortical Regions	
	sex-matched									**↑ volume:** lateral ventricles, temporal horns of lateral ventricles, 3rd & 4th ventricles	duration (left: R = 0.656,p = 0.002; right: R = 0.755,p = 0.001) & age (left: R = 0.656,p = 0.007; right: R = 0.691, p = 0.004)
Jonak et al., 2020a	Same as above			Same as above	Same as above		Struct. MRI			↓ volume of MGN	
Grochowski et al., 2021	N = 15 (33.1 ± 7.2yrs) Age- and sex-matched			N = 15 (36.2 ± 14.9yrs) Disease: 1-41yrs	G11778A (15)		Struct. MRI			**↑ volume:** hippocampal fissure, hippocampal tail and body, subiculum body, all CA body, molecular layer HP body, GC-ML-DG body, whole hippocampal volume **↓ volume:** right fimbria	Volume of hippocampal fissure with disease duration (R = 0.675,p = 0.005) Volume of fimbria with disease duration (R = -0.595, p = 0.018)
Rizzo et al., 2012	N = 22 (37 ± 17yrs) Age- and sex-matched 1 post-mort. (♀75yrs)	N = 11 (45 ± 15yrs) Normal-sight.		N = 22 (33 ± 11yrs) Disease: 1–35yrs 1 post-mort. (♀75yrs) Disease: 53yrs	G11778A (22: 8 asymp.) G3460A (10: 3 asymp.) T14484C (1 LHON) Post-mort.: G3460A	Idebenone (22 LHON) VA recovery (3 LHON)	Struct. MRI DWI Cell. Imag.			**Between groups:** No difference in MD of prefrontal and cerebellar white-matter	
D'Almeida et al., 2013	N = 15 (26.2 ± 11.5yrs; [7-44yrs]) Age-matched	N = 15 (29.3 ± 13.5yrs; [8-47yrs]) Normal-sight.			G11778A (15)		Struct. MRI Retino. fMRI	**Between asymp. & controls:** No difference in V1 cortical thickness	**Between asymp. & controls:** - ↑ V2 cortical thickness, if age ≤ 21yo (N = 7 asymp.) - ↑ V3 cortical thickness, if age > 21yo (N = 8 asymp.)	**Between asymp. & controls:** No difference in cortical thickness of pre- and post-central gyri	Outer-macular RNFL thickness with:- V2 cortical thickness (r = 0.582,p = 0.023) - V3 cortical thickness (r = 0.537,p = 0.039)Age with (for N = 7 asymp. aged ≤ 21yo only):- V2 cortical thickness (r = -0.857, p < 0.001)- V3 cortical thickness (r = -0.833, p = 0.001)
	N = 24 (31.3 ±	Same as above			Same as above		Struct. MRI		↑ V2 and V3 cortical		Outer-macular

(*continued on next page*)

V1 AND OTHER SUBCORTICAL AND CORTICAL REGIONS – STRUCTURAL CHANGES

Reference	Normal-Sight. Controls (M ± SD age; [Range])	DISEASE STAGE			Mutation Type (N Individuals)	Notes	MRI Modalities	REGION OF INTEREST			Correlates
		Asymp. (M ± SD age; [Range])	Acute	Chronic LHON (M ± SD age; [Range])				V1	Extrastriate Cortex	Other Cortical Or Subcortical Regions	
Mateus et al., 2016	13.5yrs; [7-54yrs]) Age-matched						Retino. fMRI		thickness, esp. in peripheral regions		RNFL thickness with: - V2 cortical thickness (r = 0.712,p = 0.0075)- V3 cortical thickness (r = 0.706,p = 0.0083)
Long et al., 2019	N = 15 (31.9 ± 10.2yrs; [11-44yrs]) Age and sex-matched	N = 14 (37.1 ± 12.7yrs; [9-52yrs]) Normal-sight.			G11778A (8) G3460A (2) T14484C (4)		Struct. MRI DTI			**AD**: no difference ↓ **FA**: bilat. anterior thalamic radiations, bilat. corticospinal tracts, major and minor forceps, bilat. IFOF and left SLF ↑ **MD**: bilat. anterior thalamic radiations, bilat. corticospinal tracts, minor forceps, bilat. IFOF, bilat. ILF, left SLF and bilat. uncinate fasciculi ↑ **RD:** bilat. anterior thalamic radiations, bilat. corticospinal tracts, major and minor forceps, bilat. IFOF, bilat. ILF, bilat. SLF, and bilat. uncinate fasciculi	
Zhang et al., 2021	N = 36 ([9-44yrs]) Age and sex-matched		N = 19 (21.4 ± 11.6yrs; [10-57yrs]) Disease: 0.27 ± 0.22yrs	N = 34 (26.9 ± 11.7yrs; [13-53yrs]) Disease: 9.5 ± 10.6yrs	G11778A (41: 14 acute) T14484C (9: 5 acute) G3460A (3 chronic)		Struct. MRI DTI			Preserved rich-club organization ↓ **FA,** ↑ **RD:** esp. in non-rich club components Abnormal feeder connections within dorsal visual areas, and between basal ganglia & dorsal	

(*continued on next page*)

V1 AND OTHER SUBCORTICAL AND CORTICAL REGIONS – STRUCTURAL CHANGES											
Reference	Normal-Sight. Controls (M ± SD age; [Range])	DISEASE STAGE			Mutation Type (N Individuals)	Notes	MRI Modalities	REGION OF INTEREST			Correlates
		Asymp. (M ± SD age; [Range])	Acute	Chronic LHON (M ± SD age; [Range])				V1	Extrastriate Cortex	Other Cortical Or Subcortical Regions	
										visual area. Abnormal local connections between auditory cortex & dorsal and ventral visual area, between basal ganglia & ventral visual area	

MGN: medial geniculate nucleus; LOC: lateral occipital cortex; OFC: occipital fusiform cortex; OFG: occipital fusiform gyrus; TFC: temporal fusiform cortex; RNFL: retinal nerve fibre layer; pRNFL: peripapillary RNFL; DWI: Diffusion-weighted imaging; DTI: Diffusion-Tensor imaging; FA: fractional anisotropy; MD: mean diffusivity; RD: radial diffusivity; AD: axial diffusivity; CA: Cornu Ammonis; MTG: middle temporal gyrus; IT: inferior temporal gyrus; SMG: supramarginal gyrus; SLF: superior longitudinal fasciculus; ILF: inferior longitudinal fasciculi; IFOF: inferior fronto-occipital fasciculi; bilat.: bilateral.

Table 4. Structural changes observed in V1, and beyond V1 of LHON individuals. Table from Chow-Wing-Bom et al., 2022, NeuroImage: Clinical.

1.4.3.1.4. Functional changes

Connectivity across two brain regions can be assessed by quantifying how well neural signal fluctuations, as expressed in the functional MRI BOLD signal in these regions, are temporally coupled with each other (i.e., *functional connectivity*). By identifying regions with strongly correlated BOLD response time courses, it is possible to identify *networks* of brain regions that are presumably strongly co-activated during perception and cognition and therefore 'wire together' into functional units. These correlations can even be present during rest, i.e., resting state networks (Rosazza & Minati, 2011; Smitha et al., 2017; Seitzman et al., 2019).

Using resting-state fMRI, Rocca et al. (2011) found reduced spatiotemporal coupling in secondary visual networks of 13 adults with chronic LHON compared to 13 age- and sex-matched controls, more specifically in the right lateral occipital cortex and the right temporal occipital fusiform cortex (Table 5; Figure 2B). This reduction correlated with disease duration and temporal RNFL and was paired with qualitatively reduced structural connectivity between right V1 and right lateral occipital cortex, as measured by DTI. These results suggest that extensive central retinal damage and loss of structural integrity along the visual pathways in chronic LHON, may be accompanied by reduced functional and structural connectivity between V1 and higher-order visual regions.

In contrast, Rocca et al. (2011) also found *increased* spatiotemporal coupling in primary and secondary visual networks and in various non-visual networks, accompanied by increased structural connectivity in DTI in these regions (Table 5). These changes may reflect potential compensatory responses that may involve cross-modal plasticity (Rocca et al., 2011; Manners, et al., 2015). However, whether changes in non-visual areas are caused by LHON or because of blindness is still unclear.

To date, no MRI study has directly investigated changes in visual function (e.g., visually evoked BOLD responses) in LHON patients. Yet, MRI studies in other retinal diseases suggest that changes in visual evoked activity may have important applications for monitoring functional change after treatment (see response to Q5 in section 1.6). Adapting and combining existing functional MRI paradigms and modelling approaches to study functional changes in LHON could shed light on potential links between cortical and behavioural changes in vision.

V1 AND OTHER SUBCORTICAL AND CORTICAL REGIONS – FUNCTIONAL CHANGES

Reference	Controls (M ± SD age; [Range])	DISEASE STAGE			Mutation Type (N Individuals)	Notes	MRI Modalities	REGION OF INTEREST			Correlates
		Asymp. (M ± SD age; [Range])	Acute	Chronic (M ± SD age; [Range])				V1	Extrastriate Cortex	Other Cortical Or Subcortical Regions	
Rocca et al., 2011	13 normal-sight. (M = 35.2yrs; [19-59yrs]) Age- and sex-matched			13 LHON (M = 35.6yrs; [20-61yrs]) Disease: 2-34yrs	G11778A (8) G3460A (3) T14484C (2)		Struct. MRI RS-fMRI DTI	**Primary visual network of chronic LHON:** ↑ resting-state fluctuations in left cuneal cortex & right supracalcarine cortex	**Secondary visual networks of chronic LHON:** – ↑ resting-state fluctuations in left OFG & bilat. occipital poles - ↓ resting-state fluctuations in temp. OFC, corresponding with ↑ struct. connectivity between right V1 and right temp. OFC - ↓ resting-state fluctuations in right LOC, corresponding with ↓ struct. connectivity between right V1 and right LOC	**↑ resting-state fluctuations in chronic LHON:** - Right STG (incl. primary auditory cortex) - SMG, corresponding with ↑ struct. connectivity between right auditory cortex and right SMG	Disease duration with resting-state activity- Left cuneal cortex (r = 0.87,p = 0.003)- Right occipital pole (r = 0.87,p = 0.003) - Right LOC (r = -0.77, p = 0.01)- Right STG (r = 0.83,p = 0.02) Average RNFL thickness with resting-state activity- Left cuneal cortex (r = 0.88,p = 0.002) - Right STG (r = 0.79,p = 0.05)

LOC: lateral occipital cortex; OFC: occipital fusiform cortex; OFG: occipital fusiform gyrus; TFC: temporal fusiform cortex; SMG: supramarginal gyrus; STG: superior temporal gyrus; bilat.: bilateral; temp.: temporal.

Table 5. Functional changes observed in V1, and beyond V1 of LHON individuals.

Table from Chow-Wing-Bom et al., 2022, NeuroImage: Clinical.

1.4.3.2. Acute LHON

Few MRI studies have investigated changes in neural structure and function in the first year after initial LHON diagnosis. This time window, known as the acute phase, is marked by rapid degeneration of retinal ganglion cells leading to acute and severe loss of visual function.

In line with several case studies involving acute LHON patients (Batioğlu et al., 2003; Honda et al., 2006; Lamirel et al., 2012), Blanc et al. (2018) reported T2 hyperintensities in the most proximal portion of the optic nerve and in the part extending to the optic chiasm of 28 acute LHON adults (Table 2). In T2-weighted images, hyperintensities may have several causes including axonal loss, demyelination, or trauma-related gliosis (growth of glial cells). Images consistent with swelling of the optic nerve and chiasm are often detected by neuroradiologists examining T2-weighted MRI images during the acute phase (Phillips et al., 2003; Ong et al., 2013; Mercuri et al., 2017; Lamirel et al., 2012; Blanc et al., 2018; Table 2). However, Blanc et al. (2018) did not find that mutation type related to any notable differences in signal brightness in the optic nerve and chiasm in the early (<3months) versus late (3-12months) acute phase.

Clinical MRI is often performed with gadolinium, a paramagnetic contrast-enhancing agent administered via intra-vascular injection. It shortens the T1 time of the extracellular and extravascular spaces that it can reach, which is governed by the local physiology. Findings of enhanced gadolinium-induced contrast has led to speculation about inflammation in several case studies of acute LHON, potentially reflecting the disruption of the blood-brain barrier as a disease process or some type of auto-immune syndrome (Phillips et al., 2003; Vaphiades et al., 2003; Ong et al., 2013; Mercuri et al., 2017; Batioğlu et al., 2003; Lamirel et al., 2012; Blanc et al., 2018). However, other studies, including the large-N study by Blanc et al. (2018), did not replicate this finding (Mashima et al., 1998; Honda et al., 2006; Thouin et al., 2013; Blanc et al., 2018). Thus, these inflammatory processes may not always be present at the time of the MRI evaluation.

Currently, most MRI studies targeting changes in the acute phase of LHON are qualitative single-case studies (Table 2), with abnormalities detected by expert neuroradiologists not blind to the diagnosis. To better understand the post-retinal

neural mechanisms involved early on in LHON and their role in prognosis, objective, longitudinal quantitative MRI measures are needed. This is challenging however, as LHON is a rapidly progressing disease with a very short time window for investigating structural changes during the acute phase.

1.4.3.3. Unaffected LHON carriers (asymptomatic LHON)

Not all individuals carrying LHON-specific point mutations in their mitochondrial DNA develop the disease. These individuals are in the *asymptomatic* phase, and usually have good visual acuity, normal ocular examination, and no changes on the projection surface of the eye (i.e., fundus). Comparing asymptomatic individuals who do versus do not go on to develop LHON may provide important insights into pre-clinical markers that predict versus protect from this disease. To date, only a few neuroimaging studies have investigated changes in the brain of asymptomatic LHON individuals (Rizzo et al., 2012; D'Almeida et al., 2013; Mateus et al., 2016; Long et al., 2019; Tables 2-4).

Whilst asymptomatic carriers do not suffer from clinically meaningful levels of visual impairment, they may present with subclinical reduction of chromatic sensitivity and visual field sensitivity, mostly within the paracentral ring (D'Almeida et al., 2013; Mateus et al., 2016; Long et al., 2019). Evidence for thickening of the most peripheral macular rings and retinal nerve fibre layer (RNFL), especially in the inferior and temporal quadrants, were also found in asymptomatic carriers (Savini et al., 2005; Mateus et al., 2016; Long et al., 2019; Carelli et al., 2019). This is in line with the swelling of the RNFL reported in the early stage of the disease (i.e., acute). However, whether this swelling during the acute phase is caused by similar processes as the swelling in asymptomatic LHON carriers is unclear (Savini et al., 2005; Barboni et al., 2005; Mateus et al., 2016; Long et al., 2019).

When investigating retinotopic visual cortex of 15 asymptomatic LHON carriers, all harbouring the m.G11778A variant, D'Almeida et al. (2013) reported increased cortical thickness in V2 and V3 of asymptomatic carriers compared to age-matched controls, whilst no difference in V1 thickness was found between groups (Table 4). These extra striate changes appeared to be driven by visual area-specific differences between the younger and older asymptomatic carriers: the thickening of V2 relative to controls was most prominent in young asymptomatic LHON carriers (≤ 21yrs; N=7),

whilst the thickening of V3 was most evident in older asymptomatic carriers (>21yrs; N=8). In a follow-up study by Mateus et al. (2016) involving the same cohort of asymptomatic LHON carriers, greater cortical thickness was mainly observed in parts of V2 and V3 regions encoding the peripheral visual field, when compared to controls (Table 4). The authors suggested that these findings may reflect reorganisation of the cortex of asymptomatic LHON carriers, due to sub-clinical loss of paracentral visual field sensitivity and increased thickness of the most peripheral macular ring measured in these carriers (D'Almeida et al., 2013; Mateus et al., 2016; Table 4). Thus, notable effects of genetic variants may already be present at a cortical level in the asymptomatic stage when LHON genetic carriers do not present with clinically meaningful vision loss or scotoma. Moreover, longitudinal changes in the visual regions initially identified in these studies could offer new potential biomarkers of LHON that can be monitored to track the evolution of the disease. That said, what biological processes are responsible for the reported greater thickness of visual cortex in normally sighted asymptomatic LHON carriers is currently unclear.

When investigating water diffusivity in the brain of 11 asymptomatic LHON carriers using DTI, Rizzo et al. (2012) found no difference in mean diffusivity in optic radiations, prefrontal WM, or cerebellar WM compared to age- and sex-matched controls (Tables 3-4). Long et al. (2019) also observed no group differences in diffusion along the visual pathway from the retina to V1 in 14 asymptomatic LHON carriers compared to age-matched controls, but they did observe restricted diffusion (i.e., reduced FA and increased MD) in white-matter tracts connecting visual areas to more anterior brain regions (i.e., the bilateral inferior fronto-occipital fasciculi and bilateral inferior longitudinal fasciculi; Table 4). These changes in central white matter tracts mainly affected radial diffusivity, which has been linked to demyelination of the white-matter tracts, rather than axial diffusivity (Wheeler-Kingshott & Cercignani, 2009; Winklewski et al., 2018).

The lack of detectable reduced diffusivity in primary visual pathways of asymptomatic LHON carriers contrasts with studies in chronic patients with similar sample size (Milesi et al. 2012: N=13; Manners et al., 2015: N=17; Ogawa et al., 2014: N=6; Takemura et al., 2019: N=7), and suggests that this neural marker of LHON may predominantly develop around or after clinical onset of LHON. However, widespread changes in neural connectivity beyond the primary visual system, in DTI markers

linked to demyelination, may indicate the existence of more widespread impacts on white matter, and potentially myelin integrity, in LHON gene carriers. These pre-clinical changes may be relevant to the co-morbidity of LHON with other demyelinating diseases such as multiple sclerosis. Moreover, understanding if and how these subclinical changes in neural physiology and function impact on the quality of life of asymptomatic LHON carriers, and their likelihood of developing clinical LHON, could be beneficial for patient care.

1.5. Recovery after pharmacological therapy: from behaviour to brain measures

Although there is no cure for LHON yet, idebenone has been proven safe to be used for the treatment of LHON and has shown positive outcomes for improving vision in LHON patients (Catarino et al., 2017). Several studies have reported bilateral or unilateral recovery of visual acuity and visual field sensitivity in small subsets of patients, with some even recovering a visual acuity of 1.0 in decimal units (i.e., “20/20 vision”) on the Snellen chart (Rizzo et al., 2012; Manners et al., 2015; Catarino et al., 2017; Pemp et al., 2021). However, recovery is far from ubiquitous in LHON patients treated with idebenone, and depends on several factors such as mutation, age of onset, disease duration, presence of other diseases such as multiple sclerosis, and duration of treatment. Moreover, beneficial effects can take as long as 30 months to emerge (Carelli et al., 2019). Evidence of improvements in brain measures have also been reported in LHON patients treated with idebenone using MRI. Greater volume and diameter of the optic nerves have been found in treated patients compared to untreated patients (Grochowski et al., 2020: N=6 treated and N=9 untreated patients), specifically in the part close to the optic chiasm. Lower mean diffusivity values have also been reported in optic radiations and non-visual regions of treated compared to untreated patients, including in the anterior cingulum, genu of corpus callosum, olfactory tracts bilaterally, and the left prefrontal WM, as measured in DTI (Manners et al., 2015: N=11 treated and 6 untreated patients). Additionally, Rizzo et al. (2012) reported that structural integrity measures of the optic radiations could help discriminate between LHON patients without and with a history of significant recovery after disease onset, as defined by a 2-line increase on the Snellen chart (N=6 out of 22 treated patients had a history of significant visual recovery). In contrast, Manners

et al. (2015) found no relationship between diffusion parameters in post-geniculate visual structures and visual recovery.

In sum, MRI study results show that idebenone may help improve visual function by preventing widespread WM damage in the brain of LHON patients. However, a clear understanding of what mediates these effects and why they are variable and slow is still lacking.

1.6. Conclusions of the literature review

We have reviewed the insights gained from MRI studies into changes occurring in LHON beyond the retina and summarised these in Figure 2. In the introduction, we raised five questions about the post-retinal neural profile of LHON and in this concluding section we discuss the degree to which these questions have been answered.

Q1&2: Which changes in neural function and structure occur beyond the retinal ganglion cell layer? What are the mechanistic causes of these neural changes, and which microstructural process might they reflect?

Pre-geniculate visual structures: With the acute onset of LHON symptoms, reflected first in rapid central vision loss, many MRI studies have revealed swelling of the optic nerve (Phillips et al., 2003; Ong et al., 2013; Mercuri et al., 2017; Lamirel et al., 2012; Blanc et al., 2018; Table 2; Figure 2A), which tends to subside after the acute phase (i.e., the first 12 months). A reduction of volume in the optic nerve and tract also occurs after onset of the acute phase, paired with decreased FA and increased MD. Together, this indicates less restricted diffusion along the primary optic projection from the eye to the LGN (Milesi et al., 2012; Wang et al., 2017; Table 2; Figure 2A). At present it is unclear whether the loss in neural structure and diffusivity in the optic nerve and tract reflect axonal loss, swelling, or demyelination. The question of when most of this loss occurs in these regions also remains unanswered; studies reporting correlations between these measures and disease duration in chronic patients suggest that this is a gradually progressing process, but findings for optic nerve, chiasm, and tracts are somewhat conflicting (correlation: Inglese et al., 2001; versus no correlation: Barcella et al., 2010; Milesi et al., 2012; Wang et al., 2017; Jonak, Krukow, Symms, et al., 2020).

Geniculate and post-geniculate visual structures: LHON not only affects the optic nerves, but also the central nervous system structures they project to (Figure 2A). Reductions of volume have been measured in the LGN, optic radiations, and V1 of chronic patients (Barcella et al., 2010; Jonak, Krukow, Jonak, et al., 2020; Tables 3-4). These are paired with less restricted diffusion in these structures (Rizzo et al., 2012; Milesi et al., 2012; Ogawa et al., 2014; Manners et al., 2015; Takemura et al., 2019; Table 3). Again, it is unclear whether this primarily reflects demyelination or axonal loss, and findings conflict about whether these changes are progressive with disease duration, so it is not clear why and when they occur. However, despite showing no noticeable changes in DTI measures of diffusivity along the visual pathways, there is already a measurable increase in cortical thickness in the low-level visual cortex in carriers of the LHON gene variants who do not show symptoms (Rizzo et al., 2012; Long et al., 2019; Tables 3-4). This suggests that brain alterations may occur even before symptoms become clinically significant.

Beyond the primary visual cortex: Though deficits are primarily vision-related, changes/differences have been observed beyond early visual areas in LHON patients (Figure 2B). Reductions of volume and less restricted diffusion have been found in subcortical areas (Jonak, Krukow, Symms, et al., 2020; Figure 2), in structures involved in the auditory system (Manners et al., 2015; Long et al., 2019; Jonak, Krukow, Jonak, et al., 2020), and in frontal regions (Manners et al., 2015; Long et al., 2019). Increased volume has also been reported in the ventricles (Jonak, Krukow, Symms, et al., 2020) and the hippocampus (Grochowski et al., 2021), and were correlated with disease duration and age. Together, these findings suggest potential cross-modal deficits in LHON and raise the question of more general neural pathological mechanisms. Indeed, LHON and MS are known comorbidities, with evidence of shared locations of brain lesions (Pfeffer et al., 2013; Inglese et al., 2001; Matthews et al., 2015). This co-occurrence of LHON with other demyelinating diseases may suggest shared mechanisms between the two diseases, in particular regarding the demyelination processes.

Q3: How do changes in neural structure and function predict visual outcome?

Less MRI research has focussed on function/structure relationships, so little is known about how neurological changes beyond the retina in LHON contribute to

patient vision. However, several studies have demonstrated that neural markers of LHON have functional relevance. In non-expressing carriers, sub-clinical reductions in paracentral visual field sensitivity and RNFL thickness were linked to abnormal thickness in visual cortex that encodes the corresponding visual field locations (D'Almeida et al., 2013; Mateus et al., 2016), thus demonstrating early subclinical functional impact of LHON-linked mutations. Moreover, the fact that reductions of volume in post-geniculate visual structures correlate with RNFL thickness (Barcella et al., 2010; Jonak, Krukow, Jonak, et al., 2020; Table 3) suggests that post-geniculate dystrophies are linked to the loss of RGCs, either resulting from the same pathological process at RGC death, or from neuronal deterioration due to loss of visual inputs. Two studies in chronic patients also showed that optic nerve and tract diffusivity were less altered in individuals with better visual acuity outcomes after idebenone (Milesi et al., 2012; Wang at al., 2017).

In the post-geniculate pathway, structural integrity measures of the optic radiation could discriminate patients with significant visual recovery from those without (Rizzo et al., 2012). This suggests that some brain alterations may potentially be reversible after treatment or compensated by mechanisms that are yet to be fully explored. With current gene-therapy treatments already showing promising outcomes for visual recovery in LHON, it becomes essential to better understand how changes observed in MRI support these changes in visual function.

Q4: What are the key challenges and limitations for MRI research on LHON?

Conflicting findings are abundant in the MRI literature on LHON; for example, regarding whether disrupted diffusivity along the visual pathway is due to axonal loss, demyelination, or both (Ogawa et al., 2014; Takemura et al., 2019), and whether volume loss and changes in diffusion in pre-geniculate visual structures progressively worsen with disease duration (correlation: Inglese et al., 2001; Rizzo et al., 2012, versus no correlation: Barcella et al., 2010; Milesi et al., 2012; Wang et al., 2017; Manners et al., 2015; Jonak, Krukow, Symms, et al., 2020; Jonak, Krukow, Jonak, et al., 2020). This in part stems from the inclusion of adults with chronic LHON presenting comorbidities with other demyelinating diseases such as multiple sclerosis (Inglese et al., 2001), potential treatment with idebenone (Rizzo et al., 2012), and the genetic

variability of the disease. As all these factors affect both prognosis and recovery, they are likely to present with different underlying neural profiles.

MRI findings of LHON are also limited because the disease is relatively rare, and the onset and progression to near-blindness is very rapid. As result, most studies have a small sample size and patients are usually only recruited in the chronic phase of LHON. This limits the generalisability of the results and the power to detect subtle differences in neural disease markers. As a result, we have little understanding of how early-stage disease progresses over time in visual brain regions beyond the retina. With the development of regenerative treatments such as gene therapies (see response to Q5 below), insight in these early processes and how they may interact with treatment will become crucial in coming years. Further work would benefit from larger sample sizes as well as recruiting patients in various stages of the disease. However, the fast progression of the disease represents a challenge, and the latest and most informative functional and structural MRI measures of the visual brain may not be readily available in all places. New advances in quantitative MRI technology may help address this issue (see response to Q5 below).

A final challenge of this research is that imaging of visual brain structures can be particularly difficult due to their tissue properties. For example, comparisons of MRI measures of the optic nerve and other visual structures is complicated by the fact that the optic nerves are particularly difficult to image due to their small size, and their proximity to orbital cavities (Hoch et al., 2017). The latter can cause signal dropout and severe eye-movement-related image artifacts. Imaging this structure typically requires a restricted volume to achieve sufficient resolution in clinically feasible acquisition times. As a result, MRI sequences are differentially optimised to visualise either the optic nerves or tracts and other structures, meaning that they are usually investigated in separate studies and patients. This makes it hard to assess progression of the disease along the visual pathway in the same patient.

Q5: What are the most important open questions about LHON that MRI could help resolve?

Recently, novel imaging methodologies have been developed that have the potential to provide more direct ways to assess microstructural changes *in vivo*. For instance, quantitative MRI measures can be used in biophysical modelling to calculate

metrics that directly characterise biological properties of the tissue, such as the g-ratio, which quantifies the ratio of axonal diameter with and without the myelin sheath (Mohammadi & Callaghan, 2021). This estimate has the potential to differentiate demyelination (reduced g-ratio) from inflammation (unchanged g-ratio). When combined with longitudinal studies, this could help disentangle contributions of demyelination, inflammation, and axonal loss to the LHON profile. Moreover, these quantitative measures are scanner independent. This provides exciting scope for improving sample sizes in this field by permitting comparable data collection across multiple specialist centres, and by increasing the reliability of longitudinal research in individual patients.

Though neuroimaging studies have provided insight into how LHON impacts beyond the retina during the disease, our understanding of the neural mechanisms supporting visual recovery is still in its infancy. For example, it is presently unclear what causes the spontaneous functional recovery in a small but substantial percentage (<20%) of patients with LHON, and in particular those with the T14484C variant. To date, no neuroimaging studies have investigated spontaneous recovery in LHON, nor any differences in neural structure and function between genotypes that may facilitate this. Potential explanations for this recovery include the reviving of deactivated but viable RGCs (Acaroğlu et al., 2001; Sharkawi et al., 2012), re-myelination of axons, or functional compensation processes at the level of visual cortex or LGN (D'Almeida et al., 2013; Rocca et al., 2011). Such functional compensation may, for example, involve increased allocation of neural resources to spared retinal regions (Baseler et al., 2002; Baker et al., 2005; Castaldi, et al., 2020) or altered attentional processes (Dumoulin & Knapen, 2018), as observed in other types of visual field loss. Whilst important, investigating spontaneous recovery in LHON is challenging as it is unpredictable and thus would require regular measurement.

Another important future direction will be to gain better insight into the early dynamics of visual pathway structure and function loss in LHON. This will be valuable in defining a treatment window for gene therapy and evaluating treatment impact. Recent approaches work by injecting patients with an adeno-associated virus (AAV2/2-ND4) that safely replaces affected mtDNA in the mitochondrial complex I, to prevent loss of RGCs (Koilkonda et al., 2014; Wan et al., 2016; Newman et al., 2021).

Two recent clinical trials that use this approach revealed significant improvements of visual acuity and contrast sensitivity in the treated eye. After 2 years, more than 70% of LHON patients' acuity measures improved, to an equivalent of 0.3logMAR, in their treated eye (Newman et al., 2021; Wan et al., 2016; Yu-Wai-Man et al., 2020; Moster et al., 2020). Surprisingly, however, similarly improved acuity after 2 years was also observed in the non-injected eye, complicating the interpretation of these results (Yu-Wai-Man et al., 2020). It is likely, however, that this change is pertinent to treatment, as a recent large study which compared an indirect LHON control group to the change observed after gene therapies, showed a progressive improvement of visual acuity from 12 to 52 months in the treated group compared to the external control group, which became significant after 18 months and clinically significant after 48 months. This bilateral benefit raises questions about whether a transfer effect is operational at the viral level only or also involves neural plasticity. Functional MRI could help address these questions by measuring how and when neural visual function for input from both eyes changes after gene therapy.

MRI could be a powerful technique capable of sensitively detecting the recovery of function and structural integrity in response to treatment. The value of fMRI as an outcome measure for gene therapy has been demonstrated in Leber's Congenital Amaurosis (LCA), a condition associated with severe blindness from birth accompanied by nystagmus and light sensitivity (Ashtari et al., 2011; Ashtari et al., 2015). Ashtari et al. found that after gene therapy in 3 LCA patients, cortical responses in visual areas were higher for high- and medium contrast checkerboard patterns presented to the treated compared to the untreated eye, whilst behavioural assessments showed only modest improvement. The distribution of cortical activation also correlated partially with visual field maps measured behaviourally. These results suggest that visual function after gene therapy is restored, with potential enhancement of contrast sensitivity, at least at the cortical input stage. Functional MRI appeared to be sensitive to treatment-mediated changes in the brain well before the emergence of behavioural improvements. Similar benefits of fMRI for gene therapy assessment have also recently been demonstrated for achromatopsia, a congenital disease that disrupts the function of cone photoreceptors. In 2 out of 4 treated patients, fMRI measures revealed that when cone photoreceptors in the retina were stimulated no retinotopically organised response was measurable in primary visual cortex before

treatment. After treatment, a clear response emerged that was paired with an improvement in perception (Farahbakhsh et al., 2022).

Final Summary

In sum, MRI has provided important insights into the neural aetiology of LHON and its wider impacts beyond the optic nerve, as well as into the potential neural mechanisms of treatment effects. However, many questions remain to be resolved, including which processes explain these changes at the microstructural level and their commonality with other neurological diseases, the timing of these changes and how they relate to visual function, and the causes of recovery observed in some cases. To address these important questions and pave the way for future MRI applications that can inform emerging new treatments of LHON, it will be crucial to collect data from larger groups of patients, separate out neuropathology for different phenotypes, improve ways of measuring visual function at the brain level in LHON, and utilise recent quantitative MRI approaches to distinguish between candidate recovery mechanisms such as remyelination of affected CNS fibre tracts or restoration of central vision function.

1.7. Objectives and overview of the thesis work

The aim of this PhD project is to use magnetic resonance imaging (MRI) modalities to better understand structural and functional changes beyond the retina in Leber Hereditary Optic Neuropathy (LHON).
Specifically, I aim to:

- Investigate the causes of neural changes along the visual pathways, and whether they reflect demyelination or axonal loss (**Chapter 2**),
- Address the lack of functional measures in LHON, by developing an fMRI approach that maps visual field loss at the level of the cortex in patients (**Chapters 3-4**),
- Explore how these brain-based visual field loss measures can offer potentially useful endpoints for clinical trials, by linking them to retinal and behavioural measures used in clinics (**Chapter 4).**

In **Chapter 2**, I investigated the microstructural processes driving structural changes in LHON. To achieve this, I collected and combined a rich diffusion MRI dataset and a multi-parametric mapping (MPM) dataset, with histology-derived biophysical models of tissue microstructural characteristics. This allowed me to (i) capture structural changes and (ii) disentangle between demyelination and axonal degeneration along the visual pathways, especially within the optic tracts and radiations. This work presented specific challenges: First, head and eye movements can severely impact the quality of the innovative structural MRI images I aimed to collect. To mitigate these effects, I used a head motion-restricting device in the scanner and ran pilots to optimise MPM and diffusion MRI scanning parameters. Second, while existing tools supported segmentation of the optic radiations, segmenting the optic tracts was particularly challenging in patients due to reduced MRI contrast around this structure. I overcame this by developing a custom segmentation approach tailored to the optic tracts. Finally, I implemented a novel toolbox for advanced modelling of microstructural tissue as it was being developed by collaborators, which required careful trouble shooting and quality control checks. Through this work, I confirmed previously reported structural changes in LHON and

provided new insights into the balance between demyelination and axonal degeneration, advancing understanding of the underlying mechanisms in LHON.

In **Chapters 3 and 4**, I aimed to address the lack of sensitive functional measures of vision loss across the visual field in LHON. The large central scotoma (up to 10-15º from fixation) and associated fixation difficulties complicate the measurement of visual function, resulting in limited functional measures and understanding of visual processing in patients. To address this, I developed a functional MRI (fMRI) approach that combines a contrast sensitivity task with population receptive field (pRF) mapping to measure contrast sensitivity changes across the visual field at the cortical level. To enable this in LHON patients, I had to address challenges linked to the presence of dense, central scotoma, including the need for (i) large-field presentation and (ii) fixation-free retinotopic mapping to link cortical responses to visual field locations. Therefore, I designed a large-field stimulation set-up in MRI, allowing for a 43º diameter presentation area whilst preserving the possibility for monitoring and tracking the participants' eyes in the scanner. I also used a fixation-free retinotopic atlas (the Benson atlas; Benson et al., 2012; Benson et al., 2014) to relate cortical responses to visual field locations in patients. As existing solutions were not optimised for large-field and accurate eccentricity modelling, I worked with collaborators (Noah Benson) on a novel solution to enhance the atlas accuracy for mapping cortical responses in periphery. In **Chapter 3**, I developed and tested this fMRI approach in normal-sighted controls, demonstrating that the method reliably quantified known differences in sensitivity across eccentricities (up to 20º) and visual field quadrants in this group. Crucially, these differences were still present when using the optimised fixation-free atlas, making the approach applicable to LHON patients who cannot be retinotopically mapped due to poor fixation from the central scotoma. In **Chapter 4**, I applied this fMRI approach in LHON patients, i.e., combining the contrast sensitivity fMRI task with the fixation-free retinotopic atlases. I evaluated the accuracy of this approach against retinal and behavioural measures of visual field loss. Using this method, I was able to map visual field defects at the cortical level in patients, with various degrees of correspondence to clinical measures.

In summary, the work in this thesis utilises a wide range of innovate approaches, to provide new insights into the impacts of LHON on the optic pathway

from retina to brain. This results in novel ways of characterising the impacts of severe eye disease on the brain and visual function, reliably and sensitively. These findings have important implications for clinical trials, offering new brain-based measures to assess therapeutic outcomes and potential bottlenecks. We know that gene therapies have promising impacts on acuity but given the widespread visual field loss in this disease, the new brain-based markers of visual function could offer better insights into the therapeutic outcomes that are important for shaping patients' visual experiences.

2. Measuring the integrity of the visual pathways in Leber Hereditary Optic Neuropathy (LHON)

In this chapter, I investigate post-retinal neural changes in LHON, a mitochondrial disease leading to severe vision loss. Understanding the specific type of degradation (axonal vs. myelin loss) is important for potential neuroplasticity and treatment. To build a cohesive biological model of myelin versus axonal integrity in LHON, I implement a novel MRI approach combining diffusion MRI and multi-parametric mapping (MPM) with computational modelling. By doing so, I reveal distinct patterns of axonal loss and demyelination along the visual pathways:

- In optic tracts: I demonstrate significant, concurrent, axonal loss and demyelination, alongside marked volume reduction.
- In optic radiations: I find substantial damage to axonal structure and organisation without volume loss, with axonal loss extending from LGN to V1 while demyelination is localised near V1.
- I also show volume reduction in the lateral geniculate nucleus (LGN), as well as reduced volume and cortical thickness in V1 – particularly in regions representing central vision (3-15º eccentricity).

Together, these findings provide converging *in vivo* evidence of neural degeneration in LHON, bridging the gap between histology and *in vivo* imaging. This offers potential quantitative biomarkers for tracking disease progression and assessing the effectiveness of emerging gene therapies in LHON.

2.1. Structural MRI insights into post-retinal changes in LHON

When retinal tissue degenerates in eye disease, downstream neural pathways are also affected. Understanding the processes that underlie these downstream changes – e.g., demyelination versus axonal content loss – can offer key insights into effective therapy. Some processes may be more amenable to repair and could be

tracked to assess therapeutic success. Until recently, these microstructural mechanisms could only be measured via post-mortem histology (Sadun et al., 2000; Carelli et al., 2004). Now, advances in *in vivo* brain microstructure imaging enable biophysical models of microstructural diffusion properties (Mohammadi & Callaghan, 2021) that estimate tissue properties such as myelin- and iron content or axonal volume in living patients. Notably, combining axonal and myelin volume estimates yields the MR g-ratio, which has been shown in mouse models to be (highly) predictive of an aggregate estimate of the true distribution of microscopic g-ratios within a voxel (West et al., 2016). Since the g-ratio (axon inner diameter divided by total axon+myelin diameter) directly governs conduction velocity (Rushton, 1951; Drakesmith et al., 2019; Clark et al., 2022), the possibility of tracking it *in vivo* raises a key question: can we link these microstructural changes to neural function and recovery, thereby guiding more targeted and effective therapies?

Here we investigate this question in Leber Hereditary Optic Neuropathy (LHON), a mitochondrial eye disease that impacts retinal ganglion cells and causes severe central vision loss, primarily in adult males. LHON is a disease that could greatly benefit from better microstructural characterisation: post-mortem histology in a handful of patients reveals both demyelination and substantial axonal loss, particularly of small-diameter fibres, in pre-geniculate optic nerves (axonal loss: Figure 3A&B; Sadun et al., 2000; Rizzo et al., 2012; Pan et al., 2012; Coussa et al., 2019; demyelination: Figure 3C; Carelli et al., 2004), but the prevalence of these processes in the wider patient population, and beyond the optic nerve is unclear. With novel gene-based sight-rescue therapies emerging for LHON, it is crucial to characterise post-retinal microstructural repair dynamics and establish reliable *in vivo* metrics to ensure effective transmission of retinal signals to the cortex.

MRI studies in LHON using standard methodologies, have identified volume loss of grey and white matter, diffusion reduction, and myelin marker loss in the optic nerves and tracts (Inglese et al., 2001; Barcella et al., 2010; Milesi et al., 2012; Ogawa et al., 2014; Wang et al., 2017; Takemura et al., 2019; Jonak et al., 2020). A small number of MRI studies on the optic radiations also show variable results – some reporting reduced white matter volume in optic radiations (Barcella et al., 2010) and others not (Takemura et al., 2019). Diffusion MRI studies of the optic radiations are more consistent in reporting significant reductions in fibre integrity (Rizzo et al., 2012;

Milesi et al., 2012; Manners et al., 2015; Ogawa et al., 2014; Takemura et al., 2019), particularly near V1 (Ogawa et al., 2014; Takemura et al., 2019). These may reflect microstructural alterations affecting axonal organisation and myelination, potentially indicative of neurodegenerative processes. Quantitative T1 metrics, as used by Takemura et al. (2019), also suggest potential changes in macromolecular content like myelin or iron content.

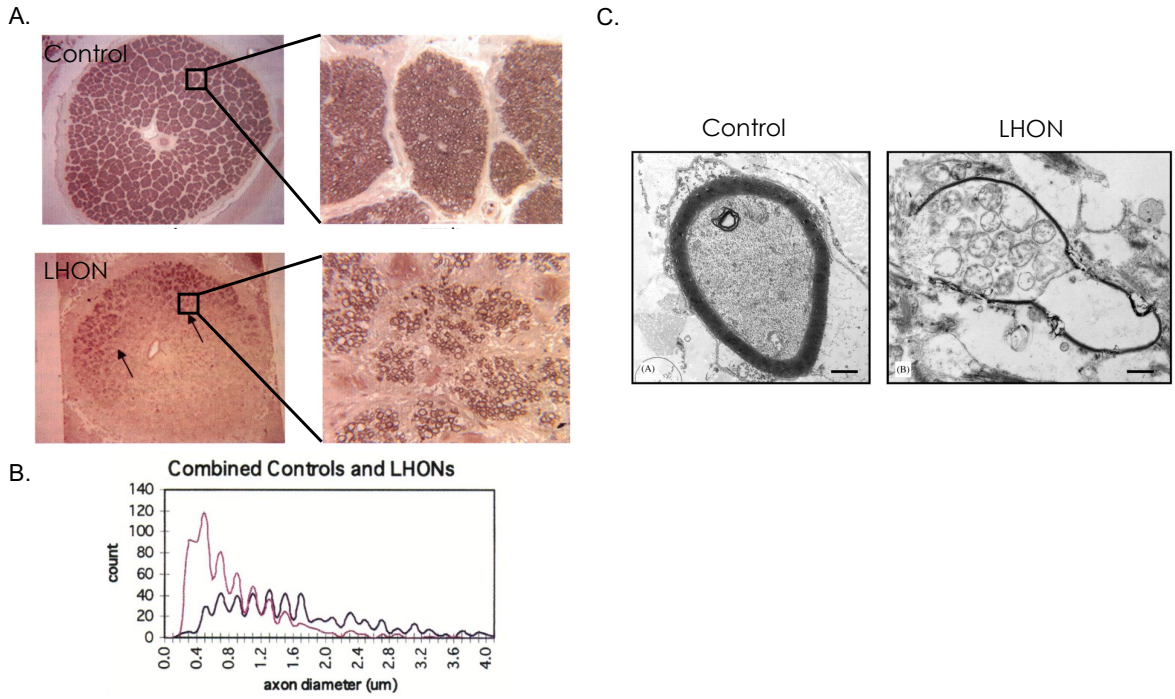

Figure 3. Histology shows reduced axon and myelin integrity of optic nerve in LHON
(A) Cross-sections of normal (top) and LHON-11778 optic nerves (bottom), stained with p-phenylenediamine to visualize axonal fibres. LHON shows marked optic atrophy with fewer, predominantly larger, preserved fibres. (B) Axon-diameter distribution reveals a reduced frequency of small fibres in LHON (black) compared to controls (dark pink). Images in panels A&B are from Sadun et al., 2000, Trans. Am. Ophthalmol. Soc. (C) Electron micrographs of normal (left) and LHON-affected (right) optic nerves show mitochondrial accumulation in axoplasm and myelin thinning in LHON. Image from Carelli et al., 2004, Prog. Retin. Eye Res.

Together, MRI studies, in line with histology, suggest changes consistent with both reduced myelin and axonal loss in LHON. However, there is substantial variability across MRI studies, likely due to the indirect nature of conventional MRI-based assessments of tissue integrity. Standard water diffusion-weighted imaging (DWI) measures, including diffusion tensor imaging (DTI) provide macro-level measures that are influenced by multiple physiological and methodological factors. These limit their explanatory power as well as their specificity and sensitivity to underlying biological

processes. For example, (semi-)quantitative markers such as fractional anisotropy (FA) in white matter are sensitive to a range of microstructural changes, including myelin and axonal loss and changes in axonal organisation. Similarly, quantitative MRI techniques like qT1, and semi-quantitative measures such as magnetisation transfer saturation (MT_{sat}), are sensitive to changes in macromolecular content. Therefore, in white matter, where myelin is the most common macromolecule, qT1 and MT_{sat} are highly sensitive to myelin content changes. However, they can also be influenced by other factors beyond myelin content, such as inflammation and iron content. While these metrics offer valuable insights, their lack of specificity complicates interpretation, particularly in complex pathologies like LHON where multiple tissue components may be affected simultaneously.

Our aim is to address these challenges by developing histologically calibrated imaging biomarkers that distinguish axonal loss and demyelination-related pathology in along the visual pathway in LHON via a multi-modal framework. We integrate quantitative MRI (qT1, MTsat) with diffusion metrics and computational tissue modelling to build a unified biological model of tissue loss, rather than treating each measure in isolation. This approach would not only enhance the specificity and sensitivity of our measures of structural integrity but also provides a framework for tracking disease progression and therapeutic outcomes. Specifically, our approach combines diffusion-weighted imaging and computational modelling of microscopic tissue characteristics with multiparameter mapping (MPM). MPM models three MRI contrasts to provide quantitative assessments of tissue properties sensitive to macromolecular content like myelin and iron. Each map offers a different perspective on neural tissue properties. The qT1 (longitudinal relaxation time) map measures how quickly tissues return to equilibrium state after excitation, which is influenced by water movement, myelin, and iron levels. The magnetisation transfer saturation (MT_{sat}) map quantifies interactions between free-water protons and macromolecule-bound protons, such as those in myelin. Prior MRI studies have linked qT1 and MT_{sat} values to myelin content, making them valuable metrics for studying (de-)myelination processes (Takemura et al., 2019; York et al., 2022). However, these measures are also affected by factors like inflammation (Vavasour et al., 2011) and thus must be interpreted carefully when studied in isolation. By integrating findings from multiple measures, we can achieve a more reliable and comprehensive understanding of the

underlying tissue changes, providing a clearer picture of myelination-related processes at work.

Diffusion MRI measures tissue microstructural integrity by tracking water molecule diffusion. Traditional diffusion tensor imaging (DTI) fits a diffusion tensor model at the whole-voxel level, producing metrics such as fractional anisotropy (FA), which captures any preferential diffusion directions, and mean diffusivity (MD), indicating diffusion magnitude. Additional measures include axial diffusivity (AD), representing diffusion along the primary direction of white matter tracts, and radial diffusivity (RD), representing diffusion perpendicular to the tracts. While FA and MD reflect overall tissue integrity, AD and RD have been linked to axonal and myelin integrity, respectively (Wheeler-Kingshott & Cercignani, 2009; Winklewski et al., 2018). Recent approaches have expanded beyond conventional metrics, enabling modelling of biophysical diffusion parameters that are related to microscopic tissue properties. For example, the white matter tract integrity (WMTI)-Watson model provides detailed insights into the intra- and extra-axonal environments. This model estimates parameters like the axonal water fraction (f), which is proportional to the relative diffusion signal from the intra-axonal space and thus the axons, as well as the diffusivity within axons (D_a) and in the surrounding extra-axonal space, either in parallel or perpendicular directions to the axons ($D_{e,para}$ and $D_{e,perp}$). Additionally, this model provides an approximation for the axonal alignment (Watson parameter κ), reflecting the organisational structure of axons within bundles.

We hypothesise that axonal degeneration and demyelination should have distinct effects on this family of diffusion MRI metrics. Axonal degeneration should reduce FA, AD, axonal water fraction (f), and axonal alignment (κ), whilst increasing MD. It may also elevate RD, $D_{e,para}$, and $D_{e,perp}$, due to axonal loss and the subsequent extracellular space expansion. In contrast, demyelination should lower FA and axonal alignment, and raise RD, $D_{e,para}$, and $D_{e,perp}$, with minimal changes to AD and axonal water fraction. These patterns reflect the loss of myelin's restrictive effects while maintaining intact axonal structures.

Finally, combining microstructural diffusion properties with MPM measures of myelin content in the tissue enables the calculation of the MR g-ratio, which quantifies the ratio between the inner and outer radii of myelinated axons (Figure 4). Initially quantified through histology, this metric has shown good correspondence with *in vivo*

MRI estimates, although challenges remain in calibrating MRI parameters to accurately reflect histological measurements of the axonal and myelin volume fractions. By estimating MR g-ratio, we can access the extent to which optic pathways in LHON show:

- no change overall as compared to controls (resulting in an unchanged MR g-ratio),
- inflammation processes (also resulting in an unchanged MR g-ratio but with proportional increase in volume of the axon and myelin sheath),
- a proportional loss of axon and myelin (also resulting in an unchanged MR g-ratio but with proportional reduction in volume of the axon and myelin sheath),
- more demyelination versus axonal degeneration (reflected by increased MR g-ratio and more pronounced reduction in volume of the myelin sheath),
- more axonal degeneration versus demyelination (reflected by decreased MR g-ratio and more pronounced reduction in volume of the axon).

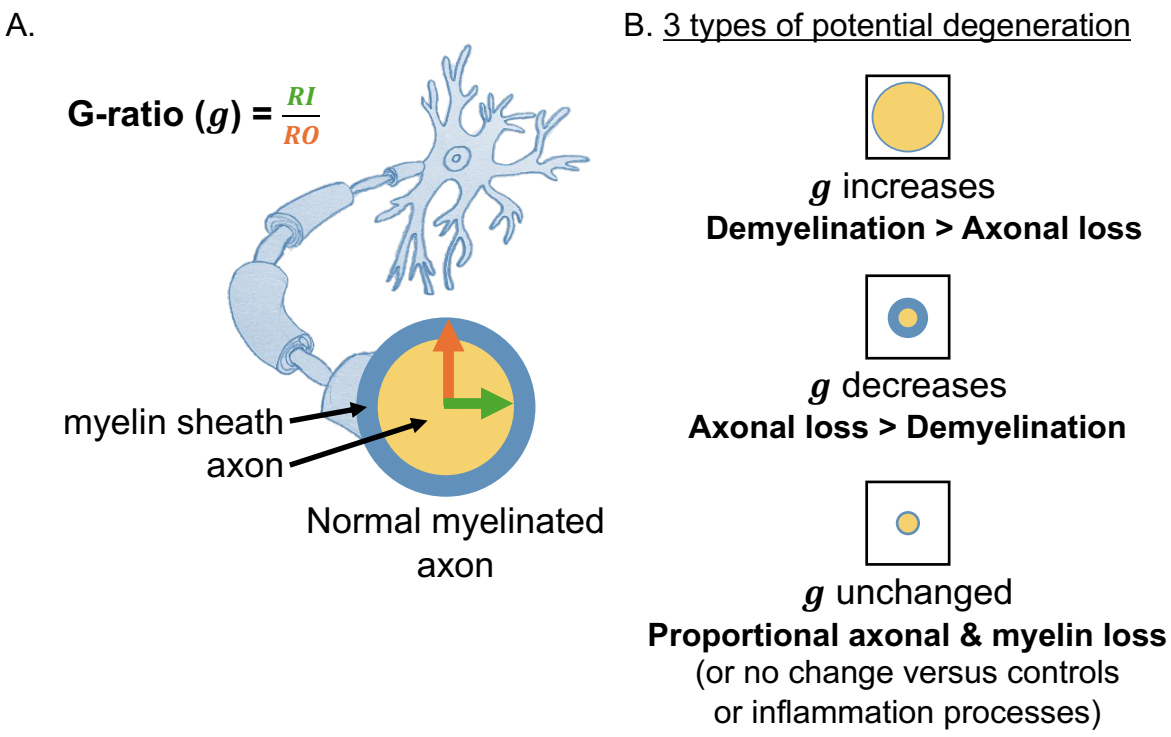

Figure 4. Visualising g-ratio changes as indicators of axonal health.

(A) Schematic illustration of a normal myelinated axon, with the MR g-ratio defined as $g = \frac{RI}{RO}$.

(B) Three degeneration patterns illustrated by g-ratio changes and reflecting proportional changes in the fraction of axonal and myelin contents within a voxel: increased g-ratio (more demyelination than axonal degeneration), decreased g-ratio (axonal loss), and unchanged g-

ratio (proportional axonal and myelin loss or no change with respect to controls or infllammation processes).

2.2. Methods

2.2.1. Participants

We recruited 24 healthy controls (mean±SD: 33.9±10.7yo; 13M) for structural MRI scans (Table 6). All participants had normal or corrected-to-normal vision with no other ocular pathologies and were drawn from the local staff at University College London and UCL-approved recruitment platform. We also recruited 13 chronic LHON patients (mean±SD: 36.8±10.1yo; 10M), all genetically confirmed with one of the three most common mutations: eight with m.11778G>A, four with m.14484T>C, and one with m.3460G>C (Table 6). The average disease duration for LHON patients was 16.3±13.7 years, and all were in the chronic phase of the disease (> 1 year). Written informed consent was obtained from all participants, and the study was approved by the HRA/HCRW and Research Ethics Committee (IRAS 258959; REC 20/YH/0336).

We matched participants as closely as possible on demographics as those can influence brain structural properties, including age, sex, and body mass index (BMI; Table 6). Mann-Whitney U shows that there were no group differences (controls vs. LHON) in age ($W = 125, p = 0.3366$), and BMI ($W = 98, p = 0.0668$). Similarly, Chi-Square tests showed that there were no differences in sex distribution ($\chi^2 = 1.0151, p = 0.3137$). For analyses of the optic tracts, we excluded one control due to poor tract segmentation, resulting in 23 healthy controls and 13 LHON patients when assessing differences in DTI and qT1 metrics in this structure.

Variable	**LHON (*n*=13) M (SD)**	**HC (*n*=24) M (SD)**	***W***	**χ^2 (df)**	***p***
Age (years)	36.8 (10.1)	33.9 (10.7)	125	–	0.3366
Sex (% male)	10M:3F 76.9	13M:11F 54.2	–	1.0151 (1)	0.3137
BMI (weight/height^2)	25.1 (3.8)	22.5 (2.5)	98	–	0.06689
Mitochondrial mutation	11778G>A (61.5%) 14484T>C (30.8%) 3460G>A (7.7%)	–	–	–	–
Duration of duration from symptoms onset (years)	16.3 (13.7)	–	–	–	–

LHON: Leber Hereditary Optic Neuropathy; HC: Healthy Controls; W: Mann-Whitney U test; χ^2 = Chi-Square test; M = mean; SD = standard deviation; df = degree of freedom

Table 6. Demographic and clinical characteristics of LHON patients (n = 13) and healthy controls (HC, n = 24).
Group comparisons were conducted using the Mann-Whitney U test for continuous variables and Chi-Square test for categorical variables. LHON participants are further characterised by mitochondrial mutation type and duration since symptom onset.

2.2.2. Stimulus & apparatus

Participants were presented with a spider-web grid in the scanner and asked to fixate a central white dot whenever possible. They were also instructed to remain still throughout the session, which was facilitated using an MRI-safe head-cast (Minimum Motion device – MinMo) developed at the BUCNI centre. The MinMo system used inflatable cushions positioned below the inion, neck, and around the ears, to minimise head movement with minimal effort. For additional comfort, participants were provided with ear protection and the option to listen to music or podcasts through MRI-compatible earphones designed at the MRI centre.

2.2.3. Data acquisition

Data were collected on a 3T PRISMA (Siemens), using a 30-channel coil – a modified version of the Siemens 32 channel head coil.

The multi-parametric mapping (MPM) protocol consisted of spin echo and stimulated images (11 nominal angles) acquired with 3DEPI to map the B1+ transmit field, B0 images to correct for distortions in the EPI data, and three contrast weightings: T1-weighted (T1w) images, proton density-weighted (PDw) images, and magnetisation transfer-weighted (MTw) images. T1w, PDw, and MTw images were acquired at 0.8mm isotropic resolution with a phase-encoding trajectory of 'Partitions in Lines' meaning that the faster phase encoded direction was right-left and the slow phase-encoded direction was anterior-posterior, and an angulation of 30º, chosen to minimise eye motion artefacts associated with fixation difficulties in patients (see Appendix 1 for details). Each contrast was preceded by a short, low-resolution scan (8mm isotropic) for correcting inter-scan motion during pre-processing. The total acquisition time for the protocol was approximately 28mins.

Diffusion MRI (dMRI) data were acquired using a reversed-phase encoding (blip-up/blip-down) spin-echo EPI scheme to enable susceptibility distortion correction.

The entire acquisition was performed with both Anterior–Posterior (AP, “blip-up”) and Posterior–Anterior (PA, “blip-down”) phase-encoding directions, using identical imaging parameters across both directions. These included 2 mm isotropic resolution, a multi-band acceleration factor of 2, and 150 diffusion-weighted directions distributed across four b-values: b = 0 s/mm² (15 directions), b = 500 s/mm² (30 directions), b = 1000 s/mm² (45 directions), and b = 2300 s/mm² (60 directions). To optimise scan time, the 150 diffusion-weighted directions were split into three acquisition pairs, each comprising one AP and one PA run with interleaved b-values. Pair 1 included 49 directions, pair 2 had 50 directions, and pair 3 had 51 directions. Each run lasted approximately 6 minutes and 30 seconds. The field of view encompassed the whole brain, aiming to include the optic tracts as fully as possible.

Lastly, a T1-weighted structural image was acquired using an MPRAGE sequence with a voxel resolution of 1 mm isotropic, 208 slices, FOV 256 × 256 × 208 mm, flip angle 9º, TR = 2.3 s, TE = 2.86 ms, TI = 900 ms, bandwidth 240 Hz/Px, echo spacing 7.1 ms, and a total acquisition time of 5 minutes and 30 seconds. This MPRAGE was used for facilitating further cortical surface reconstruction in FreeSurfer.

2.2.4. Data pre-processing

2.2.4.1. Diffusion MRI and biophysical parameters analysis using ACID Toolbox

DICOM images from the Diffusion MRI (dMRI) protocol were converted to NIFTI format using dcm2niix (v.20200330) to standardize the datatype format (INT16) across participants, before being processed with the ACID toolbox (version 06/02/2025). The ACID toolbox is an extension of the Statistical Parametric Mapping (SPM) software and provides advanced tools for processing and modelling dMRI data from the brain, spinal cord, and ex-vivo samples (David et al., 2024). It incorporates state-of-the-art artifact correction, diffusion and kurtosis tensor imaging, and biophysical modelling to estimate microstructural white matter properties.

Diffusion MRI volumes, collected with AP (blip-up) and PA (blip-down) phase-encoding directions, were first converted to ACID-compatible format via the Startup module. These volumes underwent corrections for eddy-current distortions and motion, denoising with an adaptive method, Rician bias correction, and hyper-elastic susceptibility artifact correction (Figure 5). Pre-processed blip-up and blip-down datasets were merged, from which diffusion tensor and kurtosis maps were computed.

Finally, DTI and DKI maps were fitted with the WMTI-Watson model to estimate biophysical parameters. This model separates the diffusion MRI signal into intra- and extra-axonal compartments and outputs biophysical parameters such as axonal water fraction (f), intra-axonal diffusivity (D_a), extra-axonal diffusivities ($D_{e,per}$ and $D_{e,para}$), and axonal alignment (κ). Additional details on these steps are available in Appendix 2.

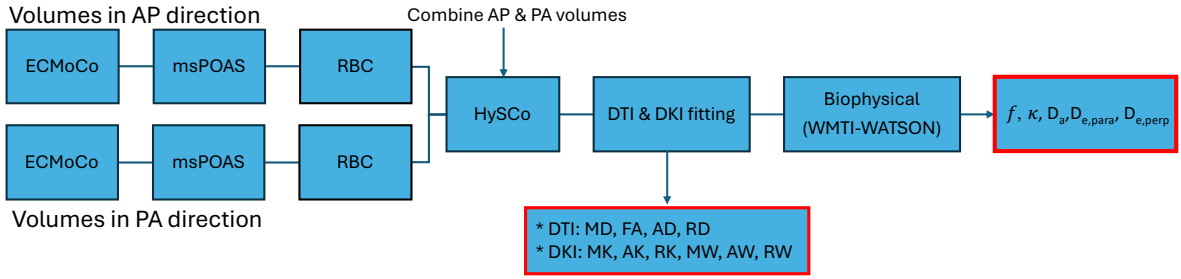

Figure 5. Diffusion MRI processing steps using the ACID Toolbox
ECMoCo: eddy-current and motion correction; msPOAS: multi-shell position-orientation adaptive smoothing; RBC: Rician bias correction; HySCo: hyper-elastic susceptibility correction; DTI/DKI: diffusion tensor/kurtosis imaging; FA: fractional anisotropy; MD/AD/RD: mean/axial/radial diffusivity; MK/AK/RK: mean/axial/radial kurtosis; MW/AW/RW: mean, axial and radial kurtosis tensor; f: axonal water fraction; κ: axonal alignment; D_a: diffusivity inside the axons; $D_{e,para}$/$D_{e,perp}$: diffusivity outside and parallel/perpendicular to the axons.

2.2.4.2. MPM analysis using hMRI Toolbox

The hMRI toolbox is an open-source extension of the SPM software designed for quantitative MRI (qMRI) data processing (Tabelow et al., 2019). It streamlines the creation of parameter maps related to brain tissue microstructure, using multi-parameter mapping (MPM). By correcting for instrumental biases such as transmit (B1+) and receive fields, as well as model imperfections, e.g. due to imperfect RF spoiling, the toolbox ensures accurate and reproducible measurements across different scanners and sites. These allow for physically accurate assessments of tissue properties, such as macromolecular content, facilitating *in vivo* histology and multi-site data integration.

Prior to processing, images from the MPM protocol were converted from DICOM to NIFTI format using the hMRI toolbox's DICOM import module. The volumes were re-oriented to a standard pose, corrected for biases (B1+ and RF sensitivity) and imperfections, and fitted with the MPM model (Earnst Equation) to generate

quantitative maps (Figure 6). This resulted in four key maps: longitudinal magnetisation rate (R1 = $\frac{1}{qT1}$), effective transverse relaxation rate (R2* = $\frac{1}{qT2^*}$), proton density (PD), and magnetisation transfer saturation (MT_{sat}). Additional details on these steps are available in Appendix 2.

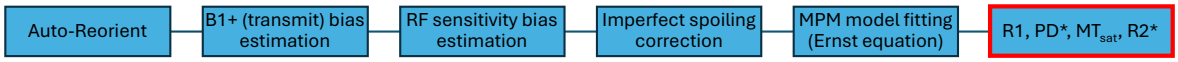

Figure 6. MPM processing steps using the hMRI toolbox.
RF: Radio Frequency; MPM: Multi-Parametric Mapping; R1: longitudinal relaxation rate; PD: effective proton density; MT_{sat}: magnetisation transfer saturation; R2*: effective transverse relaxation rate.*

2.2.4.3. Putting it all together

Brain reconstruction and maps co-registration to subject-native space

FreeSurfer's recon-all module was used to perform brain and surface reconstruction, using the structural MPRAGE image. Metrics maps from hMRI and ACID toolboxes were then co-registered to the MPRAGE image for each individual using FreeSurfer's *bbregister* module, without resizing the voxel resolution of metrics maps. This resulted in all maps being in the same space, i.e., the subject-native space.

Modelling the MR G-Ratio

Co-register maps were then used to compute the MR g-ratio map following the steps described in Clark et al. (2022). The MR g-ratio is an estimate reflecting the ratio of the inner radius of an axon to its total radius (i.e., inner radius + myelin sheath). An increase in its value likely reflects demyelination, as the total radius will decrease. In contrast, a decrease in g-ratio likely reflect axonal loss, as the inner radius decreases (Figure 4). However, it should be noted that if both mechanisms occur concurrently or processes of inflammation are in place, no change in g-ratio can be expected as compared to controls.

To compute MR g-ratio estimates in the brain, we first down-sampled the MPM magnetisation transfer saturation (MT_{sat}) map to match the voxel resolution (2mm isotropic) of the diffusion axonal-water fraction (f) map. The myelin-volume fraction

(MVF) map was then computed by multiplying voxels in the down-sampled MT_{sat} map with a scaling factor α equal to 0.1683 (Clark et al., 2022). Both f and MVF maps were then used to obtain the axonal volume fraction (AVF) map: $AVF = (1 - MVF) * f$. The MR g-ratio map was finally computed using the AVF and MVF maps (Equation 1).

$$MR\ gratio = \sqrt{1 - \frac{MVF}{MVF + AVF}}$$

Equation 1. MR g-ratio calculation.

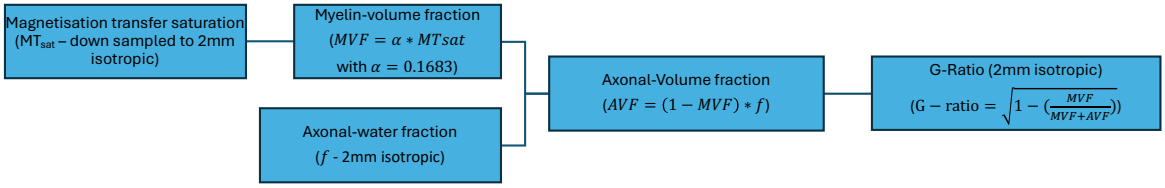

Figure 7. Processing steps for computing the MR g-ratio.
MT_{sat}: magnetisation transfer saturation; f: axonal water fraction; MVF: myelin volume fraction; α: scaling factor; AVF: axonal volume fraction.

2.2.5. Segmenting brain regions of interest

2.2.5.1. Lateral geniculate nucleus and other thalamic nuclei

FreeSurfer Sub-Cortical segmentation module was applied to the structural MPRAGE image to segment the thalamic nuclei. We extracted per individual, the left and right lateral geniculate nuclei (LGN) and medial geniculate nuclei (MGN), which are the visual and auditory cores in the thalamus, respectively. We also extracted the anterior (AV) nuclei as a control region.

2.2.5.2. Early visual cortex (V1-V3)

The primary, secondary, and third visual cortex (V1, V2, and V3) were derived from the Benson atlas template fitted to the participant's structural cortical surface, using *neuropythy* (Benson et al., 2012; Benson et al., 2014; Benson & Winawer, 2018). This approach also provides cortical surface maps of eccentricity (up to 90º), polar angle, and population receptive field (pRF) size estimates.

2.2.5.3. Optic tracts

Segmenting the optic tract (OT) in Leber Hereditary Optic Neuropathy (LHON) patients from diffusion-weighted imaging (DWI) presented significant challenges, likely due to the disease-related degeneration. Standard settings that effectively identified the OT in controls failed to detect probabilistic white matter tracts (streamlines) in most LHON patients. Additionally, there was no highly accurate segmentation atlas specific to the OT; the atlas labels that we tried (e.g., using FreeSurfer's optic chiasm label as a seed region) led to the inclusion of non-OT regions in the mask, potentially biasing the results. To address this issue and successfully identify tracts in both patients and controls, we developed a custom OT segmentation procedure which uses a more liberal streamline identification setting in MRTrix3.0.

To create an optic tract region of interest (ROI), we first used applied pyAFQ to control data to generate probabilistic streamlines between two coronal planes intersecting the OT and a posterior thalamus mask (Yeh, 2022). These streamlines, created in native diffusion space, were then binarized and averaged across control individuals in MNI-2mm space ("control-derived pyAFQ OT mask"). While effective in controls, pyAFQ failed to accurately identify OT streamlines in LHON patients.

We therefore then used MRTrix to identify the OT in patients and controls, using matching methodology across groups. Streamlines were first generated between a manually defined optic chiasm (drawn on the average b0 image) and lateral geniculate nucleus (LGN – FreeSurfer's label, resliced to native diffusion space using a nearest interpolation method). We also manually defined two coronal planes intersecting the OT, serving as intermediary waypoints that the OT streamlines should travel through. Using MRtrix's *tckgen*, we generated 5000 streamlines meeting these criteria per subject. While the resulting streamlines included the optic tract, they also encompassed additional fibre bundles in most participants. Therefore, to refine the segmentation:

(1) We retained only OT streamlines that (i) originated in the optic chiasm, and (ii) passed through ≥60% the control-derived pyAFQ OT mask (registered to native diffusion image), and (iii) terminated within this control OT mask.

(2) We excluded outlier OT streamlines by requiring all retained streamlines to fall within ±3 median absolute deviations of their median streamline trajectory.

Final OT streamlines were binarized, visually inspected, and co-registered to each subject's MPRAGE image. This allowed us to confirm anatomical accuracy of

the OT in each participant, which was critical to ensure that adjacent tissues that are affected by LHON were erroneously included in the analysis of the optic tract.

The segmented optic tracts overlaid on MPRAGE image are shown for all participants in Appendix 3.

2.2.5.4. Optic radiations and vertical occipital fasciculi

To segment the optic radiations, we first identified 10M streamlines in the whole brain using MRTrix3.0, only keeping tracts with lengths between 30 and 250mm. This tractogram was used as input in pyAFQ to segment out the optic radiations, using ROIs defined in MNI space and transformed to each participant's native space to constrain the segmentation (Figure 8). First, two start/end ROIs (V1 and central thalamus including LGN) and two inclusion ROIs (i.e., coronal planes intersecting the optic radiation path) were defined and only streamlines within 3mm of both inclusion ROIs' centroids were retained. Three exclusion ROIs (temporal pole, occipital pole, posterior thalamus) were then applied and any streamlines within 3mm of exclusion ROIs' centroids were excluded to clean the outputs from crossing fibres. Resulting streamlines were cleaned further by removing outlier fibres based on average length and mean Gaussian distance from the bundle core in pyAFQ, only retaining streamlines within ±3SD from the core and terminating within 3mm of start/endpoint ROIs' centroids (V1 and central thalamus including LGN) to avoid partial volume effects. The segmented optic radiations overlaid on MPRAGE image are shown for all participants in Appendix 3.

We also segmented the left and right vertical occipital fasciculi (VOF), a group of fibre bundles lateral to the optic radiations and connecting the dorsal and ventral occipital cortices (Figure 9). Our aim was to check whether our MPM measures could identify that this white matter structure is less myelinated than the optic radiations, as demonstrated in a previous MRI study (Takemura et al., 2019). First, two start/end ROIs were defined and only streamlines from the whole brain tractogram within 3mm of the ROIs' centroids were preserved. Resulting streamlines were then cleaned by removing outlier fibres based on average length and mean Gaussian distance from the bundle core, excluding any streamlines located outside ±3SD from the core. Finally, only streamlines terminating within 3mm of start/endpoint ROIs' centroids were retained to avoid partial volume effects.

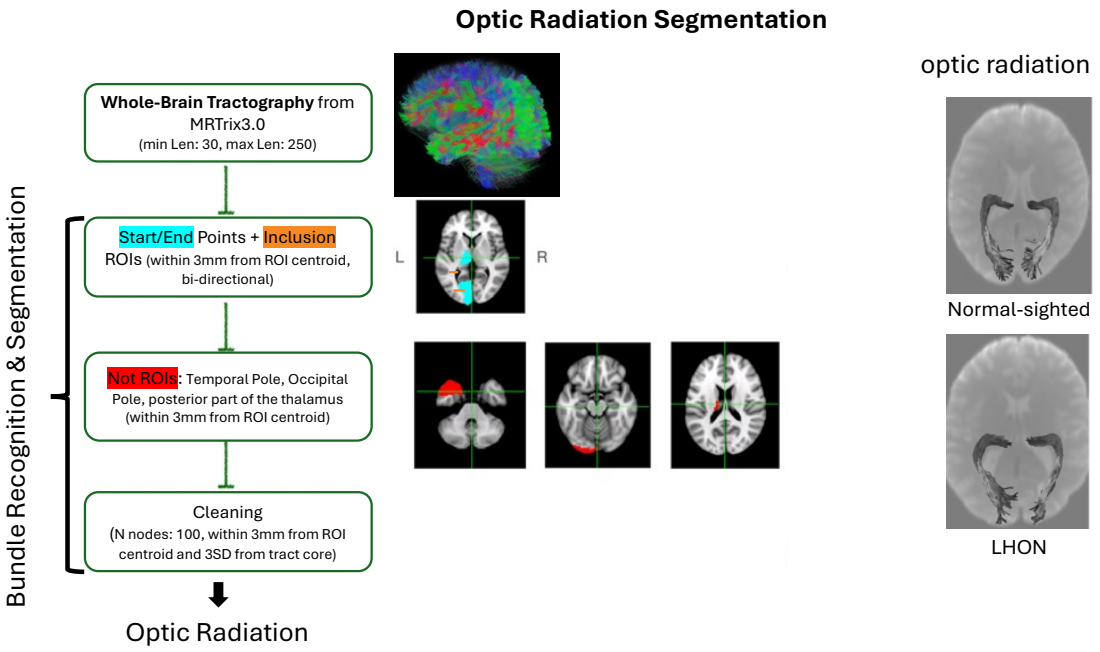

Figure 8. Bundle segmentation: Optic Radiations

Left: Tractography workflow using MRtrix3.0, including ROI-based filtering and bundle cleaning. Middle: Intermediate segmentation stages visualised on brain scans. Right: Comparison of optic radiation structure between control and LHON participants.

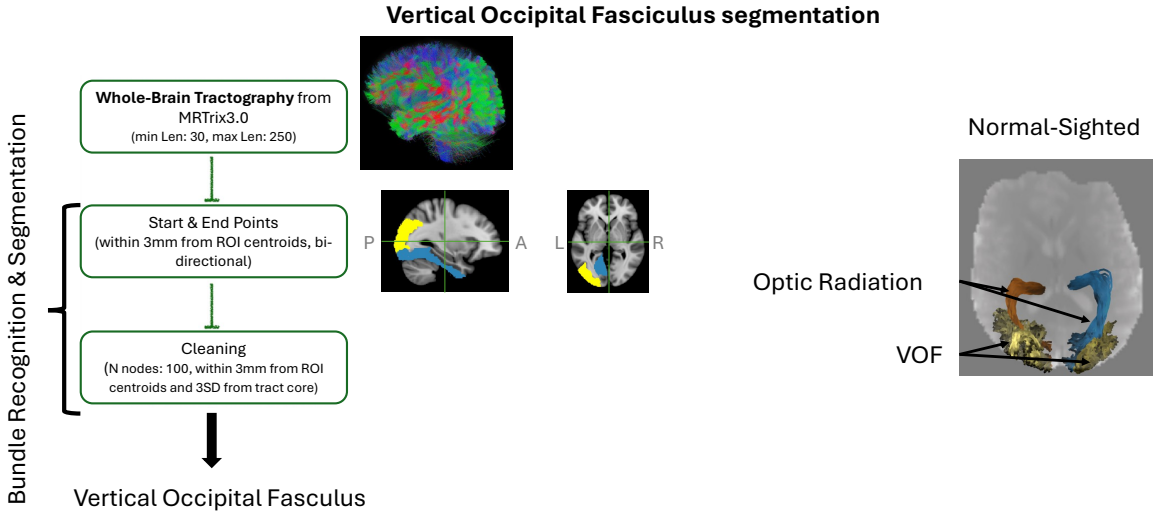

Figure 9. Bundle segmentation: Vertical Occipital Fasciculi

Left: Tractography workflow using MRtrix3.0, including ROI-based filtering and bundle cleaning. Middle: Intermediate segmentation stages visualised on brain scans. Right: Segmented VOFs in a normal-sighted participant, with reference to adjacent optic radiations.

2.2.6. Extracting tract profiles for white-matter fibres

To extract diffusion-derived and MPM-derived metrics along the optic tracts, optic radiations, and VOF, we sampled our measures of interest at 100 equidistant locations (nodes) along the trajectories of each white matter bundle in pyAFQ.

Specifically, individual streamlines are first weighted using Gaussian weighting based on their proximity to the mean pathway of the bundle. This ensures that streamlines closer to the central or "mean" pathway of a bundle are given higher weights, while those farther away contribute less to the overall calculation. The bundles are then reoriented using standardised centroids derived from atlas models, computed from the streamlines across healthy controls, ensuring consistency across subjects. Diffusion and MPM measures of interest are then sampled at 100 evenly spaced points, or nodes, along the length of the bundle. These values are finally averaged across streamlines at each node to produce a smooth, weighted tract profile.

For optic radiations and VOF, the first and last 20 nodes were removed to exclude voxels where data could be noisy due to potential crossing fibres and proximity to tissue boundaries. For optic tracts, we excluded the first and last 25 nodes corresponding to the regions where the tracts are close to the optic chiasm and the LGN, and likely less accurately segmented. Finally, measurements from left and right fibre bundles were averaged for each node and the final profiles were visualised to illustrate variations in metrics along the bundle for analysis and interpretation.

2.2.7. Sampling of qT1 and MT_{sat} values across V1 cortical depths

To extract qT1 and MT_{sat} values across cortical depths, we first sampled qT1 and MT_{sat} data sets from the FreeSurfer-defined pial to grey–white matter boundary labels, in increments of 10% cortical thickness using FreeSurfer *mri_vol2surf*. By doing so, we aimed to check whether our MPM measures could identify gradual decline in myelination between the grey-matter boundary and the cortical pial surface. At each depth, the data were smoothed with a 4-mm full width half maximum (FWHM) 2D kernel, resulting in qT1 and MT_{sat} values projected across 11 cortical depth fractions (ranging from 0 to 1, in 0.1 increments; Sereno et al., 2013). Finally, qT1 and MT_{sat} values within the V1 region were extracted using the V1 label, which was generated by fitting the Benson atlas to the MPRAGE image.

2.2.8. Extracting volumetric measurements

Volumetric measurements were obtained for the optic tracts, optic radiations, vertical occipital fasciculi (VOF), early visual areas (V1–V3), and thalamic nuclei (LGN, MGN, and AV). Volumes of the thalamic nuclei for each participant were extracted directly from FreeSurfer's thalamic segmentation module, averaged across left and right ROIs, and normalised to the participant's total thalamic volume, also estimated by FreeSurfer.

White matter volumes (optic tracts, optic radiations, and VOF) were estimated for each participant by first generating binary masks from the streamline distributions of each fibre bundle obtained in DTI space (2mm-isotropic voxel resolution). The volume was then calculated by multiplying the number of voxels within the mask by the voxel size (2 mm^3), averaged across left and right tracts, and normalised to the individual's total cerebral white matter volume, as estimated by the FreeSurfer *recon-all* pipeline.

Finally, cortical surface data – including thickness, surface area, and eccentricity – were extracted from both hemispheres across visual areas V1–V3 using FreeSurfer and the Benson retinotopic atlas (Benson et al., 2012; Benson et al., 2014). Volumes were computed in surface space by multiplying surface area by mean cortical thickness within each region of interest. To account for individual differences in brain size and cortical morphology, we normalised all measures prior to averaging across hemispheres: for each individual, volume was expressed as a percentage of their estimated total intracranial volume (eTIV; obtained from FreeSurfer), thickness was normalised to the subject's mean thickness across V1–V3, and surface area was normalised to the total V1–V3 surface area. To assess spatial variation across the visual field, volume, thickness, and surface area data were further subdivided into eccentricity bins (0–3°, 3–15°, 15–30°, and 30-90º) using estimates from the Benson atlas. For V1, eccentricity values were corrected using adjusted maps to account for central field biases (see Chow-Wing-Bom et al., 2025 for methodology). Vertices were filtered by visual area and eccentricity bin, and within each bin, mean thickness, total area, and volume (area × thickness) were calculated. This surface-based approach offers several advantages over standard volumetric estimates derived from anatomical atlases (e.g., Desikan-Killiany and Destrieux atlases). The Benson atlas enables more precise delineation of visual areas based on retinotopic organisation, rather than relying solely on anatomical landmarks, which may not entirely align with functional

boundaries. Moreover, surface-based analysis allows for the decomposition of volume into its constituent components – surface area and cortical thickness – enabling more detailed investigations of structural variation.

2.2.9. Statistical analyses

For diffusion and MPM metrics, we analysed differences across Group, ROI (optic radiations, VOF), nodeID (i.e., the computed nodes along the segmented fibre bundle using a linear mixed-effects models (LME) fitted by restricted maximum likelihood (ReML) in R. For each metric, we included fixed effects for Group, ROI (only when comparing myelin markers between white matter fibres), nodeID, as well as for covariates (age, sex, and BMI), with random intercepts for subjects to account for within-subject variability.

To test differences in MPM myelin markers between the VOF and optic radiation, we used to following model:: $metric \sim Group * ROI * nodeID + age + sex + BMI + (1 \mid SubjectID)$. To compare the structural integrity of optic tracts and radiations across patients and controls, we used a similar LME model but without the ROI factor.

To test differences in MPM myelin markers across cortical depths, we used the following LME model: $metric \sim Group * Depth + age + sex + BMI + (1 \mid SubjectID) + (1 \mid Depth{:}SubjectID)$, with Depth defined as an ordered factor. Here, $(1 \mid Depth{:}SubjectID)$ corresponds to a random slope nested within each subject to account for correlations across depths within participants due to the small number of voxels in each cortical depth bins.

To investigate morphological differences between patients and controls, we applied LME models to structural metrics including grey and white matter volume, cortical thickness, and surface area. Each model included fixed effects for Group, ROI, age, sex, and BMI, with random intercepts for subjects: $metric \sim Group * ROI + age + sex + bmi + (1 \mid SubjectID)$. For V1, we also investigated changes across eccentricities, by including $Eccentricity$ as an additional fixed effect: $Metric \sim Group * ROI * Eccentricity + age + sex + bmi + (1 \mid SubjectID)$.

All visualisations were generated using data that had been de-trended for age, sex, and BMI effects. Post hoc pairwise contrasts between groups were computed using the *emmeans* package, with Bonferroni correction applied for multiple comparisons.

Finally, to investigate whether changes in the optic tracts and radiations were associated with retinal integrity and visual function, we performed correlations with global peripapillary retinal nerve fibre layer (pRNFL) thickness (derived from OCT), visual acuity, and disease duration. Given the binocular nature of the visual pathways, pRNFL and visual acuity values were averaged across both eyes. Brain-based metrics were de-trended for age, sex, and BMI. Data normality was assessed using the Shapiro–Wilk test to determine the appropriate correlation method—Pearson's r for normally distributed data, or Kendall's tau (τ) for non-normal data. We selected Kendall's τ over Spearman's rho (ρ) for non-parametric data due to its greater robustness and statistical efficiency in small sample sizes.

2.3. Results

2.3.1. Disrupted white matter integrity along the optic tracts and optic radiations: sanity checks using standard DTI and MPM metrics

As biophysical modelling approaches are novel and our imaging protocols differ from those used in previous literature, we first aimed to validate our measures. We assessed sensitivity and specificity via two sanity checks:

First, qT1 and MT_{sat} should reproduce known myelination gradients across major white matter tracts: the optic radiations versus vertical occipital fasciculus (OR more myelinated than VOF; Takemura et al., 2019), and across V1 cortical depths (deep cortical layers more myelinated than superficial layers; Sereno et al., 2013).

Second, the standard DTI metrics derived from our protocols should align with prior LHON diffusion findings of reduced tissue integrity (Milesi et al., 2012; Rizzo et al., 2012; Ogawa et al., 2014; Manners et al., 2015; Takemura et al., 2019), and increased qT1 (only in the optic tracts; Takemura et al., 2019). As LHON is rare and heterogeneous, MRI samples are typically small and results can be variable. Therefore, replication is of particular importance for interpreting findings of individual studies.

Myelination gradients can be recovered with MPM measures across white matter tracts and across cortical depths

We first investigated whether qT1 and MT_{sat} can capture known variations in myelination. The optic radiation is more myelinated than the Vertical Occipital Fasciculus (VOF). This means qT1 should be *higher* in the VOF than the optic radiations, and MT_{sat} should be *higher*. As predicted, we found higher qT1 values in VOF versus optic radiations in both group (Figure 10A; Controls OR-VOF: N=24, $t_{8837} = -17.015, p_{bonf} < 0.0001$; Patients OR-VOF: N=13, $t_{8837} = -3.692, p_{bonf} = 0.0009$), replicating the results of an identical comparison by Takemura et al., (2019). Unexpectedly, however, we found no significant enhancement in MT_{sat} across the optic radiations and VOF in controls (Figure A4.1 in Appendix 4, OR-VOF: $t_{8837} = -0.696, p_{bonf} = 1$). In patients, we found *reduced* MT_{sat} values in the optic radiations, indicative of lower myelin content relative to the VOF (OR-VOF: $t_{8837} = -13.364, p_{bonf} < 0.001$). Furthermore, qT2* values were consistently higher in the VOF compared to the optic radiations, in both controls ($t_{8837} = -101.737, p_{bonf} < 0.001$) and LHON patients ($t_{8837} = -54.009, p_{bonf} < 0.001$; Figure A4.1 in Appendix 4). Since qT2* is sensitive to iron deposits (Yan et al., 2012), these findings may indicate a presence of fewer oligodendrocytes and lower associated iron levels in the VOF compared to the optic radiations. Since MT_{sat} – a metric more specific to myelin than qT1 – does not differ between VOF and optic radiations in controls, the observed higher qT1 values in the VOF may therefore reflect differences in iron content rather than myelination. The reduction in MT_{sat} in patients' optic radiations is consistent with a degree of demyelination specific to the optic radiation. A caveat for this interpretation is the challenge of segmenting the VOF, as modelled fibres may include nearby tracts beyond the VOF itself.

We also investigated variations in myelination across cortical depths in V1 for both healthy controls and LHON patients (Figure 10B&C). In line with a reduction in myelination from the grey–white matter boundary to the pial surface, we found systematic increases in qT1 and decreases in MT_{sat} values from deep to superficial V1 layers (i.e., from small to large depth fractions). Post-hoc comparisons confirmed significant differences between successive depths in both groups, with all p-values < 0.0001 (Bonferroni-adjusted for 55 tests). These results demonstrate that gradients in MPM measures across cortical depths, align with known myelination patterns of the tissue (Sereno et al., 2013).

In summary, our results highlight differences in qT1 and qT2* between the optic radiations and the VOF in controls and patients, but not in MT_{sat}. While qT1 differences between the optic radiations and VOF in controls have previously been interpreted as capturing known differences in myelination of these white matter tracts, our results suggest that these differences may in fact be driven by iron content rather than myelin levels, whereas in patients, some degree of demyelination may also contribute. Additionally, we confirmed consistent declines in myelination across cortical depths in both controls and patients, evidenced by increases in qT1 and decreases in MT_{sat} from deep to superficial V1 layers. Together, these results underscore the value of complementary MPM metrics in characterising tissue composition differences in the brain.

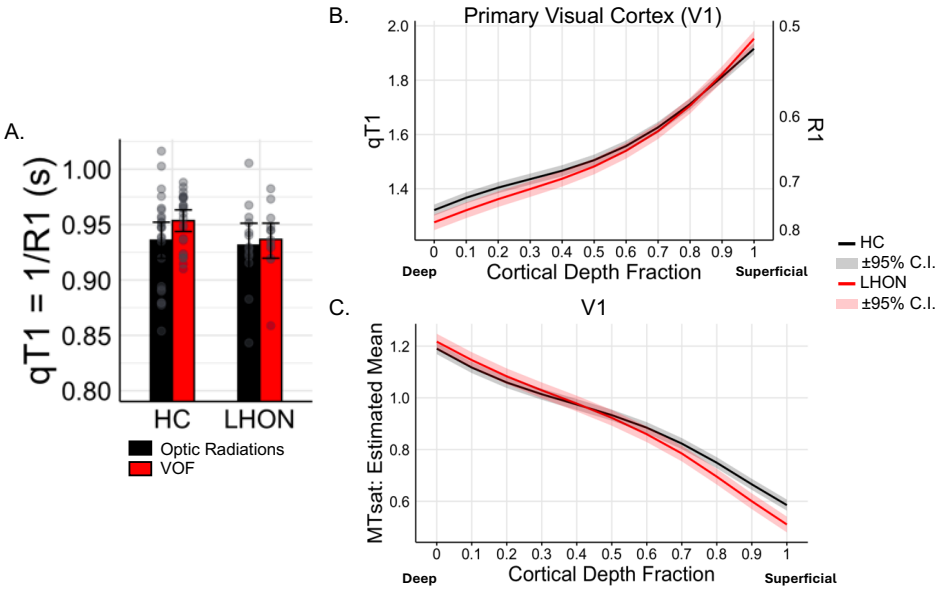

Figure 10. Myelination differences are reflected in MPM measures, in controls and LHON patients.

(A) Optic radiations (black) show greater myelination than VOF (red), reflected by lower qT1 values in both healthy controls (HC) and LHON patients. Light grey dots show individual data; error bars indicate 95% confidence intervals. (B) qT1 profiles across V1 cortical depths in HC (black) and LHON (red). (C) MT_{sat} profiles across V1 cortical depths in HC (black) and LHON (red). Shaded areas and error bars represent 95% confidence intervals.

Diffusion Tensor Imaging measures along the optic pathways

We then compared standard DTI metrics between LHON and controls, along the optic pathways.

In the optic tracts, FA was significantly reduced in LHON patients (Figure 11C; $F_{1,36.5} = 5.6087; p < 0.02328$), and this was consistent along the entire length of the tracts ($p_{bonf} < 0.01$ for all 50 locations). This suggests widespread white matter integrity alterations in the optic tracts, aligning with findings from Takemura et al. (2019).

In the optic radiations, FA was also significantly reduced (Figure 11D; $t_{32.9} = 7.193; p_{bonf} < 0.0001$), with the effect becoming more pronounced near V1 ($p_{bonf} < 0.01$ for the last 80% of the radiations). These findings point to significant disruptions in white matter organisation, particularly in regions closer to the visual cortex, again aligning with findings from Takemura et al. (2019).

We also investigated differences in MD, RD, and AD between groups along these structures (see Figure A5.1 in Appendix 5), and here our results show discrepancies from Takemura et al. (2019). Specifically, we found unchanged MD ($F_{1,50.1} = 2.4686;\ p = 0.1224$) and RD ($F_{1,44.9} = 0.0007;\ p = 0.9787$) in the optic tracts and AD ($t_{32.7} = -0.599; p_{bonf} = 1$) in the optic radiations. These highlight the variability in DTI measures, especially for AD and RD, which are often interpreted as linked to axonal and myelin loss respectively.

In conclusion, significant FA reductions in the optic pathways of LHON patients indicate widespread white matter disruptions. The pronounced FA loss near V1 and discrepancies in MD, RD, and AD underscore the complexity of DTI measures and their variability in detecting axonal and myelin changes in the optic tracts and radiations of LHON patients. These findings highlight the need for multimodal approaches to better understand the contributions of axonal and myelin damage in LHON pathology.

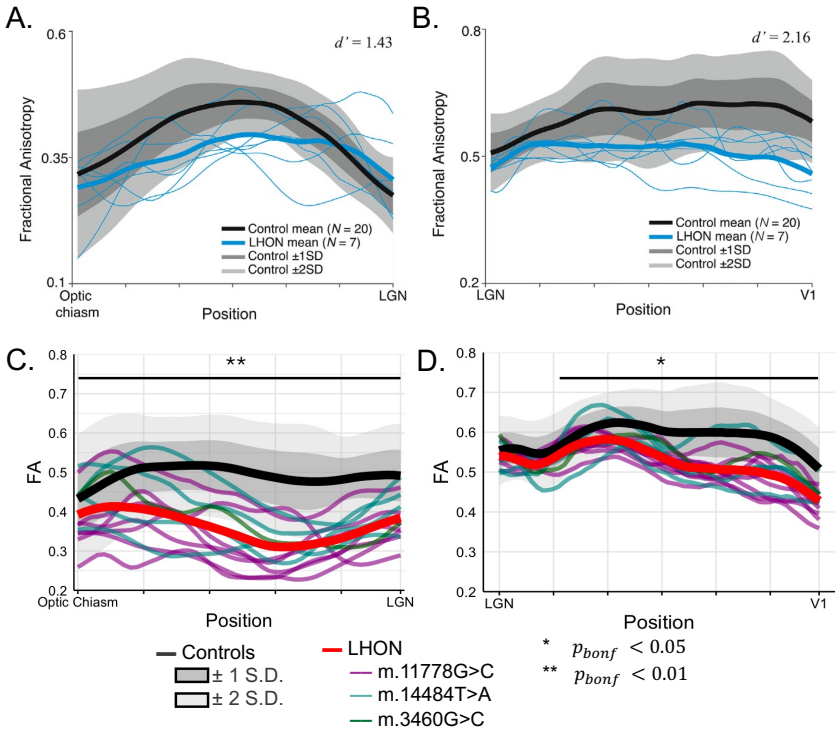

Figure 11. Reduced white-matter integrity along the optic tracts and radiations, in LHON. (A, B) Fractional anisotropy (FA) along the optic tracts (optic chiasm to LGN) and optic radiations (LGN to V1), from Takemura et al., 2019, NeuroImage: Clinical. Black line shows control mean; shaded areas indicate ±1 (dark grey) and ±2 (light grey) standard deviations. Thick blue line shows LHON mean; thin blue lines represent individual LHON profiles. (C, D) FA along the optic tracts and radiations from our study. Black line shows control mean with ±1 and ±2 SD shaded areas. Red line shows LHON mean; individual LHON profiles are color-coded by mutation: purple (m.11778G>C), cyan (m.14484T>A), and dark green (m.3460G>C).

Multi-Parametric Mapping measures along the optic pathways

We next compared MPM metrics between LHON and controls, along the optic pathways.

In the optic tracts, we found an overall increase in qT1 in patients as compared to controls (Figure 12C; $F_{1,36.3} = 144.1070$; $p < 0.0001$), aligning with findings from Takemura et al. (2019). Expanding on these findings, our analysis revealed an overall increase in qT2* ($F_{1,44.6} = 44.2968$; $p < 0.0001$) and PD ($F_{1,33.7} = 88.8799$; $p < 0.0001$), along with a marked decrease in MT_{sat} ($F_{1,40.5} = 267.2671$; $p < 0.0001$) in the optic tracts of patients relative to controls. These results point to a loss of macromolecular content in the optic tracts, in line with both demyelination and axonal

degeneration. These effects were also present at all locations along the length of optic tracts (Figure A5.2 in Appendix 5; qT1, PD, qT2*, and MT_{sat}: $p_{bonf} < 0.001$ for all locations), contrasting the localised reduced RD seen in DTI metrics. Together, DTI and MPM results are consistent with altered WM integrity in the optic tracts, and with axonal degeneration and demyelination.

In the optic radiations, no overall significant change in qT1 was detected in LHON patients compared to controls (Figure 12D; $t_{32.4} = 0.409, p_{bonf} = 1$), consistent with Takemura et al. (2019). Similarly, no overall significant differences between LHON patients and controls were observed for qT2* ($t_{32.4} = -2.371, p_{bonf} = 0.0953$) and MT_{sat} ($t_{32.5} = 1.183, p_{bonf} = 0.9812$). However, we found a notable, overall increase in PD in the optic radiations of LHON patients ($t_{33.3} = -3.687, p_{bonf} = 0.0032$), suggesting higher water content indicative of structural damage. Further examination along the length of optic radiations revealed increased PD, coupled with reduced qT2* and MT_{sat}, localised to the portion of the radiations close to V1 in LHON patients (see Figure A5.2 in Appendix 5; PD: $p_{bonf} < 0.05$ for the second half of the radiations; qT2*: $p_{bonf} < 0.05$ for the last 30% of the radiations; MT_{sat}: $p_{bonf} < 0.05$ for the last 20% of the radiations). These findings stand in contrast to the effects noted in the optic tracts and suggest a degree of demyelination confined to the segment of the optic radiations near V1 in LHON patients.

In summary, our results align with key findings from Takemura et al. (2019), demonstrating marked dystrophy of white matter integrity along the optic pathways in LHON patients. Our results support the hypothesis of widespread axonal loss and demyelination in the optic tracts, with some localized demyelination observed near V1 in the optic radiations. However, the extent of axonal degeneration in the optic radiations remains uncertain. Critically, standard DTI and MPM measures may not accurately capture axonal loss and demyelination in the optic pathways. These limitations likely arise because these methods do not directly model microstructural tissue properties and can be influenced by confounding factors such as the presence of crossing fibres. By using a multi-metric approach combined with advanced modelling of microstructural tissue properties, we may achieve a more histologically accurate assessment of axonal and myelin loss, and gain more specific insights into the dynamics of white matter changes in LHON.

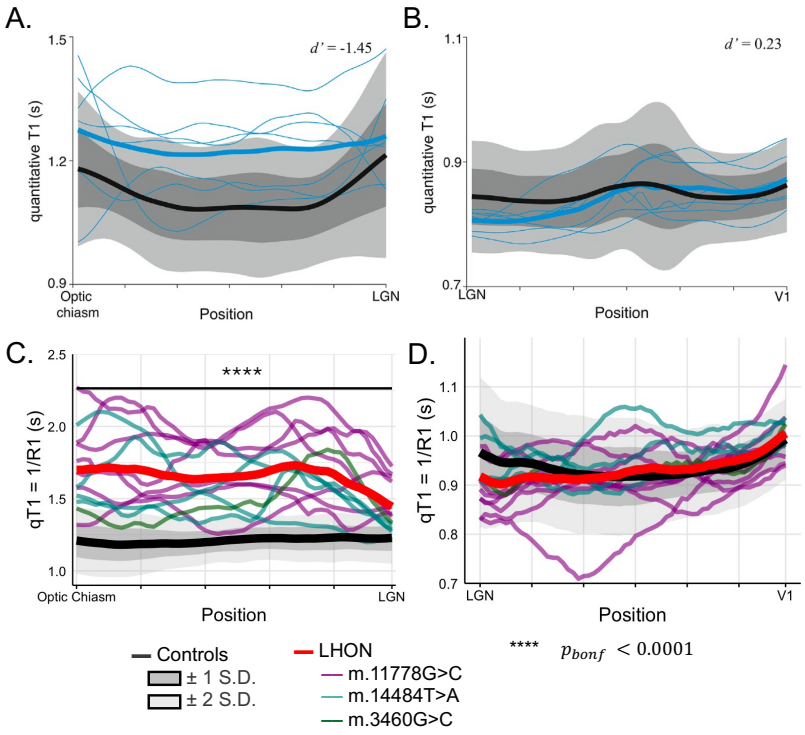

Figure 12. Differential qT1 variability in LHON: Increased qT1 in optic tracts vs. stable qT1 in optic radiations.

(A, B) qT1 along the optic tracts (chiasm to LGN) and optic radiations (LGN to V1), from Takemura et al., 2019, NeuroImage: Clinical. Black line shows control mean; shaded areas indicate ±1 (dark grey) and ±2 (light grey) SD. Thick blue line shows LHON mean; thin blue lines represent individual LHON profiles. (C, D) qT1 along the optic tracts and radiations from our study. Black line shows control mean with ±1 and ±2 SD shaded areas. Red line shows LHON mean; individual LHON profiles are color-coded by mutation: purple (m.11778G>C), cyan (m.14484T>A), dark green (m.3460G>C).

2.3.2. Additional insights from state-of-the-art structural MRI measures: evidence of demyelination and axonal loss

Biophysical parameters along the optic pathways

Advances in diffusion MRI modelling using diffusion kurtosis imaging (DKI) measures have provided new ways to model intra and extra-axonal compartments, by generating measures of microstructural tissue properties. These tissue properties are closer to the histological gold standard when they are derived from multi-shell DWI data (e.g. DKI) as compared to DTI measures (Papazoglou et al. 2024). Here, we wanted to investigate whether these biophysical parameters could provide further

insights on the mechanisms underlying demyelination and axonal degeneration along optic pathways in LHON.

In the optic tracts of LHON patients, we observed a significant overall reduction in axonal water fraction (f; $F_{1,42.1} = 69.1206, p < 0.0001$) and axonal alignment ($\kappa$; $F_{1,40} = 8.0558, p = 0.0071$). Regional analysis along the tracts confirmed consistent reductions in both metrics across all locations (Figure A5.3 in Appendix 5; f and κ: $p_{bonf} < 0.01$ at all locations). In contrast, no significant group differences were found in intra-axonal diffusivity (overall: D_a; $F_{1,51.8} = 0.0217, p = 0.88347$) or in parallel diffusivity in the extra-axonal space (overall: $D_{e,para}$; $F_{1,52} = 0.8867; p = 0.8867$), either overall or regionally. Although perpendicular extra-axonal diffusivity differed on average between groups ($D_{e,per}$; $F_{1,48.2} = 8.6921; p = 0.004917$), regional analysis revealed no significant variation along the tracts. These findings suggest structural and organisational damage to the axons of the optic tracts, reflected in reduced axonal density and coherence, without significant changes in intra- and extra-axonal diffusivity. Post-mortem histology indicates that smaller-diameter optic nerve fibres are preferentially affected in LHON, while larger fibres may be relatively preserved (Sadun et al., 2000; Pan et al., 2012; Coussa et al., 2019). We speculate that this selective loss manifests as disorganised fibre bundles and reduced axonal integrity, while preserving diffusivity within and around the remaining axons.

In the optic radiations, we identified an overall reduction in axonal water fraction (f; $t_{32.9} = 9.291, p_{bonf} < 0.0001$) and alignment ($\kappa$; $t_{32.7} = 6.413, p_{bonf} < 0.0001$). These were paired with significant increases in intra-axonal diffusivity (D_a; $t_{32.8} = -7.197, p_{bonf} < 0.0001$), and parallel and perpendicular diffusivities outside the axons ($D_{e,para}$; $t_{32.7} = -6.973, p_{bonf} < 0.0001$; $D_{e,per}$: $t_{33.2} = -5.934, p_{bonf} < 0.0001$). Further analysis revealed widespread reductions in f and κ, alongside increases in D_a, $D_{e,para}$, and $D_{e,per}$ along the optic radiations, with more pronounced alterations near V1 (Figure A5.3 in Appendix 5; f: $p_{bonf} < 0.0001$ at all locations; κ: $p_{bonf} < 0.05$ for the last 75% of the radiations; D_a: $p_{bonf} < 0.01$ at all locations; $D_{e,para}$: $p_{bonf} < 0.05$ for the last 93% of the locations; $D_{e,per}$: $p_{bonf} < 0.05$ for the last 75% of the radiations). These results highlight substantial damage to the axonal structure and organisation of the optic radiations, paired with pronounced changes in intra- and extra-axonal diffusivity, which may reflect a combination of demyelination and axonal degeneration.

MR g-ratio along the optic pathways

The MR g-ratio, defined as the ratio between the inner and outer radii of a myelinated axon, is calculated using AWF and MT_{sat} measures. These are first converted to estimates of the axonal and myelin volume fractions – AVF and MVF respectively. The MR g-ratio enables further differentiation between demyelination and axonal degeneration mechanisms.

In the optic tracts of LHON patients, we observed an overall increase in the g-ratio ($F_{1,55} = 28.1553;\ p < 0.0001$), indicating more pronounced demyelination relative to axonal loss. This was supported by significant reductions in both axonal volume fraction(AVF: $F_{1,47.2} = 32.5398;\ p < 0.0001$) and myelin volume fraction (MVF: $F_{1,45.7} = 119.9688; p < 0.0001$), suggesting concurrent degeneration of both the myelin sheath and axons. Additionally, when examining changes along the length of the optic tracts, we found an increase in g-ratio only in the portion of the tracts close to the optic chiasm (Figure 13C; $p_{bonf} < 0.05$ only for the first 20% of the tracts), while reduced AVF and MVF were found across all locations (Figure 13E&G; AVF: $p_{bonf} < 0.0001$; MVF: $p_{bonf} < 0.0001$, for all locations). This suggests more pronounced myelin loss compared to axonal loss near the optic chiasm. However, the effects of both mechanisms appear to counterbalance each other as we move towards the LGN, as evidenced by a gradual shift towards a net zero change in the MR g-ratio. These findings align with our DTI, biophysical, and MPM measures, as well as post-mortem histological findings of demyelination and axonal loss in the optic nerves of LHON patients (Sadun et al., 2000; Carelli et al., 2004; Pan et al., 2012; Coussa et al., 2019).

In the optic radiations of LHON patients, we found an overall reduction in g-ratio ($t_{33.3} = 3.144, p_{bonf} = 0.014$) and AVF ($t_{33.3} = 9.687, p_{bonf} < 0.0001$); and no overall change in MVF was observed ($t_{32.4} = 1.655, p_{bonf} = 0.4301$). When examining more location-specific changes along the optic radiations, we identified a localised reduction in g-ratio in the portion of the radiations close to the LGN (Figure 13D; $p_{bonf} < 0.05$ for the first 42% of the radiations), along with widespread reductions in AVF (Figure 13F; $p_{bonf} < 0.0001$ for all locations). MVF was decreased only in the portion of the radiations close to V1 (Figure 13H; $p_{bonf} < 0.05$ for the last 21% of the radiations). This difference in the location of AVF and MVF reductions along the optic radiations gives rise to the reduced g-ratio close to the LGN, while no change in g-

ratio is observed in the rest of the structure. Combined with our other measures, these findings suggest that while axonal integrity is impaired along the optic radiations in LHON, demyelination may not be continuously occurring along these fibres, but become more pronounced closer to V1.

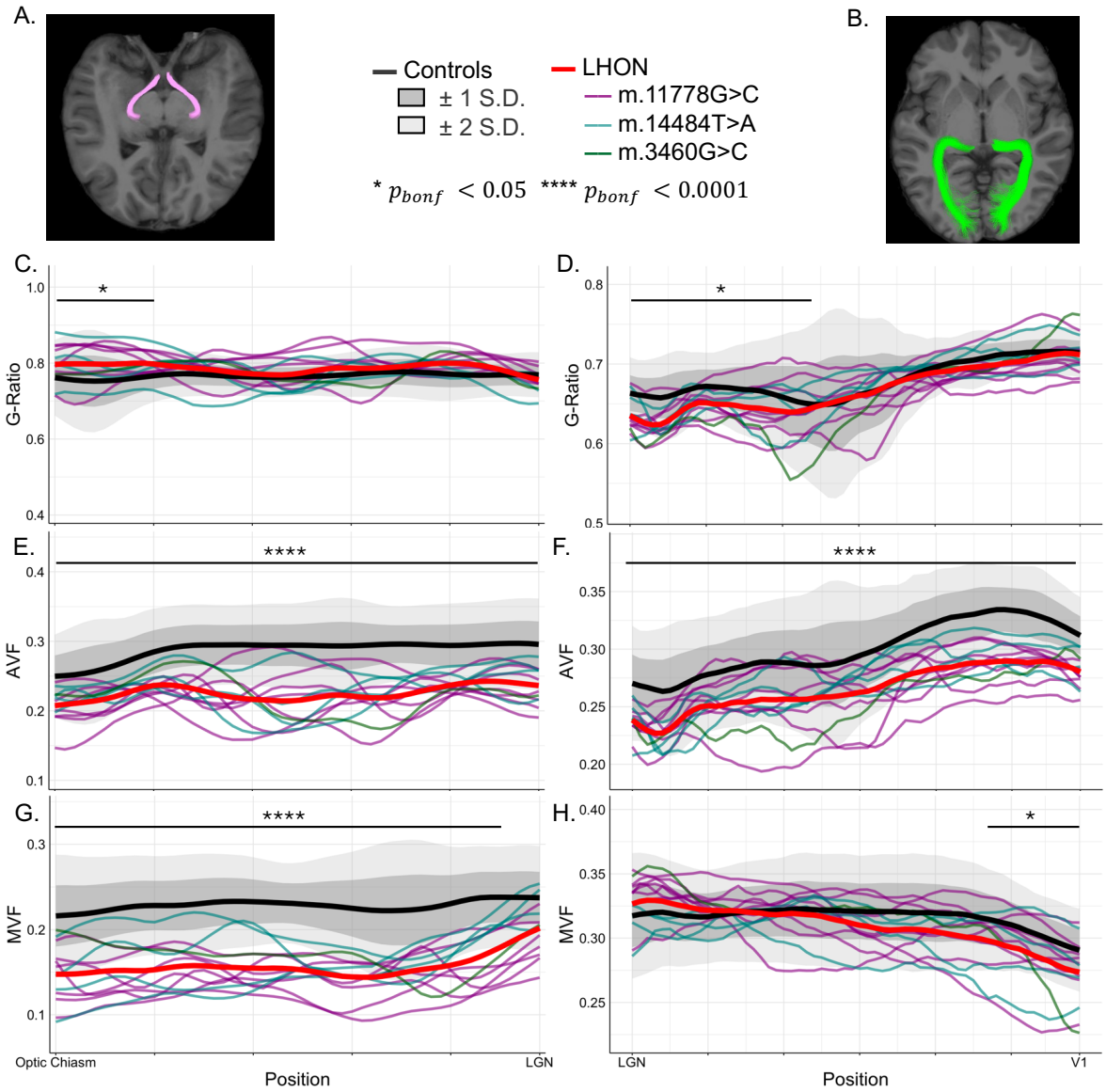

Figure 13. Axonal degeneration and demyelination along the optic tracts and optic radiations in LHON.

(A) Segmented optic tracts in a control participant, overlaid on their MPRAGE image. (C, E, G) G-ratio, axonal volume fraction (AVF), and myelin volume fraction (MVF) along the optic tracts (chiasm to LGN). (B) Segmented optic radiations in a control participant, overlaid on their MPRAGE image. (D, F, H) G-ratio, AVF, and MVF along the optic radiations (LGN to V1). Black line shows control mean; shaded areas indicate ±1 (dark grey) and ±2 (light grey) SD. Red line shows LHON mean; individual LHON profiles are color-coded by mutation: purple (m.11778G>C), cyan (m.14484T>A), dark green (m.3460G>C).

Correlations of myelin and axonal volume fractions with measures of retinal integrity and visual function.

We investigated whether myelin volume fraction (MVF) and axonal volume fraction (AVF) in the optic tracts (Figure 14) and optic radiations (Figure 15) are associated with retinal integrity and visual function. Specifically, we examined correlations with global peripapillary retinal nerve fibre layer (pRNFL) thickness (derived from OCT), visual acuity, and disease duration. Given the binocular nature of the visual pathways, pRNFL and visual acuity values were averaged across both eyes. Due to the small sample size and non-normal distribution of MVF and AVF, we used Kendall's tau (τ) for correlation analyses, reporting both τ coefficients and corresponding p-values.

In the optic tracts (Figure 14), we observed a trend toward a negative correlation between MVF and visual acuity ($\tau = -0.419, p = 0.062$), but not between AVF and visual acuity ($\tau = -0.202, p = 0.369$). Other correlations in the optic tracts also did not reached significance. Specifically, MVF showed non-significant associations with pRNFL thickness ($\tau = 0.156, p = 0.531$), whilst we observed a trend toward a positive correlation between AVF and pRFNL thickness ($\tau = 0.422, p = 0.089$, respectively). Neither AVF or MVF metrics correlated with disease duration (MVF: $\tau = 0.051, p = 0.807$; MVF: $\tau = 0.231, p = 0.272$). These suggest that reductions in myelin content in the optic tracts may be associated with worsening visual acuity (i.e., higher logMAR values), whilst loss of axonal content may be directly reflecting damages to the retinal ganglion cells (RGCs).

In the optic radiations (Figure 15), AVF also showed a trend toward a negative correlation with visual acuity ($\tau = -0.388, p = 0.084$), and a positive trend with disease duration ($\tau = 0.359, p = 0.088$), which contrasts with the findings in the optic tracts. MVF did not correlate with visual acuity ($\tau = 0.14,\ p = 0.534$), and the remaining correlations were similarly non-significant (MVF vs pRNFL: $\tau = -0.111,\ p = 0.655$; AVF vs pRNFL: $\tau = 0.244, p = 0.325$; MVF vs disease duration: $\tau = 0.128, p = 0.542$).

These findings reinforce the notion of a differential balance between myelin and axonal loss along the visual pathway in LHON. In the optic tracts, both demyelination and axonal degeneration appear to contribute to visual impairment, as suggested by trends with visual acuity and pRFNL OCT thickness. In contrast, the optic radiations

show associations between AVF and both visual acuity and disease duration, while MVF does not – suggesting axonal loss may be more prominent and progressive in this region. This may be due to MVF being averaged across the entire tract, potentially masking localised demyelination near V1 (as shown in Figure 13) and reducing the sensitivity of MVF to detect meaningful correlations. The lack of significant correlations with pRNFL thickness in both regions may reflect a more complex relationship between retinal and post-retinal degeneration. While none of the correlations reached statistical significance, the consistent trends suggest the potential of AVF and MVF as sensitive markers of visual dysfunction. These preliminary results highlight the need for larger, longitudinal studies to better characterise the spatial and temporal dynamics of white matter pathology in LHON and their relationship to clinical outcomes.

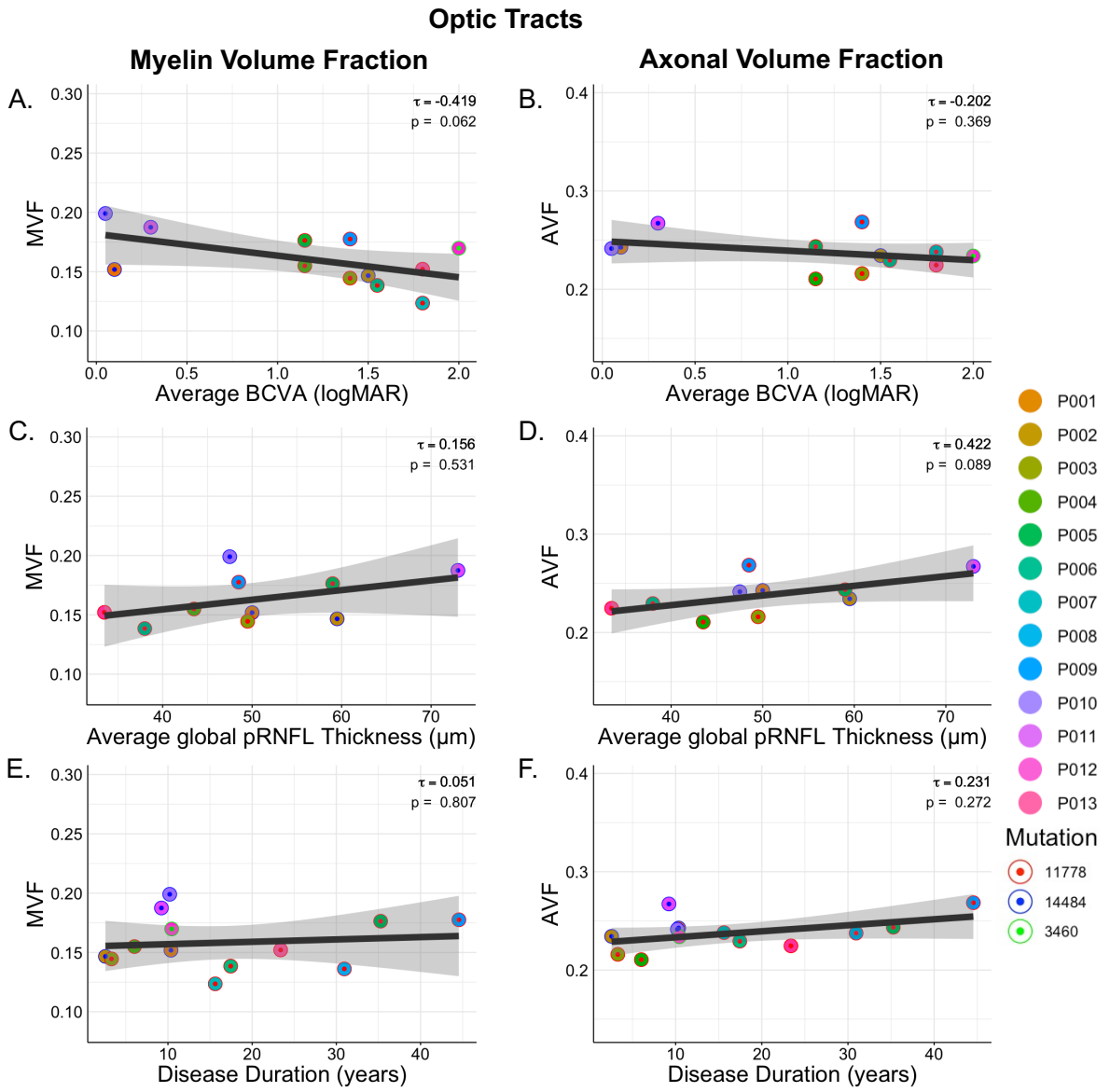

Figure 14. Associations between optic tract microstructure and clinical measures in LHON patients.

Scatter plots show relationships between myelin volume fraction (MVF) and axonal volume fraction (AVF) in the optic tracts and clinical variables: best-corrected visual acuity (BCVA, logMAR), disease duration, and global peripapillary retinal nerve fibre layer (pRNFL) thickness. Each point represents an individual subject (P001–P013). Regression lines (black) are shown for visual reference. (A-B) Trends toward negative correlations between MVF/AVF and visual acuity, suggesting that reductions in myelin and axonal content may be associated with worse visual function. (C-F) No significant associations were observed with disease duration or pRNFL thickness, for AVF or MVF. Correlation coefficients (τ) and p-values are reported for each comparison.

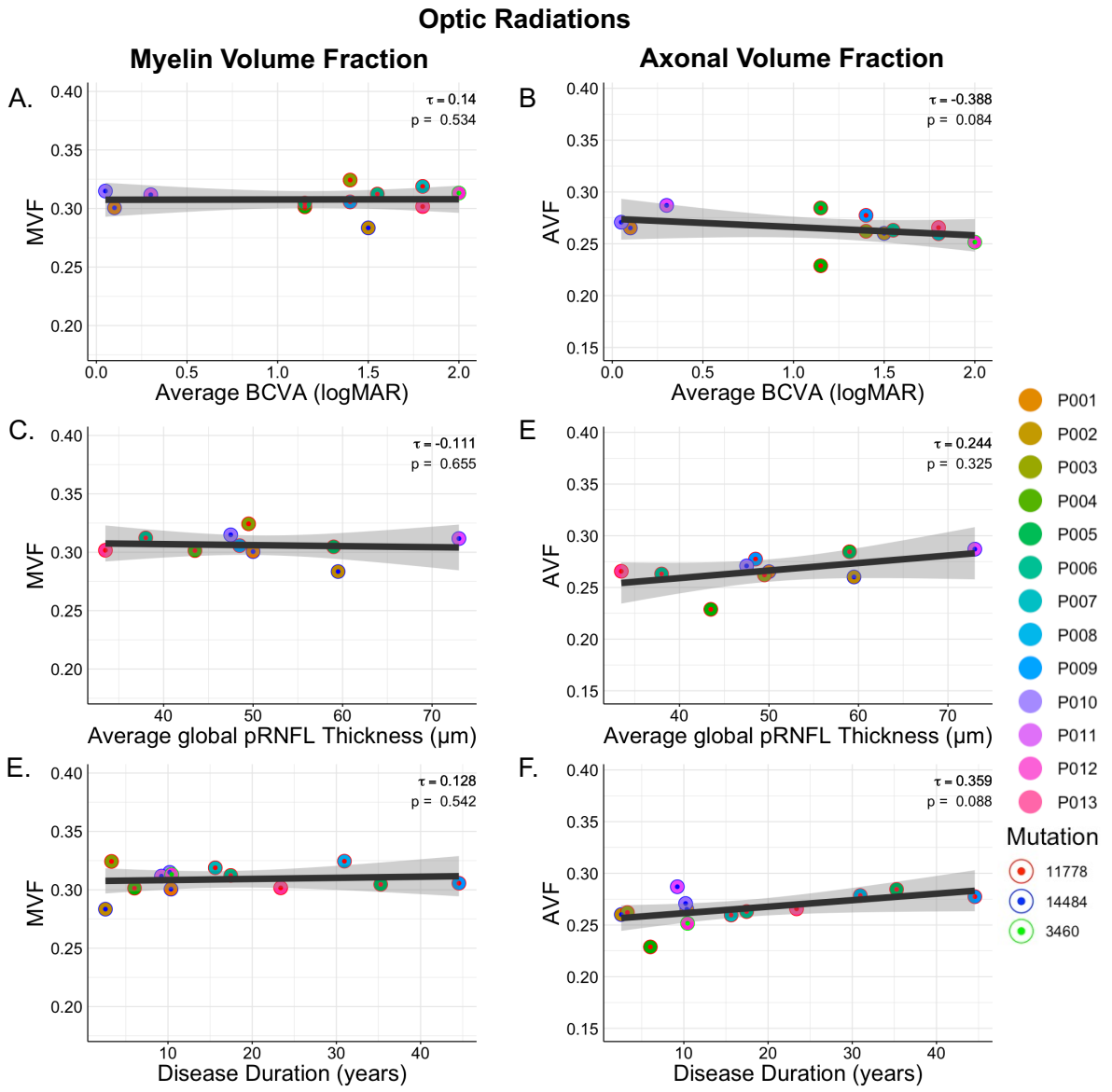

Figure 15. Associations between optic radiation microstructure and clinical measures in LHON patients

Scatter plots show relationships between myelin volume fraction (MVF) and axonal volume fraction (AVF) in the optic radiations and clinical variables: best-corrected visual acuity (BCVA, logMAR), disease duration, and global peripapillary retinal nerve fibre layer (pRNFL) thickness. Each point represents an individual subject (P001–P013). Regression lines are shown for visual reference. (A,C, E) No significant associations were observed for MVF. (B) Trend toward a negative correlation between AVF and visual acuity. (F) Similar trend with disease duration, suggesting that axonal degeneration in the optic radiations may be progressive and functionally relevant. (D) No significant association between AVF and pRNFL thickness. Correlation coefficients (τ) and p-values are reported for each comparison

2.3.3. Regional brain morphometric changes in LHON

Volumetric analyses also revealed distinct structural differences along the visual pathways in LHON patients compared to controls (see Appendix 6). A significant reduction in optic tract volume was observed ($t_{31} = -4.569, p < 0.0001$; Figure A6.1) in LHON patients, consistent with degeneration of retinal ganglion cell (RGC) axons. The lateral geniculate nucleus (LGN) of the thalamus also showed markedly reduced volume in LHON patients ($t_{1780} = 7.054, p < 0.0001$; Figure A6.1), whereas no significant changes were detected in the medial geniculate nucleus (MGN; $t_{1780} = 0.694, p_{bonf} = 1$; Figure A6.1) or the anteroventral nucleus (AV; $t_{1780} = 0.106, p_{bonf} = 1$; Figure A6.1). In contrast, no volumetric differences between controls and patients were found in the optic radiations ($t_{58.6} = 0.700, p_{bonf} = 1$; Figure A6.1) or the vertical occipital fasciculus ($t_{58.6} = -1.923, p_{bonf} = 0.2374$; Figure A6.1).

Finally, within the cortex, we found reduced volume only in V1 of LHON patients ($t_{35.8} = 2.915, p_{bonf} = 0.0183$; Figure A6.1), notably between 3-15º of the visual field projection on V1 cortex ($t_{55.2} = 3.239, p_{bonf} = 0.0244$; Figure A6.2), in line with that visual field loss is typically most pronounced in the central 15 degrees. This change in mean volume was accompanied by reduced mean cortical thickness ($t_{46.8} = 2.752, p_{bonf} = 0.0252$), whereas no change in overall V1 surface area was found between groups ($t_{37.2} = 2.280, p_{bonf} = 0.0853$). No change in overall volume, cortical thickness, or surface area was observed for V2 and V3 between groups.

2.4. Discussion

Our findings highlight the complex interplay of axonal degeneration and demyelination along the visual pathways in LHON patients, with nuanced differences between optic tracts and radiations. While our measures showed significant axonal loss and demyelination in the optic tracts, the gradient of damage in the optic radiations showed more pronounced changes towards V1, indicates potential ongoing demyelination and axonal loss. The MR g-ratio findings provide additional insights into the proportional changes between axonal diameter and myelin thickness. The optic tracts exhibit a more balanced interplay between axonal loss and demyelination, as reflected by a stable MR g-ratio in these fibres, while the optic radiations reveal a

gradient of damage starting with more pronounced axonal loss versus myelin loss near the LGN before both mechanisms are gradually balancing each other out towards V1.

Volume alterations along the visual pathways.

We observed tissue volume loss in LHON, along the visual pathways using LME models in R with age, sex, and BMI as covariate factors (see Figures A6.1 & A6.2 and Table A6.1 in Appendix 6). Unlike Takemura et al. (2019), we found reduced volume in the optic tracts of LHON patients, consistent with post-mortem measures of optic nerve deterioration (Sadun et al., 2000; Carelli et al., 2004; Pan et al., 2012; Coussa et al., 2019). This discrepancy in findings likely reflects different segmentation strategies. Volume of the lateral geniculate nucleus (LGN) was also significantly reduced, aligning with post-mortem evidence of reduced soma size and cell density (Rizzo et al., 2012) and a previous MRI study (Jonak, Krukow, Jonak, et al., 2020). This reduction was specific to the LGN, sparing other thalamic nuclei, thus reflecting neurodegeneration in the thalamus in LHON specific to the visual pathway.

Conversely, no changes were found in the optic radiations, in line with findings from Takemura et al. (2019) but not from Barcella et al. (2010). Interestingly, this lack of volumetric change contrasts with the altered microstructural integrity found in the optic radiations. One possible explanation lies in the methodology used to estimate volume: the optic radiation masks were derived from white matter streamlines estimated through tractography, with the boundaries of the masks defined by the outermost extent of the white matter bundle. If the microstructural damage is primarily confined to the central core of the bundle, it may not substantially affect the overall spatial extent of the mask and, consequently, may not be captured by volumetric measures. This underscores the importance of integrating volumetric and microstructural analyses to comprehensively characterise white matter changes in LHON. Future work that segments optic radiation fibres based on their termination zones in V1 could offer a more refined assessment of region-specific volumetric alterations in this condition.

In V1 of LHON patients, we also observed reductions in volume and cortical thickness, whilst V2 and V3 remained unchanged. Thinning of V1 could have different disease-related causes, including potential neuronal loss (fewer neurons, reduced dendritic arborisation), synaptic pruning or degeneration (loss of synaptic

connections), and/or changes to supporting cells (e.g., myelin or glia). In contrast, we found no change in V1 area suggesting that the topographic representation of the visual field remains intact. Eccentricity analysis further revealed reduced volume in V1 regions representing 3-15º from fixation, suggesting localised V1 atrophy, in line with dense central scotoma in LHON patients and align with findings from Barcella et al. (2010). These changes are not present in V1 of asymptomatic LHON patients (D'Almeida et al., 2013; Mateus et al., 2016), suggesting that these are either direct consequence of RGC loss and/or secondary to blindness.

Together, our results highlight neurodegeneration primarily affecting vision-related structures in LHON, potentially linked to demyelination and axonal degeneration in optic radiations, especially in their portion close to V1. However, whether the loss of optic radiation integrity in LHON precedes the loss of V1 integrity, or vice-versa, cannot be directly answered at this stage. Further work including a larger sample size and different stages of the disease are needed to better understand the temporality of these morphometric changes. Additionally, evidence of structural changes in vision-related brain regions have also been reported in other conditions like achromatopsia and macular degeneration, where visual deprivation – whether congenital or acquired – leads to measurable alterations along the visual pathways (Prins et al., 2016; Lowndes et al., 2021; Hanson et al., 2022; Molz et al., 2022; Brown et al., 2023; Maimon-Mor et al., 2024). These findings reinforce the importance of assessing cortical viability when considering restorative treatments.

Both demyelination and axonal loss are at play in the optic tracts.

MRI findings in the optic tracts showed reduced FA, reduced AD (typically linked to axonal loss), and increased RD (typically linked to demyelination), in line with significant axonal loss and demyelination. However, no change in MD was found suggesting that a balance between these two processes such as both axonal loss and demyelination equally affect these pre-geniculate fibres. Increased qT1 and qT2*, alongside decreased MT_{sat}, align with myelin loss, while reduced axonal water fraction (f) and alignment (κ) could be markers of axonal disorganisation and content degeneration. These changes are in line with post-mortem histological studies showing reduced axon density (Sadun et al., 2000; Pan et al., 2012), and reduced myelin sheath thickness (Carelli et al., 2004). Additionally, we found overall reductions

of diffusivity outside and perpendicular to the axons ($D_{e,per}$), which indicates potential further extracellular changes such as demyelination; however, with no significant change in diffusivity intra-axonal (D_a) or parallel to the axons ($D_{e,para}$). We speculate that these could reflect some degree of retained structural integrity at the microstructural level, for example, in preserved, larger, myelinated axons (Sadun et al., 2000; Pan et al., 2012; Coussa et al., 2019).

Axonal degeneration is primarily occurring in the optic radiations.

In the optic radiations, we found a different pattern of structural changes than in optic tract – with reduced FA, and increased RD and MD, pointing to ongoing demyelination and axonal loss, but the unchanged AD suggests some preserved axonal integrity. The overall increase in PD in MPM findings indicates higher water content, likely from cellular damage, while no overall changes in qT1, qT2*, and MT_{sat} suggest that macroscopic myelin properties remain relatively stable. We also found reduced axonal water fraction (f) and alignment (κ) in the optic radiations, with increased $D_{a,}$ $D_{e,para}$, and $D_{e,per}$. These parameters reflect axonal loss and disorganisation, along with changes within the axonal and extracellular spaces at the microstructural level. Moreover, we found a gradient of damage along the length of the optic radiations, with more pronounced changes towards V1. With no histological evidence of LHON-related alterations in the optic radiations available to date, we speculate that these changes reflect more complex dynamics than those observed in the optic tracts of these patients. Whilst increased $D_{e,para}$, and $D_{e,per}$ support the existence of both axonal and myelin loss, the increase in D_a could likely reflect swelling of the remaining optic radiations' axons. These would be detrimental for efficient signal transmission from the LGN to V1, with potential delays or disruptions in signal processing. This highlights the need for further work on modelling these effects as well as post-mortem studies investigating demyelination and axonal degeneration in the optic radiations of LHON patients.

The balance between axonal degeneration and degeneration is not homogenous along the optic pathways.

MR g-ratio findings provide deeper insights into the underlying mechanisms of neural changes, particularly on the dynamics of axonal degeneration and

demyelination in the optic tracts and radiations. In the optic tracts, both axonal loss and demyelination are occurring, as evidenced by the reduced AVF and MVF, respectively. We also found an overall increase MR g-ratio in this pre-geniculate structure, suggesting more pronounced demyelination versus axonal degeneration. This increase seems to be localised to the portion of the tracts close to the optic chiasm, likely reflecting the damages to the optic nerves observed in post-mortem studies. These structural alterations are further supported by correlation analyses, which revealed trends toward negative associations between MVF and visual acuity, and positive associations between AVF and pRFNL thickness. These suggest that degeneration of both tissue components may contribute to functional visual impairment and may directly reflect damages to the RGCs. However, the absence of significant correlations with disease duration may reflect a complex, potentially non-linear relationship between retinal and post-retinal degeneration.

In contrast, in the optic radiations, a decreased MR g-ratio, especially near the LGN, indicates disproportionate axonal loss compared to myelin loss. Crucially, as we move towards V1, both AVF and MVF are decreased, resulting in an unchanged MR g-ratio. The shift in balance between axonal degeneration and demyelination along the optic radiations reflects a complex interplay of these mechanisms and may reflect a transition from axon-dominant to more balanced degeneration along these fibres. Correlation analyses support this interpretation: AVF, but not MVF, demonstrated trends toward associations with both visual acuity and disease duration, suggesting that axonal degeneration may be the predominant and potentially progressive mechanism in this region. The lack of MVF correlations may be attributable to averaging of this measurement across the entire fibre, which masks the localised demyelination near V1, as shown in Figure 13.

But what could explain this shift in balance in the optic radiations? The cell bodies of neurons whose axons form the optic radiations are in the LGN and a post-mortem study has found that these are reduced in size and density in LHON (Rizzo et al., 2012). Therefore, the decrease in MR g-ratio near the LGN, alongside decreased AVF, may reflect direct neuronal injury leading to axonal damage without significant co-occurring myelin loss, potentially by targeting larger fibres. This loss of axon content without demyelination has been observed in post-mortem histology of the brain and spinal cord of patients with acute Multiple Sclerosis (Bjartmar et al., 2001),

a neurodegenerative disorder that shares comorbidities with LHON. However, as we move towards V1, the unchanged MR g-ratio might reflect degradation of myelin among intact myelinated axons, balancing out the loss of axons and resulting in a net zero change in g-ratio. This could explain potential localised V1 atrophy (see Figure A6.2 in Appendix 6); however, the question of whether the loss of optic radiation integrity precedes the loss of V1 integrity, or vice-versa, cannot be directly answered at this stage. Collectively, these findings highlight the spatial complexity of white matter pathology in LHON and highlight the utility of combining microstructural imaging with functional correlations to elucidate disease mechanisms.

Conclusion and implications for future gene-therapies

In summary, the visual pathways of LHON patients exhibit distinct patterns of axonal loss and demyelination. Our findings provide converging evidence of axonal and myelin loss along the visual pathways from multiple MRI modalities, showcasing the sensitivity of our measures in quantifying histologically accurate markers of WM alterations. These changes along both pre- and post-geniculate fibres have significant implications, not only for the structural integrity of the optic pathways but also for their functional integrity. Myelin acts as an insulating layer by surrounding the axons and facilitating the processing of sensory information. Therefore, the loss of myelin and axons along the visual pathways would likely result in less efficient nerve signal conduction and thus contribute to deficits in vision. This is further reflected in the observed trends between AVF and MVF and visual acuity, suggesting a potential link between tissue integrity and functional outcomes, despite the lack of statistical significance. Future studies that differentiate fibres based on the visual field information they carry (central vs. peripheral) could further clarify the functional impact of these demyelinating changes.

Moreover, the differences in dynamics of white-matter alterations between optic tracts and optic radiations might reflect different causes of degradation in LHON and different timelines – i.e., either they are direct consequences of the RGC loss or secondary to input deprivation. In fact, it is likely that the changes in optic tracts and LGN are direct consequences of the RGC loss, given these are the continuation of the optic nerve axons between the optic chiasm and LGN. However, in the post-geniculate optic radiations, we cannot conclude on whether changes are caused directly by the

same (as yet unknown) factors underlying sudden RGC loss, by secondary effects of visual deprivation, or by a combination of both. Interestingly, these fibres seem to follow a different degenerative trajectory than the optic tracts, even after several years of visual impairment, which could suggest a delayed or progressive mechanism of white matter degeneration that is not solely dependent on the initial retinal damage. Further studies looking at longitudinal changes in these visual structures, as well as post-mortem histology in the optic radiations of LHON patients, could shed light on the causality and temporality of the deteriorations.

Still, understanding the specific patterns of axonal and myelin loss and discrepancies between optic tracts and radiations is crucial for understanding disease progression and visual recovery – either spontaneous or after gene-therapy intervention. Our MRI findings provide new insights on LHON by bridging the gap between histology and brain measures and offer new, potential, outcome measures for quantifying loss, but also recovery, in visually impaired populations. Although the optic pathways undergo drastic axonal degeneration and demyelination, some of the fibres are still preserved in both optic tracts and radiations which is promising for future clinical trials. Ultimately, these MRI-based approaches could even contribute to the development of targeted gene therapy interventions that aim to address both axonal degeneration and demyelination to ultimately halt or even reverse the progression of vision loss in LHON patients. This expands the scope for improved visual outcomes and quality of life for those affected by this debilitating condition.

3. Mapping cortical contrast sensitivity across the visual field: method implementation and validation in simulated and pathological vision loss (Chow-Wing-Bom et al., 2025, *eLife*)

In this chapter, I introduce an fMRI-based method to map contrast sensitivity across the visual field without requiring precise fixation. To do this, I combine large-field stimulation with variable spatial frequencies and contrast levels to model V1 sensitivity up to 20º in the periphery. Using this approach:

- I demonstrate consistent and reproducible cortical sensitivity patterns across eccentricities and quadrants in normal-sighted individuals.
- Moreover, I successfully detect simulated and disease-related visual field deficits at the cortical level.
- Crucially, I validate the use of a structure-based retinotopic atlas as a fixation-free alternative to pRF mapping, with minimal loss of sensitivity.

Together, these findings show that this fMRI-based approach provides a clinically relevant tool for assessing and monitoring visual function in patients with impaired fixation or severe vision loss.

3.1. Why is it important to quantify contrast sensitivity at the level of the cortex?

At least 2.2 billion people world-wide experience blinding eye diseases that emerge or progress across the lifespan, with 1.1 billion living with vision loss in 2020 (Bourne et al., 2021; World Health Organization, 2019). Accurate characterization of visual function is critical for optimal intervention and patient support, but fraught with challenges. The gold clinical standard measure is visual acuity, the highest spatial resolution that can be discerned. This index mainly relies on a well-functioning fovea, the small retinal area with the highest density of photoreceptors, which processes the central 0-2 degrees around fixation. However, many forms of visual impairment do not

affect the fovea alone. The vast majority of our visual input comes from peripheral vision, which provides coarse but invaluable information (Alvarez, 2011; Oliva, 2005) – nearly all daily functions critically depend on intact functionality of the wider visual field, including driving, crossing the street, social function, mobility, and even reading (Lange et al., 2021). Accordingly, impairment of tissue beyond the fovea and its projections drastically affects function and quality of life (Lange et al., 2021; Lisboa et al., 2013; Roh et al., 2018; Subhi et al., 2017).

The impacts of impairments across the wider visual field can be measured with various types of visual field tests, ranging from the finger counting visual confrontation field test to more complicated and/or computerized tests (e.g., standard automatic perimetry, kinetic perimetry, microperimetry). Computerized tests typically involve measuring sensitivity to the luminance contrast of a target relative to a background at different visual field locations while the participant's gaze is fixed on a central point. In some cases (e.g., microperimetry), sensitivity measurements are paired with fundus imaging, offering greater precision in linking visual field functions to specific retinal locations. These tests can provide critical additional insights into function-relevant disease evolution and recovery beyond acuity scores alone, by identifying regions of reduced light sensitivity or blind spots beyond the fovea.

However, visual field testing comes with challenges and limitations, and as a result, the inclusion of visual field measures in sight-rescuing therapy trials is limited. Firstly, it requires prolonged fixation and sustained visual attention. This can be very challenging for patients with severe vision loss, who often struggle to fixate, and strain to detect even high-intensity stimuli. This can lead to long and unpleasant testing sessions with unreliable results. Secondly, as perception is inherently subjective and effortful, patients may vary in their criteria for visual recognition, and in their ability to report visual signals that are weakened or distorted by disease.

Functional MRI (fMRI) has recently been proposed as a promising alternative to measure visual field loss, as it requires no overt task, and instead measures visual sensitivity directly from brain responses. Population receptive field (pRF) mapping fMRI can measure which parts of the cortex respond to which parts of the visual scene. This is achieved by measuring local changes in cortical blood oxygenation in response to high-contrast stimuli such as flickering checkerboards that systematically traverse the visual field. These neural timeseries are then fit with a retinotopic spatial tuning

function. The fMRI signal strength in a cortical region that encodes a specific visual field location provides information about visual sensitivity in this location (Dumoulin & Wandell, 2008). This approach has recently been used to accurately recover blind spots in the visual field detected with visual field perimetry (Pawloff et al., 2023; Ritter et al., 2019; Halbertsma et al., 2021). These results in turn suggest that fMRI may be a useful tool to monitor disease progression and recovery in visually impaired patients.

However, there are also significant challenges associated with this pRF mapping. Because pRF models require knowledge of where visual stimuli fall on the retina, this approach requires accurate and sustained fixation. If fixation is poor, the visual field locations assigned to cortical regions will be displaced, leading to noise or bias in the pRF maps. Additionally, most fMRI studies measure vision across a small central part of the visual fields (~10 degrees of eccentricity) which will not capture critical dynamics in the periphery. Finally, most studies use a single maximum contrast stimulus to assess visual function (Broderick et al., 2022; Farahbakhsh et al., 2022; Liu et al., 2006; O'Connell et al., 2016; Ritter et al., 2019; Halbertsma et al., 2021). This is suboptimal for at least two reasons: First, it may reduce the ability to detect subtle but clinically important changes that do not result in complete sensitivity loss or recovery. Second, with a single contrast stimulus, it becomes more difficult to determine whether a reduction in fMRI signal across sessions or brain regions reflects vision-related changes or other factors. Together, these factors currently limit the utility of neuroimaging-based visual field tests.

In this study we sought to develop fMRI methods for measuring visual field sensitivity to address these challenges, and to test its utility in artificial and realistic cases of visual field loss. Rather than presenting a single maximum contrast eccentricity-scaled checkerboard in a pRF mapping protocol, observers viewed large-field sinusoidal gratings at a range of contrasts without strict requirement to fixate. We used a large screen set up (40° diameter) to measure visual function across a large expanse of the visual field. To quantify visual sensitivity, we fit a simple cortical contrast response model to voxel timeseries evoked by the gratings, avoiding reliance on arbitrary signal amplitude thresholds. We first tested if this approach could sensitively and reliably quantify predicted contrast sensitivity differences across eccentricity and polar angle dimensions of the entire visual field (Figure 2), using a short, patient-friendly protocol in sighted controls. Critically, to achieve this we linked

cortical contrast sensitivity estimates to visual field locations using retinotopic tuning estimates obtained in a separate session. However, for patients with severe vision loss it is infeasible to obtain accurate pRF measures due to poor ability to fixate a central target. We therefore also evaluated the approach using the structure-based atlas of retinotopic values developed by Benson et al. (Benson et al., 2012; Benson et al., 2014; Benson & Winawer, 2018). This atlas estimates retinotopic tuning based on the alignment of structural features of cortex (e.g., surface curvature) to a mean atlas of those features. Once a brain is aligned to the structural atlas, a similar atlas of retinotopic maps that are defined on the structural atlas are used to estimate the polar angle and eccentricity maps for the individual subject. To increase accuracy of the Benson atlas for our large-field stimuli, we subsequently fit these eccentricity estimates to the Horton and Hoyt (1991) model of cortical magnification in each individual.

We demonstrate that our approach can recover, at a cortical level, known sensitivity changes across the visual field. V1 neuronal populations encoding the central visual field show the highest sensitivity to high spatial frequencies, whilst those encoding the periphery are most sensitive to low spatial frequencies. We also find greater sensitivity in V1 regions receiving visual inputs from the horizontal compared to vertical quadrants, and from the lower compared to upper quadrants. Crucially, these effects are detectable at the individual level and repeatable across visits, suggesting our approach will be suitable for detecting visual field sensitivity changes over time (e.g., due to learning, ageing, disease progression, or recovery). Moreover, when using the Benson atlas instead of individual pRF measures to link neuronal responses to visual field locations, we still detect these effects, although with slightly reduced sensitivity. We also demonstrate the clinical relevance of this approach by recovering a simulated scotoma, characterized by a ring of visual field loss around fixation, as well as visual field loss in a patient with a neurodegenerative disorder causing large areas of visual field loss. We conclude that this approach, i.e., the combination of cortical contrast sensitivity testing, large field stimulation, and a large-field calibrated retinotopic atlas, may be particularly useful for quantifying visual recovery in patients, whether spontaneous or following gene-therapy interventions, and for linking brain-based activations to behavioural performance.

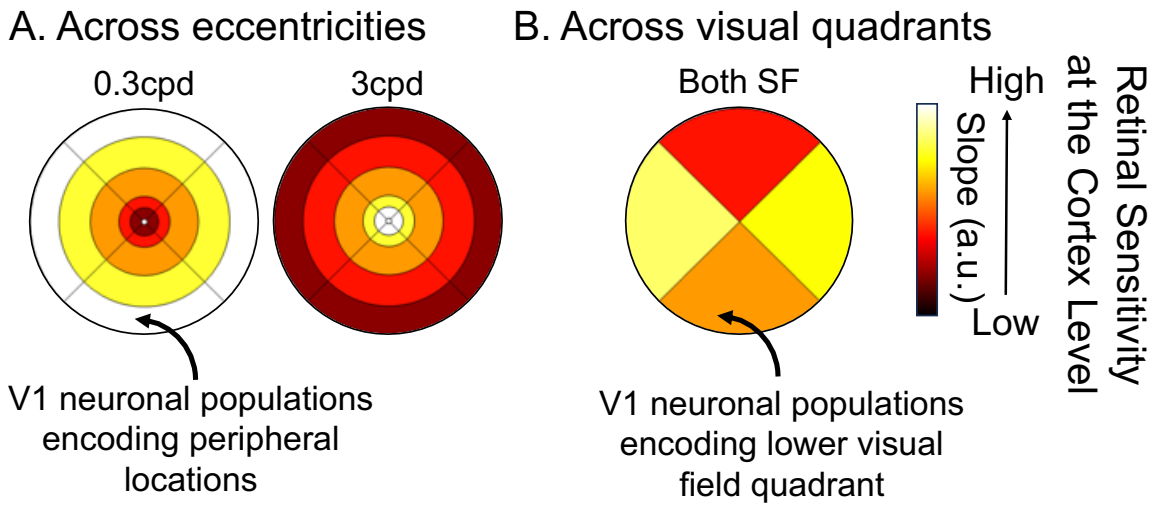

Figure 16. Expected changes in cortical contrast sensitivity in typically sighted controls for low (0.3 cycles per degree – cpd) and high (3.0 cpd) spatial frequencies.
(A) Across eccentricities. (B) Across visual field quadrants. With reference to eccentricity, we expect higher sensitivity of V1 neuronal populations to 1) lower spatial frequencies in the periphery, and 2) higher spatial frequencies in the centre of the visual field. By comparison, we expect both high and low spatial frequency stimulation to evoke greatest sensitivity in V1 neuronal populations encoding the left and right visual quadrants, less in the lower, and least in the upper quadrant. Image from Chow-Wing-Bom et al., 2025, eLife.

3.2. Methods

3.2.1. Participants

We collected data from 7 healthy controls (mean±SD: 29.6±4.7yo; 1M). All controls either had normal or corrected to normal vision, with no other ocular pathologies, and were recruited from the local staff and student pool at the University College of London. We also recruited a patient with Leber Hereditary Optic Neuropathy (M, 45.5 years old, mutation: m.11778G>A, disease duration: 36.1 years). All participants signed a written informed consent to participate in the study, and this study was approved by HRA/HCRW and Research Ethics Committee (IRAS 258959; REC 20/YH/0336).

3.2.2. Stimulus & apparatus

Stimuli were programmed in MATLAB 2020b (MathWorks, Natick, Massachusetts, USA) using the Psychtoolbox-3, and displayed using an EPSON LB-1100U projector (resolution: 1920x1200 pixels, 60Hz, projected area: 43.2x27cm). Because the projector was too bright and to reduce discomfort in the scanner, a circular neutral density filter (ND4 Plus+; Urth, Byron Bay, Australia) was placed in front of the projector to reduce light intensity by 4 times without altering the colours. The projector was also gamma-corrected to ensure accurate representation of the intended contrast levels and spatial frequencies used in our experiments. In all tasks, stimuli were embedded in circular aperture of 42.3x42.3º diameter. To achieve the large field-of-view, the front part of the 64-channel MRI coil was removed, and stimuli were back-projected onto a screen positioned close to the participant's head inside the bore (see Appendix 7.1). Participants viewed the stimuli through a mirror, for a total viewing distance of 34cm. Throughout the session, participants were constantly reminded to remain still to minimize head and body motion, and eye motion and alertness were monitored using an EyeLink 1000Plus device (SR Research, Ottawa, Canada). In all tasks, participants were asked to report when the colour of a central fixation dot changed.

3.2.3. fMRI contrast sensitivity task

Participants were presented binocularly with achromatic sine-wave gratings, flickering at a temporal frequency of 2Hz and varying in contrast levels and spatial frequencies. Contrast levels were defined as Michelson contrast ($C = \frac{L_{max}-L_{min}}{L_{max}+L_{min}}$), where L_{max} and L_{min} are maximum and minimum luminance. Each stimulus, presented for 13s, featured a specific contrast level (either 7.5, 42.2, 60, or 100%) and spatial frequency (either 0.3 or 3 cycles per degree). Stimuli were then followed by 2s of a grey background (0% contrast) to minimize the experience of after-effects. Each combination of contrast level and spatial frequency was shown three times within a run, arranged in a pseudo-random sequence, for a total of 9 repetitions per combination (i.e., 3 runs). Eight additional blocks of 15-second rest periods with a grey background were introduced to allow sufficient baseline. One healthy control also performed a version of the task in which we masked a region of the visual field with a

grey, annular ring, covering 3º-8º eccentricity to simulate loss of visual inputs (i.e., artificial scotoma).

3.2.4. Population receptive field (pRF) mapping

To investigate how distinct regions of the visual field map onto the cortex, we collected pRF mapping data using a standard ring-and-wedge stimulus (Dumoulin & Wandell, 2008). Participants were presented binocularly with a black-and-white checkerboard, phase-flickering at a temporal frequency of 2Hz, and at maximum contrast level. The stimulus spanned up to the boundaries of the circular aperture (i.e., 42.3x42.3º diameter), and was scaled across eccentricity to account for cortical magnification. Three runs of 352 volumes were collected per participant.

3.2.5. MRI acquisition

Data were collected at the Birkbeck-UCL Centre for NeuroImaging (BUCNI, London, UK), on a Siemens PRISMA 3 Tesla scanner.

Functional data were acquired using a 64-channel head coil with the front part removed, to allow an unobstructed view of the screen whilst ensuing enough signal from the remaining 40 effective channels covering the side and back of the head. T2*-weighted echo-planar imaging were collected with an accelerated multiband sequence kindly provided by CMRR (version R016a , https://www.cmrr.umn.edu/multiband; Cauley et al., 2014; Xu et al., 2013); multi-band factor: 4, voxel resolution: 2mm isotropic, FOV: 212x212x96mm, flip angle: 60º, repetition time (TR): 1000ms, echo time (TE): 35.2ms, echo spacing: 0.56ms, bandwidth: 2620Hz/Px, with 48 transverse slices angled to be approximately parallel to the calcarine sulcus whilst avoiding the orbital cavities). The same sequence was used to acquire 4 additional scans in the opposite phase-encoding direction, to allow B_0 deformation correction in the pre-processing steps.

A T1-weigthed structural image was acquired with a 30-channel coil, using MPRAGE sequence (voxel resolution: 1mm isotropic, 208 slices, FOV: 256 x 256 x 208mm, flip angle: 9º, TR = 2.300s, TE = 2.86ms, TI = 900ms, bandwidth: 240Hz/Px, echo spacing: 7.1ms, acquisition time: 5min30s). It should be noted that all patients and a few control participants participated in both the functional and structural Chapter 1) sessions, resulting in the same MPRAGE image used for processing in both parts.

3.2.6. Data analysis

Segmentation of the anatomical scan and reconstruction of cortical surfaces were performed in FreeSurfer 7.1.1 (Dale et al., 1999).

Functional data were pre-processed using a combination of AFNI 24.1.22, FreeSurfer and FSL 6.0.7.12 commands. The following steps were followed for both the contrast sensitivity task and the pRF mapping task. First, initial correction for distortions caused by field inhomogeneity was performed using a blip-up/blip-down approach (AFNI's *unWarpEPI.py* program), and the first 4 volumes of each run were discarded using FSL's *fslroi* program. Then an alignment scan was created from the volume out of all collected runs that contained the least amount of voxel outliers using AFNI's *3dToutcount*, *3dTstat* and *3dcalc* programs. This alignment scan was then co-registered to the MPRAGE image using FreeSurfer's *bbregister* program, resulting in a rigid-body transformation matrix. In case of misregistration, the alignment scan was defined as one of the single-band reference scans, before re-running the co-registration step. Motion correction was then carried out by aligning each functional volume from all runs to the previously defined alignment scan using AFNI's *3dvolreg* program.

3.2.6.1. Processing of contrast sensitivity task

To accurately capture neural activity across various eccentricities and polar angle locations, minimal smoothing (0.5mm FWHM Gaussian blur) was applied to the contrast sensitivity task data using FSL's *3dmerge* program. The contribution of each contrast/spatial frequency combination to the BOLD signal was modelled using the general linear model (GLM) approach in SPM12 (https://www.fil.ion.ucl.ac.uk/spm/), with motion parameters as additional regressors. This step resulted in volumetric images of β-values, each reflecting the specific contribution of a given contrast/spatial frequency combination to the baseline BOLD signal. These resulting images were then projected onto the individual's cortical surface using FreeSurfer's *mri_vol2surf* program (Fischl et al., 1999), with no surface smoothing and the default fractional projection along surface of 0.5. The latter sets the fraction (0,1) of the cortical thickness at each vertex to project along the surface. Surface-projected images were finally converted into a MATLAB-compatible format for further analysis using SamSrf's *samsrf_mgh2srf* program.

3.2.6.2. Processing of pRF mapping task

Pre-processed volumes from the pRF mapping task were projected onto the cortical surface using FreeSurfer's *mri_vol2surf* program. Here, we used the previously generated rigid-body transformation matrix to ensure accurate spatial alignment and smoothed on the cortical surface with a Gaussian kernel with a FWHM of 3mm.

The resulting outputs were then converted into a MATLAB-compatible format for further analysis. pRF estimates were computed by fitting a 2D Gaussian model to the data, using the SamSrf toolbox (version 7.13; https://github.com/samsrf), resulting in three pRF parameters for each vertex on the cortical surface: the x- and y-coordinates of the pRF centre, and the pRF size (σ). Eccentricity and polar angle maps were computed from the x- and y-coordinates.

3.2.7. Regions-of-interest

In this study, we were interested in how visual information across the visual field is processed in early visual areas, notably in the primary visual cortex V1. Early visual regions were manually delineated for each participant in SamSrf v7.13, based on the output of the pRF fitting procedure and standard functional criteria to identify borders between V1, V2, and V3 (DeYoe et al., 1996; Engel, 1997; Sereno et al., 1995). In this report, we focused our interest on V1, given its crucial role in the initial processing of basic visual features like spatial frequency and contrast.

3.2.8. Quantifying eccentricity- and location-dependent variations in sensitivity

3.2.8.1. Using subject-specific pRF estimates

At this stage, for each vertex on the cortical surface, we obtained β-values for each tested contrast/spatial frequency combination in the contrast sensitivity task, as well as pRF parameters resulting from the fitting of the pRF model to the pRF data (Figure 17). β-values from the contrast sensitivity task in each vertex were then filtered based on ROI location (V1) and pRF parameters ($R^2 \geq 0.05$; pRF size: ≤6).

To assess contrast sensitivity, we modelled the neural response (i.e., β-values) in V1 as a linear function of the square root of the contrast values ($R(C) = a * \sqrt{C}$). This model rests on the assumption of a monotonic relationship between the

presented stimulus contrast level and the resulting BOLD response and has been used in previous work by Buracas and colleagues to investigate contrast sensitivity at the cortex level in healthy controls (Buracas et al., 2005; Buracas & Boynton, 2007). Steeper slopes within this context indicate greater V1 contrast sensitivity.

We fit this model for each vertex separately, for each participant and spatial frequency (0.3 and 3cpd) condition. The intercept was constrained to be zero, as the distribution of β-values is expected to be centred on zero when the contrast is zero (i.e., when no stimulus is presented). Next, the resulting V1 slope estimates were binned and averaged over five regions using pRF eccentricity estimates: 0.5º-2.5º, 2.5º-4.5º, 4.5º-9.5º, 9.5º-15º, and 15º-20º. These bins relate to the clinical definition of visual space based on anatomical landmarks, corresponding to the fovea, parafovea, perifovea and two near-periphery regions, respectively. Similarly, slope estimates were spatially constrained within a ±45º-wedge centred on each cardinal meridian to investigate asymmetries as a function of pRF polar angle locations, thus dividing the visual space between the upper, lower, left and right quadrants. These wedges were also derived from the polar angle estimates obtained with pRF mapping.

For each participant, average slopes for each eccentricity bin and polar angle wedge were then projected back into their corresponding visual field locations. This resulted in heat-maps of V1 contrast sensitivity across eccentricities and visual field quadrants, for each tested spatial frequency condition at an individual level (Figure 17). Finally, average slopes for each eccentricity and polar angle bin from each participant were used to compute the group-level average.

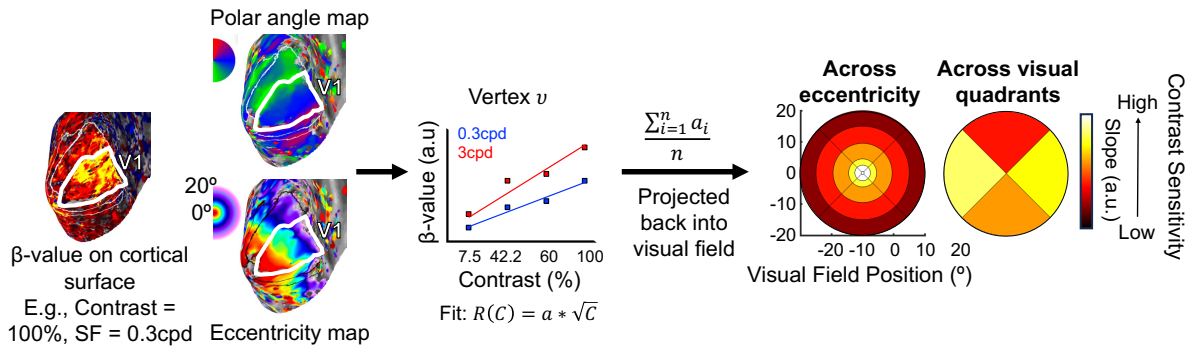

Figure 17. Estimation of cortical contrast sensitivity across the visual field.
Participants performed two fMRI tasks in the scanner: a contrast sensitivity task and a pRF mapping task. For each individual and tested spatial frequency, the contribution of each stimulus contrast level to the BOLD signal in the contrast sensitivity task was estimated using a GLM approach. Resulting β-coefficients for each contrast level were then projected onto the individual's cortical surface. For each vertex in V1, a square root function ($R(C) = a * \sqrt{C}$) was then fitted to these data, taking the estimated slope a as measure of cortical contrast sensitivity. V1 slopes were finally averaged across vertices based on their eccentricity and polar angle preference as estimated with pRF mapping, and across participants. Mean slopes were then projected back into the visual space, producing a heatmap projection of V1 contrast sensitivity across eccentricities and along visual field quadrants. Image from Chow-Wing-Bom et al., 2025, eLife.

3.2.8.2. Using calibrated Benson retinotopic template atlas

The same approach was used to quantify changes in V1 contrast sensitivity across the visual field, using a retinotopic template (Benson et al., 2012; Benson et al., 2014; Benson & Winawer, 2018) instead of pRF mapping. This template was fitted to each subject's anatomical MPRAGE image using the Python library *neuropythy* (Benson et al., 2018), which provided automatic delineation of early visual regions, based on FreeSurfer's anatomical alignment. Additionally, it offered eccentricity and polar angle estimates for each vertex on the cortical surface. The advantage of this method over pRF mapping is that it does not require fixation or pRF scanning, making it a valuable tool to use when scan time is valuable or in populations where good fixation is hard to achieve.

To enhance the accuracy of eccentricity estimates in the template map, we aligned the distribution of eccentricity values from the fitted Benson template atlas with

Horton and Hoyt's model (Horton & Hoyt, 1991). This model suggests that the linear cortical magnification factor (M_{linear} in mm/º) is inversely proportional to eccentricity (E in degrees), expressed as $M_{linear} = \frac{scale}{E+shape}$, with the normalizing parameter $shape$ equal to 0.75°, as measured by Horton and Hoyt (1991). For each hemisphere, we first estimated the *scale* value based on each subject's V1 surface area and the minimum and maximum eccentricities considered in the model (0º and 90º). The mean *scale* value for the left and right V1 hemispheres across all tested controls were 15.0±0.99 and 16.0±1.09, respectively. In comparison, Horton and Hoyt (1991) measured a mean *scale* of 17.3 mm. The mean V1 surface area for the left and right hemispheres were 2700.7±358.7mm^2 and 3067.7±416.3mm^2.

We then defined a function $f(r)$ that describes how the surface area of V1 changes with eccentricity (Equation 2). This was achieved by integrating Horton and Hoyt's function over the visual field, resulting in an equation that calculates the amount of V1 surface area from the foveal confluence up to a particular eccentricity (r). Next, we sorted the input eccentricity values and calculated the cumulative surface areas. A numerical method was then employed to find the eccentricity values that match the desired distribution. This method involved iteratively adjusting the range of possible values until the calculated values closely matched the desired values. Finally, the adjusted eccentricity values were returned in their original order and values from both hemispheres were merged to provide bilateral eccentricity estimates.

$$f(r) = \pi * scale^2 * \left(log\left(\frac{r + shape}{shape}\right) - \frac{r}{r + shape}\right)$$

Equation 2. Calibrating Benson atlas: Function f(r) describing how the surface area of V1 changes with eccentricity.

3.3. Validation under normal vision

To measure visual field function, we developed a new measure of cortical contrast sensitivity, assessing the brain's ability to discriminate shapes based on luminance variations. This depends on many factors, including the size, orientation, and density of cells in different parts of the retina. As these factors change across the visual field, contrast sensitivity varies with spatial frequency and visual field location in the typical, healthy visual system. We first investigated whether our brain-based approach can reliably detect these known differences in contrast sensitivity as a

function of eccentricities and visual field quadrants, in individual normal sighted controls. We then investigated whether our approach could recover loss of visual inputs at the cortical level, either simulated in a healthy control or pathological in a patient. In each section, findings were first reported for the pRF-defined ROIs and then for the Benson-defined ROIs.

3.3.1. Spatial frequency preference changes in V1 neuronal populations across eccentricities

For high spatial frequency stimuli, we expected better sensitivity in V1 neuronal populations encoding central locations in visual space than in those encoding the periphery. In contrast, for low spatial frequency information, we expected the opposite, better sensitivity in V1 neuronal populations encoding the periphery than the centre of the visual field.

We found this expected interaction between spatial frequency and eccentricity ($\mathrm{F}_{4,24} = 28.657, \mathrm{p} < 0.001$; Figure 18) as well as a main effect of eccentricity ($\mathrm{F}_{2,24} = 12.668, \mathrm{p} < 0.001$). These effects were statistically significant at the individual participant level showing high sensitivity (Figure 18A, transparent lines show individual data; Figure 18C shows individual visual field plots; for stats, see Table A7.2.1 in Appendix 7.2).

Post-hoc tests show that V1 neuronal populations receiving inputs from the central visual field (0.5-4.5º) showed greater contrast sensitivity to high spatial frequency as compared to low spatial frequency stimuli (steeper slope for the 3cpd versus 0.3cpd condition: **0.5-2.5º**: $t(6) = 4.354, p = 0.005$; **2.5-4.5º**: $t(6) = 3.471, = 0.013$). Conversely, peripheral eccentricities in V1 (above 9.5º) showed higher contrast sensitivity to low as compared to high spatial frequency stimuli (steeper slope for 0.3cpd versus 3cpd condition **9.5-15º**: $t(6) = -4.591, p = 0.004$; **15-20º**: $t(6) = -6.615, p < 0.001$).). Between 4.5º and 9.5º, V1 contrast sensitivity was similar for both spatial frequencies ($t(6) = -0.226, p = 0.829$). Crucially, these effects remained when using retinotopic estimates based on structural scans derived from the Benson retinotopic atlas instead of the pRF-mapping measures (**0.5-2.5º**: $t(6) = 5.768, p = 0.001$; **2.5-4.5º**: $t(6) = 2.531, p = 0.045$; **4.5-9.5º**: $t(6) = -0.293, p = 0.779$; **9.5-15º**: $t(6) = -3.274, p = 0.017$; **15-20º**: $t(6) = -3.528, p = 0.012$; see Figure A7.3.1 and Tables A7.3.1. & A7.3.2. in Appendix 7.3).

These results demonstrate that our approach can detect subtle changes in visual sensitivity across eccentricities at the individual participant level, and that structure-based atlases can replace the need for pRF mapping in cases where it might otherwise be difficult or impossible to collect pRF data.

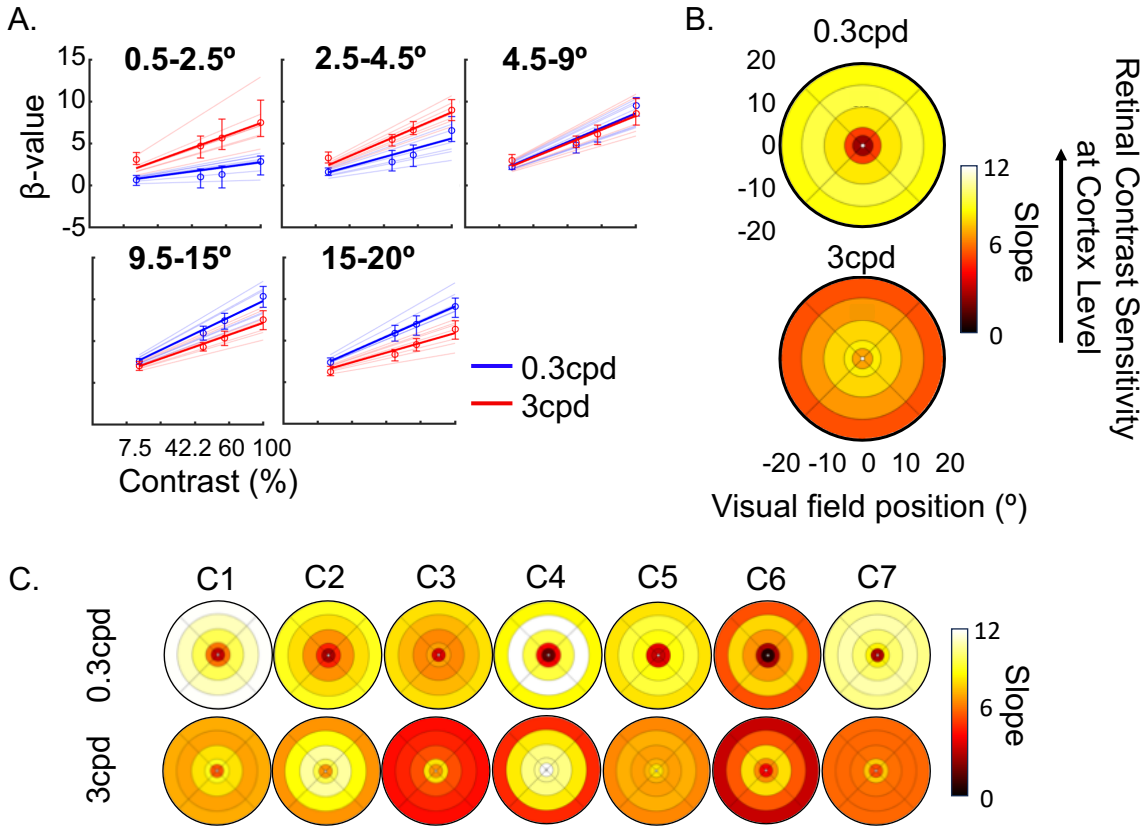

Figure 18. Spatial frequency preference V1 across the visual field.
For each participant, five eccentricity bins were defined using subject-specific pRF estimates: 0.5º-2.5º, 2.5º-4.5º, 4.5º-9.5º, 9.5º-15º, and 15º-20º. (A) Average β-values versus stimulus contrasts for low (0.3cpd; blue) and high (3cpd; red) spatial frequencies across eccentricity bins. Error bars are the 95% confidence intervals. Thick lines represent the group-level model fit, thin lines are the individual fits. (B) Slopes projected into visual space for low (0.3 cpd) and high (3 cpd) spatial frequencies. The color scale corresponds to slope estimates, with higher values indicating higher cortical contrast sensitivities. (C) Heat plots for each participant (C1-C7). Image from Chow-Wing-Bom et al., 2025, eLife.

3.3.2. V1 contrast sensitivity is not equal across the visual field quadrants

Contrast sensitivity is known to vary across the quadrants of the visual field; Previous behavioural studies have shown greater contrast sensitivity along the horizontal versus vertical meridians, and along the lower versus upper vertical

meridian (Barbot et al., 2021; Carrasco et al., 2022; Himmelberg et al., 2020, 2023). Recent fMRI studies have also shown that these asymmetries in BOLD response amplitude to single contrast gratings (Kurzawski et al., 2022; Liu et al., 2006; O'Connell et al., 2016). Therefore, we expect our fMRI approach to uncover these established asymmetry patterns at the cortical level.

Figure 19 shows how cortical contrast sensitivity in V1 varies across visual field quadrants, for the 0.3cpd and 3cpd conditions. For this analysis, we collapsed eccentricities (0.5º to 20º) into a single bin. We found a main effect of visual field quadrant location on V1 sensitivity ($F_{3,18} = 20.706, p < 0.001$). Post-hoc tests revealed that, as predicted, the cortical contrast response function had a higher slope – indicating better V1 sensitivity – along the horizontal versus vertical quadrants (Horizontal-Vertical Anisotropy – **HVA:** $t(6) = 5.908, p = 0.001$) and along the lower versus upper quadrant (Vertical Meridian Anisotropy – **VMA:** $t(6) = 4.106, p = 0.006$). Conversely, no difference in cortical contrast sensitivity was found between V1 neuronal populations encoding the left and right quadrants of the visual field (Left-Right Horizontal Meridian Anisotropy – **LRHMA:** $t(6) = 0.7197, p = 0.499$). Moreover, there was no interaction between spatial frequency and visual field quadrant positions ($F_{3,18} = 1.339, p = 0.293$), suggesting V1 visual field anisotropies are relatively constant across spatial frequencies.

Importantly, all these differences are also present in individual participants (Figure 19A, transparent lines are individual data, Figure 19C shows individual visual field plots; for stats, see Table A7.2.2. in Appendix 7.2). All participants had better V1 sensitivity in the horizontal versus vertical quadrants. 6 out of 7 participants showed asymmetries between the lower and upper quadrants. Differences in V1 sensitivity between left and right quadrants were inconsistent across participants (3 participants: left>right; 2 participants: right>left; 2 participants: non-significant), in line with no difference at the group-level. This again demonstrates the high sensitivity of our approach for identifying and quantifying sensitivity changes across the visual field, at the individual participant level, offering a potential valuable tool for assessing and addressing visual field loss in clinical populations.

We next tested if we could recover these V1 anisotropies when using retinotopic estimates based on structural scans fit with the Benson atlas instead of pRF measures (see Figure A7.3.2. and Tables A7.3.1. & A7.3.2. in Appendix 7.3). We found that the

horizontal-vertical anisotropy effect was recovered (**HVA:** $t(6) = 3.584, p = 0.012$), but that the vertical meridian anisotropy effect was not (**VMA:** $t(6) = 0.744, p = 0.485$) with this approach. These results provide evidence that our approach can still detect subtle visual field quadrant anisotropies using a structure-based retinotopic atlas, although less accurately.

While the most pronounced contrast sensitivity difference along visual field quadrants (horizontal versus vertical quadrants) was retained when the adjusted Benson atlas was used to replace pRF measurements, not all anisotropies survived. This may be because the template does not model cortical magnification differences along meridians, reducing accuracy. It is not surprising that retinotopic estimates based on structure-retinotopy relationship modelling, provides less accurate estimates of retinotopic tuning of neuron population in V1 than direct measures of the individual retinotopy. Any individual deviations from the model make it more challenging to accurately assign cortical contrast sensitivity to visual field locations, potentially decreasing the ability to detect changes in visual function across the field. Given this challenge, results with the adjusted Benson map are surprisingly similar to those based on pRF measurement, showing promise for clinical applications when pRF mapping is unfeasible.

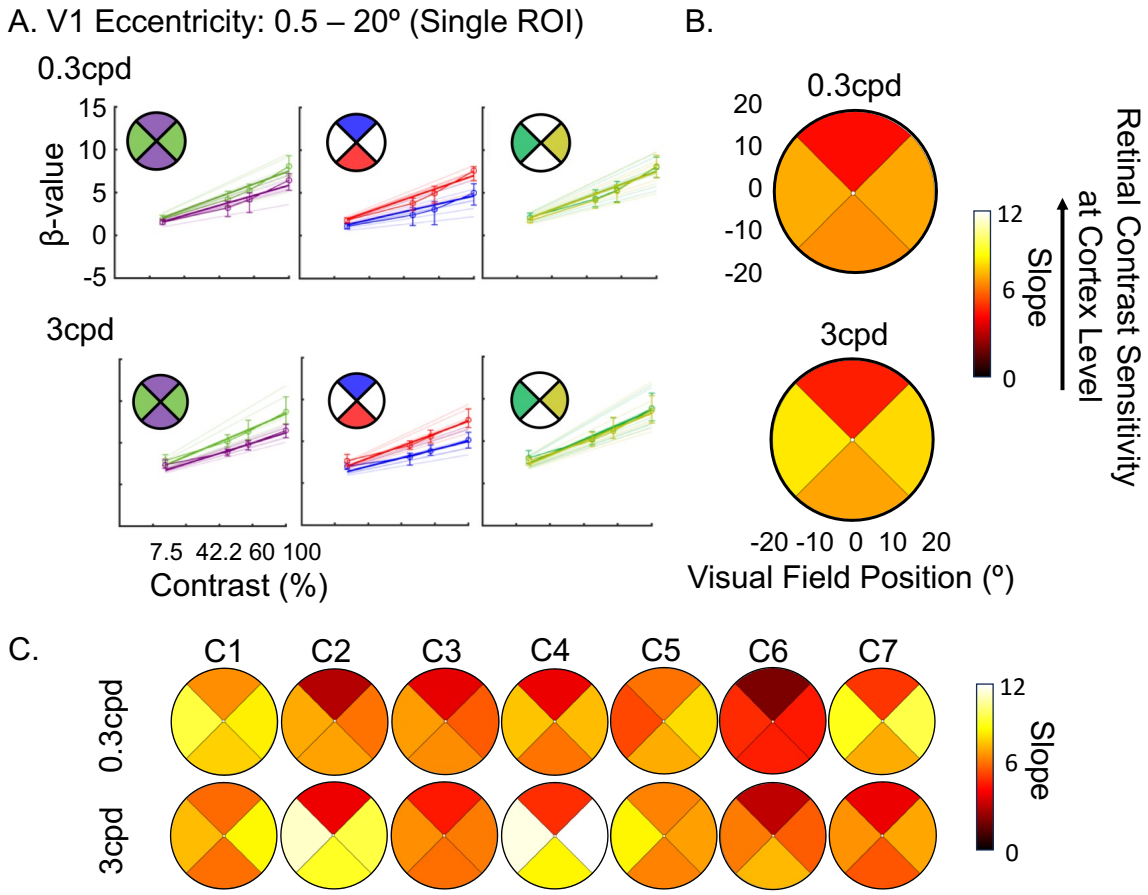

Figure 19. Anisotropies in V1 across visual field quadrants and spatial frequencies.
(A, B) Top row: low spatial frequency (0.3cpd); bottom row: high spatial frequency (3cpd). pRF estimates were used to link brain responses to visual field positions. Visual quadrants are ±45º around the cardinal meridians, with slope values for eccentricities between 0.5º-20º. Horizontal quadrants are left and right; vertical quadrants are upper and lower. (A) Average β-values versus contrast levels for each anisotropy (horizontal vs. vertical, upper vs. lower, left vs. right). Error bars are 95% confidence intervals. Thick lines correspond to average model fit, which thin lines are individual fits. (B) Slope values projected onto visual field quadrants. The colour scale represents slope estimates, with higher values indicating greater V1 contrast sensitivity. (C) Heat plots for each participant (C1-C7). Image from Chow-Wing-Bom et al., 2025, eLife.

3.3.3. V1 sensitivity differences across the visual field are reproductible across visits.

Having shown that changes in cortical contrast sensitivity across the visual space can be detected with fMRI, it is crucial to determine how reliable our measure is. This is especially important for potential applications in monitoring changes over

time. Using Spearman correlations, we measured the reliability of cortical contrast sensitivity estimates for the 0.3cpd spatial frequency condition across two repeated measurements, collected on two different days. We collected test-retest reliability measures from 4 out of 7 participants (Figure 20A-B) and benchmarked them against the correlations between the 0.3cpd condition and 3cpd spatial frequency condition, collected in the same session (Figure 20C). If measures are reliable, correlations should be higher for repeated measures with the same spatial frequency stimulus, collected on different days.

Our findings clearly show that the gradual increase in cortical sensitivity toward the periphery for the 0.3cpd condition is consistent across the two sessions (Figure 20A). Moreover, the data of individual participants show characteristic profiles that stay highly consistent. Additionally, we observed moderate-to-strong positive Spearman correlations across sessions for the 0.3cpd condition (Figure 20B; C2: $\rho = 0.5793, p < 0.001$; C4: $\rho = 0.6996, p < 0.001$; C5: $\rho = 0.4059, p < 0.001$; C6: $\rho = 0.7677, p < 0.001$), which were consistently higher than those across different spatial frequency conditions within a session (Figure 20C; one-tailed t-test: $t(3) = 2.62, p = 0.0395$; Spearman coefficients: C2: $\rho = 0.5503, p < 0.001$; C4: $\rho = 0.2158, p < 0.001$; C5: $\rho = 0.2318, p < 0.001$; C6: $\rho = 0.4993, p < 0.001$). This indicates that within participants, our measure is reliable across sessions and distinguishes effectively between patterns elicited by various spatial frequency conditions. Collectively, this suggests that our measure could serve as a robust tool for detecting changes in cortical sensitivity, such as those occurring over time or following therapeutic interventions.

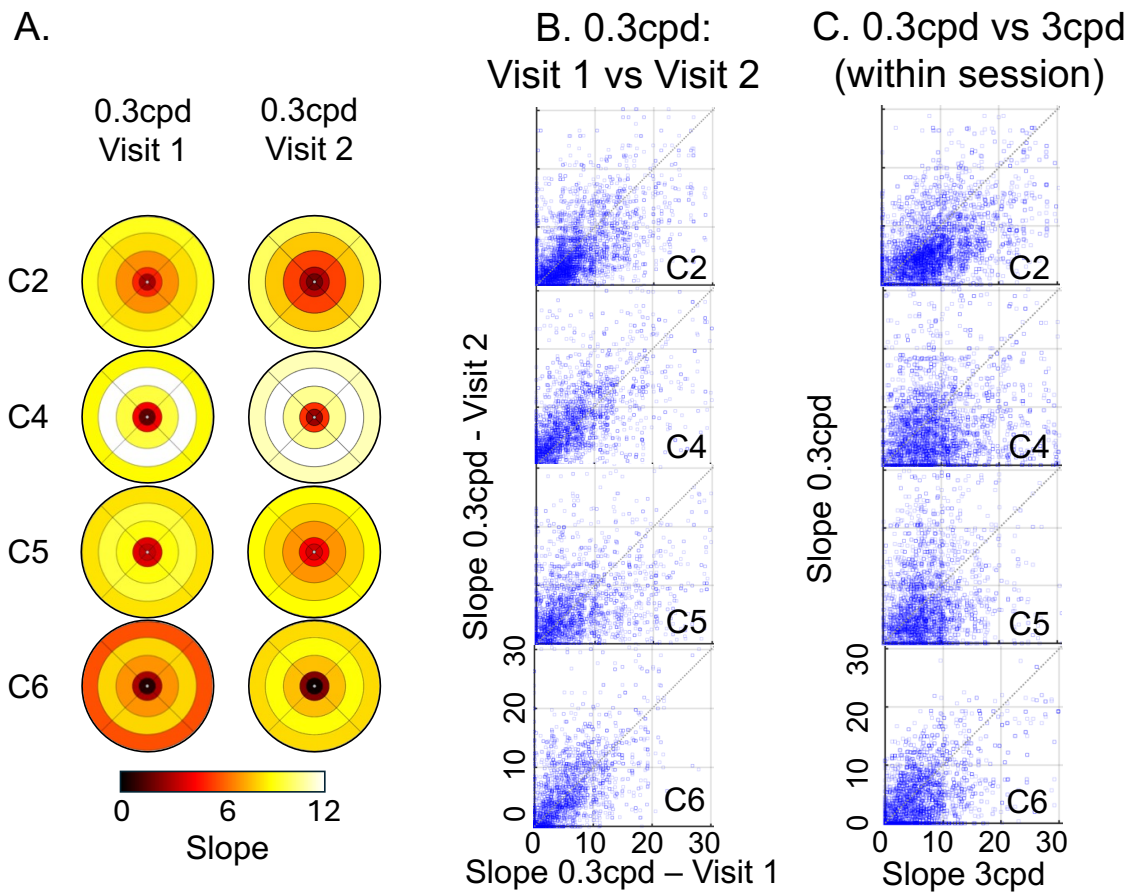

Figure 20. Reliability of V1 slopes across sessions, in 4 of the 7 controls.
(A) V1 contrast sensitivity (i.e., slopes) plotted in visual field space (using pRF estimates), showing a consistent session-independent increase in cortical sensitivity toward peripheral locations for the 0.3cpd condition. Higher slopes (warmer colours) indicate higher V1 sensitivity. (B) Slopes for the 0.3cpd condition across two visits. (C) Slopes for the 0.3cpd and 3cpd conditions collected within the same session. Image from Chow-Wing-Bom et al., 2025, eLife.

3.4. What happens to contrast sensitivity if central visual inputs are lost?

3.4.1. A test-case of simulated loss of visual inputs

In the previous sections, we showed that the slope of a square root function provides a reliable measure of contrast sensitivity in the brain of healthy controls. But can this brain-level model also quantify loss of visual inputs? To test this, we first simulated an artificial scotoma in one normal sighted participant, by masking the 3cpd stimulus with a grey annular ring between eccentricities of 3-8º (Figure 21A). We

expect smaller slope values in V1 neuronal populations that would under normal circumstances encode that part of the visual space.

As expected, we observed reduced responses in V1 locations corresponding to the artificial scotoma (Figure 21B), with increased responses along the edges of the mask. This artificial loss of visual input was also clearly present in the cortical contrast sensitivity estimate (Figure 21C&D), with significantly reduced slope steepness between 3-8º in V1. Additionally, we could recover this scotoma using the calibrated Benson template, although less accurately (Figure 21E). These results show that this measure of V1 contrast sensitivity is sensitive enough to detect loss of visual inputs in the brain at an individual level, when a complete local loss of sight is simulated, and that this approach does not crucially rely on pRF mapping data from the individual. This supports the utility of our approach in recovering patterns of vision loss and recovery at a cortical level.

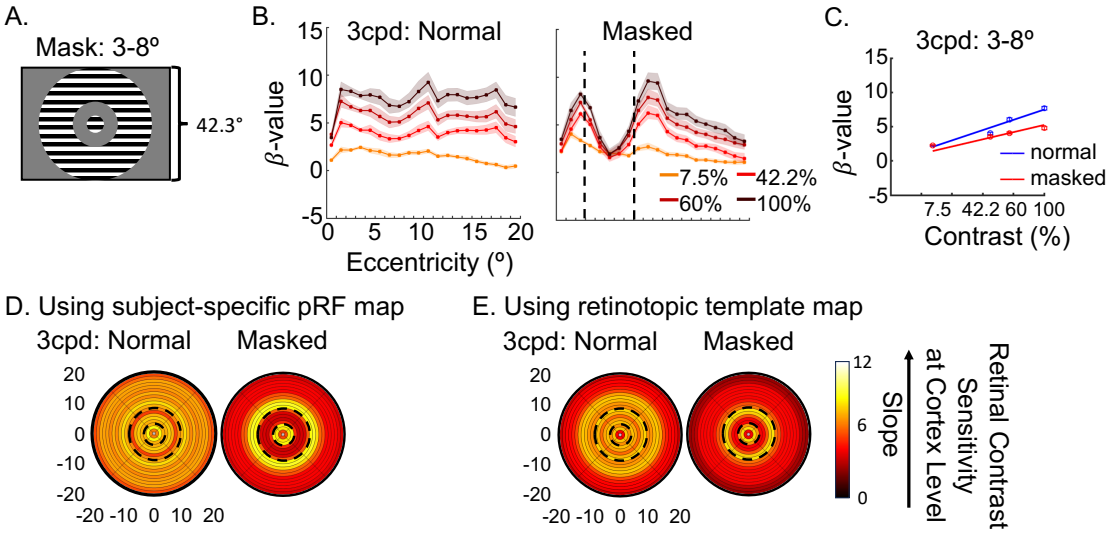

Figure 21. V1 sensitivity (i.e., slope) to 3cpd condition, in the region of the artificial scotoma (3-8º).

(A) Masked region between 3-8º eccentricity, representing the artificial scotoma. (B) Averaged -values between 0.5º-20º eccentricities in V1, under normal and masked conditions. 20 eccentricity bins of 1º were selected based on pRF estimates. The colour scale indicates the presented contrast levels, and the black dotted lines mark the boundaries of the artificial scotoma. (C) Average -values versus contrast levels in V1 neurons encoding the region of artificial scotoma (3º-8º), under normal (blue) and masked (red) conditions. Lines correspond to the model fitted to the data. (D) Slopes projected back onto the visual field under normal and masked conditions. pRF estimates were used to relate brain responses to visual field locations and to create the 1º eccentricity bins. The boundaries of the simulated scotoma

region are represented by dotted lines. The colour scale indicates slope estimates, with higher values (warmer colours) corresponding to higher V1 contrast sensitivity. (E) Slopes plotted back into the visual space using the calibrated Benson template instead of pRF estimates. Image from Chow-Wing-Bom et al., 2025, eLife.

3.4.2. Case of severe central vision loss

We next tested if brain-based cortical contrast sensitivity could recover visual field loss in a clinical patient with Leber Hereditary Optic Neuropathy (LHON; M, 45.5 years old, mutation: m.11778G>A, disease duration: 36.1 years). LHON is a neurodegenerative disease caused by mitochondrial DNA mutations, leading to acute loss of retinal ganglion cells across large visual field areas. LHON patients often present with dense, central scotoma extending up to 10-15 degrees around fixation.

As vision loss often varies between eyes, the patient underwent monocular testing for the fMRI contrast sensitivity task. For comparison, a behavioural visual field perimetry map was obtained with the Compass fundus perimeter (iCare, https://www.icare-world.com/product/icare-compass/) for each eye, using a 24-2 testing grid with a Goldmann size III target (54 locations: 52 from the 24-2 grid, 1 at fixation, and 1 at the physiological blind spot). The Compass actively tracks the retina to compensate for fixation loss, automatically repositioning targets based on current eye position. Sensitivity thresholds at each location were determined using the ZEST projection strategy implemented in the device. The patient, who had some preserved central vision, could see the fixation targets in behavioural testing and the scanner, making them an ideal participant for methods evaluation.

The Compass perimetry map revealed drastic loss of sensitivity across the visual field (Figure 22 – top row). For the left eye, the left hemifield was more affected than the right, with most severe loss in the upper-left quadrant. In contrast, the right eye showed more reduced sensitivity in the right hemifield, particularly in the upper-right quadrant.

We found correspondence between affected and non-affected visual field regions across the Compass and the fMRI contrast sensitivity measures (Figure 22). Here, V1 contrast sensitivity (i.e., slope values) was computed for the upper-left, upper-right, lower-left and lower-right quadrants to match the layout from the Compass visual field maps. Using the brain-based approach, we recovered sensitivity loss in the upper-right visual quadrant for the right eye at the cortical level, reflected in smaller

cortical contrast sensitivity slopes in V1 neuronal populations encoding that area. For the left eye, cortical contrast sensitivity was also lower in the upper-left quadrant of the visual field, but differences were less pronounced. This is in line with the observation that the left eye was the better eye, with substantially less severe vision loss in the affected regions (lighter shading, Figure 22 – top row). When using the calibrated Benson atlas instead of pRF mapping data to link neuronal responses to visual locations, this pattern was retained for the right eye, but the more subtle pattern in the left eye became noisier.

By combining large-field stimulation and contrast sensitivity modelling in fMRI, with the cortical magnification-adjusted Benson atlas, these data show how brain-based measures could provide a tool to characterize vision loss in patients without need for demanding tasks or sustained precise fixation, while highlighting challenges of detecting more subtle vision loss and pinpointing it to visual locations.

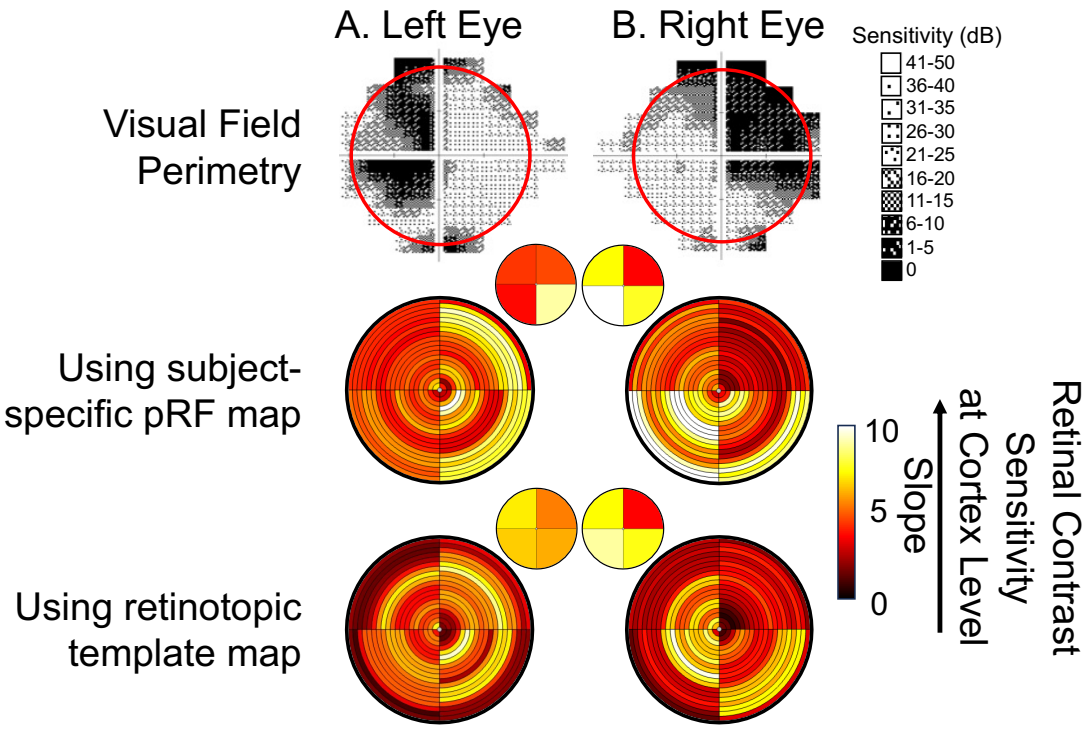

Figure 22. Correspondence between visual field perimetry map and V1 sensitivity map, in a patient with Leber Hereditary Optic Neuropathy.

(A) Left eye. (B) Right eye. Top row: Gray scale visual field map obtained with the Compass fundus perimeter (CenterVue, Padova, Italy), using Standard Perimetry display convention. Sensitivity is represented with symbols and related dB intervals, with larger values describing better sensitivity. Red circle indicates the area of the visual space stimulated in the fMRI contrast sensitivity task. Middle row: Heatmap of V1 sensitivity (i.e., slopes) across the visual

field. Here, we divided the space between the upper-left, upper-right, lower-left and lower-right quadrants (as opposed to the left, right, upper and lower quadrants used in previous sections), to match the layout of visual field perimetry maps. Slope values were averaged for each visual quadrant and 1º eccentricity bin and projected back into the visual space, using the subject-specific pRF map. Colour scale corresponds to the steepness of the slope estimate. For better visualization of sensitivity differences across quadrants, we also averaged the slopes between 0.5-20° eccentricities in each quadrant, generating a single slope value for each visual quadrant (inset heat plots). The range of slope values were reduced on the colour scale for these inset plots. Bottom: Heatmap of V1 sensitivity (i.e., slopes) across the visual field, using the Benson retinotopic template map instead of the pRF data. Image from Chow-Wing-Bom et al., 2025, eLife.

3.5. Discussion

In this study, we aimed to develop and validate an fMRI-based method for measuring cortical contrast sensitivity across the entire visual field in V1, addressing the limitations of traditional visual field tests and existing neuroimaging approaches. By integrating population receptive field (pRF) modelling with contrast sensitivity measurements of the BOLD response to large-field sinusoidal gratings varying in contrast levels and spatial frequencies, we created a quantitative, sensitive, and reliable measure of cortical contrast sensitivity. Our key findings demonstrate that this approach can accurately quantify known variations in V1 contrast sensitivity across eccentricity and polar angle, recover simulated and pathological visual field losses, and produce consistent and reliable measures both at the group and individual participant levels.

Our method successfully captured the expected variations in cortical contrast sensitivity across the visual field. Consistent with previous behavioural and fMRI studies (Aghajari et al., 2020; Broderick et al., 2022; D'Souza et al., 2016; Henriksson et al., 2008; Rovamo et al., 1984; Rovamo & Virsu, 1979; Welbourne et al., 2018), we observed that V1 neuronal populations encoding the central visual field exhibited higher contrast sensitivity for high spatial frequency (SF) stimuli, while those encoding peripheral regions were more sensitive to low SF stimuli. This aligns with the understanding that spatial frequency tuning varies across the visual field due to smaller pRF sizes and larger cortical areas dedicated to central vision (Himmelberg et al., 2023).

Additionally, our study identified anisotropies in contrast sensitivity across visual field quadrants, mirroring findings from previous behavioural studies (Barbot et al., 2021; Carrasco et al., 2022; Himmelberg et al., 2020). Specifically, we found enhanced cortical sensitivity in V1 neuronal populations responding to horizontal versus vertical locations and to lower versus upper visual field locations. Unlike earlier fMRI studies (Liu et al., 2006; O'Connell et al., 2016), which either could not assess horizontal-vertical effects or used smaller region selections, our use of large-field stimuli enabled the detection of both upper-lower and horizontal-vertical asymmetries. Moreover, by modelling cortical contrast sensitivity across multiple contrast levels, we were able to identify subtle variations in V1 neuron sensitivity that single-threshold approaches might overlook.

Crucially, these effects were significant at the individual level indicating high sensitivity, and our approach proved reliable over time. We found consistent activation patterns and moderate-to-high correlations in slope estimates for the 0.3cpd condition across two separate sessions, significantly higher than when correlating responses to different stimuli (i.e., 3cpd condition). High sensitivity and reliability are essential for detecting longitudinal changes in clinical groups, such as those occurring before and after sight-rescuing interventions. Fitting a contrast response function to the BOLD signal might offer robust estimates of visual function by minimizing the impacts of overall BOLD amplitude variability and arbitrary thresholds.

Furthermore, our method successfully identified both simulated retinal loss in a healthy volunteer and real visual field loss in a patient with Leber Hereditary Optic Neuropathy (LHON). Unlike previous fMRI studies that used high-contrast stimuli (Halbertsma et al., 2021; Farahbakhsh et al., 2022; Pawloff et al., 2023; Ritter et al., 2019) – which may not accurately represent partial vision loss due to potential saturation and the stimulation of less sensitive retinal cells – our use of multiple contrast levels offers a more nuanced assessment of cortical contrast sensitivity. This may make our method particularly suitable for evaluating treatment efficacy in cases of widespread and variable vision loss.

One limitation of this brain-based approach to visual field testing, is its reliance on pRF mapping, which requires precise fixation and can be challenging to acquire in visually impaired patients. To mitigate this, we investigated the use of retinotopic templates based on anatomical landmarks (Benson et al., 2012; Benson et al., 2014;

Benson & Winawer, 2018), thereby reducing the need for pRF data collection and facilitating the mapping of brain responses to visual field positions. Particularly at large eccentricities where, due to smaller cortical projection areas, small inaccuracies between the template and individual retinotopy can lead to large distortions in cortical visual field maps. To increase accuracy of the atlas at higher eccentricities, we adjusted the Benson eccentricity estimates to align with the cortical magnification scaling function (Horton & Hoyt, 1991). With this structure-based atlas we successfully replicated key variations in visual field function, although with reduced sensitivity compared to individual pRF measures for more subtle differences (i.e., for the less consistent upper versus lower quadrant anisotropy, and the patient's eye less affected by pathology). It is notable that cortical structure-based templates can successfully recover visual field loss. Critically, in patient groups with severe impairment such as LHON, where it is often very challenging or impossible to obtain reliable measures, even imperfect mapping between the brain and visual field could offer important improvements over available solutions for tracking functional change, and where they stem from. Further enhancing the alignment between retinotopic template atlases and individual retinotopic tuning - for example, by integrating them with functional measures using Bayesian methods (Benson & Winawer, 2018) - could improve this approach further.

While our method demonstrated high accuracy and reliability in sighted controls, further validation in patients is necessary to ensure the generalizability of our approach to measuring pathology. Next steps in this work will therefore include reconstructing diverse types of vision loss in larger patient cohorts, validating our approach for tracking pathology over time, and investigating how cortex-based visual field measures relate to and complement other visual field integrity indices such as the Compass in those contexts. Comparison of the cortical contrast sensitivity modelling approach presented here to other approaches will be another interesting direction for future research. For example, while we reasoned that using a single high contrast stimulus is likely to give less reliable measures for various reasons outlined above, this needs to be tested empirically. It is also unclear whether the square root contrast response function is optimal for patients, who are likely to show different non-linearities in their contrast response. Additionally, more extensive mapping of the spatial frequency and contrast sensitivity spaces could offer additional informative measures

such as cortical acuity and spatial frequency preferences, provided such measures are feasible with patient-friendly protocols.

In conclusion, brain-based contrast sensitivity measures could thus significantly enhance the accurate characterization of visual field function in blinding diseases, by addressing limitations of traditional visual field tests that are subjective, time-consuming, and challenging for patients with severe sight loss. By providing a reliable, quantitative measure of cortical contrast sensitivity across the visual field, fMRI may help facilitate the monitoring of disease progression and recovery, including interventions like gene therapy. Combined with our large-field stimulation setup and fixation free approaches to linking cortical sensitivity estimates to visual field locations, this method is well-suited for a wide range of visual impairments, addressing a pressing challenge in the evaluation of current clinical trials. Additionally, linking brain-based variations in function across the visual field to behavioural performance, could help bridge the gap between neural measures and functional outcomes, offering deeper insights into developmental, learning, and vision loss mechanisms. In sum, integrating cortical contrast sensitivity testing with large-field stimulation and a calibrated retinotopic atlas provides a promising tool for characterising visual field impairments, and could offer a valuable addition to existing measures of visual field loss.

4. Mapping cortical vision loss in Leber Hereditary Optic Neuropathy (LHON)

The work in this chapter is motivated by the limitations of traditional visual field (VF) testing in Leber Hereditary Optic Neuropathy (LHON), where difficulties to fixate and reduced attention hinder reliable assessment. To address this, I investigate whether the fixation-free, fMRI-based approach (Chapter 3) can offer a less demanding alternative for assessing visual field sensitivity, focusing on three main axes:

- **Structure–function relationship**: By linking fMRI-based cortical VF sensitivity to behavioural VF measures and OCT-derived retinal nerve fibre layer (RNFL) thickness, I aim to connect functional and structural measures. This approach has limited success in capturing such connection, showing only a positive association between OCT thickness and cortical visual field sensitivity.
- **Comparing cortical and behavioural visual fields**: Qualitative comparisons between fMRI and behavioural maps of VF loss reveals partial correspondence and highlight challenges in aligning data from multiple modalities.
- **Repeatability and robustness**: I evaluate the consistency of fMRI-based VF maps across low and high spatial frequency stimuli. I find that cortical sensitivity patterns are largely repeatable, supporting the robustness of the method and highlighting its potential for tracking disease progression and recovery.

Together, these preliminary findings suggest that the fixation-free, large-field fMRI approach may serve as a valuable complementary tool for tracking visual field changes in LHON, particularly in clinical trials where conventional methods are limited by poor fixation and low vision.

Leber Hereditary Optic Neuropathy (LHON) is a rare mitochondrial condition that causes severe vision loss, primarily through optic nerve degeneration. While visual acuity is the clinical gold standard for assessing vision, it primarily reflects

central vision and does not capture the broader functional impacts of visual loss. Measuring sensitivity across the visual field is essential for providing a comprehensive understanding of visual field loss, particularly in conditions like LHON where vision loss is widespread. Characteristic patterns of visual field loss often correlate with retinal thinning observed via optical coherence tomography (OCT), linking structural damage to functional deficits (Garway-Heath et al., 2000). This provides valuable insights into the progression and localisation of damage in vision-related disorders, critical for clinical decision-making.

Unfortunately, conventional visual field tests which use target detection tasks to detect light sensitivity deficits across the visual field, pose challenges for LHON patients, due to their reliance on stable fixation and sustained attention. These demands are difficult for individuals with profound central scotomas and limited ability to fixate.

Functional MRI (fMRI)-based approaches could offer a less demanding alternative by measuring neural sensitivity to visual stimuli directly from cortical responses, independent of fixation or active participation. By linking fMRI measures of cortical sensitivity to visual field locations using a retinotopic atlas, we recently suggested that it may be possible to obtain sensitive measures of visual field loss and recovery without need for precise fixation, or ability to perform a demanding detection task (Chow-Wing-Bom et al., 2025). Alongside improving measurement of field loss in severely impaired sight loss patients beyond what is currently available, this could reduce frustration and psychological burden associated with traditional visual field testing. Previous studies have demonstrated the ability of population receptive field (pRF) mapping to identify visual field deficits and structural changes (Pawloff et al., 2023; Ritter et al., 2019; Halbertsma et al., 2021), but the reliance of this method on accurate fixation, limits its applicability in patients with central sight loss.

Characterising deterioration and improvement in function across the entire visual field in patients with large field sight loss, is evidently important for capturing the full impact. Despite this, behavioural visual field and fMRI measures are not routinely included in clinical trials for sight-restoring therapies in LHON - largely due to uncertainty about their clinical utility given the challenges involved (i.e., low vision and poor fixation). As result, recent clinical trials which demonstrating small but meaningful effects in acuity, have had limited perspective on recovery beyond central vision, which

may well be substantial and meaningful for patients' daily function, as LHON frequently affects up to 15º eccentricity. Integrating complementary functional measures of field loss with measures of structural retinal integrity (i.e., OCT measures), could enhance the sensitivity and scope of clinical evaluations, providing a more comprehensive understanding of functional improvements in LHON patients. In this study, we aimed to investigate this potential.

To achieve this, we mapped visual field deficits across the visual space in a cohort of LHON patients (N=10) with our fMRI-based cortical sensitivity measures. Evaluating accuracy of these measures is challenging, as the primary motivation of this study was a lack of reliable functional measures of field loss in this population. To assess accuracy, we therefore first developed an OCT-based approach to assess associations between cortical visual field sensitivity, behavioural visual field sensitivity, and retinal structural integrity. OCT provides a structural assessment of the retinal nerve fibre layer (RNFL) of the optic nerve and is routinely obtained in LHON patients with high quality measurement. Because the optic nerve head can be segmented into specific sections that reflect retinal fibre bundles which serve specific retinal locations, it offers an indirect measure of visual field loss sections as expressed in structural dystrophy (Figure 23A). This approach had limited success. We also evaluated accuracy of the fMRI-based measures through qualitative, case-by-case comparisons with two behavioural measures: a custom, subjective visual field test and an objective, gaze-controlled perimetry test (Compass). This highlights some key challenges of cross-modal comparison, as well as potential solutions. For clinical trials, it is arguably more important to detect meaningful change in function rather than accurately pinpoint this change to a specific visual field location, and repeatability of the endpoint is key for this. While repeat sessions were beyond the scope of this thesis, we assessed the repeatability of our fMRI measures by testing if visual field loss patterns are robust across two different stimulus conditions (low and high spatial frequency gratings). On the whole, we observe some correspondence between fMRI based visual field tests and behavioural measures, and the measures appear to be repeatable, but more work is needed to establish appropriate metrics to draw confident conclusions about accuracy and repeatability. Our preliminary data are consistent with large-field fMRI as a promising complementary measure for tracking change in visual field loss when this is key for clinical decision-making and standard approaches are unreliable.

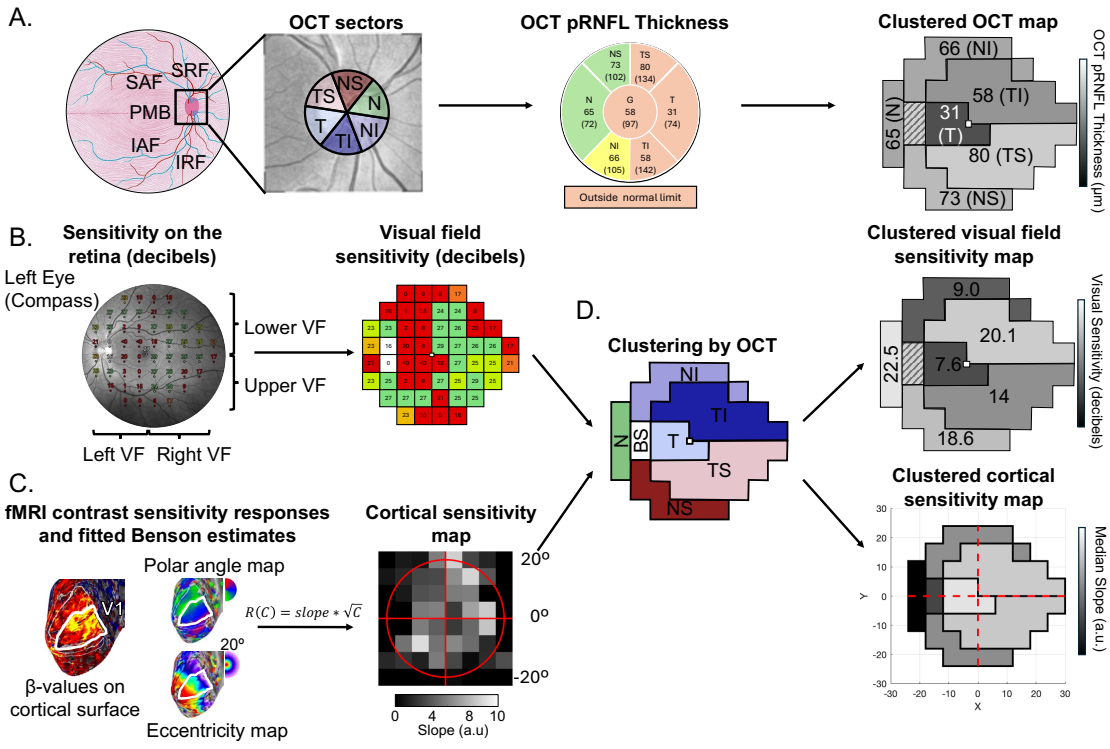

Figure 23. Multimodal assessment of visual function and structure in LHON: Relating cortical, behavioural and retinal measures.

(A) Peripapillary retinal nerve fibre layer (pRNFL) thickness was measured in six anatomical sectors using OCT and clustered according to the Garway-Heath map, which links optic nerve head regions to corresponding visual field locations. (B) Visual field sensitivity was assessed using Compass gaze-controlled perimetry (in decibels, dB), overlaid on the retinal fundus. (C) Cortical sensitivity was estimated from fMRI by fitting a contrast response function to brain activity and mapped to visual field locations using eccentricity-adjusted Benson templates. (D) Cortical (median slope) and behavioural (mean dB) sensitivities were averaged across sectors defined by the Garway-Heath map to enable cross-modal comparison. Abbreviations: VF – Visual Field; NS – Nasal-Superior; N – Nasal; NI – Nasal-Inferior; TS – Temporal-Superior; T – Temporal; TI – Temporal-Inferior; BS – Blind Spot; SRF – Superior Radiating Fibres; IRF – Inferior Radiating Fibres; SAF – Superior Arcuate Fibres; IAF – Inferior Arcuate Fibres; PMB – Papillomacular Bundle; OCT – Optical Coherence Tomography.

4.1. Methods

4.1.1. Participants

We collected fMRI data for both eyes in eleven patients with Leber Hereditary Optic Neuropathy (LHON; mean±SD: 36.6±10.9 years old; 8M), who also participated in the structural part of the study. All patients were in the chronic phase of the disease

(mean±SD: 14.4±14.1 years) and had genetically confirmed mutations in one of the three most common mitochondrial genes: six with m.11778G>A, four with m.14484T>C, and one with m.3460G>C. All patients signed a written informed consent to participate in the study, and this study was approved by HRA/HCRW and Research Ethics Committee (IRAS 258959; REC 20/YH/0336).

Visual field sensitivity maps were collected for both eyes in ten of the eleven patients using the Compass perimeter (iCare, https://www.icare-world.com/product/icare-compass/), while all patients performed a custom, more simplistic, visual field-like test outside the scanner. Additionally, optical coherence tomography (Spectralis OCT, Heidelberg Engineering, Heidelberg, Germany) data on the optic nerve head were retrieved for ten of the eleven patients, from their medical records.

4.1.2. Stimulus & tasks

Stimuli were programmed in MATLAB 2020b (MathWorks, Natick, Massachusetts, USA) using the Psychtoolbox-3, and displayed using an EPSON LB-1100U projector (1920x1200 pixels, 60Hz, 43.2x27cm projected area). To reduce brightness and discomfort in the scanner, a neutral density filter (ND4 Plus+; Urth, Byron Bay, Australia) was placed in front of the projector, reducing light intensity fourfold without altering colour. The projector was gamma-corrected to ensure accurate contrast and spatial frequency presentation.

All stimuli were presented within a 42.3º circular aperture. To achieve a wide field of view, the front of the 64-channel MRI coil was removed, and stimuli were back-projected onto a screen positioned near the participant's head (see Appendix 7.1). Participants viewed the stimuli via a mirror, for a total viewing distance of 34cm.

Throughout scanning, patients were instructed to remain still to minimize head and body motion. Those with preserved islands of central vision were given the option to respond to colour changes in a central fixation dot. Others with more extensive visual field loss were instructed to maintain forward gaze as steadily as possible. Eye movements and alertness were monitored using an EyeLink 1000Plus device (SR Research, Ottawa, Canada). In fMRI, sleepiness can be a potential problem when measuring visual responses. Due to the constraints of the fMRI set-up, we were able to directly monitor patients' alertness during testing of the right eye in the scanner;

however, whether we could monitor the left eye depended on participant placement, so this was less consistent.

4.1.3. fMRI contrast sensitivity task

Participants were presented monocularly with achromatic sine-wave gratings flickering at 2Hz, varying in contrast levels (7.5, 42.2, 60, or 100%) and spatial frequencies (either 0.3 or 1 cpd). Contrast was defined using Michelson contrast: $C = \frac{L_{max}-L_{min}}{L_{max}+L_{min}}$, where L_{max} and L_{min} are maximum and minimum luminance. Each stimulus was displayed for 13 s, followed by 2 s of a grey screen (0% contrast) to reduce after-effects. Each contrast-spatial frequency combination was shown three times per run, arranged in a pseudo-random sequence, for a total of 9 repetitions per combination (i.e., 3 runs). Eight additional 15-second rest blocks (0% contrast) were included to allow sufficient baseline.

The high spatial frequency condition differed from the 3cpd used in our previous study on sighted controls (Chow-Wing-Bom et al., 2025), to account for the lower visual acuity of LHON patients. We selected these spatial frequencies based on pilot testing: the 0.3cpd condition was chosen to remain within the visibility range of most untreated patients, while we expected central vision improvements after a gene therapy to be most pronounced around in our measures. Patient P001, who piloted the experiment, was tested with different contrast and spatial frequency parameters (see Table 7).

Finally, cortical responses in V1 were mapped to visual field locations using Benson atlas estimates, corrected for peripheral inaccuracies.

Subject ID	Best Eye	VA LE	VA RE	Spatial Frequency (per run)	Contrast Levels (per run)	Compass Perimetry	Custom visual field-like test (tested contrast %)	OCT data available from medical records
P001	LE	-0.1	0.3	0.3cpd	0.1, 0.2, 0.6, 1.3, 3.2, 7.5, 17.8, 42.2, and 80%	Yes	RE: 20%, LE: 15%	Yes
	LE	-0.1	0.3	3cpd	3.2, 7.5, 17.8, 42.2, 60, 80, and 100%			
	LE	-0.1	0.3	5cpd	0.1, 0.2, 0.6, 1.3, 3.2, 7.5, 17.8, 42.2, and 80%			
P002	RE	1.8	1.2	0.3 & 1cpd	7.5, 42.2, 60, and 100%	No	RE & LE: 35% & 100%	Yes
P003	RE	1.8	1	0.3 & 1cpd	7.5, 42.2, 60, and 100%	Yes	RE & LE: 50%	Yes
P004	LE	1.4	2.1	0.3 & 1cpd	7.5, 42.2, 60, and 100%	Yes	RE & LE: 100%	Yes
P005	LE	0.8	1.5	0.3 & 1cpd	7.5, 42.2, 60, and 100%	Yes	RE & LE: 25% & 100%	Yes
P006	LE	1.3	1.8	0.3 & 1cpd	7.5, 42.2, 60, and 100%	Yes	RE: 90%, LE: 85%	Yes
P009	LE	1.3	1.5	0.3 & 1cpd	7.5, 42.2, 60, and 100%	Yes	RE & LE: 50% & 100%	Yes
P010	LE	0	0.1	0.3 & 1cpd	7.5, 42.2, 60, and 100%	Yes	RE & LE: 25% & 50%	Yes
P011	RE	0.5	0.1	0.3 & 1cpd	7.5, 42.2, 60, and 100%	Yes	RE & LE: 15% & 50%	Yes
P012	RE	2.3	1.7	0.3 & 1cpd	7.5, 42.2, 60, and 100%	Yes	RE & LE: 75% & 100%	No
P013	LE=RE	1.8	1.8	0.3 & 1cpd	7.5, 42.2, 60, and 100%	Yes	RE & LE: 100%	Yes

Table 7. Task and stimulus tested in LHON patients.

4.1.4. Compass visual field perimetry test

Monocular visual field maps were acquired in 10 of 11 patients using the Compass fundus perimeter (iCare, https://www.icare-world.com/product/icare-compass/). A 24-2 grid with a Goldmann size III target was used, covering 54 locations: 52 test points, one at fixation, and one at the blind spot. The Compass system uses real-time retinal tracking to correct for fixation loss and automatically repositions stimuli. Sensitivity thresholds were estimated using the ZEST strategy.

Five patients maintained stable fixation on the central target; the remaining five, unable to see the target, were instructed to look straight ahead. Their ability to keep the (for them invisible) fixation target on their retinal fovea was monitored and corrected online by the experimenter. One patient (P002) did not complete the test.

For each tested eye, we obtained a 24-2 test printout (Figure 24) from which we used the following information for our analysis:

(A) Sensitivity thresholds overlaid on the fundus image. Values are in decibels (dB) and colour-coded by normative deviation: red ($p < 0.5\%$), orange-lime ($0.5\% \leq p < 5\%$), green ($p \geq 5\%$), and white making the fovea and optic disc.

(B) Grayscale visual field map using the standard perimetry convention: black = no measurable light sensitivity; increasing number of white pixels = increase in sensitivity.

(C) Fixation area (95th percentile ellipse of fixation points), with semi-axes in brackets. Larger values indicate more dispersed fixation.

(D) Fixation plot showing eye movement amplitude over time relative to the preferred retinal locus; values within the green/yellow bounds indicate acceptable fixation.

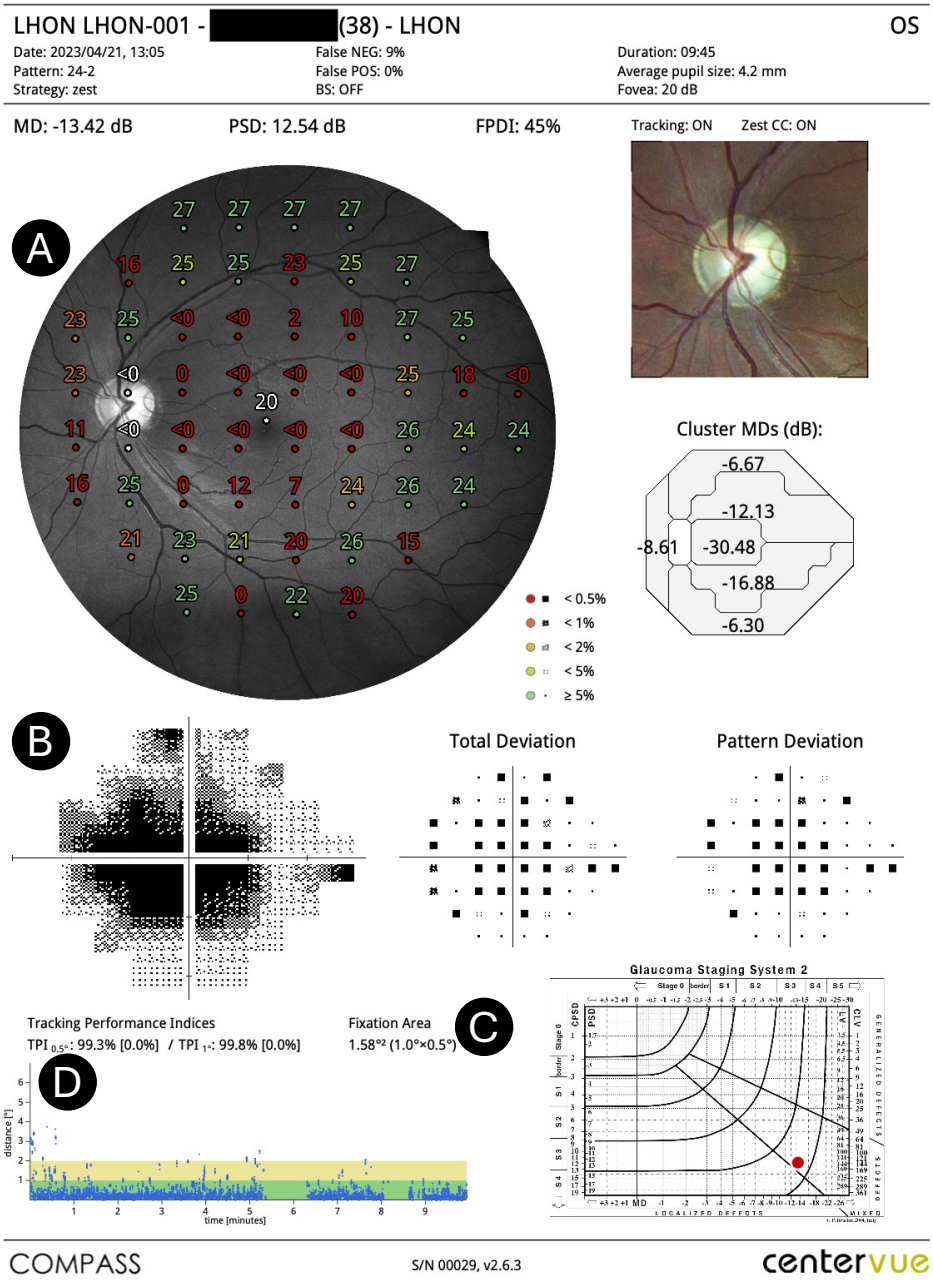

Figure 24. COMPASS report for 24-2 test.

4.1.5. Custom visual field test

We also tested all eleven patients with a quick, simplified custom visual field test outside the scanner. Stimuli were displayed once per location on a Display++ LCD monitor (1920×1080 resolution, 70 × 39.5 cm, 51 cm viewing distance, 143 cd/m² max luminance), with a total viewing area of 68.92 x 42.34°.

Participants were asked to report whether a white dot (2º diameter) presented on a grey background was “seen,” “not seen,” or “partially seen” at 56 fixed locations

across the visual field. This resulted in the grid layout provided in Figure 25, which each location spaced 6° from each other.

Critically, note that the contrast level of the dot differed between patients (Table 7), but remained constant throughout each run and chosen ad-hoc to avoid ceiling or floor effects. As a result, data are not comparable across individuals. Participants were instructed to fixate on a central dot or maintain steady gaze if fixation was not achievable.

While this custom test is less precise than Compass perimetry, it offers a major advantage in speed and ease of use, making it especially valuable for patients with limited fixation stability or fatigue.

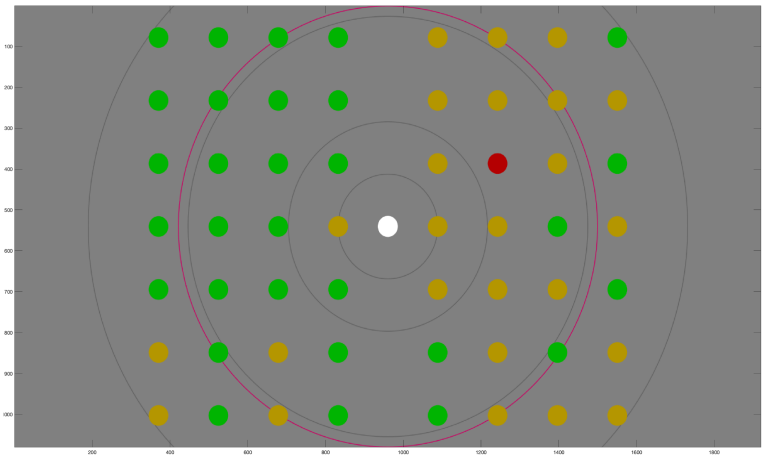

Figure 25. Grid layout used for the custom visual field test.
Example of custom visual test results from one LHON patient (P009; right eye tested at 100% Michelson contrast): Green = target seen, yellow = unsure or partially seen, red = not seen, white = fixation point. The magenta circle (not shown during the test) outlines the 20º radius area stimulated in fMRI for visualisation purposes only.

4.1.6. MRI acquisition

Functional MRI data were collected at the Birkbeck-UCL Centre for NeuroImaging (BUCNI, London, UK), using a Siemens PRISMA 3T scanner. A 64-channel head coil was used with the front section removed to provide an unobstructed screen view, while maintaining signal quality from the remaining 40 channels covering the sides and back of the head.

T2*-weighted echo-planar images were collected using a multiband-accelerated sequence (CMRR, version R016a, https://www.cmrr.umn.edu/multiband; Cauley et al., 2014; Xu et al., 2013) with the following parameters: multi-band factor =

4, voxel resolution = 2mm isotropic, FOV = 212 x 212 x 96mm, flip angle = 60º, TR = 1000ms, TE = 35.2ms, echo spacing = 0.56ms, bandwidth = 2620Hz/Px, 48 transverse slices aligned approximately parallel to the calcarine sulcus while avoiding the orbits. Four additional scans with reversed phase-encoding were acquired for B0 distortion correction.

A high-resolution T1-weighted structural image was acquired using a 30-channel coil and MPRAGE sequence (voxel size = 1 mm isotropic, 208 slices, FOV = 256 × 256 × 208 mm, flip angle = 9°, TR = 2300 ms, TE = 2.86 ms, TI = 900 ms, bandwidth = 240 Hz/Px, echo spacing = 7.1 ms, acquisition time = 5 min 30 s).

4.1.7. Data analysis

Anatomical segmentation and cortical surface reconstruction were performed using FreeSurfer 7.1.1 (Dale et al., 1999). Functional data were pre-processed using AFNI 24.1.22, FreeSurfer, and FSL 6.0.7.12. Pre-processing steps were identical for both the contrast sensitivity and pRF mapping tasks.

First, B0 distortion correction was performed using a blip-up/blip-down method (AFNI's *unWarpEPI.py*). The first four volumes of each run were discarded using FSL's *fslroi*. An alignment scan was then selected based on the lowest number of voxel outliers (AFNI's *3dToutcount*, *3dTstat* and *3dcalc*) and co-registered to the MPRAGE image using FreeSurfer's *bbregister*, resulting in a rigid-body transformation matrix. In case of misregistration, the alignment scan was defined as one of the single-band reference scans, before re-running the co-registration step; persistent misalignment was corrected manually. Motion correction was finally applied by aligning all functional volumes to the alignment scan using AFNI's *3dvolreg*.

4.1.8. Population receptive field mapping and eccentricity correction in Benson maps

Population receptive field (pRF) mapping was performed in all patients using standard wedge-and-ring checkerboard stimuli (Dumoulin & Wandell, 2008). Stimuli were presented binocularly at 2 Hz flicker and full contrast, spanning a 42.3° circular aperture and scaled for cortical magnification. Each participant completed three runs of 352 volumes.

Due to frequent fixation instability in patients, we also applied a calibrated Benson retinotopic atlas (see Section 3.2.8.2) to generate fixation-independent eccentricity and polar angle maps. To improve eccentricity accuracy, especially in peripheral regions, we adjusted the atlas using a cortical magnification factor (CMF in mm/º) model from Horton & Hoyt (1991): $CMF = \frac{scale}{shape+E}$, where E is eccentricity, with default parameters shape = 0.75 and scale = 17.3 for a V1 surface area of 2500 mm^2. For each participant, an individualized scale parameter was estimated by integrating the CMF over their V1 surface area (0–90°). Eccentricity values were then refined by numerically solving the inverse CMF relationship (Equation 2) using a binary search algorithm, ensuring alignment between cortical surface area and visual field representation.

4.1.9. Qualitative comparison between cortical and behavioural visual field sensitivity.

Cortical measures of visual field sensitivity were obtained using the model-based approach as in Section 3.2.8. Briefly, for each cortical vertex, we fit a contrast response function of the form $R(C) = a * \sqrt{C}$, where C represents stimulus contrast and a reflect sensitivity of local neuronal populations. These fits were based on β-values from a general linear model applied to fMRI data across tested spatial frequencies. Steeper slopes (a) indicate higher cortical sensitivity.

Slope estimates were then projected into visual space using eccentricity and polar angle coordinates from the eccentricity-adjusted Benson atlas (Chow-Wing-Bom et al., 2025). The visual field was segmented into 8 x 8 grid, consisting of 6°×6° squares with the centre of each square spaced 6° from each other, mirroring the spatial layout used in perimetry. Unlike previous quadrant- or eccentricity-based analyses used in normal sighted controls (Chow-Wing-Bom et al., 2025), we opted for this grid pattern in patients because the visual defect in LHON is often heterogenous across the visual field, and averaging data in a more categorical way (i.e., eccentricity bins and quadrants) could smooth over more subtle changes in cortical sensitivity. We therefore opted for a more assumption free way of plotting.

The resulting cortical sensitivity maps were qualitatively compared to behavioural visual field data from Compass perimetry and the custom visual field test.

4.1.10. Quantitative comparison between cortical, behavioural and retinal measures.

We next quantified visual field loss using three modalities: cortical sensitivity (fMRI), behavioural sensitivity (Compass perimetry or custom test), and peripapillary RNFL thickness (OCT). All visual field maps registered to OCT sectors using the Garway-Heath map (Garway-Heath et al., 2000; Figure 23), which assigns each visual field location to one of six RNFL sectors: nasal-superior (NS), nasal (N), nasal-inferior (NI), temporal-superior (TS), temporal (T) and temporal-inferior (TI). NS/N/NI correspond to peripheral fields, while TS/T/TI represent central and paracentral (including foveal) regions.

For both cortical and behavioural visual field maps, data were clustered by sector. Compass thresholds were averaged (mean) per each sector, and cortical sensitivity (fMRI slope values), assigned to visual field locations via the adjusted Benson atlas, were summarised by the median slope per sector.

Finally, global sensitivity metrics were calculated by averaging across all six sectors, for both cortical and behavioural data, while global OCT pRNFL thickness was extracted from clinical OCT reports. These global metrics were used to assess the relationship between cortical, retinal, and behavioural measures.

To do this, we used linear mixed-effect models in R. For all participants, the association between OCT-derived pRFNL thickness and fMRI-derived cortical sensitivity was modelled as: $CorticalVF \sim OCTThickness * WhichEye * SF + (1 | SubjectID)$. Here, $WhichEye$ denotes the best versus worse eye, and SF refers to spatial frequency (high versus low). However, due to fixation instability, only five of the eleven patients had reliable Compass data. For these, the relationship between OCT pRNFL thickness and behavioural sensitivity was modelled as: $BehaviouralVF \sim OCTThickness + (1 | SubjectID)$. Additionally, we examined the correspondence between behavioural and cortical sensitivity in these five patients, using the model: $CorticalVF \sim BehaviouralVF * WhichEye * SF + (1 | SubjectID)$.

4.1.11. Reliability assessment of cortical visual field measures

To assess the reliability and individual specificity of our grid-based cortical visual field (VF) maps, we conducted correlation analyses across multiple dimensions using fMRI contrast sensitivity data from eleven LHON patients. Each cortical VF map

consisted of 64 values derived from 3×3° cortical squares, generated separately for each eye (best and worse) and spatial frequency (SF: low and high).

First, to evaluate the reliability of visual loss patterns, we correlated cortical VF maps for low and high SF stimuli, within each eye ("within-eye" analysis). In contrast, we assessed across-eyes consistency by correlating cortical VF maps for the best and worse eyes, within each unique SF condition ("across-eyes" analysis). As visual field defects are eye-specific, we expect cortical sensitivity patterns to be more consistent within eyes rather than between eyes and yield stronger correlations. This was tested at the group-level by comparing the obtained Pearson correlations using a paired t-test.

Second, to test whether the spatial pattern of cortical VF sensitivity (and loss) was more similar within individuals than across individuals, we performed a cross-subject permutation analysis (10,000 iterations). For each iteration, we computed the Person correlation between the low SF cortical sensitivity map of a given participant and the high SF cortical sensitivity map from a randomly selected participant (cross-subject, within-eye analysis). This was performed separately for the best and worst eyes, and averaged. Additionally, we assessed across-eye similarity by correlating the cortical sensitivity map from the best eye of one participant with the one from the worse eye of a randomly select participant, under the same SF condition (cross-subject, across-eye analysis). This made it possible to quantify the degree to which cortical visual field representations are individual-specific or shared across patients, and consistent across stimulus conditions.

4.2. Results

4.2.1. Quantification across modalities: Integrating information from cortical, behavioural and retinal measures

First, we investigate whether there was a relationship between measures of retinal integrity (OCT), visual field sensitivity (Compass), and cortical sensitivity (fMRI). In LHON, lower global OCT peripapillary retinal nerve fibre layer (pRFNL) thickness has been reported, resulting from RGC damage, and we expected this to correlate with reduced visual field sensitivity and fMRI cortical sensitivity. First, as outlined in Figure 23, we assessed sectoral relationships across modalities and spatial frequencies using the Garway-Heath layout (see Appendix 8.1 for figures). However,

this resulted in no significant sectoral associations across modalities: between cortical VF and OCT thickness (low SF: $F_{5,88} = 0.19, p = 0.966$; high SF: $F_{5,88.8} = 0.21, p = 0.958$), between behavioural VF and cortical VF (low SF: $F_{5,33.1} = 2.34, p = 0.063$; high SF: $F_{5,32.7} = 1.86, p = 0.128$), or between OCT thickness and behavioural VF ($F_{5,31.9} = 0.80, p = 0.557$).

We next compared global V1 cortical sensitivity to global OCT pRNFL thickness and global behavioural VF sensitivity. We found that a decrease in pRNFL thickness was significantly associated with a decrease in global V1 cortical sensitivity (Figure 26C), as indicated by a positive relationship between these measures ($\beta = 0.064$; $t_{29.8} = 2.859$; $p = 0.008$). There were no significant effects of eye and spatial frequency. Relationships between global pRNFL thickness and global behavioural VF sensitivity, and between global behavioural VF and global cortical VF sensitivities, were only performed in 5 patients (P001, P005, P009, P010, and P011), who met criteria for fixation stability and map quality with Compass perimetry (see methods; Figure 26B). As expected given the small samples, none of the relationships reached statistical significance (Behavioural VF versus OCT: $\beta = 0.546$; $t_{4.24} = 2.095$; $p = 0.100$; Figure 26A; Cortical versus behavioural VF: $\beta = 0.089; t_{7.87} = 1.199; p = 0.2653$; Figure 26B).

These findings highlight the interplay between retinal structure and cortical visual function in LHON pathology, but do not successfully solve the problem of localising visual field loss. It is possible that the retinal nerve fibre-based clustering of visual locations in the Garway-Heath approach offers a suboptimal model of LHON pathology, and other comparison approaches might be more suitable.

We therefore next proceeded to a qualitative comparison between behavioural and cortical visual field sensitivity measures, with the aim to explore various challenges with alignment of test modalities across the varying clinical profiles in LHON, to ultimately inform further approaches to evaluating accuracy.

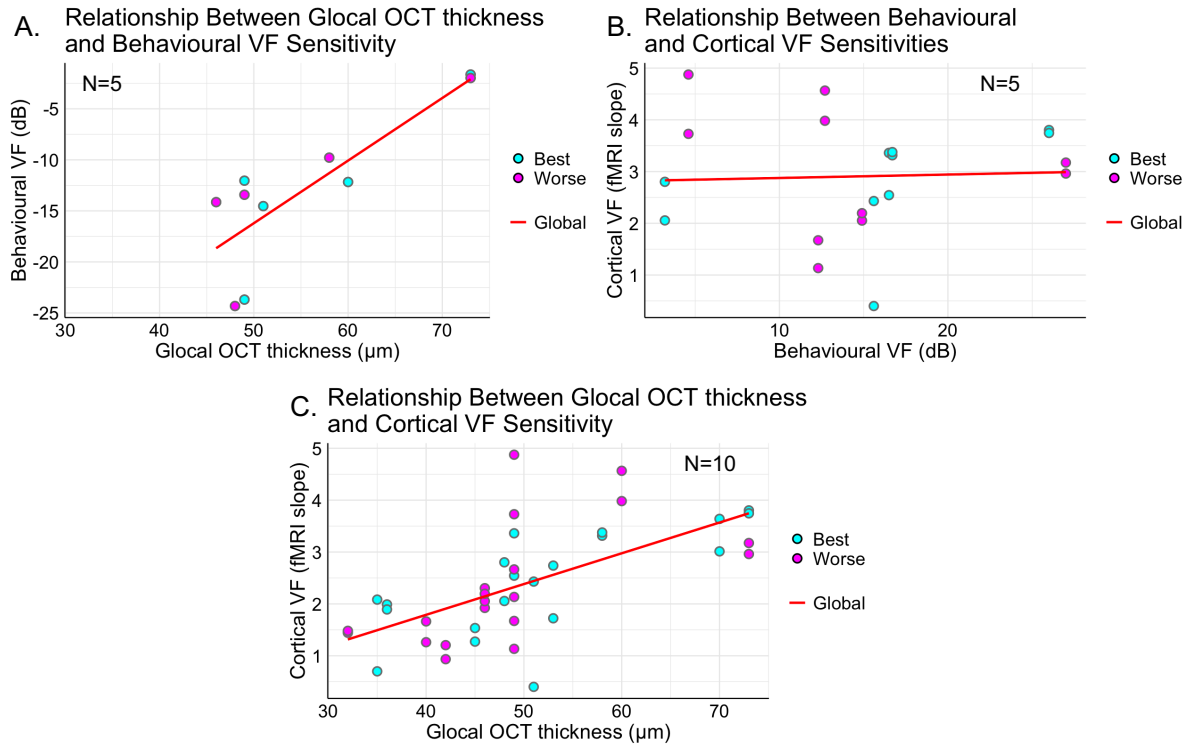

Figure 26. Relationships between global OCT peripapillary retinal nerve fibre layer (pRNFL) thickness, behavioural visual field (VF) sensitivity, and cortical VF sensitivity, in LHON patients.

(A) Positive trend between global OCT pRNFL thickness and behavioural VF sensitivity (N=5), with eye-specific data shown for better (blue) and worse (purple) eyes. (B) No significant relationship between behavioural and cortical VF sensitivity (N=5). (C) Significant positive association between global OCT pRNFL thickness and cortical VF sensitivity (N=10). Red lines indicate the linear regression fit, showing the overall trend between the two measures.

4.2.2. Visual field sensitivity: a qualitative assessment of cortical and behavioural correspondence

There are significant challenges in aligning behavioural and cortical visual field maps, as these can be distorted by many factors, including inaccurate mapping of cortical responses to visual field locations, differences in metrics (i.e., regarding norms, range, standardisation), differences in testing parameters (e.g., target size, tested contrasts), and measurement noise and bias, for example due poor fixation, head movement, and attention. We lack a trustworthy ground-truth, so the best solutions are not obvious.

To chart these challenges, and identify solutions, we next present behavioural and cortical visual field measures from 5 of the 11 patients. These highlight four

representative scenarios: (i) good fixation, good Compass test reliability indices, and good correspondence between visual sensitivity measures, (ii) good fixation, good Compass reliability, but less obvious correspondence between visual sensitivity measures, (iii) good fixation, good Compass reliability, but poor correspondence between visual sensitivity measures, and (iii) unreliable fixation. For each patient, we plot:

(A) Compass sensitivity thresholds (in dB) overlaid on fundus images, colour-coded by deviation from normative values (red: $p < 0.5\%$, orange–lime: 0.5%–5%, green: ≥5%, white: fovea/optic disc). Reliability is assessed via false positives (responses without stimulus), false negatives (missed responses to brighter repeated stimuli), and blind spot responses (reactions to stimuli at the blind spot). According to iCare guidelines, values exceeding 25% for any of these indices may indicate reduced test reliability. Additionally, an average pupil size below 3.0 mm is also considered a potential indicator of poor reliability.

(B) Fixation plot and area from Compass, showing eye movement amplitude over time, relative to the preferred retinal locus, and the 95th percentile ellipse of fixation points – larger areas indicate more dispersed fixation. Values within the green and yellow bound indicate acceptable fixation. As eye movements are tracked and compensated in real time during stimulus presentation, they do not necessarily compromise test reliability.

(C) Compass visual field sensitivity maps, where black indicates no sensitivity and increasing white pixels reflect higher sensitivity.

(D) Custom visual field maps, with black (invisible), grey (unsure), and white (clearly visible) points; target contrast levels are indicated per eye.

(E, F) Cortical contrast sensitivity maps for low (0.3cpd) and high (1 or 3cpd) spatial frequency gratings. Dark squares indicate low sensitivity (flat contrast response function slopes), bright squares indicate higher sensitivity (steep slopes).

Data from the remaining six patients are included in Appendix 8.1. For comparison, we plotted the average cortical visual field sensitivity maps from the same normally sighted participants described in Chapter 3, using the same grid layout applied to patient data (Figure 27). These control participants viewed the achromatic sinewave grating stimuli binocularly, under two spatial frequency conditions (0.3 cpd and 3 cpd).

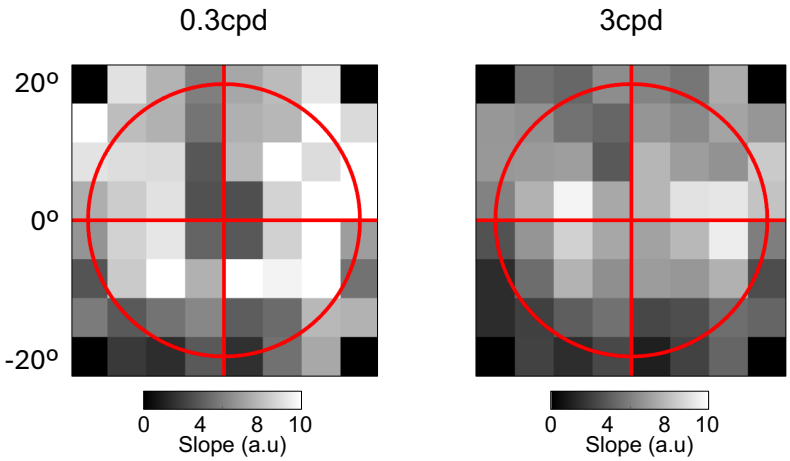

Figure 27. Average cortical visual field sensitivity in normally sighted controls (N=7). Data are from the same participants as in Chapter 3 but organised into the same grid pattern used in patients for reference. Participants view the stimuli binocularly. The calibrated Benson atlas was used to relate fMRI cortical responses to visual field locations. Left: fMRI-based V1 sensitivity maps for low spatial frequency (0.3 cpd). Right: fMRI-based V1 sensitivity maps for high spatial frequency (3 cpd). Dark squares indicate low cortical sensitivity (flat slopes); bright squares indicate higher sensitivity (steeper slopes).

4.2.2.1. Reliable central fixation with good correspondence between cortical and behavioural measures of visual field sensitivity.

We present data from two patients, P001 and P005 (Figure 28A-B and Figure 29A-B), who maintained stable central fixation but exhibited different mutations and visual field loss patterns.

Patient P001 (m.14484T>C, ~10.5 years post-onset) had better visual acuity in the left eye (-0.1 logMAR) than the right (0.3 logMAR). Compass perimetry showed large central scotomas with preserved peripheral sensitivity (Figure 28C), which were also captured – though likely less precisely – by the custom visual field test (Figure 28D). Discrepancies between these two tests may be due to differences in test parameters, notably target size (Compass: ~0.43º; Custom test: 2º) and the fact that each location was only tested once at a fixed, single contrast level in the custom test (left eye: 15%, right eye: 20%). Importantly, fMRI-based V1 sensitivity maps aligned well with behavioural data, showing reduced cortical sensitivity in central regions and preserved peripheral responses (Figure 28E-F). Notably, cortical maps captured quadrant-specific deficits, and sensitivity was lower for high spatial frequencies.

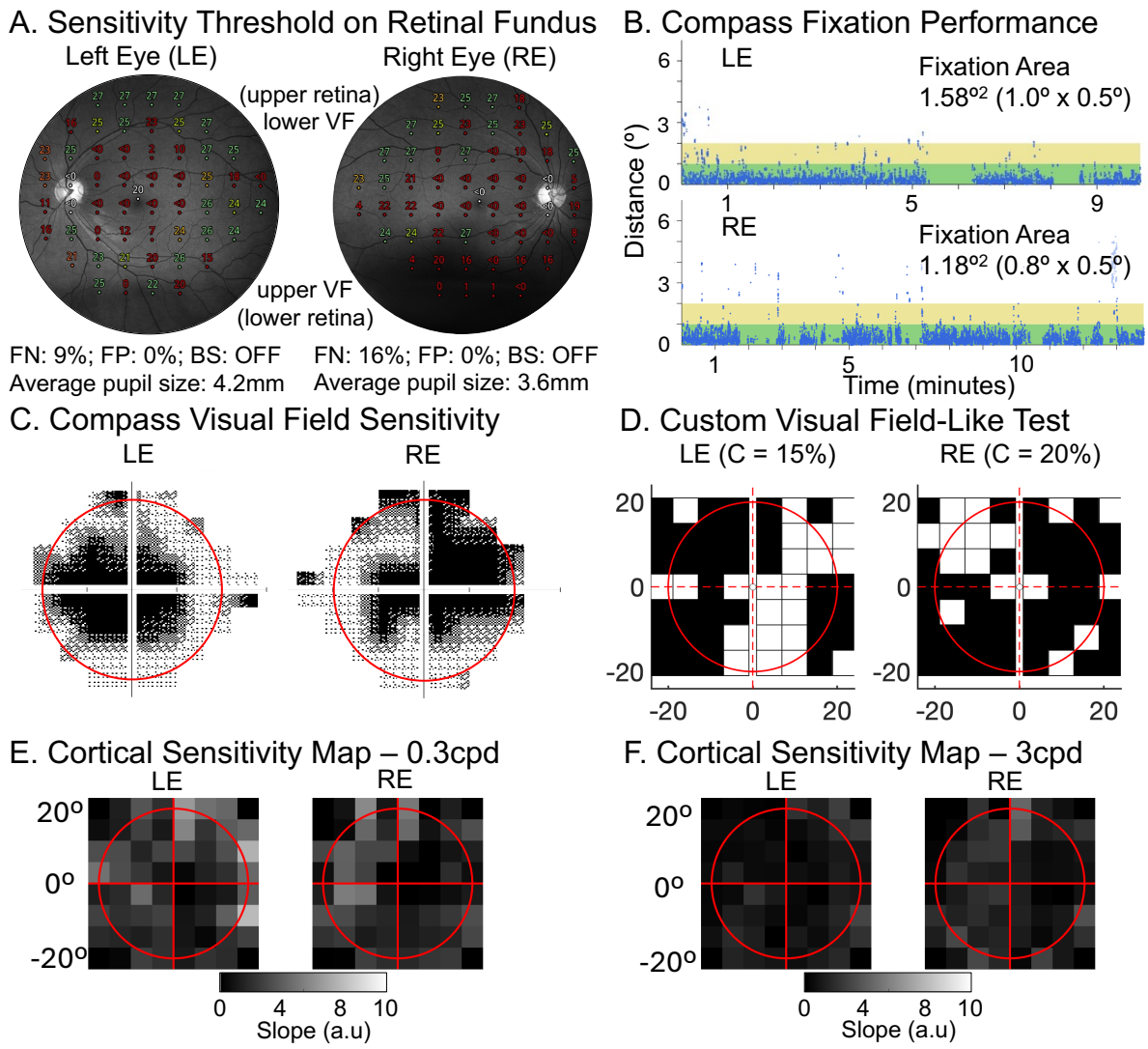

Figure 28. Case of P001: Good fixation, Compass reliability, and correspondence between visual field sensitivity measures.

(A) Compass sensitivity thresholds overlaid on the fundus image. Colours reflect normative total deviation: green (p ≥ 5%), orange (p < 5% and ≥ 0.5%), red (p < 0.5%), with white marking the fovea and optic disc. (B) Eye-tracking traces; values within the green/yellow bound indicate acceptable fixation stability. (C) Compass perimetry maps: black indicates no measurable sensitivity; increasing white pixels within each 3×3° grid point reflect higher sensitivity. (D) Custom visual field test: black = target not seen, grey = unsure, white = clearly seen. Target contrast per eye is shown in brackets. (E-F) fMRI-based V1 sensitivity maps for low (0.3 cpd) and high (3 cpd) spatial frequencies. Dark squares indicate low cortical sensitivity (flat slopes); bright squares indicate higher sensitivity (steeper slopes).

Patient P005 (m.11778G>A mutation, ~35.5 years post-onset) showed better acuity in the left eye (0.8 logMAR) than the right (1.5 logMAR). Compass perimetry revealed scotomas primarily in the upper-left and lower-left quadrants of the left eye,

and in the upper-right quadrant of the right eye (Figure 29C). These patterns were also evident in the custom visual field test (fixed at 25% contrasts for both eyes; Figure 29D). fMRI-based V1 sensitivity was reduced in the same affected quadrants (Figure 29E-F), though the correspondence between behaviour and cortex, is less apparent on visual inspection than in the previous patient. The difference in cortical sensitivity between the low and high SF grating was larger for P001 than P005, likely because the tested high-frequency stimulus was within P005's visibility range (0.3cpd vs. 1cpd for P005; 0.3cpd vs. 3cpd for P001).

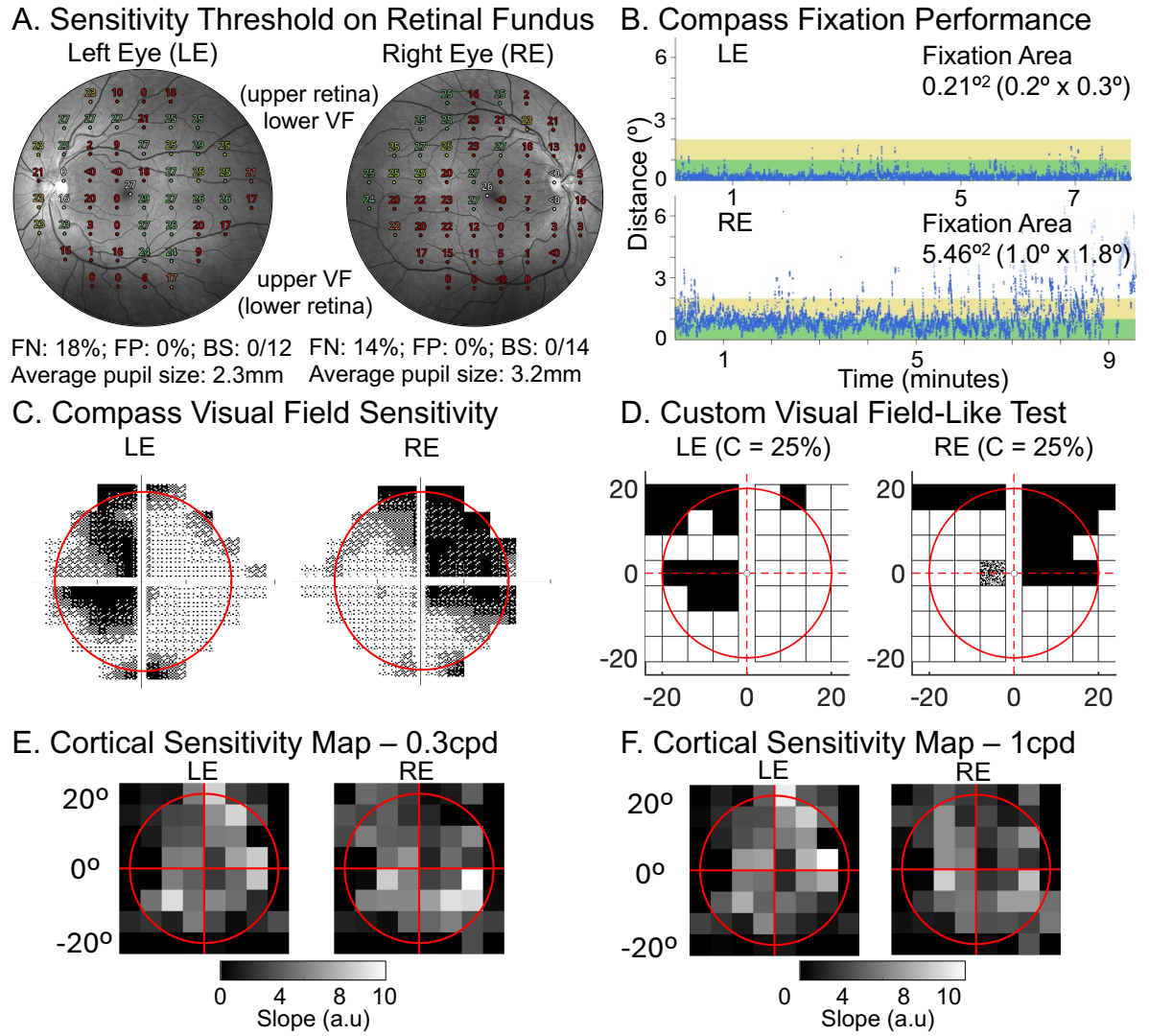

Figure 29. Case of P005: Good fixation, Compass reliability, and correspondence between visual field perimetry measures.

(A) Compass sensitivity thresholds overlaid on the fundus image. Colours reflect normative total deviation: green (p ≥ 5%), orange (p < 5% and ≥ 0.5%), red (p < 0.5%), with white marking the fovea and optic disc. (B) Eye-tracking traces; values within the green/yellow bound indicate acceptable fixation stability. (C) Compass perimetry maps: black indicates no measurable

sensitivity; increasing white pixels within each 3×3° grid point reflect higher sensitivity. (D) Custom visual field test: black = target not seen, grey = unsure, white = clearly seen. Target contrast per eye is shown in brackets. (E-F) fMRI-based V1 sensitivity maps for low (0.3 cpd) and high (1 cpd) spatial frequencies. Dark squares indicate low cortical sensitivity (flat slopes); bright squares indicate higher sensitivity (steeper slopes).

4.2.2.2. Reliable fixation but less obvious correspondence between cortical and behavioural measures of visual field sensitivity

Patient P009 (m.11778G>A mutation, ~44.7 years post-onset) had better visual acuity in the left eye (1.3 logMAR) than the right (1.5 logMAR). Compass perimetry showed widespread scotomas in both eyes, with some preserved sensitivity in the upper-right quadrant of the left eye and upper-left quadrant of the right eye (Figure 30C). These patterns were partially reflected in the custom test (fixed 50% contrast for both eyes, Figure 30D). For the left eye, aligning with Compass measures, fMRI-based V1 maps showed reduced cortical sensitivity in the left hemifield of the left eye, especially at higher spatial frequencies (Figure 30E-F), although the preserved upper-right quadrant was not well captured. For the right eye, cortical maps partially aligned with Compass results – showing reduced sensitivity in the upper-right quadrant and increased sensitivity in the upper-left – but could not clearly distinguish the large scotoma in the right, lower visual field. It seems that the cortical maps for the right eye more closely resembled the custom test results than those from the Compass (the number of false negatives exceeds quality thresholds for the right eye).

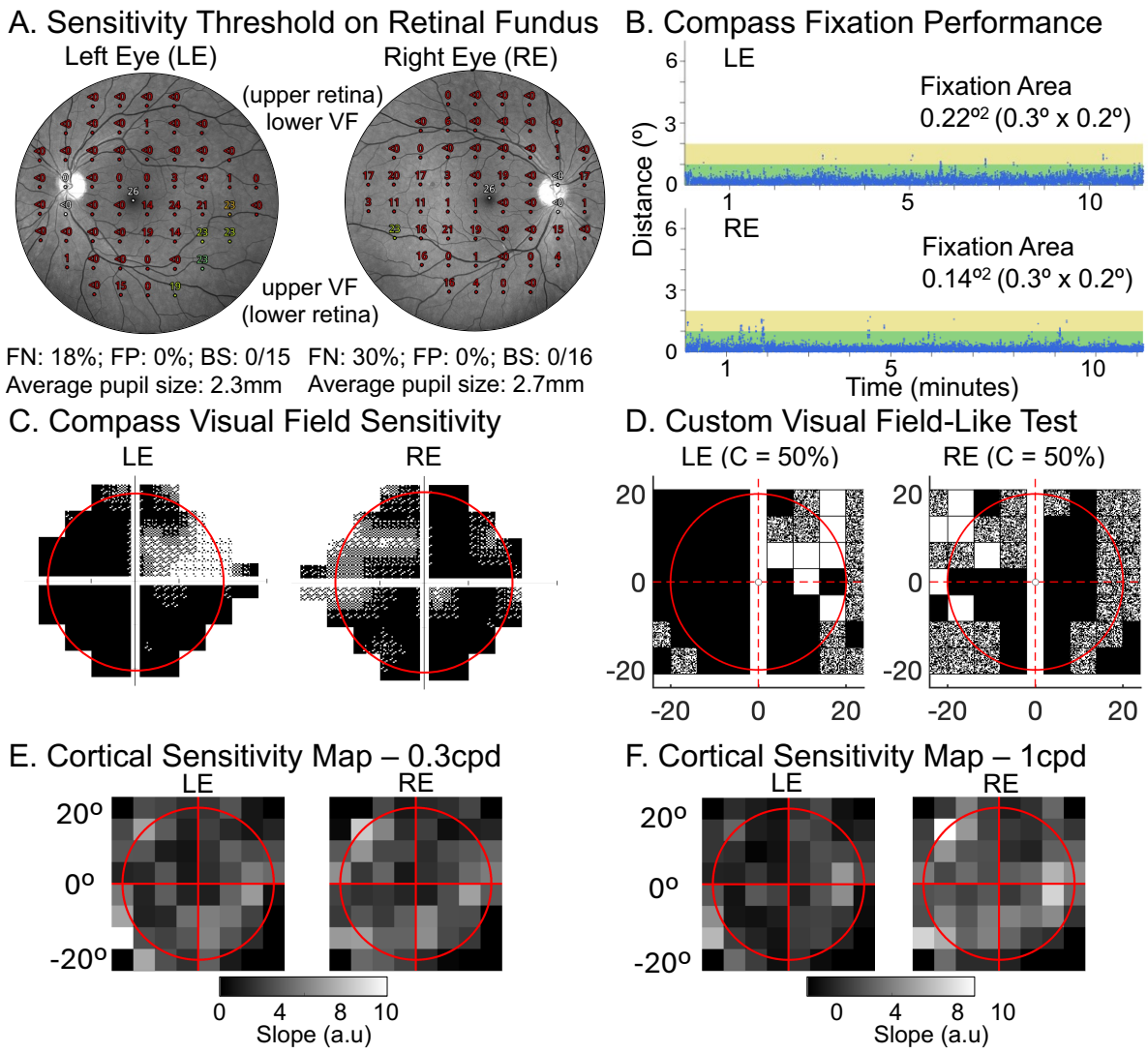

Figure 30. Case of P009: Good fixation, Compass reliability (at least for left eye), but less obvious correspondence between visual field sensitivity measures.

(A) Compass sensitivity thresholds overlaid on the fundus image. Colours reflect normative total deviation: green ($p \geq 5\%$), orange ($p < 5\%$ and $\geq 0.5\%$), red ($p < 0.5\%$), with white marking the fovea and optic disc. (B) Eye-tracking traces; values within the green/yellow bound indicate acceptable fixation stability. (C) Compass perimetry maps: black indicates no measurable sensitivity; increasing white pixels within each 3×3° grid point reflect higher sensitivity. (D) Custom visual field test: black = target not seen, grey = unsure, white = clearly seen. Target contrast per eye is shown in brackets. (E-F) fMRI-based V1 sensitivity maps for low (0.3 cpd) and high (1 cpd) spatial frequencies. Dark squares indicate low cortical sensitivity (flat slopes); bright squares indicate higher sensitivity (steeper slopes).

4.2.2.3. Reliable fixation but poor correspondence between cortical and behavioural measures of visual field sensitivity

Patient P011 (m.14484T>C mutation, ~9.4 years post-onset) had relatively high acuity, which was better in the right eye (0.1 logMAR) than the left (0.5 logMAR). Compass perimetry showed largely preserved sensitivity in both eyes, with only a mildly enlarged scotoma bilaterally and a small central scotoma in the right eye (Figure 31C). This was consistent with the custom visual field test (fixed 15% contrast for both eyes; Figure 31D). In stark contrast, fMRI revealed widespread reductions in V1 cortical sensitivity when compared to sighted control data, particularly in regions representing the central and lower visual fields (Figure 31E-F).

What can explain this unexpected discrepancy? This patient shows clear, pathologically reduced peripapillary RNFL thickness in the temporal (TS, T, and TI) sectors, which correspond to central visual field projections (Figure 32). It is therefore possible that the observed reduction in cortical function reflects subclinical retinal damage not fully captured by perimetry, potentially compensated by other brain regions. It is also possible that the fMRI data are poor or noisy, however, all markers of data quality are good, and consistent cortical VF loss patterns across independently measured spatial frequencies suggests otherwise. This highlights that behavioural and cortical visual field loss measures may in part be discrepant because they capture different, complementary aspects of pathology.

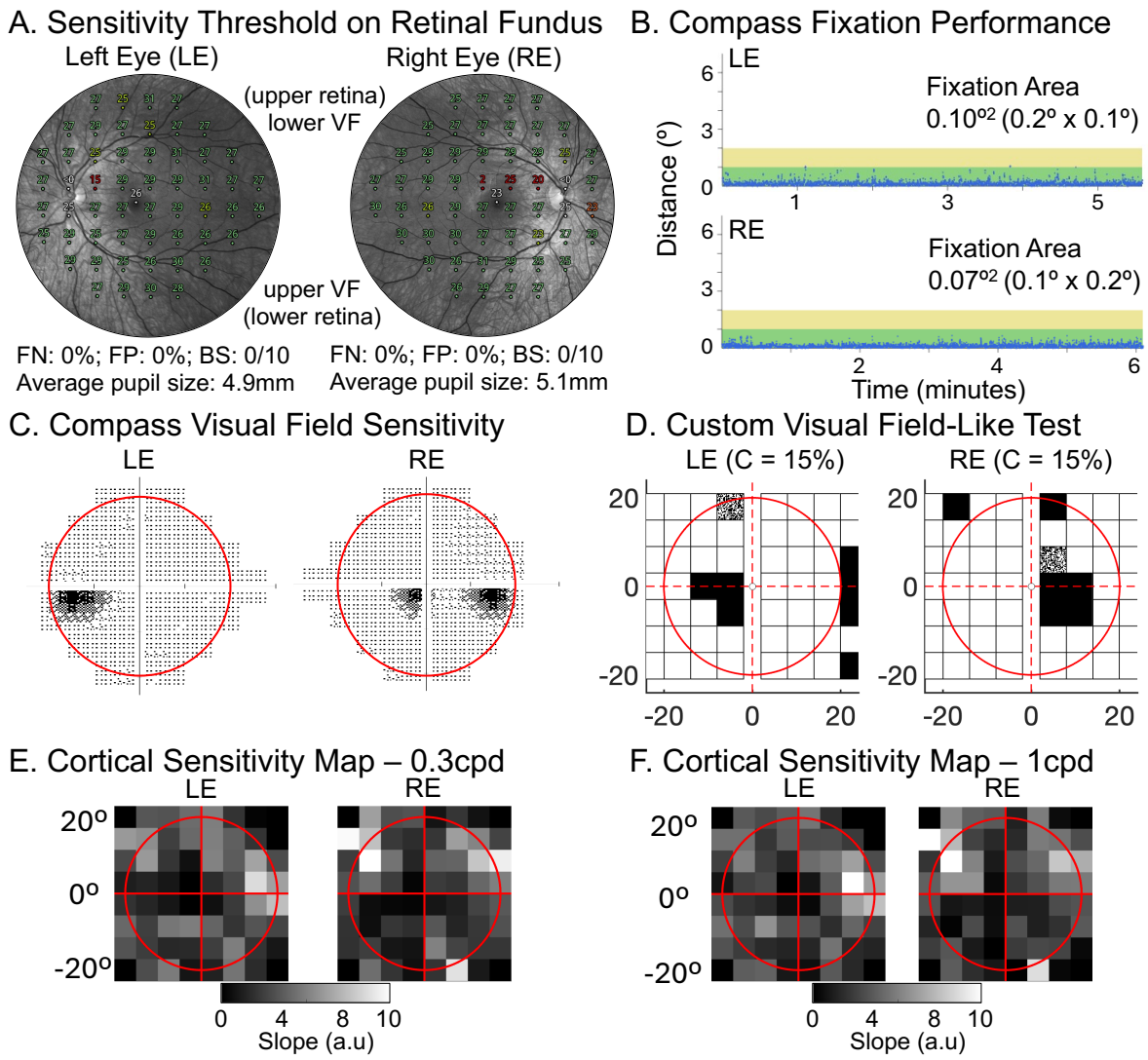

Figure 31. Case of P011: Good fixation and Compass test reliability, but poor correspondence between visual field sensitivity measures.

(A) Compass sensitivity thresholds overlaid on the fundus image. Colours reflect normative total deviation: green ($p \geq 5\%$), orange ($p < 5\%$ and $\geq 0.5\%$), red ($p < 0.5\%$), with white marking the fovea and optic disc. (B) Eye-tracking traces; values within the green/yellow bound indicate acceptable fixation stability. (C) Compass perimetry maps: black indicates no measurable sensitivity; increasing white pixels within each 3×3° grid point reflect higher sensitivity. (D) Custom visual field test: black = target not seen, grey = unsure, white = clearly seen. Target contrast per eye is shown in brackets. (E-F) fMRI-based V1 sensitivity maps for low (0.3 cpd) and high (1 cpd) spatial frequencies. Dark squares indicate low cortical sensitivity (flat slopes); bright squares indicate higher sensitivity (steeper slopes).

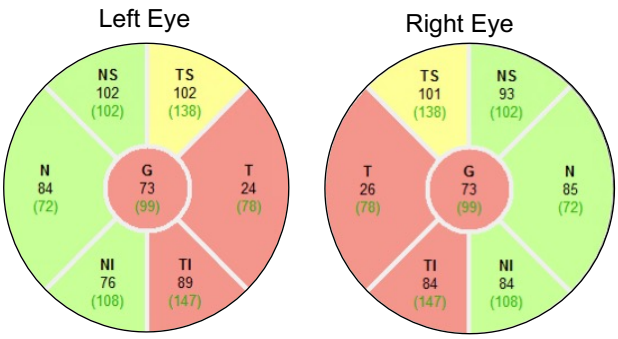

Figure 32. Case of P011: OCT peripapillary retinal nerve fibre layer (pRNFL) thickness. Sectoral pRNFL thickness maps for the left and right eyes. Each circular diagram is divided into six regions (NS, TS, N, T, NI, TI) with corresponding thickness values in micrometres. The central "G" value represents the global OCT pRNFL thickness. Colour coding reflects sectoral thickness relative to normative values: green = within normal limits, yellow = borderline thinning, and red = significant thinning.

4.2.2.4. Unreliable fixation

Patient P006 (m.11778G>A mutation) was in the chronic phase (~1.9 years post-onset). Visual acuity was better in the left eye (1.3logMAR) than the right eye (1.8logMAR), based on their medical records. We observed reduced cortical sensitivity (smaller slope values) in left hemifield for the left eye and right hemifield in the right eye. At first glance VF sensitivity and cortical sensitivity seem to correspond well (Figure 33C, E, F). However, the Compass fundus image reveals a spatial misalignment issue: the foveal and blind spot targets (indicated by white dots on the fundus image) were substantially misaligned with the fovea and physiological blind spot (Figure 33A, C). Instead, the fMRI-based cortical maps are inherently centred on the fovea. Consequently, the behavioural and fMRI-derived measures were not sampling matching retinal locations, and the visual field map needs to be shifted for accurate comparison.

This highlights the critical importance of quantifying and correcting for extrafoveal fixation biases in behavioural VF measures, for accurate and sensitive comparison over time (as fixation strategies may change).

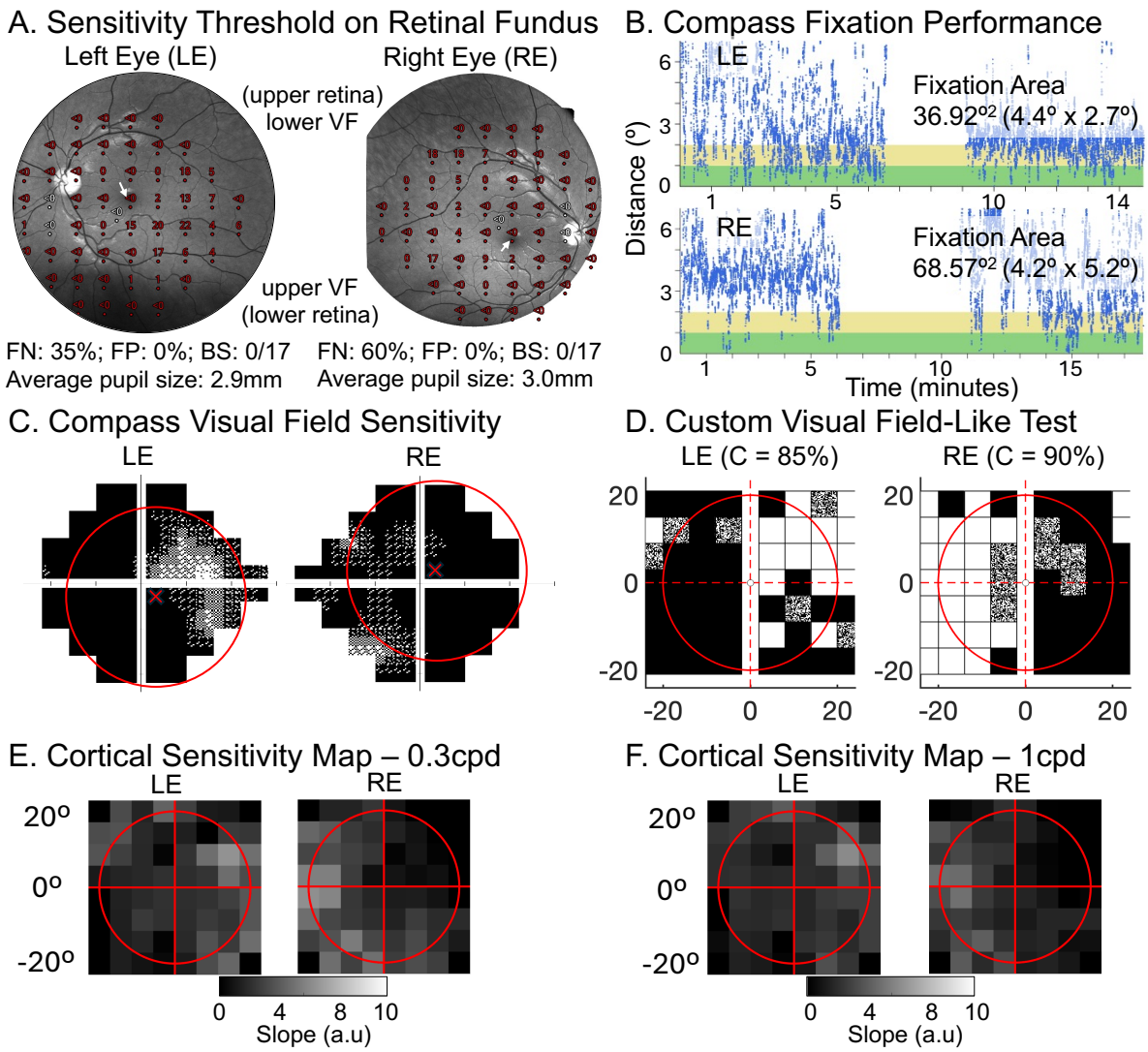

Figure 33. Case of P006: Unreliable fixation.

(A) Compass sensitivity thresholds overlaid on the fundus image. Colours reflect normative total deviation: green (p ≥ 5%), orange (p < 5% and ≥ 0.5%), red (p < 0.5%), with white marking the tested foveal and optic disc locations. The true fovea (white arrow) and blind spot were misaligned with tested points. (B) Eye-tracking traces; values within the green/yellow bound indicate acceptable fixation stability. (C) Compass perimetry maps: black indicates no measurable sensitivity; increasing white pixels within each 3×3° grid point reflect higher sensitivity. Red crosses mark the corrected map centre (fovea-aligned); red circles show the 20º fMRI-tested region (D) Custom visual field test: black = target not seen, grey = unsure, white = clearly seen. Target contrast per eye is shown in brackets. (E-F) fMRI-based V1 sensitivity maps for low (0.3 cpd) and high (1 cpd) spatial frequencies. Dark squares indicate low cortical sensitivity (flat slopes); bright squares indicate higher sensitivity (steeper slopes).

4.2.3. Reliability and robustness of the cortical visual field mapping approach

The previous section revealed some of the challenges of aligning cortical visual field sensitivity with behavioural visual field measures and structural retinal dystrophy in LHON. However, while precise spatial localisation of visual field loss is valuable, consistency in capturing functional changes across the full affected visual field is more critical for clinical applications, such as gene therapy trials. Here, we therefore evaluate the repeatability of our fMRI-based cortical mapping approach. It was beyond the scope of this PhD work to collect repeated measurements at different timepoints (this follow-up is planned), but we can still get some insight into repeatability. This is because our dataset included two independent estimates of cortical sensitivity per eye – one using low spatial frequency stimuli and one using high spatial frequency stimuli. This makes it possible to assess repeatability of patterns of cortical visual field loss and evaluate their robustness across stimulus types.

Thus, to assess the repeatability of visual field loss patterns, we correlated the cortical sensitivity maps for one eye (best or worse) across low and high spatial frequencies (within-eyes analysis; see Figure 34A for scatter plot of slope patterns, and blue violin plot in Figure 34C for correlation distributions). For comparison, we also correlated the two maps we obtained for the same spatial frequency stimulus – one for the best and one for the worst eye (**across-eyes** analysis; see Figure 34B for scatter plot of slope patterns, and pink violin plot in Figure 34C for correlation distributions). We found that correlations were significantly higher within eyes (mean r = 0.80; range: 0.53-0.93) than across eyes (mean r = 0.39; range: -0.21-0.69; $p = 0.00065$; Figure 34C), suggesting that we mapped the visual field consistently, despite using different spatial frequencies. Importantly, however, it should be noted that this comparison is confounded – since the within-eyes comparison involves data collected within the same run, and the across-eyes comparison involves data collected in separate runs, which also leads to lower correlations. So, while more work is needed, the high correlation of visual field loss patterns across separate measures, shows promise. These findings suggest that eye-specific visual field loss affects spatial patterns across both SF conditions, while asymmetries in visual field loss across eyes may reduce the repeatability of spatial frequency dependent patterns (shown in sighted controls in Chapter 3, Section 3.3.3; Figure 20; Chow-Wing-Bom et al., 2025) across the two eyes of these patients.

To further evaluate the robustness in capturing subject-specific visual field loss patterns, we also performed a cross-subject permutation analysis (10,000 iterations), comparing cortical visual field maps across participants. Specifically, we correlated the slope values from the low spatial frequency (SF) cortical sensitivity map of each participant with the high SF map from a randomly selected different participant. This was done for both the best and worse eyes (**cross-subject within-eyes**; blue histogram in Figure 34D). We also correlated slope values from the best eye with those from the worse eye, using maps from different participants but within the same spatial frequency condition (**cross-subject across-eyes**; pink histogram in Figure 34D). We found that the true mean correlation within eyes (r = 0.80) significantly exceeded the 95th percentile of the shuffled distribution (0.29), suggesting that the spatial pattern of cortical visual field maps is reliably preserved across spatial frequencies within individuals. Similarly, the true mean correlation across eyes (r = 0.39) was also significantly above the shuffled threshold (0.23), suggesting that spatial frequency tuning is at least partially preserved across eyes, despite potential interocular asymmetries in visual field defects.

Together, these results suggest that our fMRI-based cortical visual field mapping approach is both reliable and robust, even in a visually impaired clinical population such as in LHON – although cross-session testing is needed to confirm this. This supports the potential of fMRI and our brain-based approach as sensitive and stable outcome measures for monitoring visual function and evaluating therapeutic efficacy in LHON and related conditions.

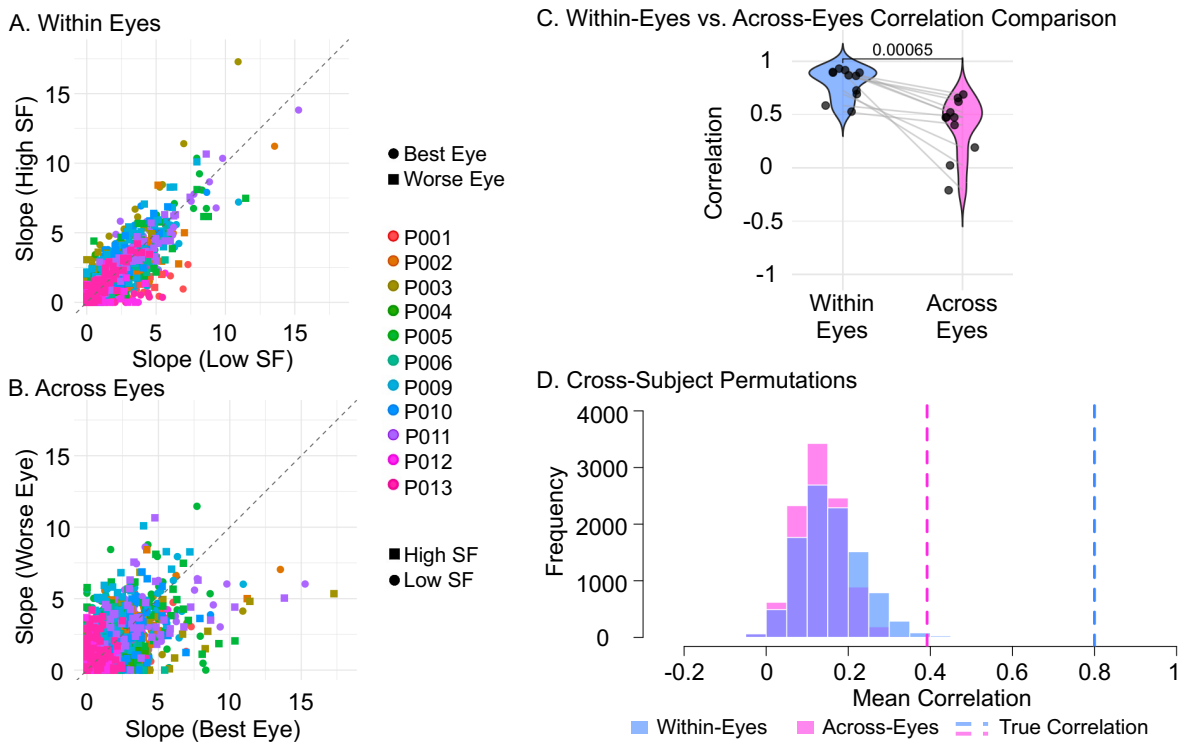

Figure 34. Reliability of cortical visual field sensitivity representations in LHON.
(A) Within-eyes reliability: scatter plot comparing slope values at low versus high spatial frequencies for each eye. Circles represent the best eye; squares represent the worse eye. (B) Across-eyes reliability: scatter plot comparing slope values between the best and worse eye for each spatial frequency. Circles represent low SF; squares represent high SF. (C) Violin plot comparing correlation coefficients within eyes and across eyes. Each dot represents an individual participant; lines connect data from the same participant. (D) Histogram of cross-subject permutation results. Blue and pink bars represent the distributions of shuffled correlations for within-eyes and across-eyes comparisons, respectively. Dashed lines indicate the true mean correlations, computed across all participants.

4.3. Discussion

We used fMRI-based contrast sensitivity mapping to obtain a fixation free measure of visual field loss. Given the challenges of using behavioural visual field measures to establish ground-truth of visual field loss, we used the Garway-Heath based approach to link the OCT to visual field measures. We also performed qualitative comparisons of behavioural visual field tests (the Compass) and our novel cortical visual field measures. We obtained mixed evidence for accuracy – OCT and cortical measures only globally correlated, independent of visual field location, and while in qualitative comparisons, some patients showed visible correspondence in field

loss across brain and behaviour, some correspondences were less clearly visible, and others clearly did not. Beyond mapping accuracy, the ability to sensitively detect changes in visual field representations is critical for tracking disease progression and evaluating therapeutic efficacy - even if the field map is distorted so the exact retinal locus of functional change is unclear. Our fMRI-based approach may offer reliable measures of visual field loss even if accuracy is hard to assess. While we were not (yet) able to collect test-retest measures in different sessions, which is critical to drawing ultimate conclusions, preliminary analyses are promising: we found high correlations between cortical visual field maps obtained with the same eye, despite using grating stimuli with different spatial frequencies. In contrast, we found lower across-eyes correlations when using the same stimulus, a comparison which in typical controls led to highly repeatable maps in Chapter 3. This potentially means that our test is sensitive to interocular asymmetries in visual field loss in these patients and can detect these reliably across different grating stimuli – although these correlation patterns were confounded with within vs across run testing so unconfounded (cross-session) repeated measurement will be necessary to confirm this interpretation.

The fact that cross-measurement modality associations between retinal structure (OCT), behavioural VF sensitivity, and cortical sensitivity were inconsistent, highlights the significant challenge of accurately measuring visual fields in people with very low central vision as in LHON, and relating these measures to each other. While we found a positive association between global OCT thickness and global cortical VF sensitivity, we found no correlations between retinal dystrophy of retinal nerve fibre bundles linked to specific visual field locations and visual field loss in these locations. These discrepancies likely reflect limited sample size and methodological differences across modalities. For instance, global OCT thickness represents fibres extending across the retina, while our fMRI and behavioural measures are constrained to a defined visual field region (up to mid-periphery), limiting direct anatomical correspondence. Future work will examine improving sensitivity for detecting cross-modality correspondences using the Garway-Heath sector approach, using deviations from the norm rather than absolute measures of OCT thickness, and cortical and behavioural visual field sensitivities (Garway-Heath et al., 2000; Figure 23).

The mixed behavioural-cortical visual field measure correspondence, with some patients showing good correspondence while others did not, may primarily be

constrained by the need for stable fixation during behavioural visual field testing (one of the key problems targeted by this study). In contrast, our fMRI approach could offer a promising alternative for assessing visual field defects in patients without the need of stable fixation, by combining fMRI with a fixation-free retinotopic template (e.g., Benson atlas). However, this method is a work in progress and there are several challenges that may limit the accuracy and reliability of cortical visual field measure in these patients, which we aim to improve on in future work. These include:

(i) Improving accuracy of the Benson atlas that links cortical regions to visual field locations: The retinotopic maps obtained with the Benson atlas become inaccurate in the periphery. While we have implemented adjustments to improve this, these adjustments remain imperfect. To further improve accuracy, we will test further adjustments (e.g., sheering of the atlas to match control data, Bayesian updating of estimates with patient pRF maps, alternative retinotopic models such as the Deep Retinotopy Toolbox; Ribeiro et al., 2021).

(ii) Improving test-reliability in the Compass perimeter: Despite being able to use fundus tracking to perform online correction of eye movements for stimulus presentation, fixation demands remain a challenge with the Compass perimeter in LHON. Unlike in the MAIA perimeter, Compass lacks eccentric fixation targets, which could benefit this population. Unfortunately, the MAIA perimeter is not adequate for testing visual field defects in LHON patients, as it only tests central vision up to 10º eccentricity falling short of the field loss extent in this disease. Future work will involve exploring different test grids and strategies to help improve test reliability using Compass.

(iii) Understanding the impact of eye motion on cortical visual field loss patterns: While in principle eye movements should minimally affect our cortical VF sensitivity measure, we have not tested this directly. It is likely that it will have some effect - eye movements can “smear” spatial information, and leave some peripheral retina temporarily unstimulated, potentially depressing sensitivity – but the degree of impact is unclear. Preliminary data from a control participant (simulating up to 2º eye movements; Appendix 7.4) suggest minimal disruption, but we are planning a follow-up of this work to test the impact of eye motion in a larger sample and using more extreme degrees of eye motion.

(iv) Optimising the contrast response model: Our current contrast response model ($R(C) = a * \sqrt{C}$) was developed in controls but may not fully capture altered contrast processing in LHON. As a next step, we plan to compare fits with modified model parameters by adjusting the exponent value (currently set to 0.5 to model a square root function) and more complex models. Another future direction is comparing our approach to the neural contrast sensitivity function (nCSF) approach developed by Roelofzen et al. (2025). This method is interesting as it could offer additional information (sensitivity and acuity), but we need to explore whether measures will be reliable for sessions and stimulus ranges feasible with this population.

In summary, our findings highlight fMRI-based cortical mapping as a potentially reliable and sensitive tool for assessing visual function in LHON, although more work is needed to improve our measures and analyses. Despite substantial challenges, this approach holds promise for tracking disease progression and evaluating therapeutic outcomes, and could be particularly worthwhile in cases where behavioural measures are limited or unreliable but clinical utility is high. This opens new avenues for studying visual processing after acquired visual loss and during recovery – either spontaneous or following gene therapy. It may offer a complementary and potentially more sensitive endpoint measure of functional rescue across the visual field in LHON. More broadly, it may offer a valuable tool for studying cortical neuroplasticity by more precisely characterising sensitivity loss in input-deprived neuron populations in patients with severe vision loss, to characterise their structural and network changes, and assessing their capacity for functional recovery after sight rescue intervention.

5. General Discussion

In this PhD I aimed to explore how Leber Hereditary Optic Neuropathy (LHON) affects the brain and to develop novel imaging tools capable of capturing structural and functional changes across the visual pathways and visual field. In doing so, I hoped to bridge clinical neuro-ophthalmology and advanced neuroimaging, offer new insights into disease mechanisms, and lay the foundation for more objective, patient-tailored assessments of visual function. This is particularly relevant with the emergence of gene therapies for LHON.

By disentangling demyelination from axonal loss along the visual pathways using novel quantitative MRI and diffusion imaging modelling approaches, I identified distinct patterns of degeneration that may inform prognosis and therapeutic targeting. The development of a fixation-independent fMRI method could further address a critical gap, by offering a sensitive outcome measure for studying vision loss and recovery in diseases with severe central field loss where this is presently challenging. This work demonstrates how advanced MRI techniques can go beyond traditional diagnostics and could offer new useful insights into the mechanisms of vision loss.

5.1. Summary of thesis findings

In **Chapter 1**, we reviewed the existing literature on LHON MRI research up to 2021, identifying the following questions as key gaps in existing knowledge:

- Which changes in neural function and structure occur beyond the retinal ganglion cell layer in LHON, and when do they occur in time, i.e., when in the disease do changes in post-retinal brain structures from optic nerve to visually driven cortex occur?
- What are the mechanistic causes of these neural changes in LHON, and which microstructural processes might they reflect, i.e., demyelination and axonal loss?
- How do changes in neural structure and function predict visual outcome?

We then addressed these questions in three empirical chapters:

In **Chapter 2**, we investigated post-retinal degeneration using novel MRI methods that combined diffusion imaging, multi-parametric mapping (MPM), and

biophysical modelling of tissue microstructure. This made it possible to disentangle axonal loss from demyelination along the visual pathways, such as:

- In the optic tracts, both axonal loss and demyelination occurred alongside significant volume reduction.
- In the optic radiations, axonal degeneration extended from LGN to V1, while demyelination was localised near V1, without volume loss.
- In the LGN and V1, we observed volume reduction and cortical thinning, particularly in regions representing central (3-15º) vision.

These findings provide *in vivo* evidence of distinct neurodegenerative processes in LHON and offer a potential tool for tracking disease progression and evaluating treatment response.

In **Chapters 3 and 4**, we aimed to address the lack of fixation-independent functional measures in LHON, which is complicating our ability to reliably assess functional loss across the visual field. In **Chapter 3**, we developed an fMRI-based method that combines large-field contrast sensitivity mapping with a structure-based retinotopic atlas. In healthy controls, this approach:

- Produced reliable and reproducible cortical sensitivity maps across eccentricities and quadrants.
- Showed good correspondence with fixation-based mapping approaches (i.e., using individual pRF mapping to link cortical sensitivity to visual field locations rather than the structure-based atlas).
- Showed potential for detecting both simulated and disease-related visual field deficits in a normally sighted control and a single LHON case, respectively.

In **Chapter 4**, we then applied this method to a larger sample of LHON patients to assess its clinical utility. The results showed:

- That our approach of using retinal structure (OCT)-based measures of visual field loss to assess the accuracy of our novel cortex based visual field test in LHON had limited success. We only found a positive association between RNFL thickness and cortical sensitivity.
- Partial correspondence between fMRI-derived and behavioural visual field maps, highlighting challenges in cross-modal alignment.
- Repeatability of cortical sensitivity patterns of visual field loss across different stimulus types, supporting the potential of our fMRI approach for longitudinal

monitoring – although more data is needed to exclude contributions of design-related confounds to this repeatability measure.

Together, these studies demonstrate that we can use advanced structural and functional imaging to characterise the neural impact of LHON and develop clinically relevant tools for assessing visual function. Particularly in contexts where traditional methods are limited by poor fixation or low vision, this could offer improvements. The structural and functional findings in this thesis may be closely linked, and this raises many interesting avenues for future research. The work highlights that sight loss in LHON reflects an interplay between retinal ganglion cell death leading to dystrophy and disorganisation along a cascade of neural pathways and processes well beyond the retinal ganglion cell layer. The functional impacts of these processes and their amenability to recovery are key next steps to study.

5.2. Future Directions: MRI Advances and Their Implications for Clinical Trials

This thesis offers new tools for understanding the biological mechanisms of vision loss in LHON and for developing objective, reliable outcome measures of vision loss. This is particularly important as gene therapies move from experimental to clinical use.

In **Chapter 2**, we show that advanced structural MRI can go beyond detecting damage: it can help explain how that damage happens. By combining diffusion imaging, multi-parametric mapping, and computational modelling of tissue microstructure, we were able to distinguish between demyelination and axonal loss along the visual pathways. This distinction is crucial – not just for the research community, but also for clinicians and pharmaceutical companies developing gene therapies – as it may reveal which types of neural damage are reversible and therefore targetable by future gene therapies aiming to maximise functional benefit. For example, in the optic tracts, we found both demyelination and axonal loss, likely reflecting direct degeneration from retinal ganglion cell (RGC) loss. In contrast, the optic radiations showed widespread axonal disruption but demyelination only near V1, suggesting a more complex, possibly activity-dependent process. If vision can recover – either spontaneously or following gene therapy – remyelination may play a key role. This could be triggered by renewed cortical activity and/or repaired glia cells

associated with RGCs, such as oligodendrocytes and astrocytes. Oligodendrocytes are essential for maintaining the integrity of myelin sheaths that insulate axons and are likely indirectly impacted by the RGC degeneration in LHON (Carelli et al., 2004; Pan et al., 2012; Karaarslan, 2019; Panfoli & Ravera, 2025), leading to slower nerve conduction and neuronal death. However, whether gene therapy for LHON, which acts on mitochondrial DNA, can restore the health or function of these glia cells remains unclear (Panfoli & Ravera, 2025). Using our imaging methods to investigate potential *in vivo* remyelination along the visual pathways could help inform this further. Axonal regeneration, while less likely, remains an exciting area of ongoing research (Cen et al., 2023; Liu et al., 2025).

To fully understand these processes, longitudinal studies are essential. While this thesis provides a snapshot of the mechanisms at play, it does not capture their evolution over time, from asymptomatic carriers to acute and chronic phases, and recovery. Most neural damage in LHON occurs within the first year post-onset, making early-stage data critical. Although recruiting patients in the acute phase is challenging – especially given that genetic confirmation takes up to 9months – the maternal inheritance pattern of LHON offers a unique opportunity for early identification. Even without immediate genetic results, family history can guide recruitment. That said, the acute phase may also involve inflammation, which could complicate interpretation and will need to be carefully accounted for in future studies. Additionally, studying asymptomatic carriers may reveal subclinical vulnerabilities in structure and function that precede clinically significant vision loss, offering further insight into early disease mechanisms and potential windows for intervention. The role of neuronal demyelination vs axonal loss of post-geniculate pathways and cortex is also of interest in other sight loss diseases. Another key future question is whether the pattern of dystrophy we observed in the optic radiation – indicating widespread axonal loss with focal demyelination near V1 - is unique to LHON and RGC degeneration, is characteristic of late-onset central vision loss, or a universal neural response to retinal deafferentation, independent of type or age of input loss. Our approach promises new insights into the sensitive periods governing neural tract formation and rescue in the developing human brain.

Chapters 3 and 4 introduced a novel fMRI-based method for mapping visual field sensitivity without requiring fixation. This could be a major step forward for

patients with severe central vision loss, potentially lead to new objective clinical trial endpoints that are less dependent on patient compliance, and show promise for repeatability, which is critical for sensitive measurement. As fMRI measures visual signal transmission directly in visual cortex, it can reveal recovery even when patients cannot use these new signals to improve task performance. For example, Ashtari et al. (2011) showed that fMRI can detect cortical recovery after gene therapy in LCA4 patients, even when psychophysical testing of contrast sensitivity suggests no improvement. Similarly, Farahbakhsh et al. (2022) found recovery of cortical cone-driven retinotopic maps after sight-rescuing intervention in 2 out of 4 patients with achromatopsia, who were born without functioning cones. Whilst this was accompanied by improvements in cone contrast sensitivity, no improvement in visual acuity was observed (Farahbakhsh et al., 2022). Neuroimaging studies in patients with cortical visual disorders like hemianopia have also shown evidence of residual visual function despite V1 damage, supported by preserved structural and functional connectivity between the LGN and hMT+/V5 (Ajina et al., 2015; Ajina & Bridge, 2018). Moreover, visual training could enhance this residual function, with increased fMRI responses in hMT+/V5 and microstructural changes in the LGN-hMT+ tract (Willis et al., 2024).

Together, these findings highlight the power of fMRI to uncover latent or subclinical visual processing – whether in retinal-origin conditions (e.g., LCA, and achromatopsia), or in cortical damage (e.g., hemianopia). They support a growing view that the brain can retain or regain visual function even when standard clinical assessments show little or no improvement, offering avenues for combining sight-restorative therapies with targeted visual rehabilitation to maximise outcomes. In LHON, we seem to observe preserved cortical responses in V1, even when behavioural measures suggested minimal function, alongside some degree of preservation of cortical, subcortical, and microstructural content along the visual pathways that may support recovery. While preliminary, our structural and functional findings suggest that some neural resources may remain available in LHON, offering a promising foundation for visual rehabilitation and recovery following gene therapy.

A key insight from this work is the patient perspective. Despite the severity of their vision loss, participants showed remarkable resilience and adaptability. Their descriptions of their visual experience often aligned with our behavioural and fMRI

measures of cortical visual field loss, which was both validating and encouraging. However, some patients found behavioural testing – especially when performed monocularly – emotionally challenging, as it made them more acutely aware of their deficits. For example, participant P002, who shows severe visual field loss, expressed frustration during the behavioural visual field test did not during passive fMRI scans. This underscores the importance of designing assessments that are not only scientifically robust but also considerate of the patient experience.

Looking ahead, there are many exciting avenues to explore. This work has attracted interest from industry partners seeking to incorporate these methods into clinical trials, an encouraging sign that the tools developed here are not only scientifically valuable but also clinically relevant. I hope that with continued development, the methods I have developed in this thesis could help transform how we monitor, understand, and ultimately treat vision loss in LHON.

One particularly important direction is to link structural and functional changes more directly. The demyelination and axonal loss we observed in regions representing central vision likely contribute to functional deficits seen in LHON. In future work I plan to segment optic radiation fibres based on their cortical terminations – distinguishing those that carry central versus peripheral visual field information – to test whether structural damage, in particular the reduced myelination markers close to V1, aligns with cortical loci of most severe functional loss. Such alignment could potentially implicate demyelination as a consequence of reduced neural activation along the optic pathway, and identify a measurable biomarker for targeted intervention. More broadly, integrating retinal, behavioural, and cortical data could help capture individual differences across multiple stages of processing, offering complementary information for improving personalised treatment strategies.

Further advances in fibre-specific tractography, contrast sensitivity mapping (e.g., the neural contrast response model by Roelofzen et al., 2025), and connective field modelling (Haak et al., 2013) could further deepen our understanding of visual processing in LHON and other eye conditions. Connective field modelling maps how one brain area "samples from" or combines signals from another nearby area, showing how information flows along the cortical hierarchy from primary sensory input regions (Haak et al., 2013). Using this method, Haak et al. (2016) showed in individuals with macular degeneration, functional connectivity between the input-deprived regions of

primary visual cortex (V1) and early extrastriate areas (V2/V3) remains largely intact and retinotopically organized, despite prolonged visual deprivation. This finding supports the idea that retinotopic organization in the visual cortex can remain stable even in the absence of input.

Building on this, recent studies have explored how the visual cortex balances stability and plasticity in congenital conditions like achromatopsia (Molz et al., 2023; Maimon-Mor et al., 2024). For example, colleagues in my lab recently applied connective field modelling to individuals with achromatopsia, who are born without functioning cone photoreceptors (Maimon-Mor et al., 2024). They found that while V1 remain structurally stable despite sensory deprivation, replicating findings by Molz et al. (2023), higher-order areas like V3 may adapt by reorganising how they read signals from V1. Specifically, they found shifts in read-out along the V1 surface eccentricity gradient away from the deprived foveal V1 cortex, and reduced connective field size, which each may optimise processing of the altered input. This highlights a potential, hierarchical, compensatory mechanism in a group experiencing sight deprivation from birth. It is unclear whether such altered connective field patterns would occur in LHON, where scotomas are typically more severe and occur much later in life. This raises questions about how the timing of vision loss affects cortical plasticity. Investigating whether the brain reorganises its connections differently in LHON compared to congenital conditions like achromatopsia could yield valuable insights into the mechanisms and limits of visual system plasticity.

5.3. Challenges encountered and future lessons

This project faced several challenges, both logistical and methodological, which ultimately taught me many valuable lessons about translational neuroscience and the realities of working across clinical and research domains. I initially started my PhD at the start of the COVID-19 pandemic (November 2019), which caused significant delays early on, completely disrupting recruitment and data collection. As result I eventually stopped the PhD and restarted completely anew in April 2021, on a Moorfields Eye Charity Fellowship which I co-wrote. Administrative issues later forced a year-long pause in patient recruitment midway during the PhD (from April 2022 to July 2023), based on which I was granted a costed extension.

Moreover, recruiting LHON patients posed additional challenges. The LHON population is small and geographically dispersed, and some individuals had contraindications for MRI, no clear confirmation of genetic mutation, or comorbid neurological conditions.

From a methodological standpoint, the main challenge was the dense central scotoma in LHON, which required careful adaptation of testing protocols. It took time to determine which behavioural and imaging measures were both feasible and meaningful, especially given the limitations of standard perimetry in this population. Developing the large-field fMRI setup was a key milestone, allowing us to stimulate beyond the central 10º of visual angle. Additionally, since traditional pRF mapping relies heavily on fixation, it was not suitable for this population. Instead, we used the Benson atlas as a fixation-free alternative to map visual space on the cortex. However, inaccuracies in peripheral eccentricity estimates posed a challenge, prompting a collaboration with Dr. Noah Benson to refine these estimates, and while this led to clear improvements the solutions are still being optimised.

Tool integration also posed challenges. The ACID toolbox used for biophysical modelling in Chapter 2 was still under development when I began. Working closely with Prof. Siawoosh Mohammadi and his team, I had to adapt and troubleshoot the toolbox throughout the project. Similarly, existing pipelines for optic tract segmentation were ineffective in this population, leading me to develop a custom segmentation approach. Another issue was the lack of signal in anterior brain regions due to scanning with only the posterior coil, which complicated co-registration between functional and structural images substantially. Resolving this required extensive testing to identify the right combination of toolbox modules. These experiences taught me the importance of flexibility in analysis strategies and the value of bridging clinical and technical perspectives for developing useful tools to study the impact of LHON in the brain, skills I now see as essential in this field.

Despite overcoming many of these challenges, several limitations remain:

- First, Compass perimetry lacks support for eccentric fixation. Although it uses eye-tracking to correct for eye movements, the absence of an eccentric fixation target likely reduced fixation stability and measurement reliability. Future work should explore alternative grid patterns and custom visual field tests tailored to patients with central vision loss.

- Next, OCT data were extracted from medical records and often outdated, as patients are typically seen only every 18 months in clinics. I was not qualified to collect OCT data directly – something I hope to address by acquiring skills in OCT acquisition, electroretinography, and alternative perimetry methods (e.g., Octopus, MAIA).
- Another limitation was that large field pRF mapping lacked a normative baseline. While the Benson atlas provided a very valuable workaround, a large-scale dataset for wide-field pRF mapping could significantly improve the accuracy of fixation-free retinotopic approaches (e.g., Benson atlas, Deep Retinotopy), which is something that I would like to address in the future as well.
- Finally, the lack of post-mortem data on the optic radiations limits our ability to validate *in vivo* findings on demyelination and axonal loss. While post-mortem studies have examined the optic nerve and LGN in LHON, to my knowledge, none have focused on the optic radiations. Although technically challenging, such data would be invaluable for validating imaging findings and understanding the mechanisms of neural change in this region.

Despite these limitations, this project successfully developed and at least part-validated novel imaging tools, generated new insights into LHON pathology, and laid the groundwork for future clinical applications.

On a personal level, this PhD has shown me that neuro-ophthalmology and visual neuroscience could greatly benefit from moving toward more integrated, patient-specific approaches. Standard tools often fall short in rare or complex conditions like LHON. To advance the field, we need:

- **Normative databases** that extend beyond central vision and include cortical and structural measures.
- **Flexible testing protocols** that accommodate patients with central vision loss or unstable fixation.
- **Closer collaboration between clinicians, engineers, and neuroscientist**s, to ensure that tools are both technically robust and clinically meaningful.
- **Greater inclusion of advanced neuroimaging in clinical trials**, as these methods can reveal structural and functional changes that

behavioural tests and standard clinical measures may miss. This could be key to identifying early biomarkers, tracking disease progression, and evaluating treatment efficacy in a more nuanced way. In the contexts of trials, these benefits could off-set the greater expense and technical requirements of MRI.

Ultimately, I believe the future lies in multimodal models of visual function – approaches that can bridge the gap between structure, function, and behaviour in a way that is both scientifically rigorous and clinically relevant.

5.4. Conclusions

In this thesis, by leveraging recent advances in structural and functional MRI, biophysical modelling, and fixation-independent visual field mapping, new tools were developed to characterise the neural impact of Leber Hereditary Optic Neuropathy (LHON) and to support the development of clinically meaningful outcome measures. These methods were applied to both healthy individuals and LHON patients, with the goal of improving our understanding of disease mechanisms and informing future therapeutic strategies.

Using advanced structural MRI, we identified distinct patterns of axonal loss and demyelination along the visual pathways, providing *in vivo* evidence of post-retinal degeneration in LHON. Functional MRI methods enabled the development of a novel, fixation-free approach to mapping visual field sensitivity, which proved reliable, potentially even in patients with central vision loss. Together, these findings suggest that structural and functional imaging can offer complementary insights into the progression and potential recovery of visual function.

Despite logistical and methodological challenges, the project successfully demonstrated the feasibility and value of using advanced neuroimaging in rare eye diseases. These tools are now being considered for use in clinical trials, where they may provide more sensitive and objective endpoints than traditional behavioural tests. This highlights the importance of integrating patient experience, clinical insight, and technical innovation.

Overall, this thesis contributes new methods and insights that can support the evaluation of emerging treatments such as gene therapy, while also advancing our understanding of the neural basis of vision loss. It underscores the need for

multimodal, patient-specific approaches in neuro-ophthalmology and sets the stage for future research that bridges structure, function, and behaviour in both health and disease.

References

Acaroğlu, G., Kansu, T., & Doğulu, Ç. F. (2001). Visual Recovery Patterns in Children with Leber's Hereditary Optic Neuropathy. *International Ophthalmology*, *24*(6), 349–355. https://doi.org/10.1023/B:INTE.0000006855.48323.f1

Aghajari, S., Vinke, L. N., & Ling, S. (2020). Population spatial frequency tuning in human early visual cortex. *Journal of Neurophysiology*, *123*(2), 773–785. https://doi.org/10.1152/jn.00291.2019

Alvarez, G. A. (2011). Representing multiple objects as an ensemble enhances visual cognition. *Trends in Cognitive Sciences*, *15*(3), 122–131. https://doi.org/10.1016/j.tics.2011.01.003

Andalib, S., Talebi, M., Sakhinia, E., Farhoudi, M., Sadeghi-Bazargani, H., Motavallian, A., & Pilehvar-Soltanahmadi, Y. (2013). Multiple sclerosis and mitochondrial gene variations: A review. *Journal of the Neurological Sciences*, *330*(1–2), 10–15. https://doi.org/10.1016/j.jns.2013.04.018

Ashtari, M., Cyckowski, L. L., Monroe, J. F., Marshall, K. A., Chung, D. C., Auricchio, A., Simonelli, F., Leroy, B. P., Maguire, A. M., Shindler, K. S., & Bennett, J. (2011). The human visual cortex responds to gene therapy–mediated recovery of retinal function. *Journal of Clinical Investigation*, *121*(6), 2160–2168. https://doi.org/10.1172/JCI57377

Ashtari, M., Zhang, H., Cook, P. A., Cyckowski, L. L., Shindler, K. S., Marshall, K. A., Aravand, P., Vossough, A., Gee, J. C., Maguire, A. M., Baker, C. I., & Bennett, J. (2015). Plasticity of the human visual system after retinal gene therapy in patients with Leber's congenital amaurosis. *Science Translational Medicine*, *7*(296). https://doi.org/10.1126/scitranslmed.aaa8791

Baker, C. I., Peli, E., Knouf, N., & Kanwisher, N. G. (2005). Reorganization of Visual Processing in Macular Degeneration. *The Journal of Neuroscience*, *25*(3), 614–618. https://doi.org/10.1523/JNEUROSCI.3476-04.2005

Barboni, P., Savini, G., Valentino, M., Montagna, P., Cortelli, P., Denegri, A., Sadun, F., Bianchi, S., Longanesi, L., & Zanini, M. (2005). Retinal nerve fiber layer evaluation by optical coherence tomography in Leber's hereditary optic neuropathy. *Ophthalmology*, *112*(1), 120–126. https://doi.org/10.1016/j.ophtha.2004.06.034

Barbot, A., Xue, S., & Carrasco, M. (2021). Asymmetries in visual acuity around the visual field. *Journal of Vision*, *21*(1), 2. https://doi.org/10.1167/jov.21.1.2

Barcella, V., Rocca, M. A., Bianchi-Marzoli, S., Milesi, J., Melzi, L., Falini, A., Pierro, L., & Filippi, M. (2010). Evidence for retrochiasmatic tissue loss in Leber's hereditary optic neuropathy. *Human Brain Mapping*, *31*(12), 1900–1906. https://doi.org/10.1002/hbm.20985

Bargiela, D., & Chinnery, P. F. (2019). Mitochondria in neuroinflammation – Multiple sclerosis (MS), leber hereditary optic neuropathy (LHON) and LHON-MS. *Neuroscience Letters*, *710*, 132932. https://doi.org/10.1016/j.neulet.2017.06.051

Baseler, H. A., Brewer, A. A., Sharpe, L. T., Morland, A. B., Jägle, H., & Wandell, B. A. (2002). Reorganization of human cortical maps caused by inherited photoreceptor abnormalities. *Nature Neuroscience*, *5*(4), 364–370. https://doi.org/10.1038/nn817

Batioğlu, F., Atilla, H., & Eryilmaz, T. (2003). Chiasmal high signal on magnetic resonance imaging in the atrophic phase of leber hereditary optic neuropathy. *Journal of Neuro-Ophthalmology: The Official Journal of the North American Neuro-Ophthalmology Society*, *23*(1), 28–30. https://doi.org/10.1097/00041327-200303000-00007

Benson, N. C., Butt, O. H., Brainard, D. H., & Aguirre, G. K. (2014). Correction of Distortion in Flattened Representations of the Cortical Surface Allows Prediction of V1-V3 Functional Organization from Anatomy. *PLOS Computational Biology*, *10*(3), e1003538. https://doi.org/10.1371/journal.pcbi.1003538

Benson, N. C., Butt, O. H., Datta, R., Radoeva, P. D., Brainard, D. H., & Aguirre, G. K. (2012). The Retinotopic Organization of Striate Cortex Is Well Predicted by Surface Topology. *Current Biology*, *22*(21), 2081–2085. https://doi.org/10.1016/j.cub.2012.09.014

Benson, N. C., & Winawer, J. (2018). Bayesian analysis of retinotopic maps. *eLife*, *7*, e40224. https://doi.org/10.7554/eLife.40224

Bjartmar, C., & Trapp, B. D. (2001). Axonal and neuronal degeneration in multiple sclerosis: Mechanisms and functional consequences. *Current Opinion in*

Neurology, *14*(3), 271–278. https://doi.org/10.1097/00019052-200106000-00003

Blanc, C., Heran, F., Habas, C., Bejot, Y., Sahel, J., & Vignal-Clermont, C. (2018). MRI of the Optic Nerves and Chiasm in Patients With Leber Hereditary Optic Neuropathy. *Journal of Neuro-Ophthalmology*, *38*(4), 434–437. https://doi.org/10.1097/WNO.0000000000000621

Bourne, R., Steinmetz, J. D., Flaxman, S., Briant, P. S., Taylor, H. R., Resnikoff, S., Casson, R. J., Abdoli, A., Abu-Gharbieh, E., Afshin, A., Ahmadieh, H., Akalu, Y., Alamneh, A. A., Alemayehu, W., Alfaar, A. S., Alipour, V., Anbesu, E. W., Androudi, S., Arabloo, J., … Vos, T. (2021). Trends in prevalence of blindness and distance and near vision impairment over 30 years: An analysis for the Global Burden of Disease Study. *The Lancet Global Health*, *9*(2), e130–e143. https://doi.org/10.1016/S2214-109X(20)30425-3

Broderick, W. F., Simoncelli, E. P., & Winawer, J. (2022). Mapping spatial frequency preferences across human primary visual cortex. *Journal of Vision*, *22*(4), 3. https://doi.org/10.1167/jov.22.4.3

Brommel, C. M., Cooney, A. L., & Sinn, P. L. (2020). Adeno-Associated Virus-Based Gene Therapy for Lifelong Correction of Genetic Disease. *Human Gene Therapy*, *31*(17–18), 985–995. https://doi.org/10.1089/hum.2020.138

Brown, H. D. H., Gale, R. P., Gouws, A. D., Vernon, R. J. W., Airody, A., Hanson, R. L. W., Baseler, H. A., & Morland, A. B. (2023). Assessing the structure of the posterior visual pathway in bilateral macular degeneration. *Scientific Reports*, *13*(1), 5008. https://doi.org/10.1038/s41598-023-31819-x

Buracas, G. T., & Boynton, G. M. (2007). The Effect of Spatial Attention on Contrast Response Functions in Human Visual Cortex. *Journal of Neuroscience*, *27*(1), 93–97. https://doi.org/10.1523/JNEUROSCI.3162-06.2007

Buracas, G. T., Fine, I., & Boynton, G. M. (2005). The Relationship between Task Performance and Functional Magnetic Resonance Imaging Response. *Journal of Neuroscience*, *25*(12), 3023–3031. https://doi.org/10.1523/JNEUROSCI.4476-04.2005

Buxton, R. B. (2013). The physics of functional magnetic resonance imaging (fMRI). *Reports on Progress in Physics*, *76*(9), 096601. https://doi.org/10.1088/0034-4885/76/9/096601

Carelli, V., Hawlina, M., Klopstock, T., Vignal-Clermont, C., & Yu-Wai-Man, P. (2019). Leber's Hereditary Optic Neuropathy – A Global Perspective. *European Ophthalmic Review*, *13*, 3–7.

Carelli, V., Newman, N. J., Caporali, L., Ross-Cisneros, F., Boschetti, E., Biousse, V., DuBois, L., Liu, H., Ancian, P., Taiel, M., & Sadun, A. A. (2024). Ocular Post-Mortem Analyses with Histopathological and Molecular Assessments in LHON Following AAV2 Gene Therapy. *Investigative Ophthalmology & Visual Science*, *65*(7), 6083.

Carelli, V., Ross-Cisneros, F. N., & Sadun, A. A. (2004). Mitochondrial dysfunction as a cause of optic neuropathies. *Progress in Retinal and Eye Research*, *23*(1), 53–89. https://doi.org/10.1016/j.preteyeres.2003.10.003

Carrasco, M., Roberts, M., Myers, C., & Shukla, L. (2022). Visual field asymmetries vary between children and adults. *Current Biology*, *32*(11), R509–R510. https://doi.org/10.1016/j.cub.2022.04.052

Castaldi, E., Lunghi, C., & Morrone, M. C. (2020). Neuroplasticity in adult human visual cortex. *Neuroscience & Biobehavioral Reviews*, *112*, 542–552. https://doi.org/10.1016/j.neubiorev.2020.02.028

Catarino, C. B., & Klopstock, T. (2017). Use of Idebenone for the Treatment of Leber's Hereditary Optic Neuropathy: Review of the Evidence. *Journal of Inborn Errors of Metabolism and Screening*, *5*, 232640981773111. https://doi.org/10.1177/2326409817731112

Cauley, S. F., Polimeni, J. R., Bhat, H., Wald, L. L., & Setsompop, K. (2014). Interslice leakage artifact reduction technique for simultaneous multislice acquisitions. *Magnetic Resonance in Medicine*, *72*(1), 93–102. https://doi.org/10.1002/mrm.24898

Cen, L.-P., Park, K. K., & So, K.-F. (2023). Optic nerve diseases and regeneration: How far are we from the promised land? *Clinical & Experimental Ophthalmology*, *51*(6), 627–641. https://doi.org/10.1111/ceo.14259

Chow-Wing-Bom, H. T., Callaghan, M. F., Wang, J., Wei, S., Dick, F., Yu-Wai-Man, P., & Dekker, T. M. (2022). Neuroimaging in Leber Hereditary Optic Neuropathy: State-of-the-art and future prospects. *NeuroImage: Clinical*, *36*, 103240. https://doi.org/10.1016/j.nicl.2022.103240

Chow-Wing-Bom, H. T., Lisi, M., Benson, N. C., Lygo-Frett, F., Yu-Wai-Man, P., Dick, F., Maimon-Mor, R. O., & Dekker, T. M. (2025). Mapping Visual Contrast Sensitivity and Vision Loss Across the Visual Field with Model-Based fMRI. *eLife*, *14*. https://doi.org/10.7554/eLife.105930.1

Clark, I. A., Mohammadi, S., Callaghan, M. F., & Maguire, E. A. (2022). Conduction velocity along a key white matter tract is associated with autobiographical memory recall ability. *eLife*, *11*, e79303. https://doi.org/10.7554/eLife.79303

Coussa, R. G., Merat, P., & Levin, L. A. (2019). Propagation and Selectivity of Axonal Loss in Leber Hereditary Optic Neuropathy. *Scientific Reports*, *9*(1), 6720. https://doi.org/10.1038/s41598-019-43180-z

d'Almeida, O. C., Mateus, C., Reis, A., Grazina, M. M., & Castelo-Branco, M. (2013). Long term cortical plasticity in visual retinotopic areas in humans with silent retinal ganglion cell loss. *NeuroImage*, *81*, 222–230. https://doi.org/10.1016/j.neuroimage.2013.05.032

Dale, A. M., Fischl, B., & Sereno, M. I. (1999). Cortical Surface-Based Analysis: I. Segmentation and Surface Reconstruction. *NeuroImage*, *9*(2), 179–194. https://doi.org/10.1006/nimg.1998.0395

David, G., Fricke, B., Oeschger, J. M., Ruthotto, L., Fritz, F. J., Ohana, O., Mordhorst, L., Sauvigny, T., Freund, P., Tabelow, K., & Mohammadi, S. (2024). ACID: A comprehensive toolbox for image processing and modeling of brain, spinal cord, and ex vivo diffusion MRI data. *Imaging Neuroscience*, *2*, 1–34. https://doi.org/10.1162/imag_a_00288

DeYoe, E. A., Carman, G. J., Bandettini, P., Glickman, S., Wieser, J., Cox, R., Miller, D., & Neitz, J. (1996). Mapping striate and extrastriate visual areas in human cerebral cortex. *Proceedings of the National Academy of Sciences*, *93*(6), 2382–2386. https://doi.org/10.1073/pnas.93.6.2382

Drakesmith, M., Harms, R., Rudrapatna, S. U., Parker, G. D., Evans, C. J., & Jones, D. K. (2019). Estimating axon conduction velocity *in vivo* from microstructural MRI. *NeuroImage*, *203*, 116186. https://doi.org/10.1016/j.neuroimage.2019.116186

D'Souza, D. V., Auer, T., Frahm, J., Strasburger, H., & Lee, B. B. (2016). Dependence of chromatic responses in V1 on visual field eccentricity and spatial

frequency: An fMRI study. *Journal of the Optical Society of America A*, *33*(3), A53. https://doi.org/10.1364/JOSAA.33.000A53

Dumoulin, S. O., & Knapen, T. (2018). How Visual Cortical Organization Is Altered by Ophthalmologic and Neurologic Disorders. *Annual Review of Vision Science*, *4*(1), 357–379. https://doi.org/10.1146/annurev-vision-091517-033948

Dumoulin, S. O., & Wandell, B. A. (2008). Population receptive field estimates in human visual cortex. *NeuroImage*, *39*(2), 647–660. https://doi.org/10.1016/j.neuroimage.2007.09.034

Engel, S. A., Glover, G. H., & Wandell, B. A. (1997). Retinotopic organization in human visual cortex and the spatial precision of functional MRI. *Cerebral Cortex*, *7*(2), 181–192. https://doi.org/10.1093/cercor/7.2.181

Farahbakhsh, M., Anderson, E. J., Maimon-Mor, R. O., Rider, A., Greenwood, J. A., Hirji, N., Zaman, S., Jones, P. R., Schwarzkopf, D. S., Rees, G., Michaelides, M., & Dekker, T. M. (2022). A demonstration of cone function plasticity after gene therapy in achromatopsia. *Brain*, *145*(11), 3803–3815. https://doi.org/10.1093/brain/awac226

Fischl, B., Sereno, M. I., & Dale, A. M. (1999). Cortical Surface-Based Analysis: II: Inflation, Flattening, and a Surface-Based Coordinate System. *NeuroImage*, *9*(2), 195–207. https://doi.org/10.1006/nimg.1998.0396

Frisén, L. (2017). Swelling of the Optic Nerve Head: A Backstage View of a Staging Scheme. *Journal of Neuro-Ophthalmology*, *37*(1), 3–6. https://doi.org/10.1097/WNO.0000000000000419

Garway-Heath, D. F., Poinoosawmy, D., Fitzke, F. W., & Hitchings, R. A. (2000). Mapping the visual field to the optic disc in normal tension glaucoma eyes1. *Ophthalmology*, *107*(10), 1809–1815. https://doi.org/10.1016/S0161-6420(00)00284-0

Grochowski, C., Jonak, K., Maciejewski, M., Stępniewski, A., & Rahnama-Hezavah, M. (2021). Alteration within the Hippocampal Volume in Patients with LHON Disease—7 Tesla MRI Study. *Journal of Clinical Medicine*, *10*(1), Article 1. https://doi.org/10.3390/jcm10010014

Grochowski, C., Symms, M., Jonak, K., Krukow, P., Wood, T., Ljungberg, E., Enseñat, J., Nowomiejska, K., Rejdak, R., Maciejewski, R., & Barker, G. J. (2020). The Evaluation of Optic Nerves Using 7 Tesla 'Silent' Zero Echo Time Imaging in

Patients with Leber's Hereditary Optic Neuropathy with or without Idebenone Treatment. *Journal of Clinical Medicine*, *9*(4), 1112. https://doi.org/10.3390/jcm9041112

Grossman, R. I., Gomori, J. M., Ramer, K. N., Lexa, F. J., & Schnall, M. D. (1994). *Clinical Applications in Neuroradiology*.

Haak, K. V., Morland, A. B., Rubin, G. S., & Cornelissen, F. W. (2016). Preserved retinotopic brain connectivity in macular degeneration. *Ophthalmic and Physiological Optics*, *36*(3), 335–343. https://doi.org/10.1111/opo.12279

Haak, K. V., Winawer, J., Harvey, B. M., Renken, R., Dumoulin, S. O., Wandell, B. A., & Cornelissen, F. W. (2013). Connective field modeling. *NeuroImage*, *66*, 376–384. https://doi.org/10.1016/j.neuroimage.2012.10.037

Halbertsma, H. N., Bridge, H., Carvalho, J., Cornelissen, F. W., & Ajina, S. (2021). Visual Field Reconstruction in Hemianopia Using fMRI Based Mapping Techniques. *Frontiers in Human Neuroscience*, *15*. https://doi.org/10.3389/fnhum.2021.713114

Hanson, R. L. W., Baseler, H. A., Airody, A., Morland, A. B., & Gale, R. P. (2022). Cortical Atrophy Predicts Visual Performance in Long-Term Central Retinal Disease; GCL, pRNFL and Cortical Thickness Are Key Biomarkers. *Investigative Ophthalmology & Visual Science*, *63*(5), 35. https://doi.org/10.1167/iovs.63.5.35

Helms, G., Dathe, H., Kallenberg, K., & Dechent, P. (2008). High-resolution maps of magnetization transfer with inherent correction for RF inhomogeneity and T_1 relaxation obtained from 3D FLASH MRI. *Magnetic Resonance in Medicine*, *60*(6), 1396–1407. https://doi.org/10.1002/mrm.21732

Henkelman, R. M., Stanisz, G. J., & Graham, S. J. (2001). Magnetization transfer in MRI: A review. *NMR in Biomedicine*, *14*(2), 57–64. https://doi.org/10.1002/nbm.683

Henriksson, L., Nurminen, L., Hyvarinen, A., & Vanni, S. (2008). Spatial frequency tuning in human retinotopic visual areas. *Journal of Vision*, *8*(10), 5–5. https://doi.org/10.1167/8.10.5

Himmelberg, M. M., Winawer, J., & Carrasco, M. (2020). Stimulus-dependent contrast sensitivity asymmetries around the visual field. *Journal of Vision*, *20*(9), 18. https://doi.org/10.1167/jov.20.9.18

Himmelberg, M. M., Winawer, J., & Carrasco, M. (2023). Polar angle asymmetries in visual perception and neural architecture. *Trends in Neurosciences*, *46*(6), 445–458. https://doi.org/10.1016/j.tins.2023.03.006

Hoch, M. J., Bruno, M. T., & Shepherd, T. M. (2017). Advanced MRI of the Optic Nerve. *Journal of Neuro-Ophthalmology*, *37*(2), 187–196. https://doi.org/10.1097/WNO.0000000000000511

Honda, H., Tsujihata, M., Ochi, M., Satoh, A., Tomita, I., & Fujikawa, A. (2006). [Hyperintense optic nerve lesion on T2-weighted MRI imaging in the acute stage of Leber's hereditary optic neuropathy: A case report]. *Rinsho Shinkeigaku = Clinical Neurology*, *46*(4), 294–296.

Horton, J. C., & Hoyt, W. F. (1991). The Representation of the Visual Field in Human Striate Cortex: A Revision of the Classic Holmes Map. *Archives of Ophthalmology*, *109*(6), 816–824. https://doi.org/10.1001/archopht.1991.01080060080030

Hudson, G., Carelli, V., Spruijt, L., Gerards, M., Mowbray, C., Achilli, A., Pyle, A., Elson, J., Howell, N., La Morgia, C., Valentino, M. L., Huoponen, K., Savontaus, M.-L., Nikoskelainen, E., Sadun, A. A., Salomao, S. R., Belfort, R., Griffiths, P., Man, P. Y. W., … Chinnery, P. F. (2007). Clinical Expression of Leber Hereditary Optic Neuropathy Is Affected by the Mitochondrial DNA–Haplogroup Background. *The American Journal of Human Genetics*, *81*(2), 228–233. https://doi.org/10.1086/519394

Huisman, T. A. G. M. (2010). Diffusion-weighted and diffusion tensor imaging of the brain, made easy. *Cancer Imaging*, *10*(1A), S163–S171. https://doi.org/10.1102/1470-7330.2010.9023

Inglese, M., Rovaris, M., Bianchi, S., La Mantia, L., Mancardi, G. L., Ghezzi, A., Montagna, P., Salvi, F., & Filippi, M. (2001). Magnetic resonance imaging, magnetisation transfer imaging, and diffusion weighted imaging correlates of optic nerve, brain, and cervical cord damage in Leber's hereditary optic neuropathy. *Journal of Neurology, Neurosurgery & Psychiatry*, *70*(4), 444–449. https://doi.org/10.1136/jnnp.70.4.444

Jonak, K., Krukow, P., Jonak, K. E., Radzikowska, E., Baj, J., Niedziałek, A., Pankowska, A., Symms, M., Stępniewski, A., Podkowiński, A., Osuchowska, I., & Grochowski, C. (2020). Decreased Volume of Lateral and Medial

Geniculate Nuclei in Patients with LHON Disease—7 Tesla MRI Study. *Journal of Clinical Medicine*, *9*(9), 2914. https://doi.org/10.3390/jcm9092914

Jonak, K., Krukow, P., Karakuła-Juchnowicz, H., Rahnama-Hezavah, M., Jonak, K. E., Stępniewski, A., Niedziałek, A., Toborek, M., Podkowiński, A., Symms, M., & Grochowski, C. (2021). Aberrant Structural Network Architecture in Leber's Hereditary Optic Neuropathy. Minimum Spanning Tree Graph Analysis Application into Diffusion 7T MRI. *Neuroscience*, *455*, 128–140. https://doi.org/10.1016/j.neuroscience.2020.12.019

Jonak, K., Krukow, P., Symms, M., Maciejewski, R., & Grochowski, C. (2020). Neuroanatomical Changes in Leber's Hereditary Optic Neuropathy: Clinical Application of 7T MRI Submillimeter Morphometry. *Brain Sciences*, *10*(6), 359. https://doi.org/10.3390/brainsci10060359

Karaarslan, C. (2019). Leber's Hereditary Optic Neuropathy as a Promising Disease for Gene Therapy Development. *Advances in Therapy*, *36*(12), 3299–3307. https://doi.org/10.1007/s12325-019-01113-2

Koilkonda, R., Yu, H., Talla, V., Porciatti, V., Feuer, W. J., Hauswirth, W. W., Chiodo, V., Erger, K. E., Boye, S. L., Lewin, A. S., Conlon, T. J., Renner, L., Neuringer, M., Detrisac, C., & Guy, J. (2014). LHON Gene Therapy Vector Prevents Visual Loss and Optic Neuropathy Induced by G11778A Mutant Mitochondrial DNA: Biodistribution and Toxicology Profile. *Investigative Ophthalmology & Visual Science*, *55*(12), 7739–7753. https://doi.org/10.1167/iovs.14-15388

Kurzawski, J. W., Gulban, O. F., Jamison, K., Winawer, J., & Kay, K. (2022). Non-Neural Factors Influencing BOLD Response Magnitudes within Individual Subjects. *Journal of Neuroscience*, *42*(38), 7256–7266. https://doi.org/10.1523/JNEUROSCI.2532-21.2022

Lamirel, C., Cassereau, J., Cochereau, I., Vignal-Clermont, C., Pajot, O., Tanguy, J. Y., Zanlonghi, X., Reynier, P., Amati-Bonneau, P., Dubas, F., Bonneau, D., & Verny, C. (2010). Papilloedema and MRI enhancement of the prechiasmal optic nerve at the acute stage of Leber hereditary optic neuropathy. *Journal of Neurology, Neurosurgery & Psychiatry*, *81*(5), 578–580. https://doi.org/10.1136/jnnp.2009.174953

Lange, R., Kumagai, A., Weiss, S., Zaffke, K. B., Day, S., Wicker, D., Howson, A., Jayasundera, K. T., Smolinski, L., Hedlich, C., Lee, P. P., Massof, R. W., Stelmack, J. A., Carlozzi, N. E., & Ehrlich, J. R. (2021). Vision-related quality of life in adults with severe peripheral vision loss: A qualitative interview study. *Journal of Patient-Reported Outcomes*, *5*(1), 7. https://doi.org/10.1186/s41687-020-00281-y

Leroy, B. P., Fischer, M. D., Flannery, J. G., MacLaren, R. E., Dalkara, D., Scholl, H. P. N., Chung, D. C., Spera, C., Viriato, D., & Banhazi, J. (2023). Gene Therapy for Inherited Retinal Disease: Long-Term Durability of Effect. *Ophthalmic Research*, *66*(1), 179–196. https://doi.org/10.1159/000526317

Lisboa, R., Chun, Y. S., Zangwill, L. M., Weinreb, R. N., Rosen, P. N., Liebmann, J. M., Girkin, C. A., & Medeiros, F. A. (2013). Association Between Rates of Binocular Visual Field Loss and Vision-Related Quality of Life in Patients With Glaucoma. *JAMA Ophthalmology*, *131*(4), 486–494. https://doi.org/10.1001/jamaophthalmol.2013.2602

Liu, T., Heeger, D. J., & Carrasco, M. (2006). Neural correlates of the visual vertical meridian asymmetry. *Journal of Vision*, *6*(11), 12. https://doi.org/10.1167/6.11.12

Liu, Z.-G., Zhou, L.-Y., Sun, Y.-Q., Ma, Y.-H., Liu, C.-M., & Zhang, B.-Y. (2025). Unlocking the potential for optic nerve regeneration over long distances: A multi-therapeutic intervention. *Frontiers in Neurology*, *15*, 1526973. https://doi.org/10.3389/fneur.2024.1526973

Logothetis, N. K. (2002). The neural basis of the blood–oxygen–level–dependent functional magnetic resonance imaging signal. *Philosophical Transactions of the Royal Society of London. Series B: Biological Sciences*, *357*(1424), 1003–1037. https://doi.org/10.1098/rstb.2002.1114

Long, M., Wang, L., Tian, Q., Ding, H., Qin, W., Shi, D., & Yu, C. (2019). Brain white matter changes in asymptomatic carriers of Leber's hereditary optic neuropathy. *Journal of Neurology*, *266*(6), 1474–1480. https://doi.org/10.1007/s00415-019-09284-2

Lowndes, R., Molz, B., Warriner, L., Herbik, A., de Best, P. B., Raz, N., Gouws, A., Ahmadi, K., McLean, R. J., Gottlob, I., Kohl, S., Choritz, L., Maguire, J., Kanowski, M., Käsmann-Kellner, B., Wieland, I., Banin, E., Levin, N.,

Hoffmann, M. B., … Baseler, H. A. (2021). Structural Differences Across Multiple Visual Cortical Regions in the Absence of Cone Function in Congenital Achromatopsia. *Frontiers in Neuroscience*, *15*. https://doi.org/10.3389/fnins.2021.718958

Maimon-Mor, R. O., Farahbakhsh, M., Hedger, N., Rider, A. T., Anderson, E. J., Rees, G., Knapen, T., Michaelides, M., & Dekker, T. M. (2024). Hierarchical cortical plasticity in congenital sight impairment. *eLife*, *13*. https://doi.org/10.7554/eLife.100404.1

Majander, A., Robson, A. G., João, C., Holder, G. E., Chinnery, P. F., Moore, A. T., Votruba, M., Stockman, A., & Yu-Wai-Man, P. (2017). The pattern of retinal ganglion cell dysfunction in Leber hereditary optic neuropathy. *Mitochondrion*, *36*, 138–149. https://doi.org/10.1016/j.mito.2017.07.006

Manners, D. N., Rizzo, G., La Morgia, C., Tonon, C., Testa, C., Barboni, P., Malucelli, E., Valentino, M. L., Caporali, L., Strobbe, D., Carelli, V., & Lodi, R. (2015). Diffusion Tensor Imaging Mapping of Brain White Matter Pathology in Mitochondrial Optic Neuropathies. *American Journal of Neuroradiology*, *36*(7), 1259–1265. https://doi.org/10.3174/ajnr.A4272

Mashima, Y., Oshitari, K., Imamura, Y., Momoshima, S., Shiga, H., & Oguchi, Y. (1998a). Orbital high resolution magnetic resonance imaging with fast spin echo in the acute stage of Leber's hereditary optic neuropathy. *Journal of Neurology, Neurosurgery, and Psychiatry*, *64*(1), 124–127. https://doi.org/10.1136/jnnp.64.1.124

Mashima, Y., Oshitari, K., Imamura, Y., Momoshima, S., Shiga, H., & Oguchi, Y. (1998b). Orbital high resolution magnetic resonance imaging with fast spin echo in the acute stage of Leber's hereditary optic neuropathy. *Journal of Neurology, Neurosurgery & Psychiatry*, *64*(1), 124–127. https://doi.org/10.1136/jnnp.64.1.124

Mateus, C., d'Almeida, O. C., Reis, A., Silva, E., & Castelo-Branco, M. (2016). Genetically induced impairment of retinal ganglion cells at the axonal level is linked to extrastriate cortical plasticity. *Brain Structure & Function*, *221*(3), 1767–1780. https://doi.org/10.1007/s00429-015-1002-2

Matthews, L., Enzinger, C., Fazekas, F., Rovira, A., Ciccarelli, O., Dotti, M. T., Filippi, M., Frederiksen, J. L., Giorgio, A., Küker, W., Lukas, C., Rocca, M. A., De

Stefano, N., Toosy, A., Yousry, T., & Palace, J. (2015). MRI in Leber's hereditary optic neuropathy: The relationship to multiple sclerosis. *Journal of Neurology, Neurosurgery & Psychiatry*, *86*(5), 537–542. https://doi.org/10.1136/jnnp-2014-308186

Mercuri, M. A., White, H., & Oliveira, C. (2017). Vision Loss and Symmetric Basal Ganglia Lesions in Leber Hereditary Optic Neuropathy. *Journal of Neuro-Ophthalmology*, *37*(4), 411–413. https://doi.org/10.1097/WNO.0000000000000524

Milesi, J., Rocca, M. A., Bianchi-Marzoli, S., Petrolini, M., Pagani, E., Falini, A., Comi, G., & Filippi, M. (2012). Patterns of white matter diffusivity abnormalities in Leber's hereditary optic neuropathy: A tract-based spatial statistics study. *Journal of Neurology*, *259*(9), 1801–1807. https://doi.org/10.1007/s00415-011-6406-1

Mohammadi, S., & Callaghan, M. F. (2021). Towards in vivo g-ratio mapping using MRI: Unifying myelin and diffusion imaging. *Journal of Neuroscience Methods*, *348*, 108990. https://doi.org/10.1016/j.jneumeth.2020.108990

Molz, B., Herbik, A., Baseler, H. A., de Best, P. B., Vernon, R. W., Raz, N., Gouws, A. D., Ahmadi, K., Lowndes, R., McLean, R. J., Gottlob, I., Kohl, S., Choritz, L., Maguire, J., Kanowski, M., Käsmann-Kellner, B., Wieland, I., Banin, E., Levin, N., … Morland, A. B. (2022). Structural changes to primary visual cortex in the congenital absence of cone input in achromatopsia. *NeuroImage: Clinical*, *33*, 102925. https://doi.org/10.1016/j.nicl.2021.102925

Molz, B., Herbik, A., Baseler, H. A., de Best, P., Raz, N., Gouws, A., Ahmadi, K., Lowndes, R., McLean, R. J., Gottlob, I., Kohl, S., Choritz, L., Maguire, J., Kanowski, M., Käsmann-Kellner, B., Wieland, I., Banin, E., Levin, N., Morland, A. B., & Hoffmann, M. B. (2023). Achromatopsia—Visual Cortex Stability and Plasticity in the Absence of Functional Cones. *Investigative Ophthalmology & Visual Science*, *64*(13), 23. https://doi.org/10.1167/iovs.64.13.23

Moore, A. T., & Yu-Wai-Man, P. (2021). Mitochondrial Disorders and the Eye: A New Era for Diagnosis. *Ophthalmology*, *128*(4), 632–633. https://doi.org/10.1016/j.ophtha.2020.12.032

Moster, M., Sadun, A., Klopstock, T., Newman, N., Vignal-Clermont, C., Carelli, V., Yu-Wai-Man, P., Biousse, V., Sergott, R., Katz, B., DeBusk, A., Blouin, L., Chevalier, C., Burguiere, P., Taiel, M., & Sahel, J.-A. (2020). rAAV2/2-ND4 for the Treatment of Leber Hereditary Optic Neuropathy (LHON): Final Results from the RESCUE and REVERSE Phase III Clinical Trials and Experimental Data in Nonhuman Primates to Support a Bilateral Effect (2339). *Neurology*, *94*(15_supplement), 2339. https://doi.org/10.1212/WNL.94.15_supplement.2339

Newman, N. J., Carelli, V., Taiel, M., & Yu-Wai-Man, P. (2020). Visual Outcomes in Leber Hereditary Optic Neuropathy Patients With the m.11778G>A (MTND4) Mitochondrial DNA Mutation. *Journal of Neuro-Ophthalmology*, *40*(4), 547–557. https://doi.org/10.1097/WNO.0000000000001045

Newman, N. J., Yu-Wai-Man, P., Carelli, V., Biousse, V., Moster, M. L., Vignal-Clermont, C., Sergott, R. C., Klopstock, T., Sadun, A. A., Girmens, J.-F., La Morgia, C., DeBusk, A. A., Jurkute, N., Priglinger, C., Karanjia, R., Josse, C., Salzmann, J., Montestruc, F., Roux, M., … Sahel, J.-A. (2021). Intravitreal Gene Therapy vs. Natural History in Patients With Leber Hereditary Optic Neuropathy Carrying the m.11778G>A ND4 Mutation: Systematic Review and Indirect Comparison. *Frontiers in Neurology*, *12*, 662838. https://doi.org/10.3389/fneur.2021.662838

Newman, N. J., Yu-Wai-Man, P., Subramanian, P. S., Moster, M. L., Wang, A.-G., Donahue, S. P., Leroy, B. P., Carelli, V., Biousse, V., Vignal-Clermont, C., Sergott, R. C., Sadun, A. A., Rebolleda Fernández, G., Chwalisz, B. K., Banik, R., Bazin, F., Roux, M., Cox, E. D., Taiel, M., … the LHON REFLECT Study Group. (2023). Randomized trial of bilateral gene therapy injection for m.11778G>A MT-ND4 Leber optic neuropathy. *Brain*, *146*(4), 1328–1341. https://doi.org/10.1093/brain/awac421

O'Connell, C., Ho, L. C., Murphy, M. C., Conner, I. P., Wollstein, G., Cham, R., & Chan, K. C. (2016). Structural and functional correlates of visual field asymmetry in the human brain by diffusion kurtosis MRI and functional MRI. *NeuroReport*, *27*(16), 1225. https://doi.org/10.1097/WNR.0000000000000682

Ogawa, S., Takemura, H., Horiguchi, H., Terao, M., Haji, T., Pestilli, F., Yeatman, J. D., Tsuneoka, H., Wandell, B. A., & Masuda, Y. (2014). White Matter Consequences of Retinal Receptor and Ganglion Cell Damage. *Investigative Ophthalmology & Visual Science*, *55*(10), 6976–6986. https://doi.org/10.1167/iovs.14-14737

Oliva, A. (2005). CHAPTER 41—Gist of the Scene. In L. Itti, G. Rees, & J. K. Tsotsos (Eds.), *Neurobiology of Attention* (pp. 251–256). Academic Press. https://doi.org/10.1016/B978-012375731-9/50045-8

Ong, E., Biotti, D., Abouaf, L., Louis-Tisserand, G., Tilikete, C., & Vighetto, A. (2013). Teaching Neuro *Images*: Chiasmal enlargement and enhancement in Leber hereditary optic neuropathy. *Neurology*, *81*(17). https://doi.org/10.1212/WNL.0b013e3182a95698

Pan, B. X., Ross-Cisneros, F. N., Carelli, V., Rue, K. S., Salomao, S. R., Moraes-Filho, M. N., Moraes, M. N., Berezovsky, A., Belfort, R., & Sadun, A. A. (2012). Mathematically Modeling the Involvement of Axons in Leber's Hereditary Optic Neuropathy. *Investigative Opthalmology & Visual Science*, *53*(12), 7608. https://doi.org/10.1167/iovs.12-10452

Panfoli, I., & Ravera, S. (2025). A viewpoint about Lenadogene nolparvovec failing to meet its primary endpoint even though it permanently corrects the m.11778G>A mutation causative of LHON. *Eye*, 1–2. https://doi.org/10.1038/s41433-025-03856-5

Papazoglou, S., Ashtarayeh, M., Oeschger, J. M., Callaghan, M. F., Does, M. D., & Mohammadi, S. (2024). Insights and improvements in correspondence between axonal volume fraction measured with diffusion-weighted MRI and electron microscopy. *NMR in Biomedicine*, *37*(3), e5070. https://doi.org/10.1002/nbm.5070

Pawloff, M., Linhardt, D., Woletz, M., Hummer, A., Sacu, S., Vasileiadi, M., Garikoitz, L. U., Holder, G., Schmidt-Erfurth, U. M., Windischberger, C., & Ritter, M. (2023). Comparison of Stimulus Types for Retinotopic Cortical Mapping of Macular Disease. *Translational Vision Science & Technology*, *12*(3), 6. https://doi.org/10.1167/tvst.12.3.6

Pemp, B., Mitsch, C., Kircher, K., & Reitner, A. (2021). Changes in Visual Function and Correlations with Inner Retinal Structure in Acute and Chronic Leber's

Hereditary Optic Neuropathy Patients after Treatment with Idebenone. *Journal of Clinical Medicine*, *10*(1), 151. https://doi.org/10.3390/jcm10010151

Pfeffer, G., Burke, A., Yu-Wai-Man, P., Compston, D. A. S., & Chinnery, P. F. (2013). Clinical features of MS associated with Leber hereditary optic neuropathy mtDNA mutations. *Neurology*, *81*(24), 2073–2081. https://doi.org/10.1212/01.wnl.0000437308.22603.43

Phillips, P. H., Vaphiades, M. S., Glasier, C. M., Gray, L. G., & Lee, A. G. (2003). Microcornea and Subluxated Lenses Due to a Splicing Error in the Fibrillin-1 Gene in a Patient With Marfan Syndrome. *Archives of Ophthalmology*, *121*(4), 579. https://doi.org/10.1001/archopht.121.4.579

Prins, D., Plank, T., Baseler, H. A., Gouws, A. D., Beer, A., Morland, A. B., Greenlee, M. W., & Cornelissen, F. W. (2016). Surface-Based Analyses of Anatomical Properties of the Visual Cortex in Macular Degeneration. *PLOS ONE*, *11*(1), e0146684. https://doi.org/10.1371/journal.pone.0146684

Puomila, A., Hämäläinen, P., Kivioja, S., Savontaus, M.-L., Koivumäki, S., Huoponen, K., & Nikoskelainen, E. (2007). Epidemiology and penetrance of Leber hereditary optic neuropathy in Finland. *European Journal of Human Genetics*, *15*(10), 1079–1089. https://doi.org/10.1038/sj.ejhg.5201828

R Core Team. (2024). *R: The R Project for Statistical Computing* [R]. R Foundation for Statistical Computing. https://www.r-project.org/

Rance, G., Kearns, L. S., Tan, J., Gravina, A., Rosenfeld, L., Henley, L., Carew, P., Graydon, K., O'Hare, F., & Mackey, D. A. (2012). Auditory function in individuals within Leber's hereditary optic neuropathy pedigrees. *Journal of Neurology*, *259*(3), 542–550. https://doi.org/10.1007/s00415-011-6230-7

Ribeiro, F. L., Bollmann, S., & Puckett, A. M. (2021). Predicting the retinotopic organization of human visual cortex from anatomy using geometric deep learning. *NeuroImage*, *244*, 118624. https://doi.org/10.1016/j.neuroimage.2021.118624

Ritter, M., Hummer, A., Ledolter, A. A., Holder, G. E., Windischberger, C., & Schmidt-Erfurth, U. M. (2019a). Correspondence between retinotopic cortical mapping and conventional functional and morphological assessment of

retinal disease. *British Journal of Ophthalmology*, *103*(2), 208–215. https://doi.org/10.1136/bjophthalmol-2017-311443

Ritter, M., Hummer, A., Ledolter, A. A., Holder, G. E., Windischberger, C., & Schmidt-Erfurth, U. M. (2019b). Correspondence between retinotopic cortical mapping and conventional functional and morphological assessment of retinal disease. *British Journal of Ophthalmology*, *103*(2), 208–215. https://doi.org/10.1136/bjophthalmol-2017-311443

Rizzo, G., Tozer, K. R., Tonon, C., Manners, D., Testa, C., Malucelli, E., Valentino, M. L., La Morgia, C., Barboni, P., Randhawa, R. S., Ross-Cisneros, F. N., Sadun, A. A., Carelli, V., & Lodi, R. (2012). Secondary Post-Geniculate Involvement in Leber's Hereditary Optic Neuropathy. *PLoS ONE*, *7*(11), e50230. https://doi.org/10.1371/journal.pone.0050230

Rocca, M. A., Valsasina, P., Pagani, E., Bianchi-Marzoli, S., Milesi, J., Falini, A., Comi, G., & Filippi, M. (2011). Extra-Visual Functional and Structural Connection Abnormalities in Leber's Hereditary Optic Neuropathy. *PLoS ONE*, *6*(2), e17081. https://doi.org/10.1371/journal.pone.0017081

Roelofzen, C., Daghlian, M., van Dijk, J. A., de Jong, M. C., & Dumoulin, S. O. (2025). Modeling neural contrast sensitivity functions in human visual cortex. *Imaging Neuroscience*, *3*, imag_a_00469. https://doi.org/10.1162/imag_a_00469

Roh, M., Selivanova, A., Shin, H. J., Miller, J. W., & Jackson, M. L. (2018). Visual acuity and contrast sensitivity are two important factors affecting vision-related quality of life in advanced age-related macular degeneration. *PLOS ONE*, *13*(5), e0196481. https://doi.org/10.1371/journal.pone.0196481

Rosazza, C., & Minati, L. (2011). Resting-state brain networks: Literature review and clinical applications. *Neurological Sciences*, *32*(5), 773–785. https://doi.org/10.1007/s10072-011-0636-y

Rościszewska-Żukowska, I., & Bartosik-Psujek, H. (2020). Optic nerve atrophy and whole and regional brain atrophy in Leber's hereditary optic neuropathy with multiple sclerosis-like disease with m.11778G>A mutation. *Multiple Sclerosis and Related Disorders*, *42*, 102071. https://doi.org/10.1016/j.msard.2020.102071

Rovamo, J., Leinonen, L., Laurinen, P., & Virsu, V. (1984). Temporal Integration and Contrast Sensitivity in Foveal and Peripheral Vision. *Perception*, *13*(6), 665–674. https://doi.org/10.1068/p130665

Rovamo, J., & Virsu, V. (1979). An estimation and application of the human cortical magnification factor. *Experimental Brain Research*, *37*(3). https://doi.org/10.1007/BF00236819

Rushton, W. a. H. (1951). A theory of the effects of fibre size in medullated nerve. *The Journal of Physiology*, *115*(1), 101–122. https://doi.org/10.1113/jphysiol.1951.sp004655

Sadun, A. A., Win, P. H., Ross-Cisneros, F. N., Walker, S. O., & Carelli, V. (2000). Leber's hereditary optic neuropathy differentially affects smaller axons in the optic nerve. *Transactions of the American Ophthalmological Society*, *90*(223–235), 687. https://doi.org/10.1016/S0002-9394(01)00947-3

Savini, G., Barboni, P., Valentino, M., Montagna, P., Cortelli, P., Denegri, A., Sadun, F., Bianchi, S., Longanesi, L., & Zanini, M. (2005). Retinal nerve fiber layer evaluation by optical coherence tomography in unaffected carriers with Leber's hereditary optic neuropathy mutations. *Ophthalmology*, *112*(1), 127–131. https://doi.org/10.1016/j.ophtha.2004.09.033

Scholl, H. P. N., & György, B. (2025). Single-Eye Gene Therapy for Leber Hereditary Optic Neuropathy. *JAMA Ophthalmology*, *143*(2), 108. https://doi.org/10.1001/jamaophthalmol.2024.5618

Schwarzkopf, D. S. (n.d.). *SamSrf* (Version 7.13) [Computer software]. Retrieved 28 May 2025, from https://github.com/samsrf

Seitzman, B. A., Snyder, A. Z., Leuthardt, E. C., & Shimony, J. S. (2019). The State of Resting State Networks. *Topics in Magnetic Resonance Imaging*, *28*(4), 189–196. https://doi.org/10.1097/RMR.0000000000000214

Sereno, M. I., Dale, A. M., Reppas, J. B., Kwong, K. K., Belliveau, J. W., Brady, T. J., Rosen, B. R., & Tootell, R. B. H. (1995). Borders of Multiple Visual Areas in Humans Revealed by Functional Magnetic Resonance Imaging. *Science*, *268*(5212), 889–893. https://doi.org/10.1126/science.7754376

Sereno, M. I., Lutti, A., Weiskopf, N., & Dick, F. (2013). Mapping the Human Cortical Surface by Combining Quantitative T1 with Retinotopy. *Cerebral Cortex (New York, NY)*, *23*(9), 2261–2268. https://doi.org/10.1093/cercor/bhs213

Sharkawi, E., Oleszczuk, J. D., Holder, G. E., & Raina, J. (2012). Clinical and electrophysiological recovery in Leber hereditary optic neuropathy with G3460A mutation. *Documenta Ophthalmologica*, *125*(1), 71–74. https://doi.org/10.1007/s10633-012-9328-z

Smitha, K., Akhil Raja, K., Arun, K., Rajesh, P., Thomas, B., Kapilamoorthy, T., & Kesavadas, C. (2017). Resting state fMRI: A review on methods in resting state connectivity analysis and resting state networks. *The Neuroradiology Journal*, *30*(4), 305–317. https://doi.org/10.1177/1971400917697342

SPM - Statistical Parametric Mapping. (n.d.). Retrieved 28 May 2025, from https://www.fil.ion.ucl.ac.uk/spm/

Stenton, S. L., Sheremet, N. L., Catarino, C. B., Andreeva, N. A., Assouline, Z., Barboni, P., Barel, O., Berutti, R., Bychkov, I., Caporali, L., Capristo, M., Carbonelli, M., Cascavilla, M. L., Charbel Issa, P., Freisinger, P., Gerber, S., Ghezzi, D., Graf, E., Heidler, J., … Prokisch, H. (2021). Impaired complex I repair causes recessive Leber's hereditary optic neuropathy. *Journal of Clinical Investigation*, *131*(6), e138267. https://doi.org/10.1172/JCI138267

Subhi, H., Latham, K., Myint, J., & Crossland, M. D. (2017). Functional visual fields: Relationship of visual field areas to self-reported function. *Ophthalmic and Physiological Optics*, *37*(4), 399–408. https://doi.org/10.1111/opo.12362

Symms, M., Jäger, H. R., Schmierer, K., & Yousry, T. A. (2004). A review of structural magnetic resonance neuroimaging. *Journal of Neurology, Neurosurgery & Psychiatry*, *75*(9), 1235–1244. https://doi.org/10.1136/jnnp.2003.032714

Tabelow, K., Balteau, E., Ashburner, J., Callaghan, M. F., Draganski, B., Helms, G., Kherif, F., Leutritz, T., Lutti, A., Phillips, C., Reimer, E., Ruthotto, L., Seif, M., Weiskopf, N., Ziegler, G., & Mohammadi, S. (2019). hMRI - A toolbox for quantitative MRI in neuroscience and clinical research. *NeuroImage*, *194*, 191–210. https://doi.org/10.1016/j.neuroimage.2019.01.029

Takemura, H., Ogawa, S., Mezer, A. A., Horiguchi, H., Miyazaki, A., Matsumoto, K., Shikishima, K., Nakano, T., & Masuda, Y. (2019). Diffusivity and quantitative T1 profile of human visual white matter tracts after retinal ganglion cell damage. *NeuroImage: Clinical*, *23*, 101826. https://doi.org/10.1016/j.nicl.2019.101826

Thouin, A., Griffiths, P. G., Hudson, G., Chinnery, P. F., & Yu-Wai-Man, P. (2013). Raised intraocular pressure as a potential risk factor for visual loss in Leber Hereditary Optic Neuropathy. *PloS One*, *8*(5), e63446. https://doi.org/10.1371/journal.pone.0063446

Vaphiades, M. S., Phillips, P. H., & Turbin, R. E. (2003). Optic Nerve and Chiasmal Enhancement In Leber Hereditary Optic Neuropathy: *Journal of Neuro-Ophthalmology*, *23*(1), 104–105. https://doi.org/10.1097/00041327-200303000-00057

Vavasour, I. M., Laule, C., Li, D. K. B., Traboulsee, A. L., & MacKay, A. L. (2011). Is the magnetization transfer ratio a marker for myelin in multiple sclerosis? *Journal of Magnetic Resonance Imaging: JMRI*, *33*(3), 713–718. https://doi.org/10.1002/jmri.22441

Wan, X., Pei, H., Zhao, M., Yang, S., Hu, W., He, H., Ma, S., Zhang, G., Dong, X., Chen, C., Wang, D., & Li, B. (2016). Efficacy and Safety of rAAV2-ND4 Treatment for Leber's Hereditary Optic Neuropathy. *Scientific Reports*, *6*(1), 21587. https://doi.org/10.1038/srep21587

Wang, L., Fan, K., Zhang, Y., Chen, Y., Tian, Q., & Shi, D. (2017). Quantitative assessment of optic nerve in patients with Leber's hereditary optic neuropathy using reduced field-of-view diffusion tensor imaging. *European Journal of Radiology*, *93*, 24–29. https://doi.org/10.1016/j.ejrad.2017.05.025

Weiskopf, N., Edwards, L. J., Helms, G., Mohammadi, S., & Kirilina, E. (2021). Quantitative magnetic resonance imaging of brain anatomy and in vivo histology. *Nature Reviews Physics*, *3*(8), 570–588. https://doi.org/10.1038/s42254-021-00326-1

Weiskopf, N., Mohammadi, S., Lutti, A., & Callaghan, M. F. (2015). Advances in MRI-based computational neuroanatomy: From morphometry to in-vivo histology. *Current Opinion in Neurology*, *28*(4), 313–322. https://doi.org/10.1097/WCO.0000000000000222

Welbourne, L. E., Morland, A. B., & Wade, A. R. (2018). Population receptive field (pRF) measurements of chromatic responses in human visual cortex using fMRI. *NeuroImage*, *167*, 84–94. https://doi.org/10.1016/j.neuroimage.2017.11.022

West, K. L., Kelm, N. D., Carson, R. P., & Does, M. D. (2016). A revised model for estimating g-ratio from MRI. *NeuroImage*, *125*, 1155–1158. https://doi.org/10.1016/j.neuroimage.2015.08.017

Wheeler-Kingshott, C. A. M., & Cercignani, M. (2009). About "axial" and "radial" diffusivities. *Magnetic Resonance in Medicine*, *61*(5), 1255–1260. https://doi.org/10.1002/mrm.21965

Winklewski, P. J., Sabisz, A., Naumczyk, P., Jodzio, K., Szurowska, E., & Szarmach, A. (2018). Understanding the Physiopathology Behind Axial and Radial Diffusivity Changes—What Do We Know? *Frontiers in Neurology*, *9*, 92. https://doi.org/10.3389/fneur.2018.00092

World Health Organization. (2019, October 8). *WHO launches first World report on vision*. https://www.who.int/news/item/08-10-2019-who-launches-first-world-report-on-vision

Xia, X., & Guo, X. (2023). Adeno-associated virus vectors for retinal gene therapy in basic research and clinical studies. *Frontiers in Medicine*, *10*. https://doi.org/10.3389/fmed.2023.1310050

Xu, J., Moeller, S., Auerbach, E. J., Strupp, J., Smith, S. M., Feinberg, D. A., Yacoub, E., & Uğurbil, K. (2013). Evaluation of slice accelerations using multiband echo planar imaging at 3 T. *NeuroImage*, *83*, 991–1001. https://doi.org/10.1016/j.neuroimage.2013.07.055

Yeh, F.-C. (2022). Population-based tract-to-region connectome of the human brain and its hierarchical topology. *Nature Communications*, *13*(1), 4933. https://doi.org/10.1038/s41467-022-32595-4

York, E. N., Meijboom, R., Thrippleton, M. J., Bastin, M. E., Kampaite, A., White, N., Chandran, S., & Waldman, A. D. (2022). Longitudinal microstructural MRI markers of demyelination and neurodegeneration in early relapsing-remitting multiple sclerosis: Magnetisation transfer, water diffusion and g-ratio. *NeuroImage: Clinical*, *36*, 103228. https://doi.org/10.1016/j.nicl.2022.103228

Yuan, J., Zhang, Y., Liu, H., Wang, D., Du, Y., Tian, Z., Li, X., Yang, S., Pei, H., Wan, X., Xiao, S., Song, L., Xiao, X., Sun, J., Wang, Z., & Li, B. (2020). Seven-Year Follow-up of Gene Therapy for Leber's Hereditary Optic Neuropathy.

Ophthalmology, *127*(8), 1125–1127. https://doi.org/10.1016/j.ophtha.2020.02.023

Yu-Wai-Man, P., Carelli, V., Newman, N. J., Silva, M. J., Linden, A., Van Stavern, G., Szaflik, J. P., Banik, R., Lubiński, W., Pemp, B., Liao, Y. J., Subramanian, P. S., Misiuk-Hojło, M., Newman, S., Castillo, L., Kocięcki, J., Levin, M. H., Muñoz-Negrete, F. J., Yagan, A., … Klopstock, T. (2024). Therapeutic benefit of idebenone in patients with Leber hereditary optic neuropathy: The LEROS nonrandomized controlled trial. *Cell Reports Medicine*, *5*(3), 101437. https://doi.org/10.1016/j.xcrm.2024.101437

Yu-Wai-Man, P., & Chinnery, P. (2000). Leber Hereditary Optic Neuropathy. In *GeneReviews® [Internet]* (Updated 2021 Mar 11). University of Washington, Seattle. https://www.ncbi.nlm.nih.gov/books/NBK1174/

Yu-Wai-Man, P., Griffiths, P. G., Brown, D. T., Howell, N., Turnbull, D. M., & Chinnery, P. F. (2003). The Epidemiology of Leber Hereditary Optic Neuropathy in the North East of England. *Am. J. Hum. Genet.*

Yu-Wai-Man, P., Newman, N. J., Biousse, V., Carelli, V., Moster, M. L., Vignal-Clermont, C., Klopstock, T., Sadun, A. A., Sergott, R. C., Hage, R., Degli Esposti, S., La Morgia, C., Priglinger, C., Karanja, R., Taiel, M., Sahel, J.-A., & LHON Study Group. (2025). Five-Year Outcomes of Lenadogene Nolparvovec Gene Therapy in Leber Hereditary Optic Neuropathy. *JAMA Ophthalmology*, *143*(2), 99–108. https://doi.org/10.1001/jamaophthalmol.2024.5375

Yu-Wai-Man, P., Newman, N. J., Carelli, V., Moster, M. L., Biousse, V., Sadun, A. A., Klopstock, T., Vignal-Clermont, C., Sergott, R. C., Rudolph, G., La Morgia, C., Karanjia, R., Taiel, M., Blouin, L., Burguière, P., Smits, G., Chevalier, C., Masonson, H., Salermo, Y., … Sahel, J.-A. (2020). Bilateral visual improvement with unilateral gene therapy injection for Leber hereditary optic neuropathy. *Science Translational Medicine*, *12*(573), eaaz7423. https://doi.org/10.1126/scitranslmed.aaz7423

Yu-Wai-Man, P., Votruba, M., Burté, F., La Morgia, C., Barboni, P., & Carelli, V. (2016). A neurodegenerative perspective on mitochondrial optic neuropathies. *Acta Neuropathologica*, *132*(6), 789–806. https://doi.org/10.1007/s00401-016-1625-2

Zhang, J., Wang, L., Ding, H., Fan, K., Tian, Q., Liang, M., Sun, Z., Shi, D., & Qin, W. (2021). Abnormal large-scale structural rich club organization in Leber's hereditary optic neuropathy. *NeuroImage: Clinical*, *30*, 102619. https://doi.org/10.1016/j.nicl.2021.102619

Zhang, Y., Huang, H., Wei, S., Qiu, H., Gong, Y., Li, H., Dai, Y., Jiang, Z., & Liu, Z. (2014). Characterization of retinal nerve fiber layer thickness changes associated with Leber's hereditary optic neuropathy by optical coherence tomography. *Experimental and Therapeutic Medicine*, *7*(2), 483–487. https://doi.org/10.3892/etm.2013.1430

Zuccarelli, M., Vella-Szijj, J., Serracino-Inglott, A., & Borg, J.-J. (2020). Treatment of Leber's hereditary optic neuropathy: An overview of recent developments. *European Journal of Ophthalmology*, *30*(6), 1220–1227. https://doi.org/10.1177/1120672120936592

Appendix

1. Chapter 2: MPM-Motion project – Effect of phase-encoding trajectory, angulation, and motion on the quality of FLASH sequence.

Introduction

Why is the phase-encoding trajectory important and interacting with motion?

"Partitions" and "Lines" are Siemens terminology and respectively map to Right-Left (RL) and Anterior-Posterior (AP) directions in our case. Here, we are interested to look at the effect of two phase-encoded directions on the acquisition of 3D brain images: "Partition inside Lines" and "Lines in Partitions". "A inside B" means that we acquire all the (k-space) lines "B" before incrementing to the next line in the "A" direction, meaning that the direction "A" is going to be acquired more distantly in time.

This means that if data are acquired using a "partitions inside lines" phase-encoding trajectory, the AP direction would be acquired much more slowly than the RL direction. We would expect artefacts to appear in the slowest direction, i.e., multiple lines along the AP direction. These artefacts would be visualised in the brain as large ringing lines that are replicas of the outer skin. In contrast, using a "lines inside partitions" phase-encoding trajectory would mean that the slowest direction of acquisition would be RL. This means that our artefacts would now present as rings running parallel to the side of the head. Consequently, in case of drastic eye movements, the artefacts caused by the eyes moving would be localised to the orbital region and less visible in the brain, which can be useful when collecting data in visually impaired patients who often present with nystagmus.

Why is the angulation important and interacting with motion?

Our motivation was to have the aliases of the eyes running along a 30º diagonal and therefore ideally missing cortex.

Why are motion effects expected to be visualised in all acquired echoes?

Our motion task (crossing legs and eye motion) happens halfway throughout a run, which will be placed in the middle of the k-space for image reconstruction. The echoes are acquired within a TR and therefore in very close temporal proximity. As a consequence, all echoes will effectively be subject to the same motion within a TR.

However, Magerkurth et al. (2011) has shown that motion can be more problematic at later TE and that, as well as a hope for consistent findings across more data, was our reason for looking at multiple echoes.

Methods

Participants (N=5; 30.3±5.3 years old; 3 females) laid down in supine position in a Siemens PRISMA 3 Tesla scanner. Head was stabilised by using HAROLD, and OMEMS MRI-compatible headphones was used to play music or a podcast of their choice. Bilateral eye-tracking was achieved using an EyeLink 1000Plus device (SR Research, Ottawa, Canada).

Image acquisition

- 30-channel coil
- T1w from MPM-0.8mm protocol, differing in their angulation and/or phase-encoding trajectory parameters (see below).
- Image reconstruction: Scanner-standard ICE, and GADGETRON (magnitude and phase images).
- Images were converted from DICOM to NIFTI format using dcm2niix, resulting in 8 echoes per image.

Tested parameters/conditions

Condition	Phase-Encoding Trajectory	Angulation	Motion
A	Partition In Line	30º	No
B	Partition In Line	30º	Yes
C	Line In Partition	30º	No
D	Line In Partition	30º	Yes
E	Line In Partition	Axial	No
F	Line In Partition	Axial	Yes

Table A1.1. Tested conditions.

Task

During the “No Motion” runs, participants were asked to fixate a central dot. During the "Motion" runs, participants were asked to cross their legs and follow a white dot on the screen with their gaze about halfway through the run. This dot was randomly

presented within a circular region covering 0-2º eccentricity for 1min. After 1 min, participants were asked to uncross their legs, signalling the end of the “motion” task.

Rating

Ratings were provided on the GADGETRON-reconstructed magnitude images. For each condition, images from echoes 1, 4, and 7 were selected and ranked on their quality by 3 neuroimaging experts. A rank of 1 described the image with the best rating/quality, while a rank of 6 depicted the image with the worst rating. Average ranks were given to images that were rated equal in quality.

Results

Phase-Encoding Trajectory

Rankings for partition in line 30º (A&B) and line in partition 30º (C&D) were averaged across participants, echoes, and motion conditions. Similar ratings were obtained for both phase-encoding trajectories (Figure A1.1).

PHASE-ENCODING TRAJECTORY		**Mean**	**SD**	**Ranks**
MEAN(A,B)	PartInLine-30º	3.3	1.4	1
MEAN(C,D)	LineInPart-30º	3.4	1.3	2

Table A1.2. Ranking of phase-encoding trajectory conditions.

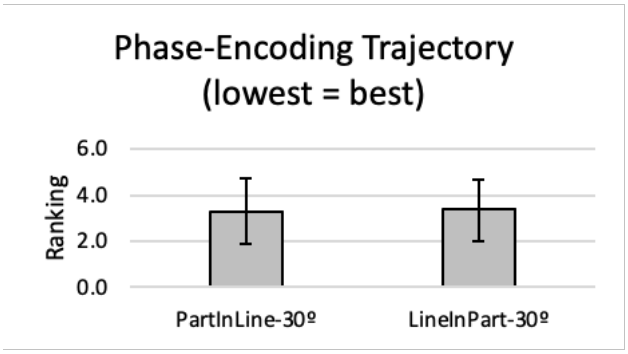

Figure A1.1. Effect of phase-encoding trajectory

Angulation

Rankings for line in partition 30º and line in partition Axial were averaged across participants, echoes, and motion conditions. Better rating (i.e., lowest value) was obtained for 30º compared to axial angulation (Figure A1.2)

ANGULATION		Mean	SD	Ranks
MEAN(C,D)	LineInPart-30º	3.4	1.3	1
MEAN(E,F)	LineInPart-Ax	3.8	1.3	2

Table A1.3. Ranking of angulation conditions.

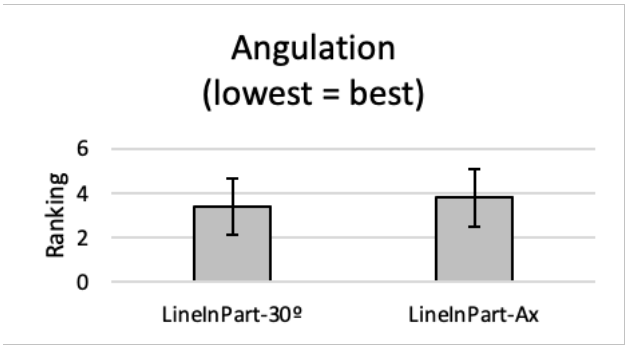

Figure A1.2. Effect of angulation

Motion

Rankings were averaged across participants and echoes, for each condition of interest. We also looked at ranks obtained for each echo (i.e., 1, 4, and 7), separately. Worst ratings (highest values) were given for motion versus no-motion conditions. Across all echoes, the "Line In Partition 30º" condition were ranked first when no motion, whilst the "Partition in Line 30º" condition was ranked first in the "motion" conditions (Figure A1.3). This pattern was also observed at an echo-level for echoes 1 and 7 (Figure A1.3B&D), but not for echo 4, for which the "Partition in Line 30º" condition showed better results in the no-motion and motion conditions (Figure A1.3C). Finally, consistent with the previous finding, conditions with axial angulation (i.e., Conditions E-F) seemed to be the worst ranked.

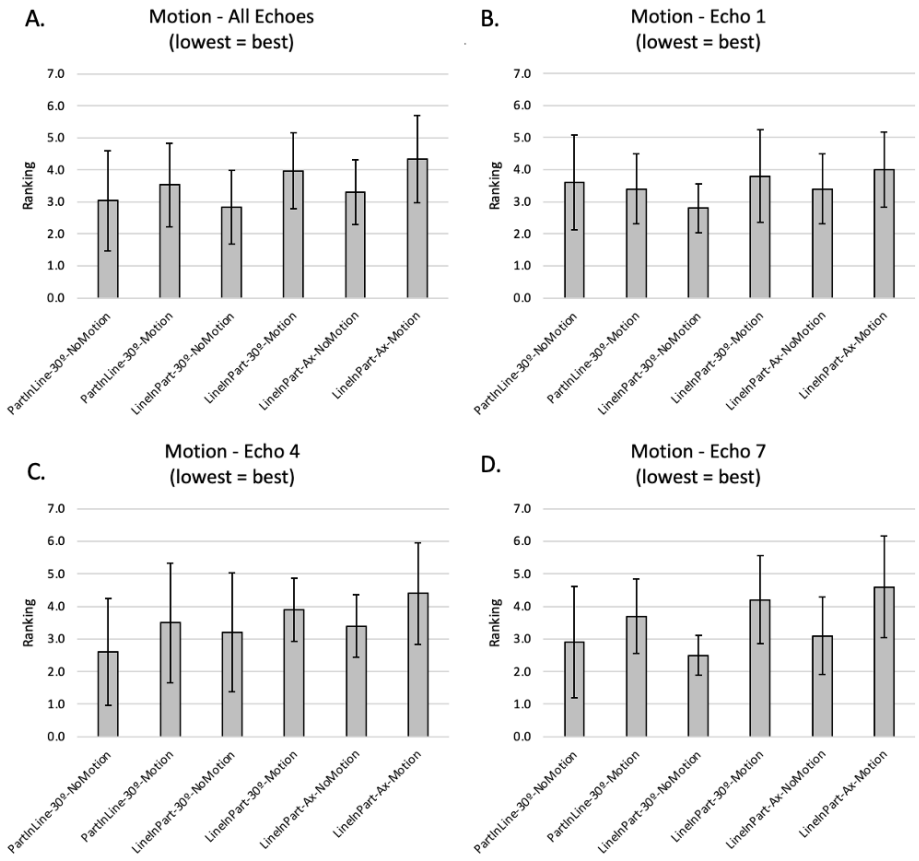

Figure A1.3. Effect of motion.

MOTION - ALL ECHOES		Mean	SD	Ranks
A	PartInLine-30º-NoMotion	3.0	1.6	2
B	PartInLine-30º-Motion	3.5	1.3	4
C	LineInPart-30º-NoMotion	2.8	1.1	1
D	LineInPart-30º-Motion	4.0	1.2	5
E	LineInPart-Ax-NoMotion	3.3	1.0	3
F	LineInPart-Ax-Motion	4.3	1.4	6
MOTION - ECHO 1		**Mean**	**SD**	**Ranks**
A	PartInLine-30º-NoMotion	3.6	1.5	4
B	PartInLine-30º-Motion	3.4	1.1	2
C	LineInPart-30º-NoMotion	2.8	0.8	1
D	LineInPart-30º-Motion	3.8	1.4	5
E	LineInPart-Ax-NoMotion	3.4	1.1	2
F	LineInPart-Ax-Motion	4.0	1.2	6
MOTION - ECHO 4		**Mean**	**SD**	**Ranks**
A	PartInLine-30º-NoMotion	2.6	1.6	1
B	PartInLine-30º-Motion	3.5	1.8	4
C	LineInPart-30º-NoMotion	3.2	1.8	2
D	LineInPart-30º-Motion	3.9	1.0	5
E	LineInPart-Ax-NoMotion	3.4	1.0	3
F	LineInPart-Ax-Motion	4.4	1.6	6
MOTION - ECHO 7		**Mean**	**SD**	**Ranks**
A	PartInLine-30º-NoMotion	2.9	1.7	2
B	PartInLine-30º-Motion	3.7	1.2	4
C	LineInPart-30º-NoMotion	2.5	0.6	1
D	LineInPart-30º-Motion	4.2	1.4	5
E	LineInPart-Ax-NoMotion	3.1	1.2	3
F	LineInPart-Ax-Motion	4.6	1.6	6

Table A1.4. Ranking of motion conditions.

Discussion

Phase-Encoding trajectory

We expected that the RL dimension being narrower than AP would be an important factor in determining which phase-encoding trajectory would result to better image quality. This meant that if RL was the inner dimension, then there would be a

smaller time period between AP increments than vice versa. Here, both “Line in Partition” and “Partition in Line” conditions yielded similar image quality, suggesting that phase-encoding trajectory had no apparent effects on image quality.

Angulation

Our motivation for acquiring data with a 30º angulation was to have the aliases of the eyes running along a diagonal and therefore, ideally missing the cortex. This was reflected in our data by better ranking attributed to images acquired with 30º angulation as compared to those acquired with axial (0º) angulation.

Whilst our expectations were met, the 30º angulation may have also provided more robust parallel imaging or encoding performance because it is exploiting variability in the coil’s sensitivity profile now in two directions, i.e., AP and head-foot. This may also be linked to anatomical structure. Future work could test this on a spherical phantom.

Conclusion

A 30º angulation seemed to provide better data quality compared to axial angulation. Additionally, the “Partition in Line 30º” (Conditions A-B) and “Line in Partition 30º” (Conditions C-D) yielded similar results, making it hard to choose which of these 30º angulation conditions give the best image quality.

References

Magerkurth, J., Volz, S., Wagner, M., Jurcoane, A., Anti, S., Seiler, A., Hattingen, E. and Deichmann, R. (2011), Quantitative T^*_2-mapping based on multi-slice multiple gradient echo flash imaging: Retrospective correction for subject motion effects. Magn. Reson. Med., 66: 989-997. https://doi.org/10.1002/mrm.22878

2. Chapter 2: MPM and Diffusion MRI preprocessing steps

2.1. Diffusion MRI – ACID toolbox: Processing steps

The Eddy-Current and Motion COrrection (ECMoCO) algorithm corrects for spatial misalignments that may occur between dMRI volumes, often caused by motion and electrical currents induced within the brain due to the rapid change magnetic fields produced by rapidly varying MRI gradients (eddy currents). If left uncorrected, these could lead to biased diffusion estimates. The algorithm corrects for spatial misalignments (i.e., motion and the four first-order eddy-current displacements: y-translation, y-scaling, x-y shearing and y-z shearing) by aligning all diffusion volumes to a target volume, using a co-registration algorithm with an affine transformation, and rotating the b-vectors by the obtained rotational parameters.

The Multi-shell Position-Orientation Adaptive Smoothing (msPOAS) is a noise reduction technique for dMRI data that preserves the details in the image (e.g., tissue boundaries). It smooths the image via an iterative adaptive algorithm, only in areas where the data is similar thus avoiding blurring edges and fine structures, by considering both the location of voxels and the direction of diffusion. Key parameters include the number of iterations that define the image smoothness (kstar), the strength of edge detection (lambda), the smoothing ratio (kappa), and the number of receiver coils that contributed to the measured signal (ncoils). An estimate of noise level (sigma) is also needed to guide the smoothing process. Here, we defined a kappa = 0.8 and sigma = 11.1, lambda = 10, kstar = 12, and ncoil = 1.

The Rician bias correction (RBC) addresses a bias that occurs in the estimation of diffusion parameters due to noise. In MRI magnitude images, voxel intensities follow a Rician distribution (or a non-central χ distribution with multiple receiver coils). When diffusion signal models are fitted, this distribution leads to a bias – the Rician bias – in the estimated tensor and kurtosis parameters, as well as in biophysical parameter estimates. This bias is particularly relevant in low signal-to-noise ratio (SNR) situations (e.g., noisy data). ACID implements two RBC approaches: the M2 approach which operates on the dMRI data using the second moment of the non-central distribution of the measured intensities and noise estimates to estimate the true voxel intensities, and an approach that modifies the parameter estimation by considering the non-

central distribution to account for the Rician bias during model fitting. Both methods need an estimate of the noise standard deviation (i.e., sigma = 11.1).

The Hyper-elastic Susceptibility Artifact Correction (HySCO) corrects for geometric distortions caused by susceptibility artifacts. These artifacts occur due to different tissues affecting the magnetic field differently (i.e., different magnetic susceptibilities), causing images to be distorted. ACID corrects for these distortions by estimating the bias field from the blip-up and blip-down images, thus making it easier to see the correct location and shape of brain structures. Corrected blip-up and blip-down images are then combined into one dataset used in further steps.

Next, diffusion tensor and diffusion kurtosis fitting steps apply mathematical models to the data to estimate how water moves in tissues. The Diffusion Tensor Imaging (DTI) model describes the anisotropic water diffusion using a diffusion tensor with six independent diffusion parameters. An assumption is that the direction of axial diffusivity is aligned with the white matter tracts, which may not be the case in complex fibre geometry such as crossing or fanning fibres. We used a non-linear least squares (NLLS) approach to fit the diffusion tensor. From this tensor, we derived rotationally invariant metrics, including fractional anisotropy (FA) and mean (MD), axial (AD), and radial diffusivities (RD). FA and MD quantify the shape and overall magnitude of diffusion. AD and RD quantify the diffusivity parallel and perpendicular to the main axis of diffusion, often linked to the integrity of axonal and myelin contents respectively. The Diffusion Kurtosis Imaging (DKI) model expands on DTI by using a kurtosis tensor (a fourth-order tensor with 15 independent parameters) to capture non-Gaussian water diffusion. Several kurtosis metrics can be estimated, including the mean (MK), axial (AK), and radial kurtosis (RK), as well as the mean (MW), axial (AW), and radial (RW) kurtosis tensor. We used an NLLS algorithm to fit the axisymmetric kurtosis tensor.

Biophysical modelling uses these axisymmetric DKI tensor metrics (AD, RD, MW, AW, RW) to separate the diffusion MRI signal into distinct signal components from various tissue compartments. ACID implements two white matter biophysical models: white-matter tissue integrity (WMTI)-Watson and neurite orientation dispersion and density imaging (NODDI)-DTI. Here we WMTI-Watson model as it uses fewer assumptions about the underlying tissue structure and estimates model parameters directly from the diffusion and DKI metrics, which can provide more

accurate and reliable results. This model assumes that there are two non-exchanging water compartments (intra- and extra-axonal tissue water). The intra-axonal compartment characterises the axons, modelled as long, thick cylinders (or "sticks") with an infinitely small diameter and with an intra-axonal diffusivity and axonal water fraction. This simplification aims to capture the highly anisotropic nature of water diffusion in axons, where water primarily moves along the axonal length. The extra-axonal space is modelled as a homogenous medium described by an asymmetrical diffusion tensor with parallel and perpendicular extra-axonal diffusivities. This represent the space outside the axons, where water diffusion is influenced and restricted by various factors such as the extracellular matrix, cell bodies, and other structures like the myelin sheath surrounding myelinated axons. This model estimation process is "generally degenerate", leading to two possible solutions: the "plus branch" assumes intra-axonal diffusivity is greater than parallel extra-axonal diffusivity, while the "minus branch" assumes the opposite. Here, we chose the “plus branch” solution as it is more biologically plausible.

This modelling step results in five biophysical parameters of microstructural tissue properties: the intra-axonal compartment is characterised by the axonal water fraction (f), and diffusivities inside the axons (D_a), the extra-axonal compartment is characterised by the diffusivity outside and perpendicular ($D_{e,per}$) or parallel ($D_{e,para}$) to the axons. Finally, the Watson axonal alignment parameter (κ) measures fibre orientation coherence, indicating how uniformly the axons are aligned.

2.2. MPM – hMRI toolbox: Processing steps

The Auto-Reorient module aims to re-orient MPM images to a standard, setting the anterior commissure at the origin and aligning both anterior and posterior commissures in the same axial plane, as defined in MNI space. This increases consistency in individual head positions before normalization or segmentation and is performed via a rigid-body alignment of a subject's structural image into the MNI space, without re-slicing of the re-oriented images.

The hMRI-toolbox then corrects for inconsistencies in MRI scans caused by the MRI machine itself, which can lead to inaccurate results. First, the transmit (B1+) bias correction addresses inhomogeneities in the strength of the B1 transmit field throughout the brain, which cause deviations in the local flip angle, by determining the

B1 transmit bias field maps (expressed in per unit of the nominal flip angle). Then, the toolbox corrects for receiver RF sensitivity bias, using the low-resolution, reverse phase-encoding images acquired prior to each MPM contrast (T1w, PDw, and MTw) to generate a receive field sensitivity map for each contrast. This step addresses any coil sensitivity driven signal intensity modulation, which arises because the MRI receiver coil's sensitivity isn't uniform across the brain, causing some areas to appear brighter or dimmer than they should. Additionally, it also accounts for inter-scan variations in sensitivity due to subject motion, ensuring more accurate quantitative MRI map. Finally, the toolbox provides a correction for imperfect spoiling, which occurs because MRI machines do not perfectly eliminate unwanted signals, leading to inaccuracies. This is dependent on the precise sequence protocol settings and can leave a residual bias in the T1w-derived longitudinal relaxation rate (R1) map if no further correction is used. This correction accounts for deviation in R1 values from the ideal scenario described by the Ernst equation.

Quantitative MRI (qMRI) parameter maps are generated through a model fitting approach. Specifically, the signal from multi-echo PDw, T1w, and MTw acquisitions is fit to the Ernst equation. This equation describes how the MRI signal intensity depends on factors like repetition time (TR), flip angle (α), and relaxation rates. From this model, we can estimate qMRI parameters, including the longitudinal relaxation rate (R1), effective transverse relaxation rate (R2*), proton density (PD), and magnetization transfer (MT_{sat}). These parameter maps provide different information about tissue properties, such as their macromolecular content – primarily myelin but also iron content (Edwards et al., 2018).

The R1 map quantifies the rate at which the longitudinal magnetisation of tissue recovers after excitation, which is determined by micro-structural tissue properties such as local mobility of water molecules, macromolecular content (myelin content and iron deposition), and the concentration of paramagnetic ions. It provides quantitative information about tissue composition, mainly lipids such as the cholesterol of myelin, with low R1 values (and thus high qT1 values) often reflecting low myelin content.

The R2* map reflects the combined effects of transversal magnetisation relaxation and magnetic field inhomogeneities. It highlights areas with susceptibility variations such as microbleeds, iron deposits or venous blood. Iron plays an essential

role in the maintenance of myelin sheaths by contributing to the biosynthesis of cholesterol and other lipids. Myelinated fibres, somata of oligodendrocytes, astrocytes, and microglia represent particularly iron-rich compartments in the cortex and have been suggested as main contributors to iron-induced R2* contrast, as compared to neocortical neurons (Edwards et al., 2018). Other factors influencing R2* contrast also include capillaries and vessels, the orientation of myelinated fibres, boundaries between different tissues, and motion and physiological artefacts.

The PD map reflects the distribution and concentration of protons within tissues, which can be helpful in assessing tissue composition and detecting variations in water content, as well as providing anatomical details. Previous studies suggest some link to myelin-content, however, large changes in PD are less likely to be exclusively from myelination. Instead, the biological membranes and other chemical components of neuronal fibres can also contribute to variations in PD contrast, such as dendrite or glial cell proliferation (Gomez et al., 2017).

Finally, the MT_{sat} map is a proxy measure of the bound-pool water fraction, providing information about the interaction between free water protons and protons bound to macromolecules and is often used a marker for myelin content. It represents the fraction of free water saturated by a single magnetisation transfer (MT) pulse during one repetition time (TR). If there is a lot of transfer of bounded-protons to free-water protons, there is a high saturation of the signal which is in turn quantified by high MT_{sat} values. In case of low myelin content (e.g., demyelination), less transfers between bounded- and free-protons should occur, and low MT_{sat} values be obtained. However, whilst empirical studies show that MT_{sat} correlates with myelin-content (York et al., 2022), it is also influenced by pathological processes unrelated to myelination such as inflammation (Vavasour et al., 2011).

3. Chapter 2: Tract segmentation results

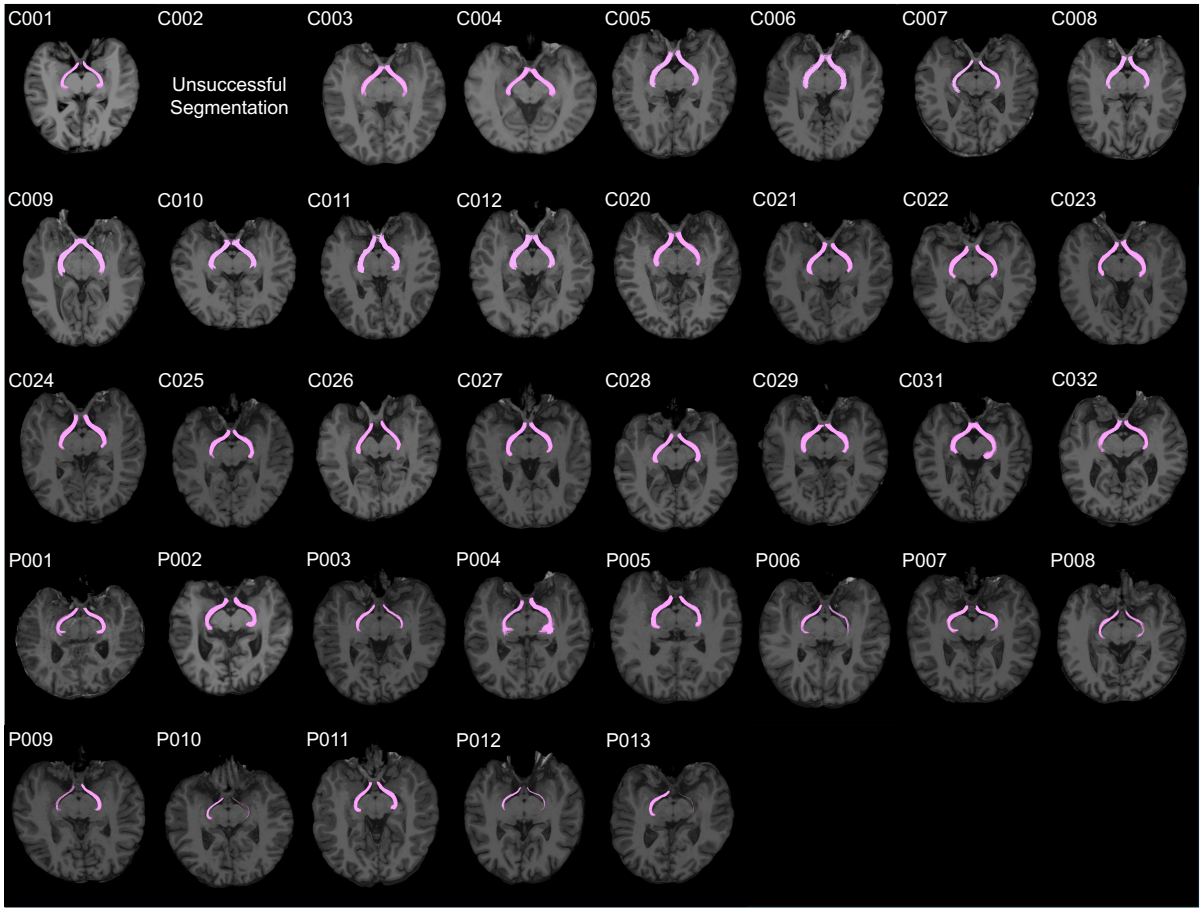

Figure A3.1. Resulting cleaned optic tracts in controls (C001-C032) and LHON patients (P001-P013).

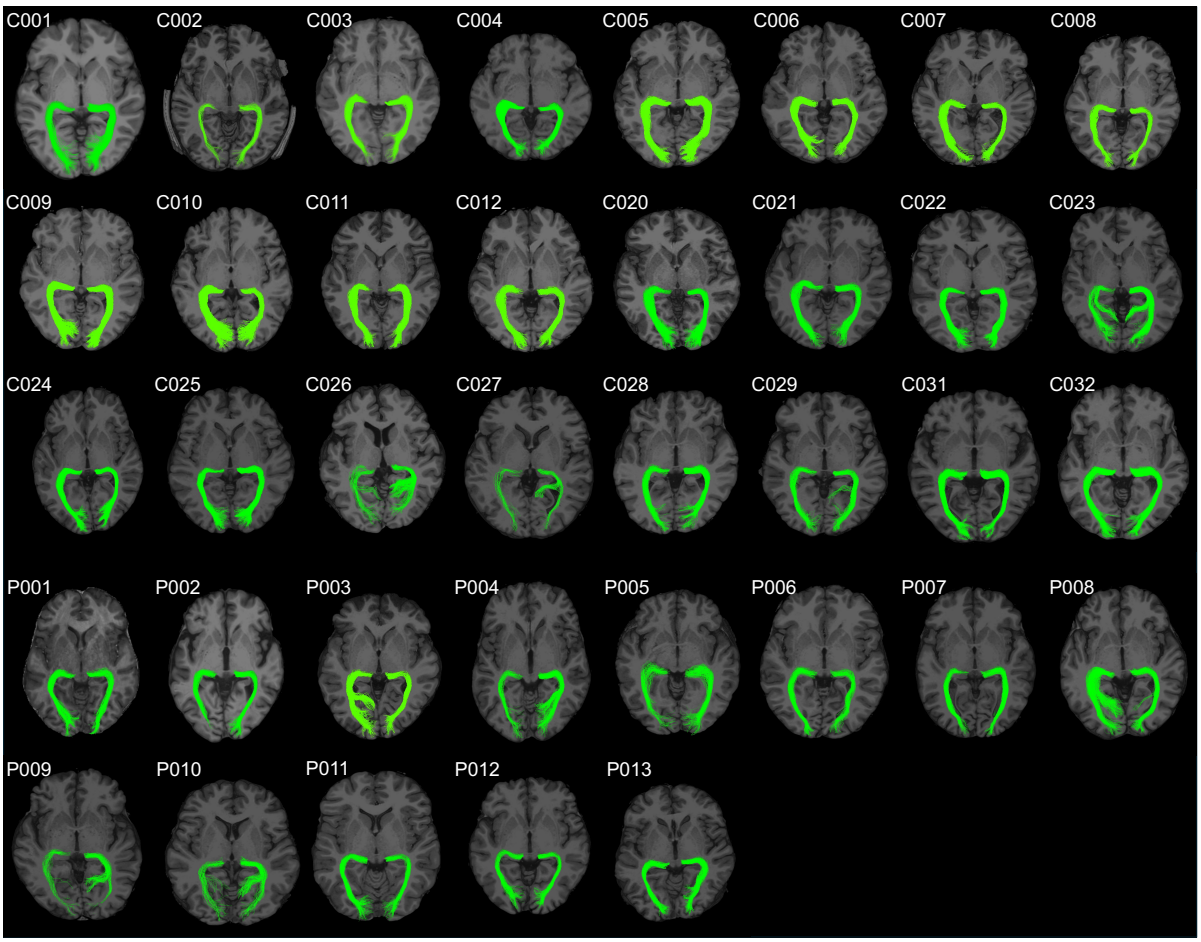

Figure A3.2. Resulting cleaned optic radiations in controls (C001-C032) and LHON patients (P001-P013).

4. Chapter 2: Sanity check for MPM measures in optic radiations and vertical occipital fasciculi, for healthy controls and LHON patients.

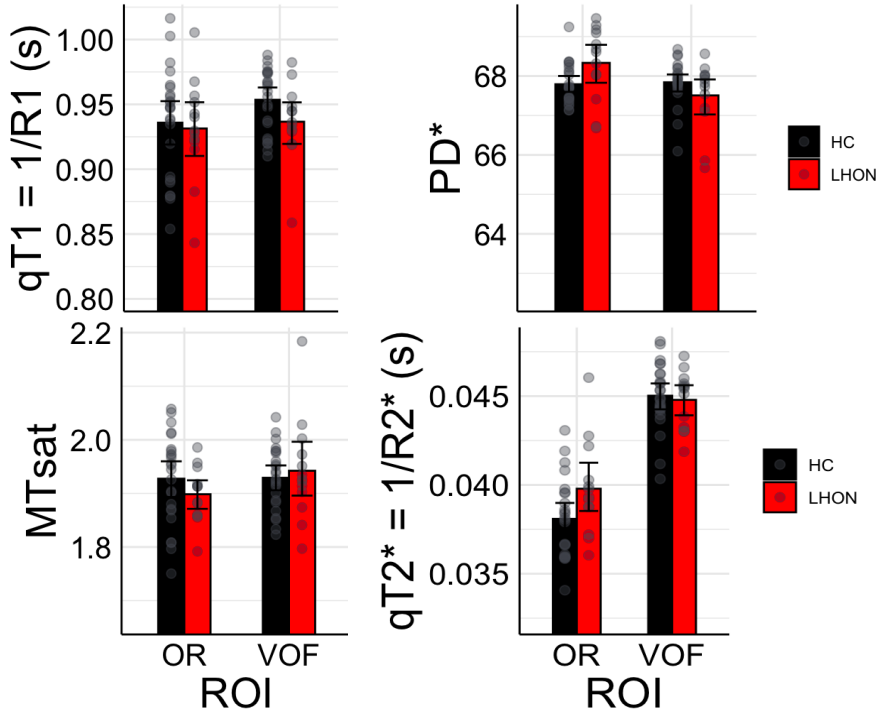

Figure A4.1. Overall MPM values obtained in Optic Radiations (OR) and Vertical Occipital Fasciculi (VOF), for healthy controls (black) and LHON patients (red).

5. Chapter 2: Diffusion MRI and MPM measures along the optic tracts and radiations

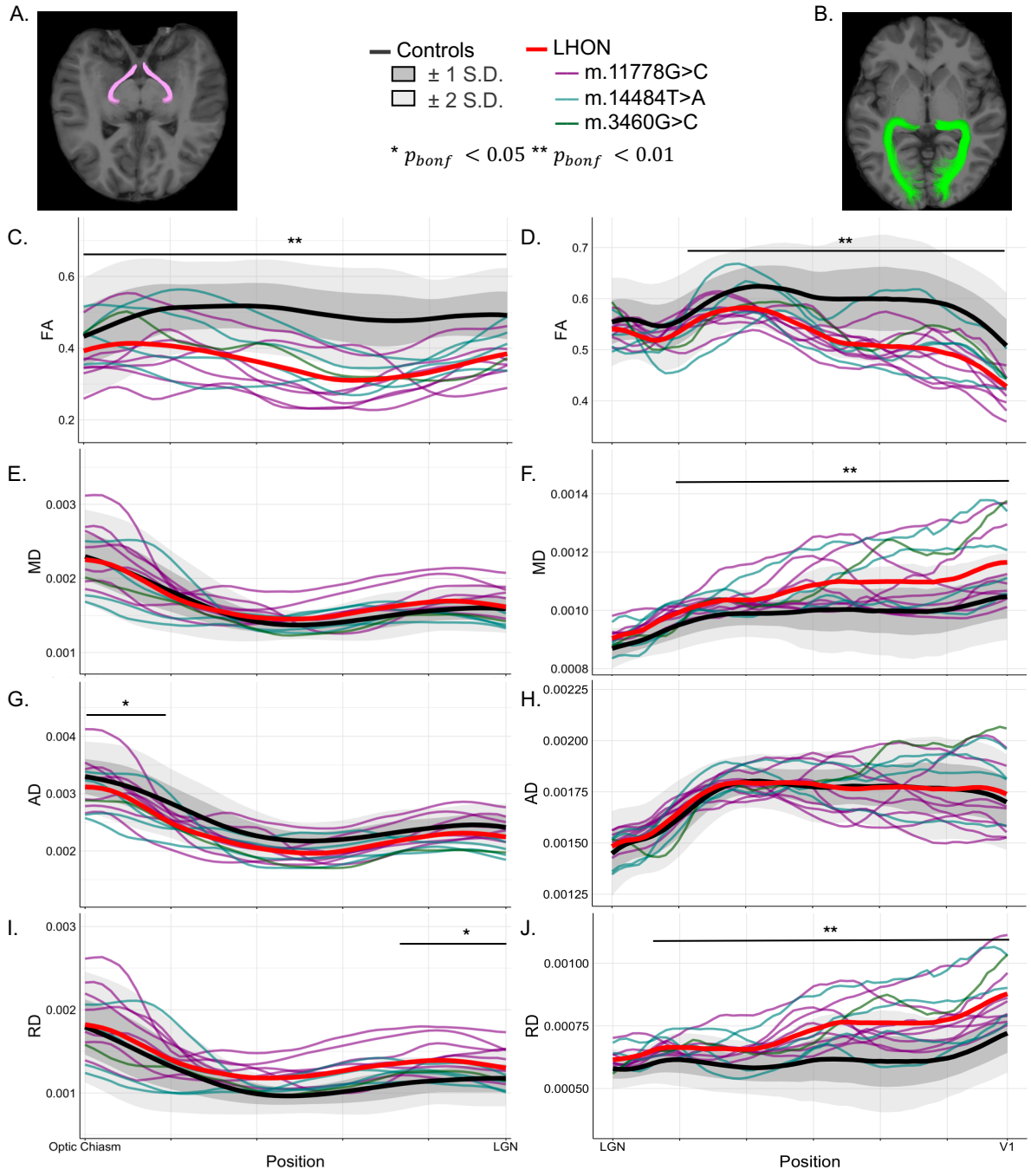

Figure A5.1. Altered diffusion tensor imaging measures along the optic pathways in LHON. (A, B) Segmented optic tracts and radiations overlaid on MPRAGE images from a control participant. (C, E, G, I): Fractional anisotropy (FA), mean diffusivity (MD), axial diffusivity (AD), and radial diffusivity (RD) along the optic tracts (optic chiasm to LGN). (D, F, H, J) FA, MD, AD, and RD along the optic radiations (LGN to V1). Black line corresponds to the control group mean, with shaded areas representing ±1 (dark grey) and ±2 (light grey) standard deviations.

Red line corresponds to the LHON group mean. Individual LHON traces are colour-coded based by mutation: m.11778G>C (purple), m.14484T>A (cyan), m.3460G>C (dark green).

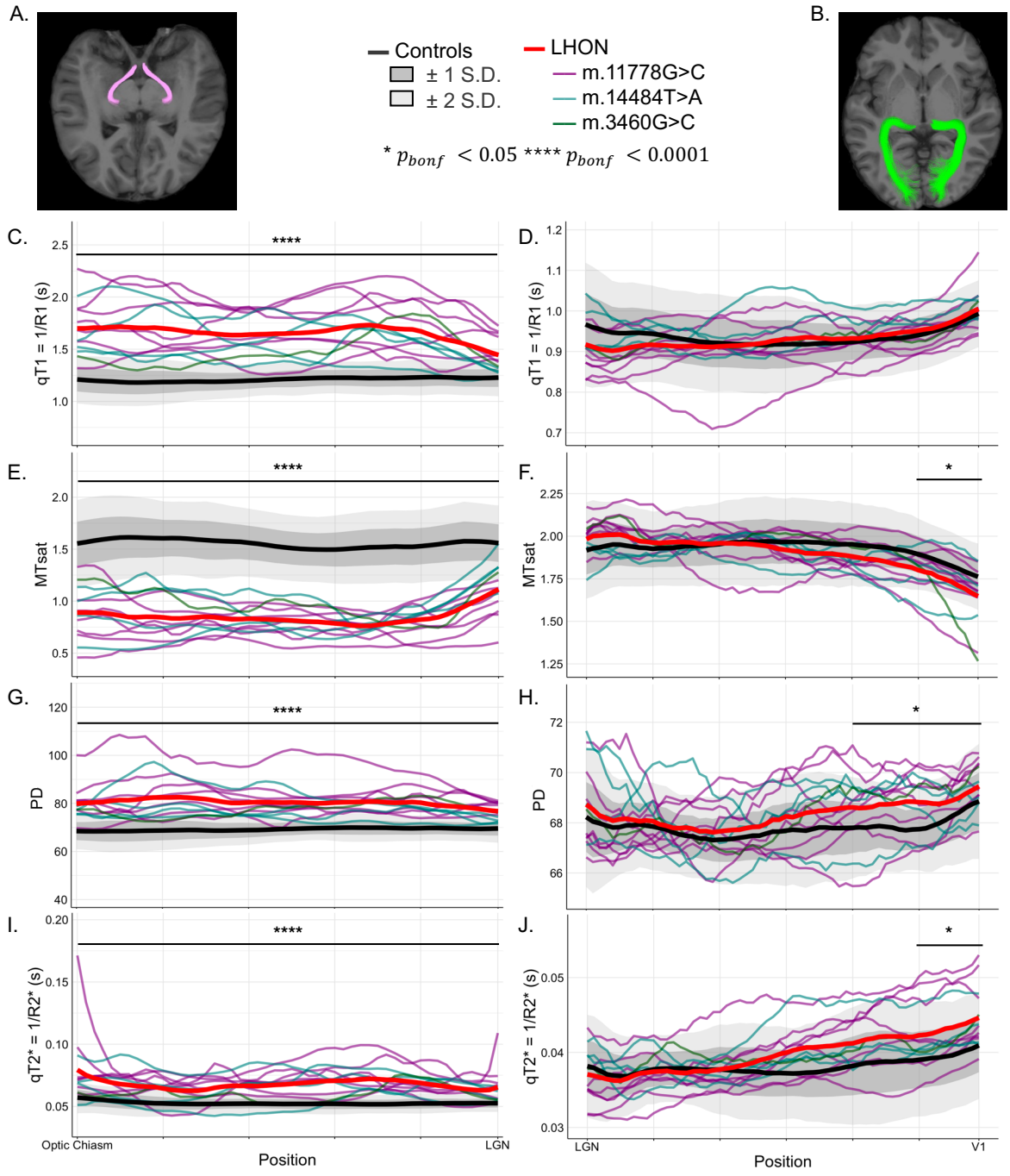

Figure A5.2. Demyelination patterns along the optic pathways in LHON.
(A, B) Segmented optic tracts and radiations overlaid on MPRAGE images from a control participant. (C, E, G, I): qT1, MT_{sat}, PD, and qT2 along the optic tracts (optic chiasm to LGN). (D, F, H, J) Same measures along the optic radiations (LGN to V1). Black line corresponds to the control group mean, with shaded areas representing ±1 (dark grey) and ±2 (light grey) standard deviations. Red line corresponds to the LHON group mean. Individual LHON traces*

are colour-coded based by mutation: m.11778G>C (purple), m.14484T>A (cyan), m.3460G>C (dark green).

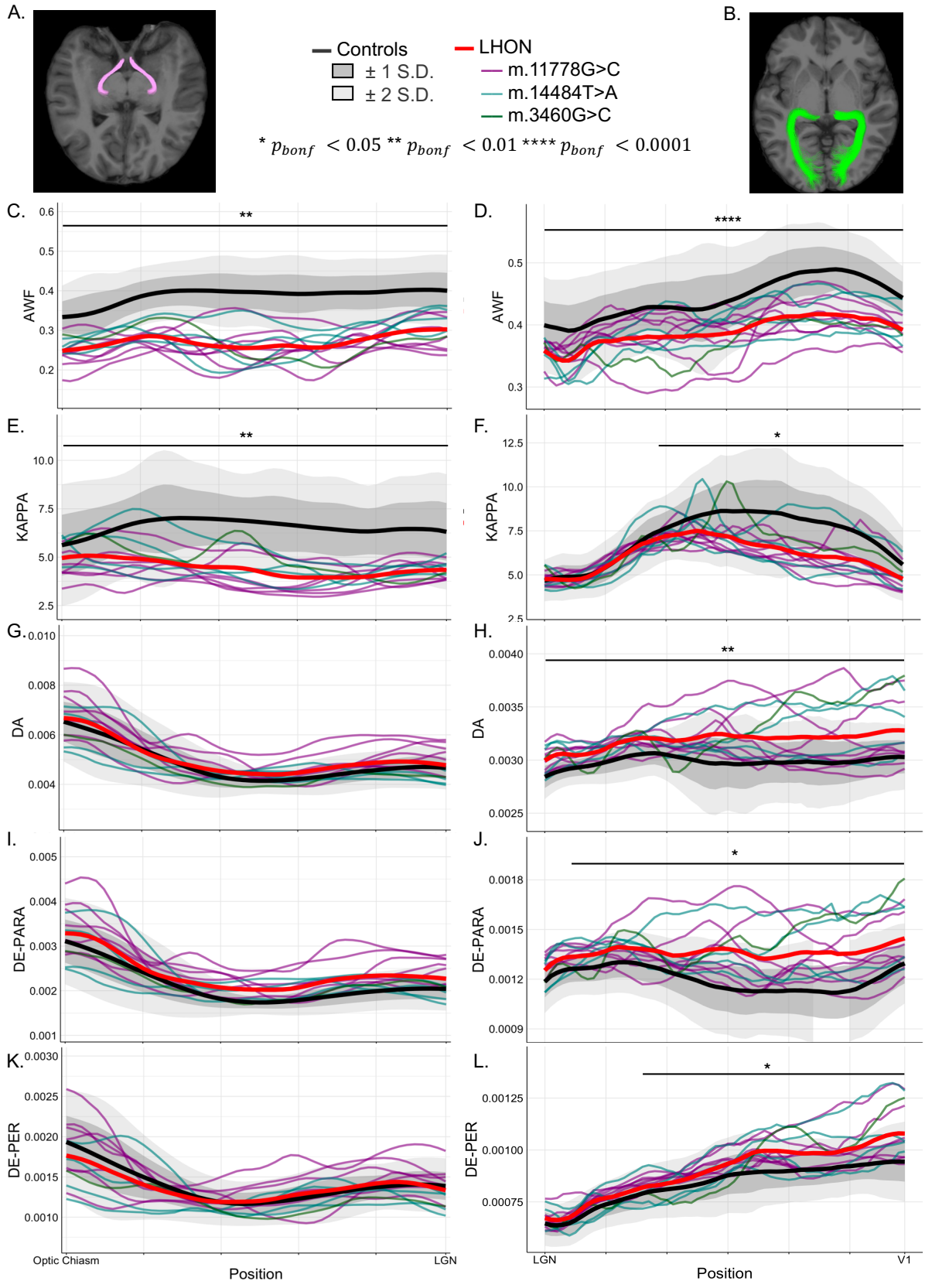

Figure A5.3. Altered biophysical parameters along the optic pathways in LHON.

(A, B) Segmented optic tracts and radiations overlaid on MPRAGE images from a control participant. (C, E, G, I, K) Axonal water fraction (f), axonal alignment (κ), diffusivity intra-axonal (D_a) and diffusivities outside, parallel ($D_{e,para}$) and perpendicular ($D_{e,per}$) to the axons, along the optic tracts (optic chiasm to LGN). (D, F, H, J, L): Same measures along the optic radiations (LGN to V1). Black line corresponds to the control group mean, with shaded areas representing ±1 (dark grey) and ±2 (light grey) standard deviations. Red line corresponds to the LHON group mean. Individual LHON traces are colour-coded based by mutation: m.11778G>C (purple), m.14484T>A (cyan), m.3460G>C (dark green).

6. Chapter 2: Morphometric measures

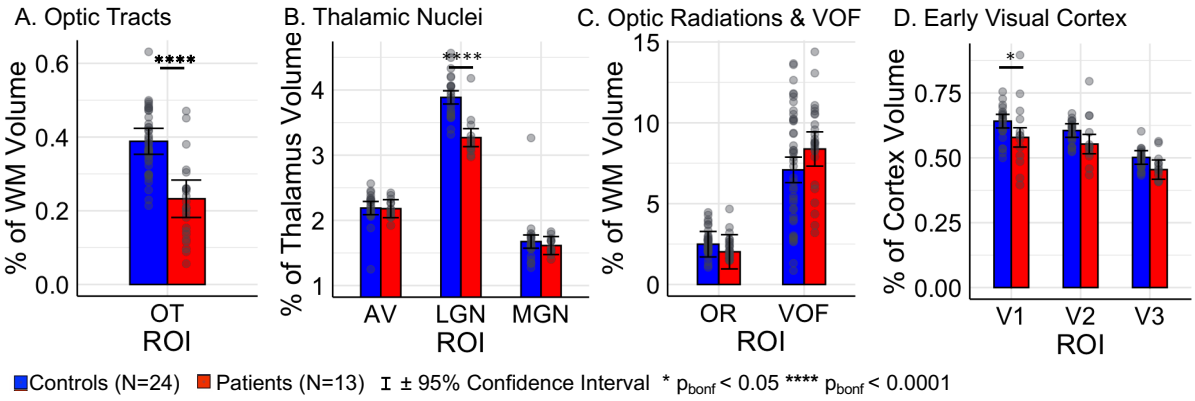

Figure A6.1. Volume changes along the visual pathway and control regions.
(A) Optic tracts (OT). (B) Subcortical thalamic nuclei: lateral (LGN) and medial (MGN) geniculate nuclei, and antero-ventral nucleus (AV). (C) Optic Radiations and Vertical Occipital Fasciculi (VOF). (D) Early Visual Cortex: primary (V1), secondary (V2), and tertiary (V3) visual cortex. Error bars correspond to 95% confidence intervals; individual data are plotted in grey.

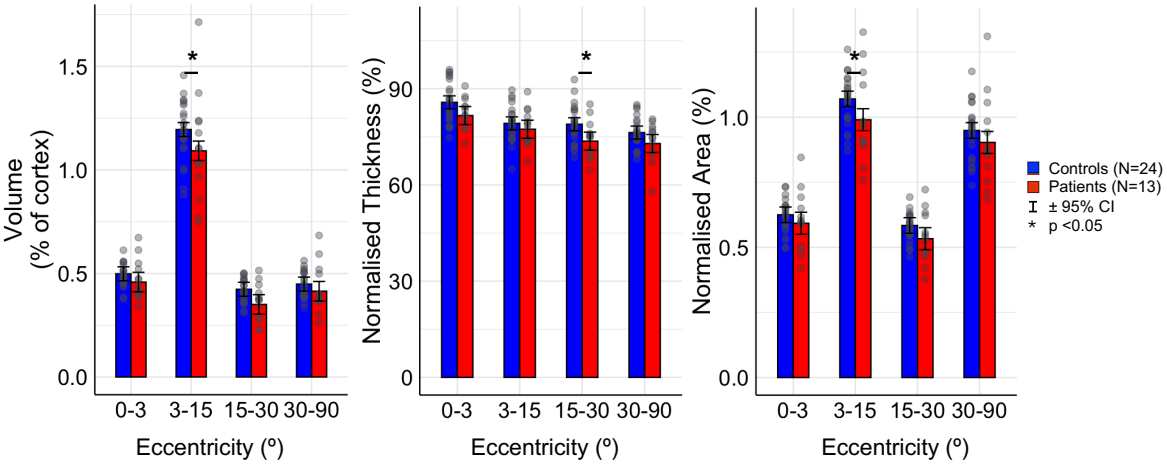

Figure A6.2. Volume, thickness and area alterations across four eccentricity bins in V1 between LHON patients and controls.
Eccentricity bins (0-3, 3-15, 15-30, 30-90°) were defined based on vertex-wise eccentricity estimates obtained with Benson Atlas. Error bars correspond to 95% confidence intervals; individual data are plotted in grey.

Region	Measure	Estimate	S.E.	df	t-value	p-value
Optic Tracts	Volume	-0.148866	0.032580	31	-4.569	**7.35e-05**
LGN	Volume	6.17e-01	0.0875	1780	7.054	**<.0001**
MGN	Volume	6.07e-02	0.0875	1780	0.694	1.0000
AV	Volume	9.31e-03	0.0875	1780	0.106	1.0000

Optic Radiations	Volume	0.47	0.672	58.6	0.700	1.0000
VOF	Volume	-1.29	0.672	58.6	-1.923	0.2374
V1 Overall	Volume	0.01170	0.00401	35.8	2.915	**0.0183**
	Thickness	3.66	1.33	46.8	2.752	**0.0252**
	Area	0.0522	0.0229	37.2	2.280	0.0853
0-3º	Volume	0.00929	0.00448	55.2	2.073	0.5139
	Thickness	4.129	1.78	141	2.325	0.2579
	Area	0.0324	0.0264	64.7	1.230	1.0000
3-15º	Volume	0.01451	0.00448	55.2	3.239	**0.0244**
	Thickness	1.825	1.78	141	1.027	1.0000
	Area	0.0798	0.0264	64.7	3.026	**0.0426**
15-30º	Volume	0.01157	0.00448	55.2	2.583	0.1498
	Thickness	5.277	1.78	141	2.972	**0.0418**
	Area	0.0508	0.0264	64.7	1.926	0.7019
30-90º	Volume	0.01145	0.00448	55.2	2.556	0.1603
	Thickness	3.418	1.78	141	1.925	0.6755
	Area	0.0459	0.0264	64.7	1.743	1.0000
V2 Overall	Volume	0.00987	0.00401	35.8	2.459	0.0566
	Thickness	1.48	1.33	46.8	1.111	0.8167
	Area	0.0537	0.0229	37.2	2.344	0.0735
0-3º	Volume	0.01129	0.00448	55.2	2.521	0.1755
	Thickness	2.063	1.78	141	1.162	1.0000
	Area	0.0493	0.0264	64.7	1.869	0.7941
3-15º	Volume	0.01314	0.00448	55.2	2.933	0.0586
	Thickness	0.402	1.78	141	0.226	1.0000
	Area	0.0840	0.0264	64.7	3.186	**0.0266**
15-30º	Volume	0.00744	0.00448	55.2	1.661	1.0000
	Thickness	2.340	1.78	141	1.318	1.0000
	Area	0.0399	0.0264	64.7	1.514	1.0000
30-90º	Volume	0.00763	0.00448	55.2	1.702	1.0000
	Thickness	1.109	1.78	141	0.624	1.0000
	Area	0.0416	0.0264	64.7	1.580	1.0000
V3 Overall	Volume	0.00844	0.00401	35.8	2.102	0.1279
	Thickness	1.81	1.33	46.8	1.363	0.5380
	Area	0.0381	0.0229	37.2	1.663	0.3141
0-3º	Volume	0.01450	0.00448	55.2	3.238	**0.0245**
	Thickness	4.604	1.78	141	2.593	0.1263
	Area	0.0509	0.0264	64.7	1.932	0.6930
3-15º	Volume	0.01001	0.00448	55.2	2.235	0.3536
	Thickness	0.771	1.78	141	0.434	1.0000
	Area	0.0494	0.0264	64.7	1.875	0.7837
15-30º	Volume	0.00437	0.00448	55.2	0.975	1.0000

	Thickness	1.512	1.78	141	0.851	1.0000
	Area	0.0238	0.0264	64.7	0.903	1.0000
30-90º	Volume	0.00488	0.00448	55.2	1.089	1.0000
	Thickness	0.369	1.78	141	0.208	1.0000
	Area	0.0282	0.0264	64.7	1.071	1.0000

Table A6.1. Statistical comparisons of grey and white matter morphology between controls and LHON patients.

For each participant, white-matter volumes were normalised by the total cerebral white matter volume, subcortical volumes by the total thalamic volume, and cortical volumes by the estimated total intracranial volume (eTIV). Cortical thickness was normalised to the subject's mean thickness across V1–V3, and cortical surface area to the total V1–V3 surface area. Linear mixed-effects models (LMM) were fitted using restricted maximum likelihood (ReML) in R. Each model included fixed effects for Group, ROI, age, sex, and BMI, with random intercepts for subjects (SubID) to account for within-subject variability. For V1-V3, we also investigated changes across eccentricities, by adding Eccentricity as an ordered fixed effect. For the optic tracts, reported estimates reflect the results from the LME model. For the other regions, reported estimates reflect pairwise comparisons between Control and LHON groups. P-values for optic radiations, LGN and V1-V3 were Bonferroni-corrected. SE: standard error; df: degree of freedom.

7. Chapter 3: Method implementation and validation in simulated and pathological vision loss (Chow-Wing-Bom et al., 2025, *eLife*)

7.1. Large-Field set-up

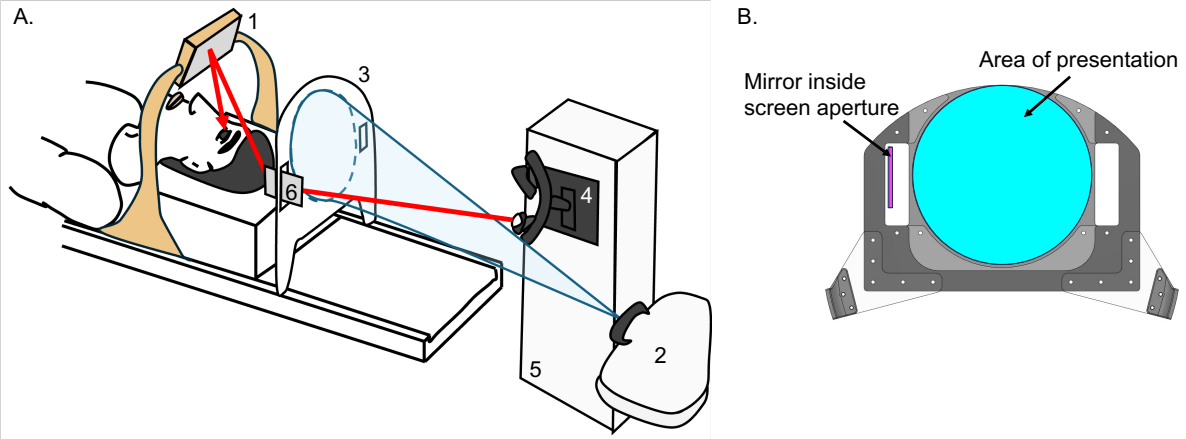

Figure A7.1. Schematic of Large-Field Set-Up.
(A) The participant lies on the scanner bed in the 64-channel coil without top to reduce obstruction and views the 40° screen via a mirror above their face (1). Stimuli are displayed using back-projection from a projector (2) outside the room, onto a screen (3) positioned behind the participant's head. The top of the screen follows the scanner bore curvature to maximise field of view. Monocular eye-tracking is achieved by mounting the illuminator and camera of the eye-tracker (4) vertically on a support (5) at the back of the scanner bore. An image of the eye is obtained via a dual-mirror set-up, including a small mirror inside an aperture cut on the side of the screen (6) and the participant mirror (1). If the right eye is being tracked, the eye-tracker is placed on the left side of the scanner bore, and the eye-tracker mirror (6) is placed in the right screen aperture. (B) Schematic of the large-field screen, with the area of stimulus presentation shown in cyan and the mirror used for eye-tracking in magenta. The mirror is positioned within one of the two rectangular apertures cut on either side of the screen. Image from Chow-Wing-Bom et al., 2025, eLife.

7.2. Individual Level Statistics

To test for contrast sensitivity differences across the visual field in individual participants, we also employed a multilevel modelling approach using the lme4 package in R (Bates et al., 2015; R Core Team, 2023). This approach reduces the impact of vertex-level variability and redundancy. The model included the square root of stimulus contrast as a continuous fixed-effect predictor, and eccentricity, polar location, and spatial frequency as categorical fixed-effect predictors, along with all

possible interactions. Again, the intercept was fixed at 0. The model also included random slopes for the square root contrast and the interaction between square root contrast and voxel-specific factors and was fit separately for each participant. In the formula notation used in the R package lme4, the model would be defined as:

$$\beta \sim 0 + SqrtContrast + SqrtContrast{:}SF + SqrtContrast{:}Eccentricity + SqrtContrast{:}PolarLocation + SqrtContrast{:}SF{:}Eccentricity + SqrtContrast{:}SF{:}PolarLocation + SqrtContrast{:}Eccentricity{:}PolarLocation + SqrtContrast{:}Eccentricity{:}PolarLocation{:}SF + (0 + SqrtContrast + SqrtContrast{:}SF \mid VoxelIdx)$$

SubID	Effects	*Df*	Sum Sq	Mean Sq	*F*-value	*Pr*(>*F*)	Signif.
C1	SF	1	3720	3720	72.49	< 2e-16	***
	Eccentricity	1	35003	35003	681.995	< 2e-16	***
	PolarLocation	3	11258	3753	73.115	< 2e-16	***
	SF:Eccentricity	1	23914	23914	465.938	< 2e-16	***
	SF:PolarLocation	3	1546	515	10.041	1.32E-06	***
	Eccentricity:PolarLocation	3	200	67	1.297	0.274	
	SF:Eccentricity:PolarLocation	3	1158	386	7.519	5.04E-05	***
	Residuals	12378	635290	51			
C2	SF	1	23704	23704	743.628	< 2e-16	***
	Eccentricity	1	13503	13503	423.609	< 2e-16	***
	PolarLocation	3	46442	15481	485.647	< 2e-16	***
	SF:Eccentricity	1	10587	10587	332.135	< 2e-16	***
	SF:PolarLocation	3	2981	994	31.169	< 2e-16	***
	Eccentricity:PolarLocation	3	2881	960	30.126	< 2e-16	***
	SF:Eccentricity:PolarLocation	3	373	124	3.899	8.52E-03	**
	Residuals	11604	369897	32			
C3	SF	1	27	27	1.374	0.2411	
	Eccentricity	1	578	578	29.019	7.33E-08	***
	PolarLocation	3	7315	2438	122.52	< 2e-16	***
	SF:Eccentricity	1	14719	14719	739.59	< 2e-16	***
	SF:PolarLocation	3	257	86	4.311	4.80E-03	**
	Eccentricity:PolarLocation	3	2225	742	37.261	< 2e-16	***
	SF:Eccentricity:PolarLocation	3	510	170	8.543	1.16E-05	***
	Residuals	9860	196225	20			

C4	SF	1	25290	25290	521.73	< 2e-16	***
	Eccentricity	1	3970	3970	81.89	< 2e-16	***
	PolarLocation	3	34475	11492	237.08	< 2e-16	***
	SF:Eccentricity	1	75054	75054	1548.38	< 2e-16	***
	SF:PolarLocation	3	2514	838	17.29	3.40E-11	***
	Eccentricity:PolarLocation	3	16417	5472	112.89	< 2e-16	***
	SF:Eccentricity:PolarLocation	3	3921	1307	26.97	< 2e-16	***
	Residuals	9896	479688	48			
C5	SF	1	554	554	16.332	5.37E-05	***
	Eccentricity	1	6717	6717	198.161	< 2e-16	***
	PolarLocation	3	886	295	8.711	9.12E-06	***
	SF:Eccentricity	1	13436	13436	396.384	< 2e-16	***
	SF:PolarLocation	3	4753	1584	46.744	< 2e-16	***
	Eccentricity:PolarLocation	3	3023	1008	29.727	< 2e-16	***
	SF:Eccentricity:PolarLocation	3	2638	879	25.939	< 2e-16	***
	Residuals	7728	261956	34			

Table A7.2.1. Results from the multilevel modelling approach in each individual participant. pRF mapping was used to link brain responses to visual field locations. Table from Chow-Wing-Bom et al., 2025, eLife.

SubID	**Effects**	***contrast***	**estimate**	**SE**	**df**	**t.ratio**	**p.value**	
C1	PolarLocation	HM>VM	5.5138156	0.3278444	12354	16.818391	8.917786e-63	***
		LVM>UVM	0.5999187	0.2796053	12354	2.145591	0.03192504	*
		LHM>RHM	0.7058217	0.1711807	12354	4.123254	3.759997e-05	***
C2	PolarLocation	HM>VM	5.533751	0.2284595	11580	24.22203	1.771783e-126	***
		LVM>UVM	4.387544	0.1852974	11580	23.67839	4.420105e-121	***
		LHM>RHM	2.288693	0.1336361	11580	17.12630	5.942464e-65	***
C3	PolarLocation	HM>VM	3.568024	0.2172194	9836	16.425896	7.786414e-60	***
		LVM>UVM	2.317875	0.1801032	9836	12.869704	1.339442e-37	***
		LHM>RHM	0.159411	0.1214377	9836	1.312697	0.1893155	
C4	PolarLocation	HM>VM	7.3408010	0.3070954	9872	23.903972	8.223761e-123	***
		LVM>UVM	3.1514598	0.2492052	9872	12.646043	2.250910e-36	***
		LHM>RHM	-0.9417519	0.1794558	9872	-5.247821	1.571031e-07	***
C5	PolarLocation	HM>VM	2.2997460	0.2874033	7704	8.001807	1.405261e-15	***
		LVM>UVM	0.2736311	0.2296279	7704	1.191628	0.2334437	
		LHM>RHM	-0.2201730	0.1728344	7704	-1.273896	0.2027387	
C6	PolarLocation	HM>VM	1.8040008	0.2259007	9336	7.985813	1.561107e-15	***
		LVM>UVM	3.2006411	0.1818476	9336	17.600678	3.057311e-68	***
		LHM>RHM	0.3046082	0.1340245	9336	2.272779	0.02306211	*
C7	PolarLocation	HM>VM	5.9085493	0.3067623	10770	19.261005	2.637528e-81	***
		LVM>UVM	2.0334164	0.2617710	10770	7.767922	8.703410e-15	***
		LHM>RHM	-0.3370417	0.1599345	10770	-2.107373	0.03510831	*
Signif. codes: 0 '***' 0.001 '**' 0.01 '*' 0.05 '.' 0.1 ' ' 1								

Table A7.2.2. Post-Hoc test on ANOVA visual quadrant position effect (PolarLocation) at the individual level. pRF mapping was used to relate brain responses to visual field locations. Table from Chow-Wing-Bom et al., 2025, eLife.

7.3. Calibrated Benson Template Atlas

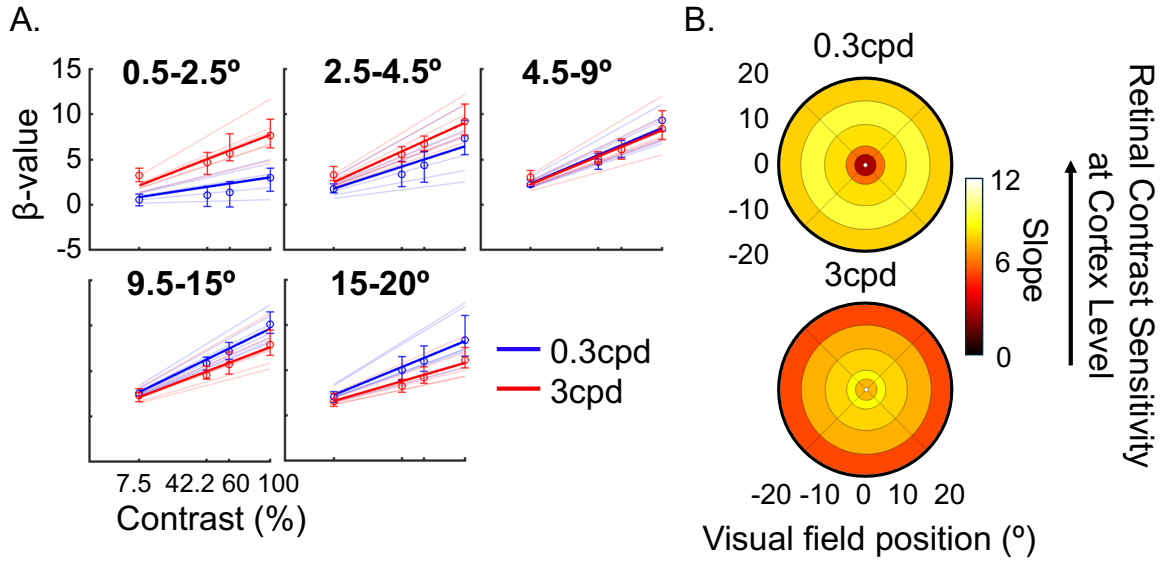

A7.3.1. V1 contrast sensitivity (i.e., slopes) across 5 eccentricity bins (0.5º-2.5º, 2.5º-4.5º, 4.5º-9.5º, 9.5º-15º, and 15-20º), defined using the calibrated Benson atlas.

(A) β-values versus contrast levels for each eccentricity bin. Blue and red lines represent the contrast sensitivity model fits for the 0.3cpd and 3cpd conditions, respectively. Thinner lines correspond to individual fits. (B) V1 contrast sensitivity index (i.e., slope) projected back into the visual space using the calibrated Benson atlas, for each eccentricity bin and spatial frequency condition. The colour scale indicates slope estimates, with higher values representing higher V1 contrast sensitivity. Image from Chow-Wing-Bom et al., 2025, eLife.

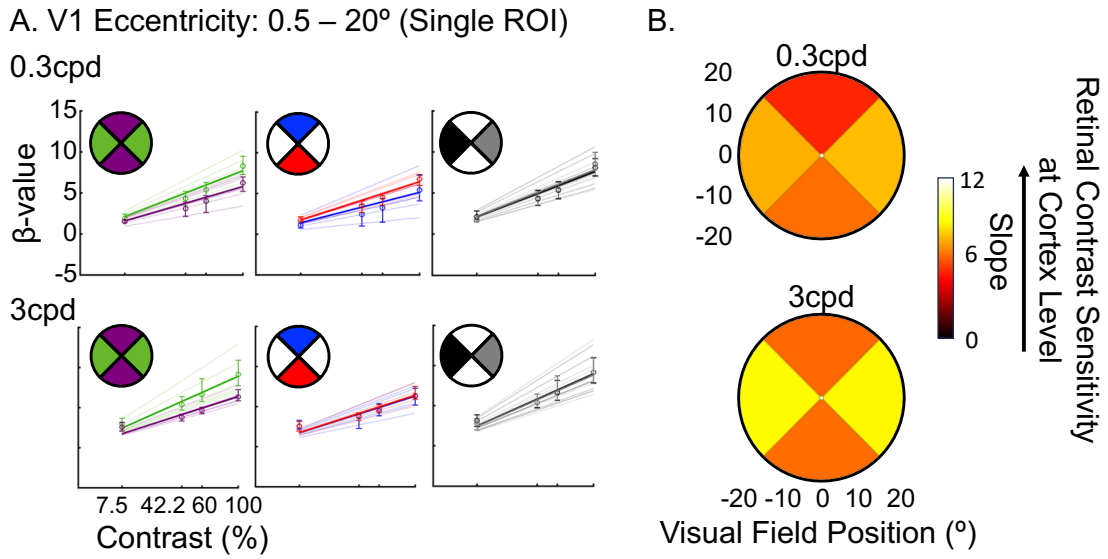

Figure A7.3.2. V1 contrast sensitivity (i.e., slopes) across visual field quadrants using the calibrated Benson atlas, for the 0.3cpd and 3cpd conditions.

Visual quadrants were defined as ±45º regions around the cardinal meridians and slope values were selected for eccentricities between 0.5-20º. Horizontal quadrants are left and right, whilst upper and lower quadrants define the vertical quadrants. (A) β-values versus contrast levels for each anisotropy effects: horizontal versus vertical, upper versus lower, and left versus right. Group-level model fits are in thick lines, whilst thinner lines correspond to individual fits. Error bars represent the 95% confidence intervals. (B) V1 contrast sensitivity index (i.e., slope) projected back into the upper, lower, left and right visual field quadrants for the 0.3cpd and 3cpd conditions. The colour scale represents slope estimates, with higher values indicating higher V1 contrast sensitivity. Image from Chow-Wing-Bom et al., 2025, eLife.

Measure of Interest: Slope	num Df	den Df	MSE	F	ges	Pr(>F)	
SF	1.0000	6.0000	31.436	0.6117	0.010887	0.4639018	
ECC	2.1650	12.9901	32.694	4.7020	0.160027	0.0270342	*
PolarLocation	1.7729	10.6374	27.316	7.0357	0.163209	0.0129521	*
SF:Eccentricity	2.2706	13.6238	7.438	29.4822	0.221807	7.552e-06	***
SF:PolarLocation	1.5885	9.5309	5.173	2.1025	0.009793	0.1783533	
Eccentricity: PolarLocation	12.0000	72.0000	5.253	2.9645	0.096634	0.0020990	**
SF: Eccentricity: PolarLocation	12.0000	72.0000	1.195	3.5212	0.028091	0.0003995	***
Signif. codes: 0 '***' 0.001 '**' 0.01 '*' 0.05 '.' 0.1 ' ' 1							

Table A7.3.1. Group-Level ANOVA analysis on slope estimates, as function of spatial frequency, eccentricities, and visual quadrant positions.
The Benson template retinotopic map was used to relate brain responses to visual field locations. Table from Chow-Wing-Bom et al., 2025, eLife.

Measure of Interest: Slope	contrast	estimate	SE	df	t.ratio	p.value
PolarLocation	Horizontal>Vertical	4.3378240	1.2101752	6	3.5844596	0.01158079
	Lower>Upper	0.5249520	0.7053736	6	0.7442184	0.48485944
	Left>Right	-0.2265194	0.3922638	6	-0.5774671	0.58462631
SF:Eccentricity	3cpd-0.3cpd: 0.5-2.5º	4.5917619	0.7960846	6	5.7679320	0.001185113
	3cpd-0.3cpd: 2.5-4.5º	2.5801243	1.0192745	6	2.5313340	0.044599322
	3cpd-0.3cpd: 4.5-9.5º	-0.2927635	0.9981812	6	-0.2932969	0.779175269
	3cpd-0.3cpd: 9.5-15º	-1.9782789	0.6042727	6	-3.2738182	0.016953076
	3cpd-0.3cpd: 15-20º	-2.2803080	0.6462658	6	-3.5284368	0.012391168

Table A7.3.2. Post-hoc t-test analysis for the visual quadrant position effect (PolarLocation) and the interaction between spatial frequency and eccentricities (SF:Eccentricity).
The Benson template retinotopic map was used to relate brain responses to visual field locations. Table from Chow-Wing-Bom et al., 2025, eLife.

7.4. Simulated Eye-Motion

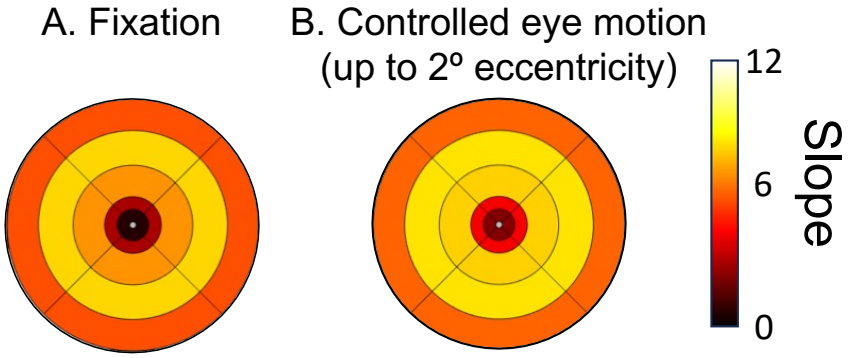

Figure A7.4. V1 contrast sensitivity (i.e., slope) to the 0.3cpd condition plotted back into visual space under fixation (A) and controlled eye-motion (B) conditions, in participant C6. pRF estimates were used to relate brain responses to visual field positions. Image from Chow-Wing-Bom et al., 2025, eLife.

8. Chapter 4: Mapping cortical visual field defects in LHON patients

8.1. Retinal-Behavioural-Cortical correspondence using the Garway-Heath sectorisation approach

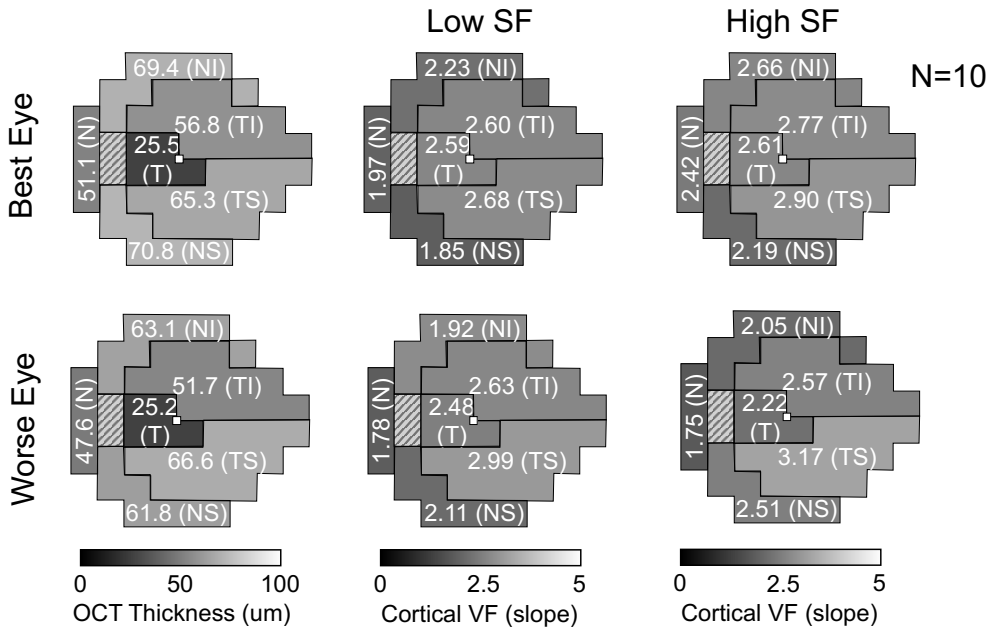

Figure A8.1. Correspondence between OCT pRNFL thickness and cortical visual field sensitivity using the Garway-Heath sectorisation approach.

Here, data are average across 10 LHON patients. Left OCT pRNFL thickness across six defined sectors, shown on a cluster map. Middle: Cortical visual field sensitivity (slope) for the low spatial frequency condition. Right: Cortical visual field sensitivity (slope) for the high spatial frequency condition. Dark colours indicate low OCT pRNFL thickness and cortical sensitivity (flat slopes); bright colours indicate higher OCT pRNFL thickness and cortical sensitivity (steeper slopes).

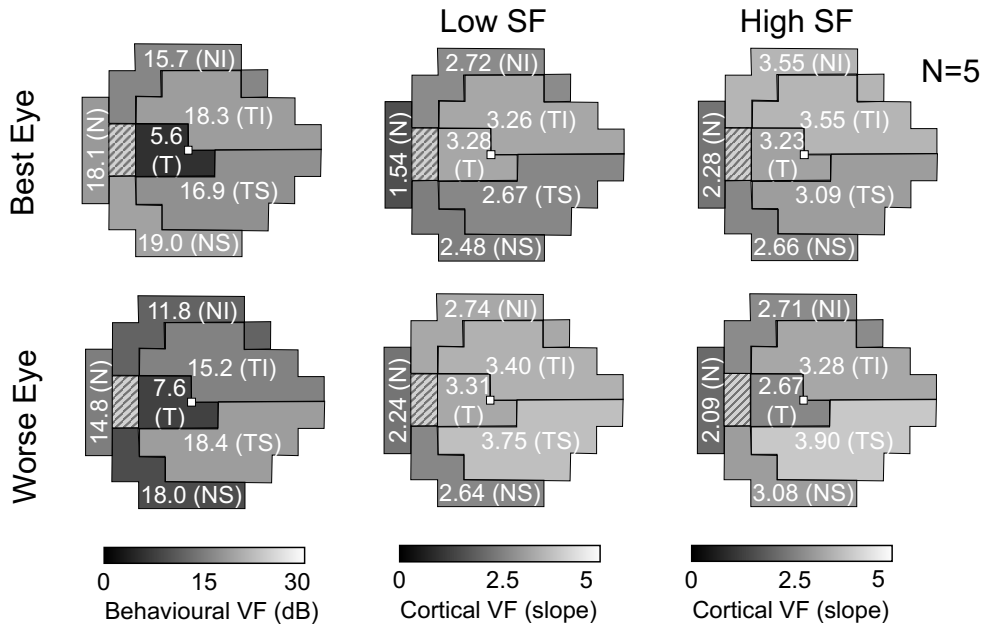

Figure A8.2. Correspondence between behavioural visual field and cortical visual field sensitivities using the Garway-Heath sectorisation approach.

Here, data are average across 5 LHON patients, who met criteria for fixation stability and map quality with Compass perimetry. Left: Behavioural visual field sensitivity across six defined sectors, shown on a cluster map. Middle: Cortical visual field sensitivity (slope) for the low spatial frequency condition. Right: Cortical visual field sensitivity (slope) for the high spatial frequency condition. Dark colours indicate low behavioural and cortical sensitivities (flat slopes); bright colours indicate higher behavioural and cortical sensitivity (steeper slopes).

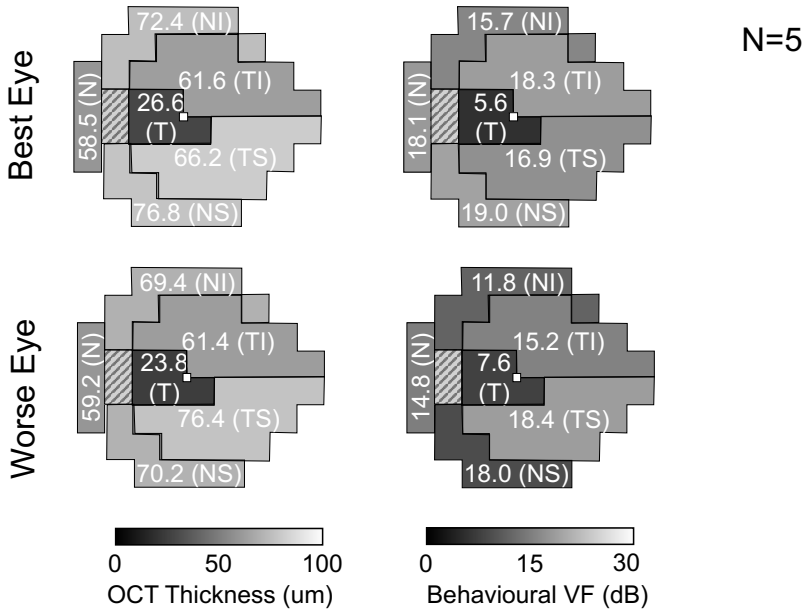

Figure A8.3. Correspondence between OCT pRNFL thickness and behavioural visual field sensitivity using the Garway-Heath sectorisation approach.

Here, data are average across 5 LHON patients, who met criteria for fixation stability and map quality with Compass perimetry. Left: OCT pRNFL thickness across six defined sectors, shown on a cluster map. Right: Behavioural visual field sensitivity for the same sectors. Dark colours indicate low OCT pRNFL thickness and behavioural sensitivity; bright colours indicate higher OCT pRNFL thickness and behavioural sensitivity.

8.2. Qualitative comparison of behavioural and cortical visual field maps in the remaining LHON patients

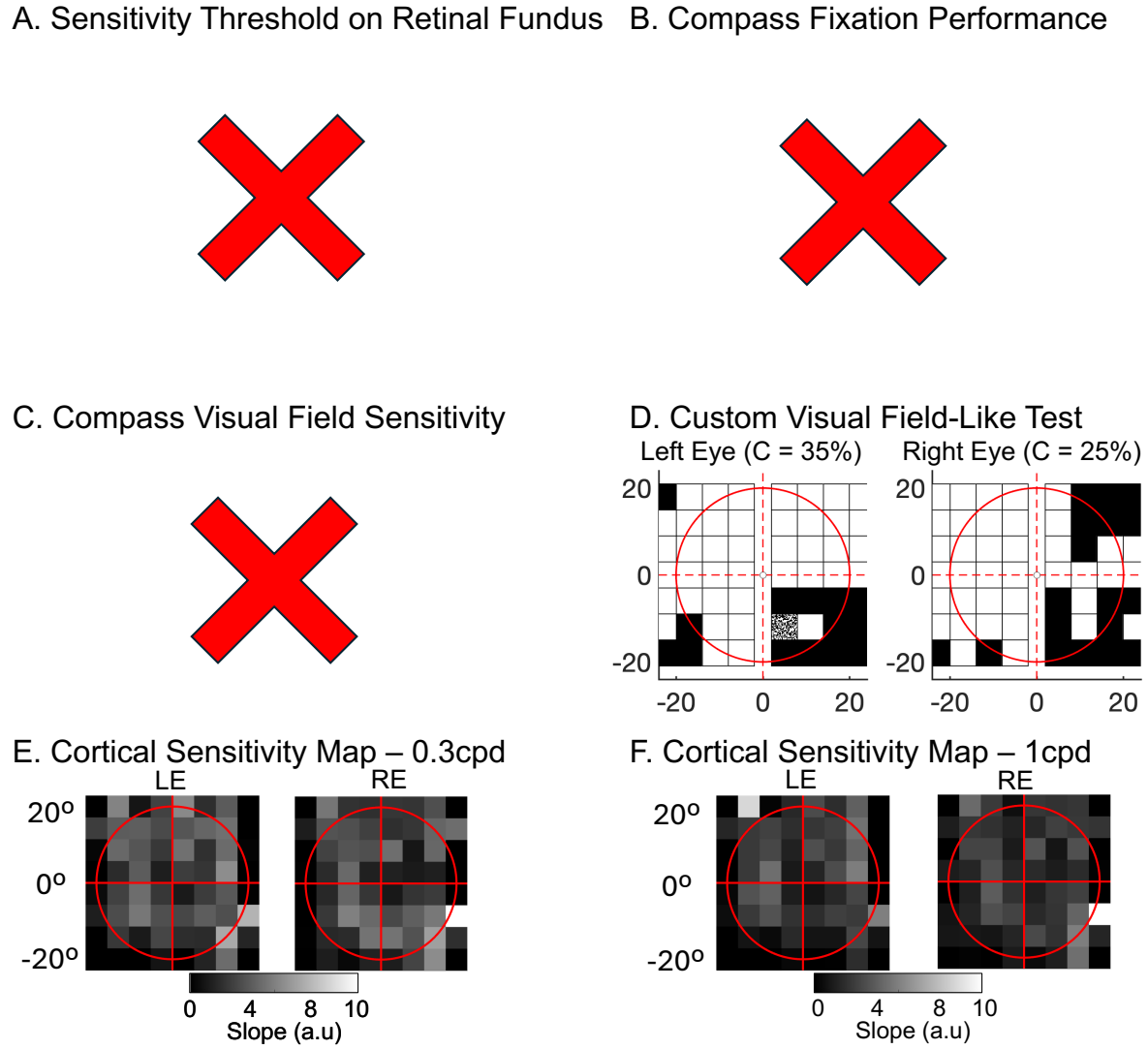

Figure A8.1. Case of P002: Unreliable fixation.
(A-C) Compass data were not collected in this patient. (D) Custom visual field test: black = target not seen, grey = unsure, white = clearly seen. Target contrast per eye is shown in brackets. (E-F) fMRI-based V1 sensitivity maps for low (0.3 cpd) and high (1 cpd) spatial frequencies. Dark squares indicate low cortical sensitivity (flat slopes); bright squares indicate higher sensitivity (steeper slopes).

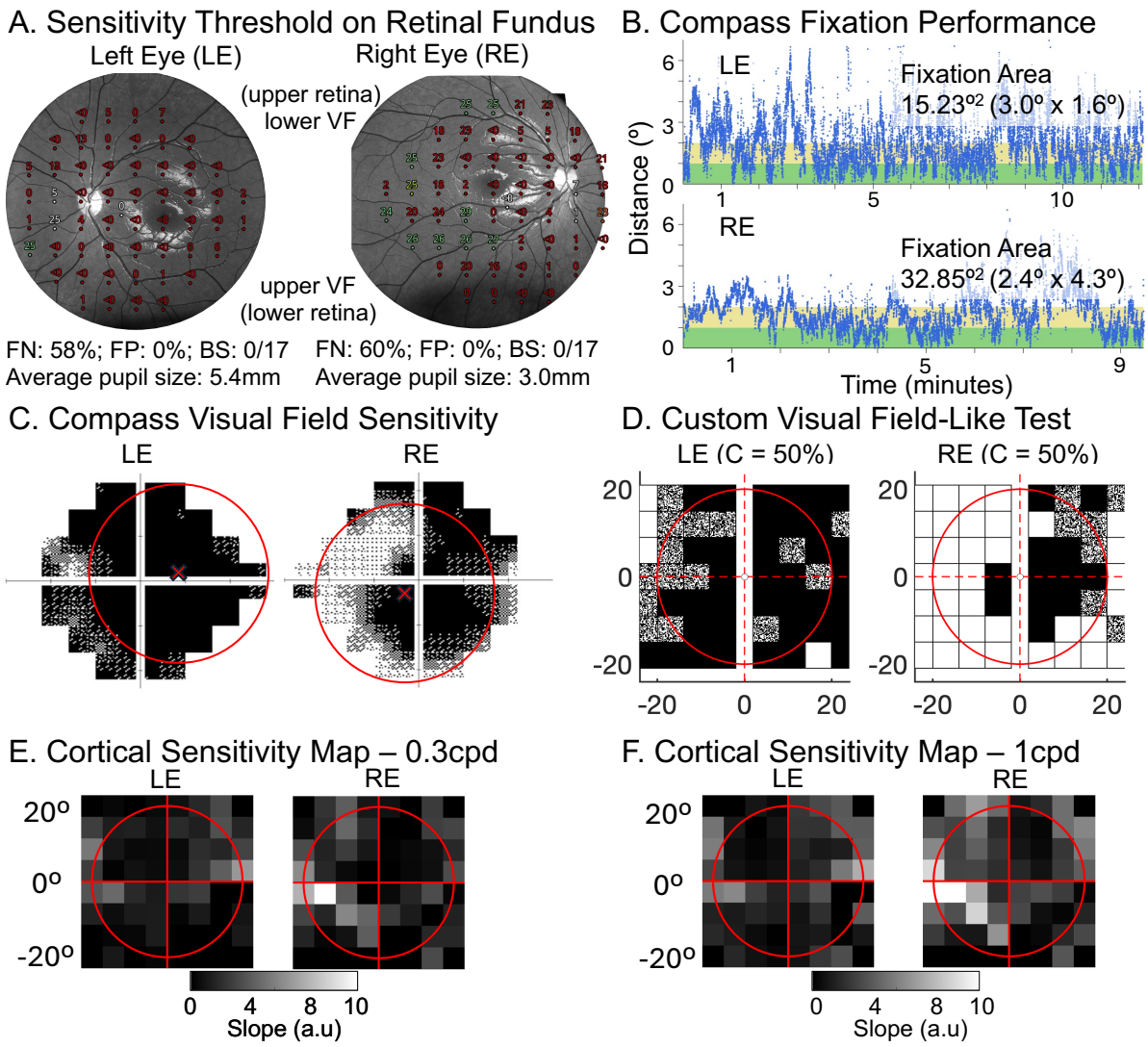

Figure A8.2. Case of P003: Unreliable fixation.

(A) Compass sensitivity thresholds overlaid on the fundus image. Colours reflect normative total deviation: green (p ≥ 5%), orange (p < 5% and ≥ 0.5%), red (p < 0.5%), with white marking the tested foveal and optic disc locations. The true fovea (white arrow) and blind spot were misaligned with tested points. (B) Eye-tracking traces; values within the green/yellow bound indicate acceptable fixation stability. (C) Compass perimetry maps: black indicates no measurable sensitivity; increasing white pixels within each 3×3° grid point reflect higher sensitivity. Red crosses mark the corrected map centre (fovea-aligned); red circles show the 20º fMRI-tested region (D) Custom visual field test: black = target not seen, grey = unsure, white = clearly seen. Target contrast per eye is shown in brackets. (E-F) fMRI-based V1 sensitivity maps for low (0.3 cpd) and high (1 cpd) spatial frequencies. Dark squares indicate low cortical sensitivity (flat slopes); bright squares indicate higher sensitivity (steeper slopes).

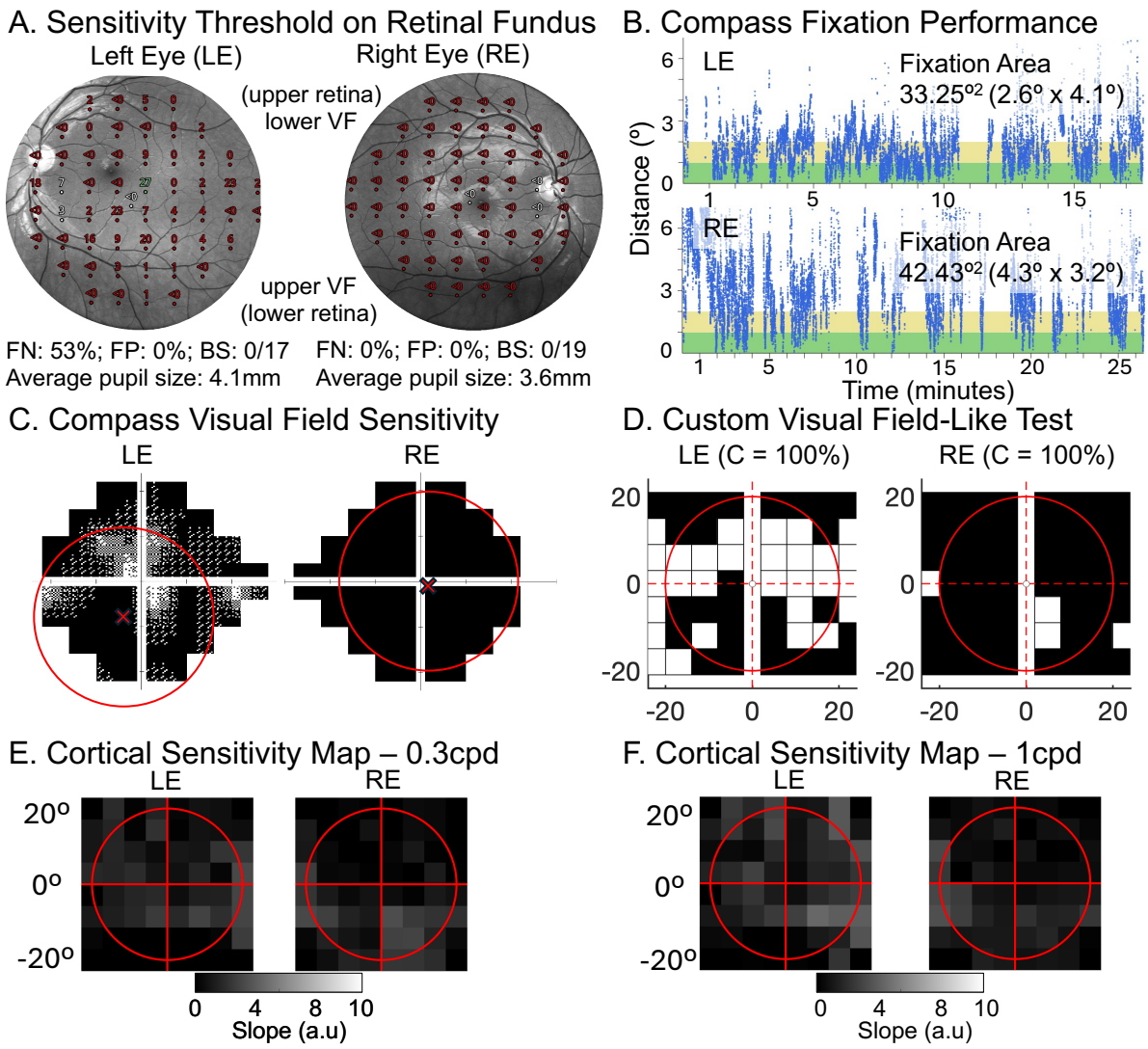

Figure A8.3. Case of P004: Unreliable fixation.

(A) Compass sensitivity thresholds overlaid on the fundus image. Colours reflect normative total deviation: green (p ≥ 5%), orange (p < 5% and ≥ 0.5%), red (p < 0.5%), with white marking the tested foveal and optic disc locations. The true fovea (white arrow) and blind spot were misaligned with tested points. (B) Eye-tracking traces; values within the green/yellow bound indicate acceptable fixation stability. (C) Compass perimetry maps: black indicates no measurable sensitivity; increasing white pixels within each 3×3° grid point reflect higher sensitivity. Red crosses mark the corrected map centre (fovea-aligned); red circles show the 20º fMRI-tested region (D) Custom visual field test: black = target not seen, grey = unsure, white = clearly seen. Target contrast per eye is shown in brackets. (E-F) fMRI-based V1 sensitivity maps for low (0.3 cpd) and high (1 cpd) spatial frequencies. Dark squares indicate low cortical sensitivity (flat slopes); bright squares indicate higher sensitivity (steeper slopes).

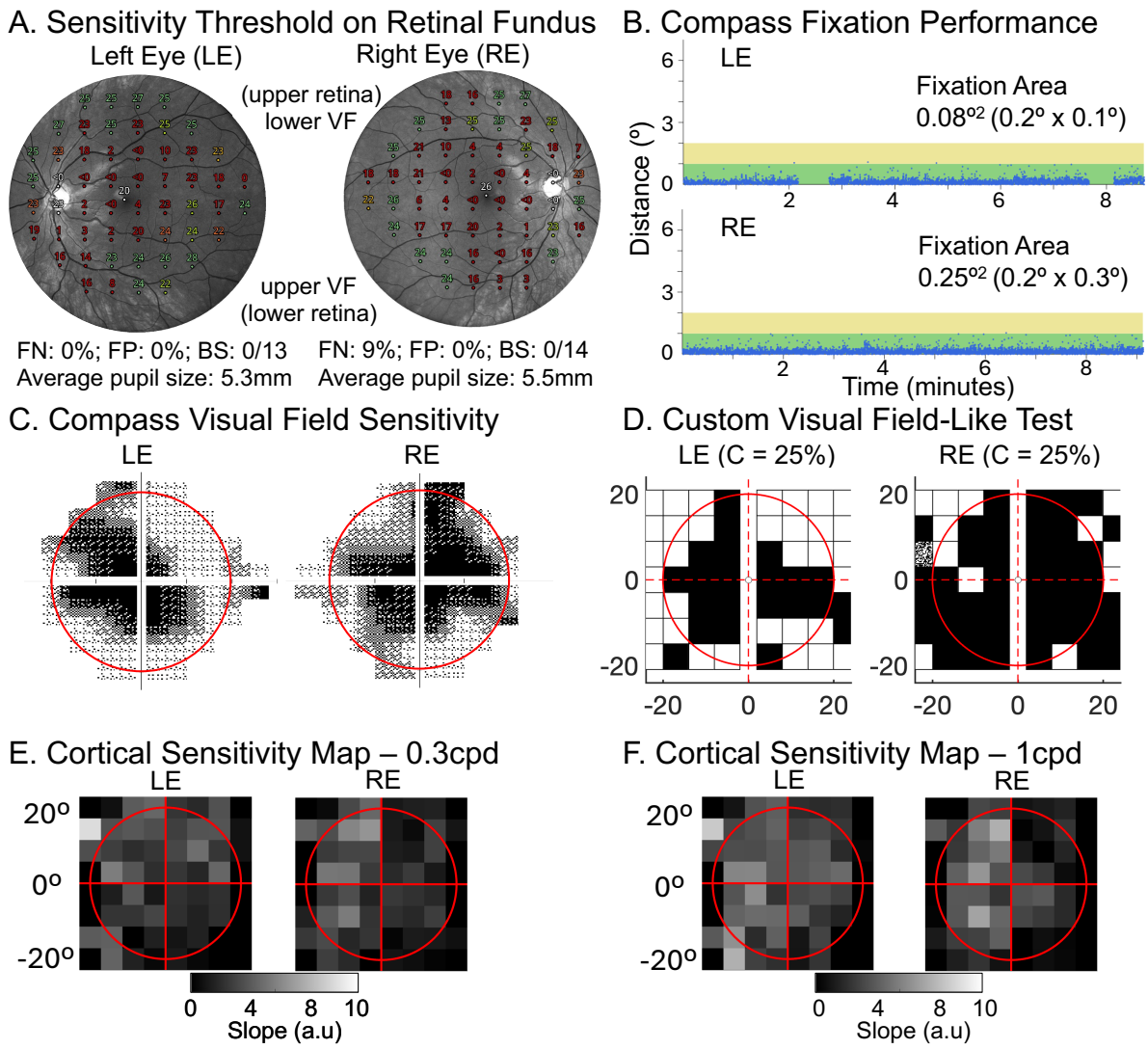

Figure A8.4. Case of P010: Good fixation, but less obvious correspondence

(A) Compass sensitivity thresholds overlaid on the fundus image. Colours reflect normative total deviation: green (p ≥ 5%), orange (p < 5% and ≥ 0.5%), red (p < 0.5%), with white marking the fovea and optic disc. (B) Eye-tracking traces; values within the green/yellow bound indicate acceptable fixation stability. (C) Compass perimetry maps: black indicates no measurable sensitivity; increasing white pixels within each 3×3° grid point reflect higher sensitivity. (D) Custom visual field test: black = target not seen, grey = unsure, white = clearly seen. Target contrast per eye is shown in brackets. (E-F) fMRI-based V1 sensitivity maps for low (0.3 cpd) and high (1 cpd) spatial frequencies. Dark squares indicate low cortical sensitivity (flat slopes); bright squares indicate higher sensitivity (steeper slopes).

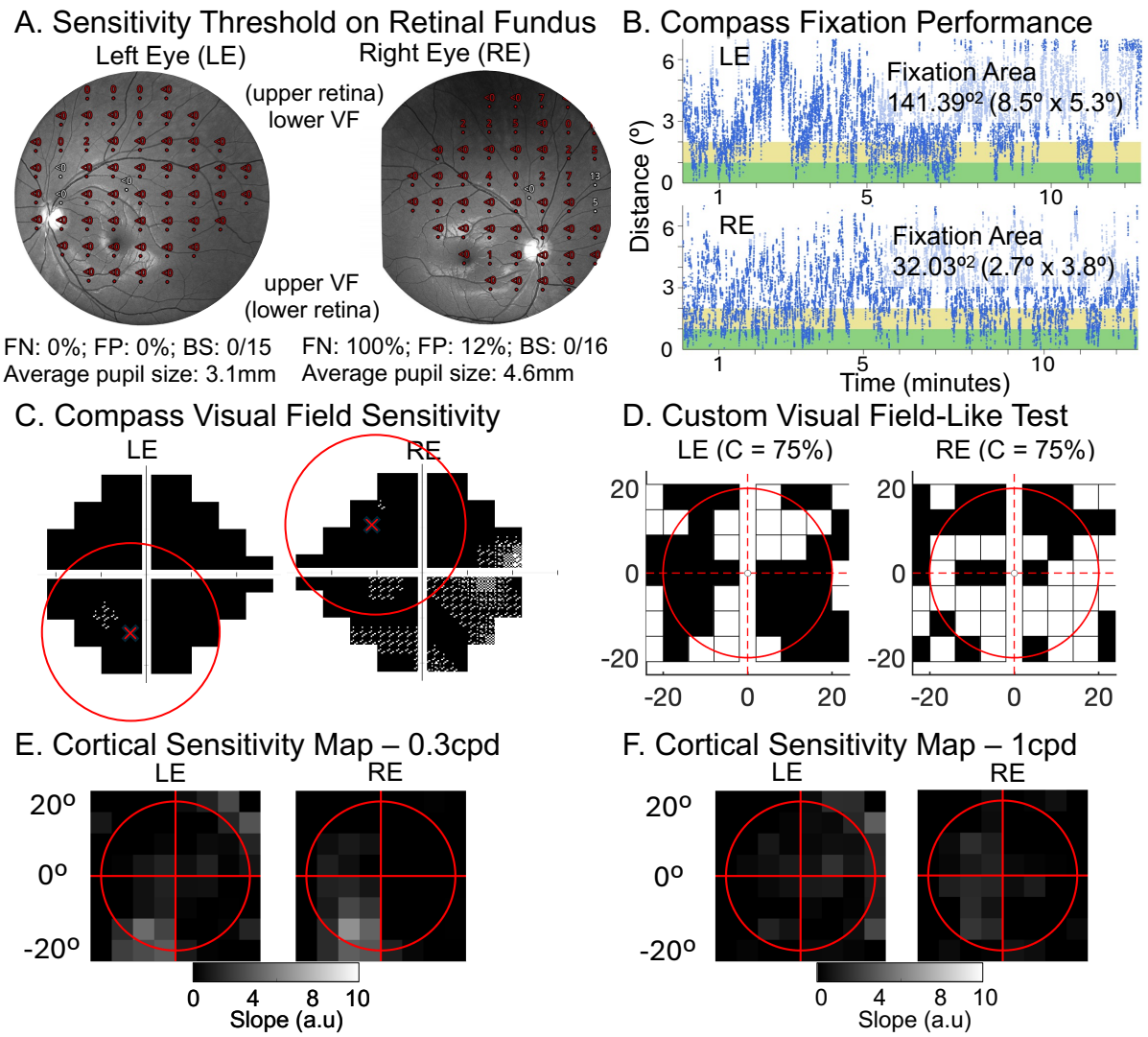

Figure A8.5. Case of P012: Unstable fixation.

(A) Compass sensitivity thresholds overlaid on the fundus image. Colours reflect normative total deviation: green (p ≥ 5%), orange (p < 5% and ≥ 0.5%), red (p < 0.5%), with white marking the tested foveal and optic disc locations. The true fovea (white arrow) and blind spot were misaligned with tested points. (B) Eye-tracking traces; values within the green/yellow bound indicate acceptable fixation stability. (C) Compass perimetry maps: black indicates no measurable sensitivity; increasing white pixels within each 3×3° grid point reflect higher sensitivity. Red crosses mark the corrected map centre (fovea-aligned); red circles show the 20º fMRI-tested region (D) Custom visual field test: black = target not seen, grey = unsure, white = clearly seen. Target contrast per eye is shown in brackets. (E-F) fMRI-based V1 sensitivity maps for low (0.3 cpd) and high (1 cpd) spatial frequencies. Dark squares indicate low cortical sensitivity (flat slopes); bright squares indicate higher sensitivity (steeper slopes).

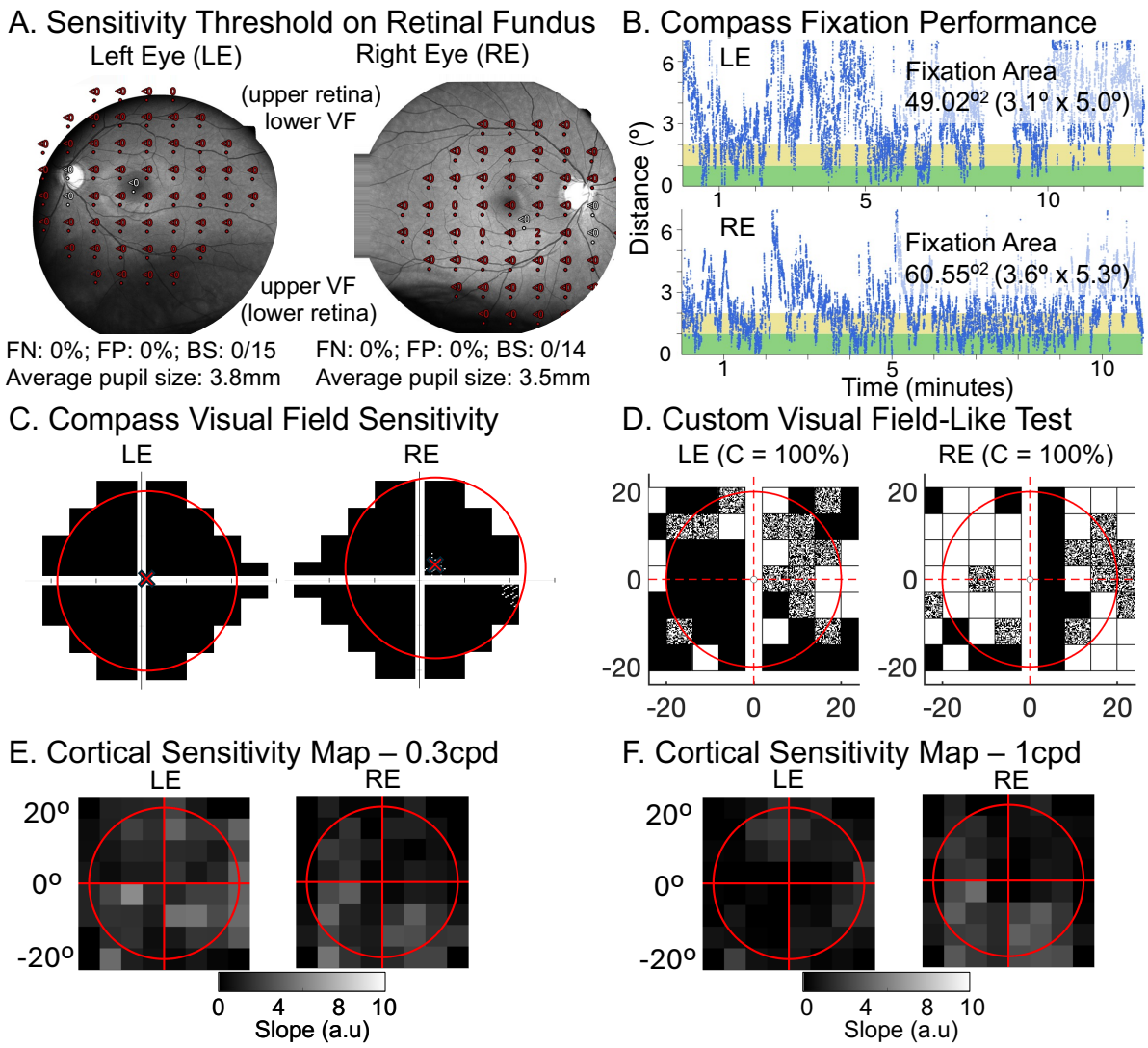

Figure A8.6. Case of P013: Unstable fixation.

(A) Compass sensitivity thresholds overlaid on the fundus image. Colours reflect normative total deviation: green (p ≥ 5%), orange (p < 5% and ≥ 0.5%), red (p < 0.5%), with white marking the tested foveal and optic disc locations. The true fovea (white arrow) and blind spot were misaligned with tested points. (B) Eye-tracking traces; values within the green/yellow bound indicate acceptable fixation stability. (C) Compass perimetry maps: black indicates no measurable sensitivity; increasing white pixels within each 3×3° grid point reflect higher sensitivity. Red crosses mark the corrected map centre (fovea-aligned); red circles show the 20º fMRI-tested region (D) Custom visual field test: black = target not seen, grey = unsure, white = clearly seen. Target contrast per eye is shown in brackets. (E-F) fMRI-based V1 sensitivity maps for low (0.3 cpd) and high (1 cpd) spatial frequencies. Dark squares indicate low cortical sensitivity (flat slopes); bright squares indicate higher sensitivity (steeper slopes).